DE-FC26-03NT41965

Separation of Fischer-Tropsch Wax Products from Ultrafine Iron Catalyst Particles

Final Technical Report

Amitava Sarkar, James K. Neathery, and Burtron H. Davis (P. I.)

Reporting Period
September1, 2003 to September 30, 2006

The University of Kentucky
Center for Applied Energy Research
2540 Research Park Drive
Lexington, Kentucky 40511-8410

ABSTRACT

A fundamental filtration study was started to investigate the separation of Fischer-Tropsch Synthesis (FTS) liquids from iron-based catalyst particles. Slurry-phase FTS in slurry bubble column reactor systems is the preferred mode of operation since the reaction is highly exothermic. Consequently, heavy wax products in one approach may be separated from catalyst particles before being removed from the reactor system. Achieving an efficient wax product separation from iron-based catalysts is one of the most challenging technical problems associated with slurry-phase iron-based FTS and is a key factor for optimizing operating costs. The separation problem is further compounded by attrition of iron catalyst particles and the formation of ultra-fine particles.

Existing pilot-scale equipment was modified to include a filtration test apparatus. After undergoing an extensive plant shakedown period, filtration tests with cross-flow filter modules using simulated FTS wax slurry were conducted. The focus of these early tests was to find adequate mixtures of polyethylene wax to simulate FTS wax. Analysis techniques for catalyst particle size distribution were also developed. Initial analyses of the slurry and filter permeate particles focused on catalyst particle attrition and the formation of ultra-fine iron carbide and/or carbon particles. The effects of chemical and physical changes of the catalyst slurry during activation/synthesis on the filtration properties were also studied.

A study of various molecular weight waxes was initiated to determine the effect of wax physical properties on the permeation rate without catalyst present. It was found that the permeate flux was inversely proportional to the nominal average molecular

weight of the polyethylene wax. Even without catalyst particles present in the filtrate, the filter membranes experience fouling during an induction period on the order of several days on-line.

Another long-term filtration test was initiated using a batch of ultrafine iron catalyst that was previously activated with CO in a separate continuous stirred tank reactor (CSTR) system. The permeate flux stabilized more rapidly than that experienced with unactivated catalyst tests.

A series of crossflow filtration experiments were initiated to study the effect of olefins and oxygenate on the filtration flux and membrane performance. Iron-based FTS reactor waxes contain a significant amount of oxygenates, depending on the catalyst formulation and operating conditions. Mono-olefins and aliphatic alcohols were doped into an activated iron catalyst slurry (with Polywax) to test their influence on filtration properties. The olefin concentrations were varied from 5 to 25wt% and oxygenates from 6 to 17 wt% to simulate a range of reactor slurries reported in the literature. The addition of an alcohol (1-dodecanol) was found to decrease the permeation rate while the olefin added (1-hexadecene) had no effect on the permeation rate. A passive flux maintenance technique was tested that can temporarily increase the permeate rate for 24 hours.

Oxidation of Fe (II) sulfate results in predominantly γ-FeOOH particles which have a rod-shaped (nano-needles) crystalline structure. Carbidation of the prepared γ-FeOOH with CO at atmospheric pressure without any mechanical stirring was found to produce iron carbides with irregular spherical layered structure residing in close proximity while carbidation with mechanical stirring results in formation of spherical carbide particles that are separated from each other. Volumetric stress generated during the carbidation

process was suggested to be responsible for the fragmentation of the nano-needle structures

An unpromoted ultrafine iron nanocatalyst (3-5 nm diameters) was used for FTS in a CSTR at 270 °C, 175 psig, $H_2/CO = 0.7$, and a syngas space velocity of 3.0 sl/h/g Fe. Carbidation with CO at 275 °C for 24 h was found to convert the initial Fe_2O_3 into a mixture of 85% $\chi - Fe_5C_2$ and the rest magnetite. The activated catalyst results in ca. 85% conversion of CO and H_2 which decreased to ca. 10% over 400 h of synthesis time and thereafter remained nearly constant up to 600 h. It was found that the catalyst deactivation was accompanied by structural evolution (by gradual in situ re-oxidation) of the catalyst from initial nearly pure $\chi - Fe_5C_2$ phase to pure magnetite after 400 h of synthesis time. The nucleation for carbide/oxide transformation was found to initiate at the center of the particle by water produced during FTS. A small amount of $\varepsilon' - Fe_{2.2}C$ phase was detected in some catalyst samples collected after 480 h of FTS could be due to CO, to H_2 or to syngas.

PSD measurements indicated nano-scale growth of individual catalyst particles and the statistical average diameters were found to increase by a factor of 4 over 600 h of FTS. Large particles with a dimension greater than 150 nm were also observed. Chemical compositions of the larger particles were found to be pure single crystals of magnetite, as revealed by EELS analysis. Carbide particles were identiied as ultrafine particles which were observed in smaller numbers during later periods of FTS. The results suggested that carbide/oxide transformation and nano-scale growth of particles continues either in succession or simultaneously but definitely not in the reverse order. An amorphous carbon rim of 3-5 nm thickness were observed around some particles after

activation and during FTS. Well ordered graphitic carbon layers on larger single crystal magnetite particles were also found. However, the maximum thickness of the carbon (amorphous or graphitic) rim does not grow above about 10 nm, suggesting that the growths of particles were not due to a continuation of carbon deposition.

Rubidium promoted iron Fischer-Tropsch synthesis (FTS) catalysts were prepared with two Rb/Fe atomic ratios (1.44 and 5) using rubidium nitrate and rubidium carbonate as Rb precursors. Rb promoted catalyst was found to result in a steady conversion with a lower deactivation rate than that of the corresponding unpromoted catalyst although the initial activity of the promoted catalyst was only about half that of the unpromoted catalyst. The composition of iron carbide phase formed after carbidation was found to be $\chi - Fe_5C_2$ for both promoted and unpromoted catalysts while for the Rb promoted catalyst, $\varepsilon' - Fe_{2.2}C$ became the predominant carbidic phase as FTS continued and the overall catalyst composition remained carbidic in nature. In contrast, the carbide content of the unpromoted catalyst was found to decline quickly with synthesis time. Results of XANES and EXAFS measurements suggested that Rb was present in an oxidized state and that the compound most prevalent in the active catalyst samples closely resembled or was that of rubidium carbonate.

Phase II of the research program involved the re-design and integration of a 4 liter slurry bubble column reactor (SBCR) with a new cross flow filtration system. The system utilized a primary wax separation device (inertial hydroclone) followed by an interchangeable Accusep or Membralox ceramic cross-flow membrane supplied by Pall Corporation.

A shakedown of the system encountered several problems with the newly-purchased progressive cavity pump used to circulate the wax/catalyst slurry though the cross-flow filter element and reactor. It was indicated that during the activation of the catalyst at elevated temperature (> 270 °C) the elastomer in the pump stator released catalyst poisons which deactivated the iron-based catalyst. Difficulties in maintaining an acceptable leak rate from the pump seal and stator housing were also encountered. Consequently, the system leak rate exceeded the expected production rate of wax; therefore, no online filtration could be accomplished.

Simulated FT wax with an ultra-fine iron catalyst was utilized for filtration demonstration experiments in the SBCR pilot plant with cross-flow filtration module. The concentration of iron present in the permeate was found to be less than 15 ppm in most of the cases. A constant flux maintenance module was developed which consists of interrupting the permeate flow for 30 seconds per half hour. This module was found to be effective in recovering the initial membrane fouling; however, the long-term steady-state flux was not achieved with the method. Flux stability was attained only after increasing the permeate off cycle to 1 hour per day in addition to 30 seconds off per half hour cycle.

TABLE OF CONTENTS

EXECUTIVE SUMMARY

A fundamental filtration study to investigate the separation of Fischer-Tropsch Synthesis (FTS) liquids from iron-based catalyst particles was initiated. Loss of catalyst particles and/or filter plugging during filtration is a major concern in the operation of slurry phase FTS reactors using iron-based catalysts. Attrition of such catalysts in slurry-phase reactors produces a significant amount of fines, making catalyst separation from the wax products difficult. During slurry-phase FTS with bubble column reactors, catalysts are generally separated from accumulated reactor wax by either internal filtration or an external settling system which circulates catalyst particles back to the reactor. Catalyst fines produced by attrition may cause filters to plug and are difficult to separate by settling. As a result, multiple filtration stages are needed in order for the waxes to be well-suited for down-stream processing requirements.

The main objective of this filtration study was to test the effectiveness of various cross-flow filtration modules with a simulated or actual FTS wax/catalyst slurry. The physical properties of the wax products from a FTS reactor can vary widely depending on the type of process implemented. In this study, the focus was on iron-based slurry-phase reaction using a high-alpha catalyst. The change in filtration properties of iron catalyst slurries was correlated with physical and chemical changes of the particles during activation and Fischer-Tropsch conditions.

Phase I encompassed the first two years of this program, where a state-of-the-art filtration test platform was utilized to study the effects of process parameters, slurry chemical/physical changes, and filter media on the permeate flux and quality (based on Fe content). The unit was capable of testing slurry batches as large as 98 liters (26 gallons) while testing several types of cross-flow filter modules. Additionally, constant flux maintenance procedures were tested with the goal of maintaining the highest achievable permeation rate over the lifetime of the filter membranes. Phase II began in year 3 of the program, when a prototype cross-flow filtration system was retrofitted to an existing slurry bubble column reaction (SBCR) unit to test the efficacy of the filtration procedures developed using the filtration test platform. This unit was also designed to allow several types of cross-flow filter media to be utilized under FTS conditions.

Phase I began with the shakedown of the filtration test platform using a Polywax 3000 wax (without added catalyst) to check out the pumps, associated process instrumentation and the permeation/back-pulse system. This also provided a worst-case scenario for the clean-fluid permeation rate of the filter medium. Attempts to pass the Polywax 3000 through a 0.1 μm membrane were not successful. Apparently, the filter medium was overwhelmed by the large molecular weight compounds of the heavy wax since no solids were present in the slurry.

Another filter module with 0.1 mm pore opening was tested with 5 wt% catalyst slurry in a wax mixture of C_{30} oil/Polywax 3000 in a weight ratio of 86:14. While operating in a continuous filtration mode, the initial permeate flux was 0.65 lpm/m^2 and steadily declined below 0.3 lpm/m^2 over a 6-day test period. The lack of long-term flux

stability was attributed to fouling from the higher molecular weight components from the Polywax 3000 and from the attrition of the catalyst particles resulting in higher concentration of fines (below 1 μm).

A subsequent 2-weeks duration test with a 5wt% catalyst in a Polywax 500 and back-pulsing displayed more stability and higher permeate flux rates (0.58 lpm/m^2 or 20.6 GPD/ ft^2). When the permeate back-pulsing was stopped, the permeate flux dropped 25% from 0.58 to 0.43 lpm/m^2. The permeate samples consistently had a bright white appearance and contained less than 1 ppm as Fe.

In order to quantify the degree of filter media fouling, a static permeation rig was constructed to test the permeability of the membranes before and after catalyst filtration tests. The curve of the membrane flux vs. trans-membrane pressure (TMP) provided a snapshot of the tube's fouling condition. Results from the permeation rig have shown a significant degree of fouling due to the Polywax simulant slurries. However, heating the cross-flow filtration elements in air returns the medium to their original state.

Following the initial shakedown phase, test slurries were processed using an unactivated, high alpha iron catalyst added to various mixtures of polyalphaolefins (Durasyn 164) and polyethylene waxes (a commercial line of products called Polywax, manufactured by Baker Petrolite). In these tests with unactivated catalyst, the lack of long-term flux stability was partly attributed to the fouling from the higher molecular weight components from the Polywax 3000 (with a nominal molecular weight of 3000 g/mole). Subsequent filtration test results with catalyst slurries prepared with Polywax 500 (average molecular weight 500 g/mole) displayed a similar decline in flux over the first 100 hours time-on-stream.

A series of tests without catalyst were also conducted using Polywax 500, 655, 725 and 855 (with average molecular weights of 500, 655, 725, and 855, respectively). The goal of this test was to quantify the effect of the molecular weight of the wax on the "clean" permeate flux. Additionally, the apparent fouling or induction period of each wax could be observed without the potential interference created by catalyst attrition. The test conditions for the "clean" wax tests were performed with a 4.2 m/s axial cross-flow velocity at 200 ^{o}C; the TMP was varied from 0.7 to 1.7 bar. The permeate flux of the Polywax 500 became stable after dropping from 0.9 to 0.65 lpm/m^2 after 5 days at 1.4 bar TMP. Subsequent test results with the higher molecular weight waxes indicated shorter, if any induction periods. However, the filter element was not removed and regenerated after the initial Polywax 500 test.

The method used to determine particle size distribution in the slurry has been shown to have severe limitations. Slurry samples taken from the filtration unit had to be extracted in o-xylene to remove the wax residue before being submitted for particle size analyses. Problems were encountered in recovering catalyst samples in the extraction thimbles (rated for 0.8 μm); over 30-50% of the catalyst particles passed through the extraction thimble indicating substantial attrition of the particles. Also, qualitative particle settling tests indicated that catalyst attrition is changing the slurry properties over

the time-scale of the filtration tests. Accordingly, a filtration test run using iron catalyst that had been activated in a CSTR system was initiated. It was anticipated that the phase transformation of catalyst to carbide form during activation in CO in addition to the increased physical attrition due to stirring in the CSTR would result in a dramatic decrease in catalyst particle size. The flux stabilized to less than 0.2 lpm/m^2 over a 24 hour period as compared to 6 days with the unactivated catalyst.

Further insight into the mechanism of catalyst attrition (i.e., chemical and physical changes) was studied for commercial development and eventual scale-up of the process. The effect of carbidation on the morphology of iron hydroxide oxide particles in the absence of any mechanical stirring was studied. Homogeneous oxidation of Fe (II) sulfate results in predominantly γ-FeOOH particles which have a rod-shaped (nano-needles) crystalline structure. Carbidation of the prepared γ-FeOOH with CO at atmospheric pressure without any mechanical stirring was found to produce iron carbides with a spherical layered structure. HRTEM and EDS analysis revealed that carbidation of γ-FeOOH particles changes the initial nano-needles morphology and generates ultrafine carbide particles with irregular spherical shape. As the carbidation was performed without any mechanical stirring, it was concluded that the difference in densities of the two phases and resulting stress induced in the particles were sufficient enough to break the needle-like structure to generate a structure which composed of spherical particles residing in close proximity. When the carbidation was performed in the presence of mechanical agitations, formation of spherical carbide particles completely separated from each other was the result.

The morphology, particle size distribution, and chemical composition of iron catalyst particles during activation/FTS was studied by HRTEM, STEM, EELS, and Mössbauer spectroscopy measurements. An unpromoted ultrafine iron nanocatalyst (3-5 nm diameters) was used for FTS in a CSTR at 270 °C, 175 psig, $H_2/CO = 0.7$, and a syngas space velocity of 3.0 sl/h/g Fe. Prior to FTS, the catalyst was activated in CO for 24 h which converted the initial hematite into a mixture of 85% $\chi - Fe_5C_2$ and the rest magnetite as found by Mössbauer measurement. The activated catalyst results in an initial high conversion (ca. 85%) of CO and H_2; however the conversions decreased to ca. 10% over 400 h of synthesis time and after that remained nearly constant up to 600 h. Mössbauer and EELS measurement revealed that the catalyst deactivation was accompanied by structural evolution (by gradual in situ re-oxidation) of the catalyst from initial nearly pure $\chi - Fe_5C_2$ phase to essentially pure magnetite after 400 h of synthesis time. Experimental data indicate that the nucleation for carbide/oxide transformation initiates at the center of the particle by water produced during FTS. Small amounts of $\varepsilon' - Fe_{2.2}C$ phase were detected in some catalyst samples collected after 480 h of FTS.

PSD measurements indicate nano-scale growths of individual catalyst particle. Statistical average diameters were found to increase by a factor of 4 over 600 h of FTS. Particles with the largest dimension greater than 150 nm were also observed. Chemical compositions of the larger particles were always found to be single crystal magnetite as revealed by EELS analysis. Small numbers of ultrafine carbide particles were identified

in the catalyst samples collected during later periods of FTS. The results suggest that carbide/oxide transformation and nano-scale growth of particles continues either in succession or at least simultaneously, but definitely not in the reverse order (in that case some larger carbide particles could be observed). EELS-STEM measurement reveals amorphous carbon rim of thickness 3-5 nm around some particles after activation and during FTS. Well ordered graphitic carbon layer on larger single crystal magnetite particles were found by EELS-STEM measurement. However the maximum thickness of the carbon (amorphous or graphitic) rim does not grow above 10 nm, suggesting that the growth of particles is not due to carbon deposition.

The effect of alkali promotion of iron based catalysts on the composition of cthe arbide phase, catalytic activity, stability, and chemical nature of the promoter during FTS were studied using Mössbauer spectroscopy, EXAFS, and XANES measurement. Rubidium promoted iron Fischer-Tropsch synthesis (FTS) catalysts were prepared with two Rb/Fe atomic ratios (1.44 and 5) using rubidium nitrate and rubidium carbonate as Rb precursors. Results of catalytic activity and deactivation studies in a CSTR revealed that Rb promoted catalyst results in a steady conversion with a lower deactivation rate than that of the corresponding unpromoted catalyst although the initial activity of the promoted catalyst was only half that of the unpromoted catalyst. Mössbauer spectroscopic measurements of CO activated and working catalyst samples indicated that the composition of iron carbide phase formed after carbidation was $\chi - Fe_5C_2$ for both promoted and unpromoted catalysts. However, in the case of the Rb promoted catalyst, $\varepsilon' - Fe_{2.2}C$ became the predominant carbidic phase as FTS continued and the overall catalyst composition remained carbidic in nature. In contrast, the carbide content of the unpromoted catalyst was found to decline quickly as a function of synthesis time. XANES and EXAFS synchrotron techniques were used to determine the chemical compound that most closely represents the state of the Rb promoter in the working catalyst. The results of these measurements suggested that Rb was present in an oxidized state and that the compound most prevalent in the active catalyst samples closely resembled, or was, that of rubidium carbonate.

Another series of tests was performed to study the effect of olefins and oxygenates on the filtration flux and performance of the filter membrane. Waxes produced from iron-based catalysts in FTS contain a significant amount of olefins and oxygenates, depending on the catalyst formulation and operating conditions. Mono-olefins and aliphatic alcohols were doped into a catalyst slurry (with a Polywax blend and 5 wt% Fe at 200^{o}C) to test their influence on filtration properties. The range of olefins (as 1-hexadecene) were varied from 0 to 29 wt% and oxygenates from 0 to 17 wt% (initial charge as 1-dodecanol) to simulate a range of reactor slurries reported in the literature.

The addition of alcohol (1-dodecanol) was found to decrease the permeation rate of a crossflow filter using activated iron slurry. However, additional increases in the alcohol did not affect the permeation rates. Side reaction products of the 1-dodecanol apparently caused a color change in the permeate from bright white to light brown. The

addition of an olefin (1-hexadecene) had little to no effect on the permeate flux and quality.

A passive flux maintenance procedure was tested in which the trans-membrane pressure is suspended for an extended period. A single test for a 75 hour "off" period had shown that the flux can be increased by over 100%, but decays back to the original steady-state flux over 24 hours. A possible flux maintenance scheme could employ two filters; one filter in the "permeate mode" while a duplicate filter is being regenerated with slurry without trans-membrane pressure.

Phase II involved installing a filtration loop with a moyno-type progressive cavity pump to circulate the FT slurry through the primary hydroclone separator, with one output returning to the reactor while the other output flows to the cross-flow elements. The prototype filtration modules are zirconia-coated steel membranes having a nominal pore size of 0.1 μm. The hydroclone was designed to lower the catalyst concentration to below 1wt% solids while the cross-flow element further "polished" the wax to get a concentration of iron below 10 ppm. The flow rate through the cross-flow filter element was to be measured by a coriolis flow meter. Quantifying the flow was important because the slurry velocity is crucial in cross-flow filtration. The wax permeate flow from the filter was limited by a control valve actuated by a reactor level controller. Hence, a constant inventory of slurry was to be maintained within the SBCR system as long as the superficial gas velocity remained constant. It was necessary to calculate changes in the gas hold-up due to a variable gas velocity so that the space velocity could be accurately quantified. This system was intended to be used throughout the study to develop an optimum cleaning program that could sustain a permeate flux rate over a many days.

The system was designed so that the wax/catalyst slurry will have two separate flow paths: (1) a low flow circuit (1-2 lpm) passing through the bubble column, and (2) a higher rate slurry path through the cross-flow filter. Several problems with the circulation pump were encountered. The pump seal initially was unable to provide an acceptable leak rate under the operating synthesis pressure. Additionally, the elastomers of the pump stator were not suitable with the FT slurry during the elevated temperatures needed for catalyst activation. Breakdown of the fluoroelastomer released catalyst poisons which quickly deactivated the iron catalyst.

In order to test the proposed filtration under real-world conditions it was decided to operate the filtration system independent of the SBCR pilot system. In lieu of FT wax produced directly from the bubble column, we prepared a test slurry containing FT wax rendered from previous pilot SBCR and CSTR reactor tests and activated ulrafine iron NANOCAT® iron catalyst. The goal of this test was to monitor and record filter flux measurements over a long term time on stream period (500+ hours). Various flux maintenance or filter cleaning procedures were employed over the long term test, attempting to stabilize the flux over time.

TASK 1. Basic Filtration Studies

Task 1.1 Fundamentals of Cross-Flow Filtration, Filtration Shakedown and Simulated Wax-Solvent Filtration Study

1.1.1. ABSTRACT

Different aspects of inertial and filter-cake mechanism for filtration of ultrafine particles in the context of slurry-phase Fischer-Tropsch synthesis have been discussed and corresponding governing equations have been summarized. Higher molecular weight components and catalyst fines from FTS are known to contribute to the fouling of filter membranes. Filtration tests with a slurry containing 5 wt% iron catalyst in a solvent that is a mixture of C_{30} oil and Polywax 3000 were conducted at 200^{o}C. The initial permeate flux was 0.65 lpm/m^2 and steadily declined to below 0.3 lpm/m^2 over a 6-day test. The lack of long-term flux stability was attributed to the possible fouling of filter medium by the higher molecular weight Polywax 3000. Filtration tests with a slurry containing 5wt% catalyst in Polywax 500 with back-pulsing resulted in better stability and higher permeate flux rates (0.58 lpm/m^2 or 20.6 GPD/ ft^2) with a concentration of Fe less than 1 ppm in the wax. When permeate back-pulsing was stopped, the permeate flux dropped 25% from 0.58 to 0.43 lpm/m^2. Results from the permeation rig have shown a significant degree of fouling due to the Polywax simulant slurries. However, calcining the cross-flow filtration elements in air returns the permeability of the filter mediums to their original state.

1.1.2. INTRODUCTION

1.1.2.1. Concept of Cross-Flow Filtration Operation

The design of a cross-flow filter system employs an inertial filter principle that allows the filtrate to flow radially through the porous media at a relatively low face velocity as compared to that of the mainstream slurry in the axial direction as shown schematically in Figure 1.1-1 [1]. Particles entrained in the high velocity axial flow field are prevented from entering the porous media by the ballistic effect of particle inertia. It has been suggested that sub-micron particles penetrate the filter medium to form a "dynamic membrane" or sub-micron layer as shown in Figure 1.1-2a. The membrane impedes further penetration of even smaller particles through a porous filter media. In many filtration applications, this filtration mechanism is valid for an axial velocity greater than 6 m/s.

A modified cross-flow filtration technique can be developed using a cross-flow filter element that is placed in a down-comer slurry recirculation line of a slurry bubble column reactor. Counter to the traditional cross-flow technique described earlier, this system uses a bulk flow rate below the critical velocity, thereby forcing a filter cake of solids to form between the filter media and the bulk slurry flow, as depicted in Figure 1.1-2b. In this mode, multiple layers of catalyst particles deposit upon the filter medium to act as a pre-filter layer [2,3]. Both the inertial and filter-cake mechanisms can be effective; however, the latter can be unstable if the filter cake depth is allowed to grow indefinitely. In the context of the slurry bubble column reactor (SBCR) operation, the filter cake could potentially occlude the slurry recirculation flow path if allowed to grow uncontrollably. Therefore, when operating in the filter-cake mode, the axial velocity

should be maintained at a level such that an adequate shear force exists along the filter media to prevent excessive caking of the catalyst that could cause a blockage in the down-comer circuit. For ultra-fine particle separation in the context of FT slurry applications, the filter medium can easily become plugged using the dynamic membrane mode filtration. Small iron carbide particles (less than 3 μm) near the filter wall are easily taken into the pores of the medium.

Filtration data taken from constant differential pressure tests shall be analyzed according to traditional filtration science techniques with some modifications to account for the cross-flow filter arrangement [4]. Resistivity of the filter medium may vary over time due to the infiltration of the ultrafine catalyst particles within the media matrix. Flow resistance through the filter cake can be measured and correlated to changes in the activation procedure and to the chemical/physical properties of the catalyst particles. First the clean medium permeability must be determined before the slurries are filtered. The general filtration equation, or the Darcy equation, for the clean medium is defined as:

$$Q_c = \frac{\Delta p \cdot A}{\mu \cdot R_m} \qquad (1)$$

where, Q_c = the clean medium filtrate flow rate ($m^3\ s^{-1}$);

μ = the liquid viscosity (Pa·s);

ΔP = driving pressure force or differential pressure across the filter medium (Pa);

R_m = clean medium resistance or the permeability/filter cake depth (m^{-1}); and

A = filter medium surface area (m^2).

Once the solids build up on the filter medium, the filter cake resistance in series with the medium must be considered. Hence, the Darcy equation becomes:

$$Q = \frac{\Delta p \cdot A}{\mu \cdot (R_m + R_c)} \qquad (2)$$

where R_c is the filter cake resistance (m^{-1}). If we assume the catalyst filter is incompressible, then the filter cake resistance depends on the mass of the catalyst deposited on the filter medium:

$$R_c = \alpha \cdot w \qquad (3)$$

where w is the mass of catalyst per unit area (kg· $m^{-2)}$ and α is the specific filter cake resistance (m· kg^{-1}). In the context of the proposed cross-flow filtration technique, we will assume that w is constant after some measured steady-state period, $t_{ss,}$ while the filter medium is exposed to a constant differential pressure and a constant axial velocity through the filter tube (see Figure 1.1-3). Initially (t = 0), the permeate stream exiting the filter encounters only flow resistance from the medium. As the catalyst begins to accumulate on the filter, the cake resistance term increases until the rate of catalyst deposited and the rate catalyst entrained into the bulk flow field are equal. Thus, a steady-state permeate flow, Q_{ss}, is attained. A mass balance of the filter cake during the unsteady state period yields the following equation for the steady-state filter loading:

$$w_{ss} = \frac{C_s}{A} \cdot \int_0^{t_{ss}} Q(t) \cdot dt - r_{ent} \int_0^{t_{ss}} dt \qquad (4)$$

where, C_s is the catalyst concentration in the bulk slurry ($kg \cdot m^{-3}$), Q(t) is the transient permeate flow rate ($m^3 \cdot s^{-1}$), t_{ss} is the approximate to reach equilibrium in the filter cake (s) and r_{ent} is the re-entrainment rate of catalyst from the filter cake into the bulk slurry ($kg \cdot m^{-2} \cdot s^{-1}$). In equation (4) we have assumed that the re-entrainment rate of catalyst from filter into the bulk slurry is constant throughout the filtration process. After steady-

state filtration is achieved ($t > t_{ss}$), the re-entrainment rate of slurry will be equal to the rate of catalyst captured on the filter cake:

$$r_{ent} = \frac{Q_{ss}}{A} \cdot C_s \qquad (5)$$

where, Q_{ss} is the steady-state permeate flow rate. Once the equilibrium filter cake mass is known, the specific resistance, α, can be calculated using equations 2 and 3. After each constant differential filtration test has ended, the filter medium was backwashed to remove the filter cake. Filtration of the slurry was then be restarted in order to check clean filter permeate flow rate, Q_c, and thus the medium resistance factor, R_m.

It is anticipated that the equilibrium filer cake mass will depend strongly on the axial velocity through the cross-flow filter assembly. The shear rate at the filter surface will increase the entrainment of the catalyst solids for a given permeate flow rate. Therefore, for each differential pressure condition, the axial velocity will be varied in order to quantify the effect of the wall shear on the filter cake resistance term.

1.1.2.2. Filtration Shakedown and Simulated Solvent-Wax Filtration

Traditionally, iron catalysts have been used for F-T synthesis when the syngas is coal-derived, because they have the ability to simultaneously carry out FTS and WGS reactions. Thus, less hydrogen is required in the feed and oxygen exits the reactor in the form of CO_2. Iron catalysts such as those used by Sasol are typically prepared by precipitation while cobalt catalysts are generally supported on high surface area oxides such as alumina, silica and titania. Both types of catalysts, and probably cobalt more so than iron, are very sensitive to sulfur poisoning. However, filtration issues in cobalt-based FTS reactors should be less problematic since catalyst supports are more attrition resistant than that of iron-based systems.

Because the Fischer-Tropsch synthesis (FTS) reaction is so exothermic, one of the major problems in control of the reaction is heat removal. Recent work has concentrated on the use of slurry phase reactors which are able to solve the problem of heat removal from this very exothermic reaction, as well as use low H_2/CO ratio syngas, provide high catalyst and reactor productivity, permit catalyst regeneration, and have relatively simple designs and low initial costs.

Catalyst attrition is a major problem in the operation of slurry phase FT reactors using iron-based catalysts [5,6]. Attrition of such catalysts in slurry reactors produces significant amounts of fines, making catalyst separation from the products difficult. During slurry phase FTS with bubble column reactors, catalysts are generally separated from accumulated reactor wax by either internal filtration or an external settling system which circulates catalyst back to the reactor. Catalyst fines produced by attrition may cause filters to plug and are difficult to separate by settling. Ultimately, the long residence time of a catalyst particle in an industrial reactor is sufficient to break down catalyst particles. Therefore, a robust filtration system is needed for FTS to be a viable technology.

Generation of fines from a SBCR can occur in 4 stages: (1) the release of nascent fine particles from the surfaces of the bulk catalyst particle that were formed during catalyst preparation; (2) initial products of attrition from physical breakage of the catalyst particles; (3) the stresses induced in formation of iron carbide crystallites, and (4) attrition during the long-term synthesis. Each of these stages present unique filtration problems during the production of FTS wax.

Some limited fundamental studies have shown that attrition resistance of iron-based catalysts depends on the type of activation the catalyst receives [7]. However, these studies have not attempted to correlate the change in filtration properties of catalyst slurries with physical and chemical changes of the particles under conventional FTS conditions. Iron-based Fischer-Tropsch (FT) catalysts undergo a series of phase transformations during activation and use.

Catalyst activation with carbon monoxide or syngas typically results in the conversion of Fe_2O_3 to Fe_3O_4 and ultimately to one or more carbides during reaction synthesis [1]. Fine particles extracted from a FTS slurry are shown in Figures 1.1-1 and 1.1-2. The slurry samples were dissolved in ortho-xylene, which is subsequently evaporated from a lacey carbon substrate. As shown in Figure 1.1-1, the iron crystallite agglomerates can be as large as 0.2 to 1.0 μm. However, iron particles on the order of 10-20 nm are also predominant as shown in Figure 1.1-2. The mobility of these smaller nm-scale particles is unknown. During the filtration process, clusters of these particles may agglomerate and make for a more efficient separation. It is also likely that a portion of these smaller crystallites migrate into the filter media and cause irreversible fouling.

Numerous separation processes have been proposed in the literature based on a variety of filtration media along with washing/cleaning techniques [8-12]. Most of these filtration methods are for primary filtration (removing wax products with reduced catalyst concentration, below 2000 ppm). Secondary filtration should reduce the catalyst concentration below about 1-15 ppm such that the wax can be compatible with downstream processes such as cracking.

1.1.3. EXPERIMENTAL

1.1.3.1. Filtration Test Platform

An existing pilot plant platform was modified into a cross-flow filtration test unit. This unit, shown schematically in Figure 1.1-6, will allow several types of cross-flow filter media to be evaluated under simulated FTS conditions. Three prototype filtration modules were received from Pall, Inc. The modules have an inlet (filtrate) and outlet (retentate) ports with ½" tubing ends, and a permeate port, located near the midpoint of the unit, as shown in Figure 1.1-7. The filters' stainless steel membranes have a nominal pore size of 0.1 μm. The surface of the filter media substrate is coated with a proprietary sub-micron layer of zirconia.

The filtration piping and instrumentation is heated via several circuits of copper heat-trace tubing. A Therminol 66 heat transfer fluid is circulated through the heat-trace tubing from an electrically-heated hot oil system. The temperature controller was calibrated to operate over a temperature range of 180 to 250^{o}C.

Data gathering and process control functions are accomplished by a National Instruments real-time computer system. A 98 liter (26 gallon) slurry mixing tank is heated by a hot-oil circulation jacket. Slurry mixtures of catalyst and wax are loaded batch-wise into the system. A Moyno (progressive cavity) pump is used to circulate the mixture through the cross-flow filter element. A manually-actuated valve, located downstream of the filter element, maintains a slurry flow rate set-point of 2 to 40 lpm.

Unfiltered slurry (or retentate) passing through the filter tube is recycled to the mixing tank. The differential pressure across the filter medium or trans-membrane pressure (TMP) is automatically controlled by a let-down valve. The permeate can be

recycled to the slurry tank for continuous filtration simulation (in order to maintain a constant solids concentration in the system) or can be collected and removed from the system to test semi-batch filtration schemes. The permeation rate is periodically measured by diverting the stream into a collection flask over a convenient time interval. Samples can be collected before the filter for characterization. In tests where the catalyst is activated, a gas pad of CO or syngas can be applied to the system; otherwise the system vapor space is purged with inert gas such as argon or nitrogen. Slurry temperature, simulating the FTS activation conditions, can be controlled up to 240^{o}C. Modular filtration media can be tested under various filtration rates, differential pressures and operating modes. The system is designed so that the filter unit can be bypassed in order to change filters while the slurry continues its circulation.

A variety of precipitated catalyst slurries mixed with various molecular weight waxes (C_{30} to C_{100}) will allow a range of effective slurry viscosities to be studied [13]. In addition, a series of filtration experiments with ultra-fine iron particles (less than 3 μm) for evaluating the "worst-case" scenario of wax/catalyst separation has been effected.

1.1.3.2. Filter Back-flush System

As shown in Figure 1.1-8, the back flush system consists of a piston pump that is triggered by a computer controlled timer. The back-flush fluid consists of cleaned permeate stored in a 40 ml tube bomb located near the suction side of the piston pump. This system was used throughout the study to develop an optimum cleaning program that can sustain a permeate flux rate over a many days.

1.1.3.3. Static Permeation Apparatus

In order to quantify the degree of filter media fouling, a static permeation rig to test the permeability of the membranes before and after catalyst filtration tests was constructed. A schematic of this apparatus is shown in Figure 1.1-9. A 4-liter vessel filled with clean/filtered C_{30} oil is heated to a temperature between 180 to 220^{o}C. The C_{30} oil is a commercial polyalphaolefin known as Durasyn 164, produced by BP/Amoco. A differential pressure or an effective TMP can be varied across the filter membrane via helium gas through a pressure regulator. The resulting permeation rate of the C_{30} oil is measured. The curve of the membrane flux vs. TMP will provide a snapshot of the fouling state of the tube.

1.1.4. RESULTS AND DICUSSION

The objective of the initial filtration trials was to test the effectiveness of various cross-flow filtration procedures with a simulated FTS slurry. The wax products from a FTS reactor can vary widely depending on the type of process implemented. In this study, the focus is on a high-alpha iron-based slurry-phase reaction process.

Typical carbon distributions for a high-alpha iron catalyst/wax slurry and a series of wax simulants (Polywax 500, 655, 725, and 855) are shown in Figure 1.1-10. The goal of this test was to quantify the effect of the wax molecular weight on the “clean” permeate flux. Additionally, the apparent fouling or induction period of each wax could be observed without the potential interference created by catalyst attrition. For the FTS wax, hydrocarbons molecules range from carbon numbers 12 to 70+. The majority of the hydrocarbons produced are straight-chain and paraffinic. For iron-based catalysts, olefins make up 50-80% or more of the compounds in carbon numbers less than about 30. A

considerable smaller portion of the FTS wax may be oxygenates, such as alcohols. In a later phase of this program, the effects of these compounds on filtration efficiency were investigated. Initially, the tests were concentrated on filtration of straight-chain paraffin compounds.

The Polywax 500 is a commercial polyethylene polymer (manufactured by Baker-Petrolite) with a narrow carbon number distribution with a nominal average molecular weight of 500. Therefore, the melting point is about 85^{o}C as compared to 90-120^{o}C for that of a typical FTS wax. In our DoE studies, we routinely used a Polywax 3000 (with a melting of >120^{o}C) product as a start-up solvent for our 1-liter CSTRs. The Polywax 3000 contains virtually no compounds with less than 70 carbons; therefore, it was useful for studying FTS chemistry since there was minimal analytical interference for quantifying the rate of FTS products formation. Furthermore, the start-up solvent remains in the reactor even at high gas flow because of its low vapor pressure.

The test conditions for the "clean" wax tests were 4.2 m/s axial cross-flow velocity at 200^{o}C; the TMP was varied from 0.7 to 1.7 bar. The permeate flux of the Polywax 500 became stable after dropping from 0.9 to 0.65 lpm/m^2 after 5 days at 1.4 bar TMP. In Figure 1.1-11, the results of a variable TMP study with the Polywax 500 are shown for 2- and 6-days online. On average, the flux was consistently 0.25 lpm/m^2 lower after 6 days time-on-stream than that of the initial flux over the 0.7-1.7 bar TMP range tested.

Subsequent test results with the higher molecular weight waxes indicated shorter, if any induction periods. However, the filter element was not removed and regenerated after the initial Polywax 500 test. Once the Polywax 500 test was completed, the wax

was drained from the system and a new batch the 655 was added, and so on. In Figure 1.1-12, the permeate flux of the Polywax 725 is plotted over a 2-day period with a TMP range of 0.4 to 1.7 bar. The flux change over the one day period was less than 0.1 lpm/m^2 at 1.7 bar. For TMP lower than 1.4 bar, the change in flux is not detectable between the two data sets.

The effect of the wax molecular weight on the permeate flux (without catalyst) in shown in Figure 1.1-13. Power law functions were fitted for each data set at 0.7, 1.1 and 1.4 bar TMP. Overall the flux varied inversely with molecular weight according to the general formula:

$$Flux = k \cdot \frac{1}{MW^{\alpha}}$$

where power-law exponent, α , varied from 2.49 to 2.88; and k = 3 x 10^7, 2 x 10^7, and 4 x 10^6 for 0.7, 1.1, and 1.4 bar TMPs, respectively.

The 1 μm cross-flow tube used for the clean wax test series (CF-12) was subjected to a static permeation test at 200°C using the Durasyn 164, C_{30} oil before and after the filtration runs. The curve of the static membrane flux vs. TMP, as shown in Figure 1.1-14, can provide a snapshot of the tube's fouling condition. The filter media was fouled with polywax after the filtration tests without catalyst present. Previously, a simple bake out procedure at 500°C was utilized to oxidize the Polywax remaining in the filter media pores. This had been an effective method to restore the filter media such that the static permeation rate was similar to that of a "new" tube. After the Polywax tests, it was decided to lower the bake out temperature to 450°C in order to gauge the sensitivity of temperature on the effectiveness of the procedure. As shown in Figure 1.1-14, the

450°C procedure restored about 50% of the media permeability. A subsequent bake out at 500°C increased the tube's permeability to approximately 60% of the "new" condition.

1.1.4.1. Shakedown Filtration Tests

During the shake-down phase of the filtration test, a batch of Polywax 3000 was melted without catalyst and heated to 200°C. This test slurry was useful for checking potential "cold" areas within the unit and its associated instrumentation lines since Polywax 3000 would solidify at a lower temperature. It also provided a worst-case scenario for the clean-fluid permeation rate of the filter medium. Unfortunately, the filter medium was not able to pass permeate with the Polywax 3000. The membrane became fouled over a period of minutes. An effort was made to purge the filter medium of the heavy wax with 210°C light (C_{30}) oil and then ortho-xylene but this was not successful. Apparently, the filter medium was overwhelmed by the large molecular weight compounds since no solids were present in the slurry.

1.1.4.2. Wax-Solvent Simulated Tests

Another filter module was tested with a mixture of 86:14% C_{30} oil/Polywax 3000 oil without catalyst. Before the catalyst was added, the unit was able to produce a steady permeate rate with a flux of 1 lpm/m^2 at a TMP of 1.38 bar. Unactivated iron catalyst was added to the wax mixture to produce a 5 wt% catalyst/wax slurry. Consequently, the permeate flux dropped from 1.0 to 0.65 lpm/m^2. The test was continued for 6 days in a continuous filtration mode (i.e., the permeate was remixed with the retentate in the 98 liter (26 gallon) recycle tank). The permeate flux measured in this test is plotted versus time on-stream in Figure 1.1-15. During the first day, the permeation flux dropped below 0.5 lpm/m^2. In the subsequent 5 days, the rate of flux decline decreased but did not

become constant. The test was ended after the flux dropped below 0.3 lpm/m^2. The lack of flux stability could be due to two factors: (1) the fouling from the higher molecular weight component contributed from the Polywax 3000, and (2) from the attrition of the catalyst particles resulting in higher concentration of fines (below 1 μm).

1.1.4.3. Filtration Tests with Polywax 500/Catalyst Slurry

After problems with the Polywax 3000 and C_{30} oil catalyst slurry, baseline filtration tests using Polywax 500 (with an average C_{25-30}) and 5 wt% iron oxide catalyst were conducted with and without permeate back-pulsing. As shown in Figure 1.1-16, the initial flux, at 205^{o}C, was nearly 0.85 lpm/m^2 (30 GPD/ft^2) at a TMP of 1.38 bar (20 psid). The test conditions were held constant throughout a week-long period (with back-pulsing) while the permeation rate was monitored. The permeation rate reached a steady-state flux rate of 0.58 lpm/m^2 (20.6 GPD/ ft^2) after 6 days with the periodic back-pulsing program. After 9 days TOS, the back-pulse program was terminated. Consequently, the permeate flux dropped 25% from 0.58 to 0.43 lpm/m^2. The test was continued another 7 days (a total of 16 days TOS) without back-pulsing and the flux rate remained nearly constant.

The quality of the permeate was quantified by iron analyses over the duration of the Polywax 500/catalyst run. Typical permeate and slurry samples are shown in Figure 1.1-17. The permeate samples consistently had a bright white appearance and contained less than 1 ppm as Fe. The dark red or black appearance of the slurry was consistent with that of an unreduced iron oxide catalyst.

1.1.4.4. Filtration Tests with Polywax 500/655 Activated Catalyst Slurry

A run using iron catalyst that had been activated in a CSTR system was initiated. Approximately 700 g of an iron catalyst was activated in two batches with a 1-liter CSTR. The activation conditions were maintained at 270^{o}C and 12 bar for 48 hours under a CO atmosphere. A wax mixture of the 81.3% Polywax 500 and 18.7wt% Polywax 655 was used as the slurry simulant in order to obtain a melting point to a typical FTS reactor wax (with melting point of approximately 95^{o}C). The resulting activated slurry was added to a similar Polywax mixture in the filtration unit such that a 9 wt% slurry was obtained. It was anticipated that the phase change to the carbide form during CO activation in addition to the increased physical attrition from the CSTR agitator would result in a dramatic decrease in catalyst particle size. In Figure 1.1-18, the permeate flux for the activated catalyst slurry is plotted versus time-on-stream. The flux stabilized to less than 0.2 lpm/m^2 over a 24 hour period as compared to 6 days with the unactivated catalyst. Previously, with the unactivated catalyst, the permeate quality was consistently less than 1 ppm as Fe; consequently, the permeate had a bright white appearance. In contrast, the permeate obtained with the activated slurry was tinted brown, but considerable lighter than the catalyst slurry sample as shown in Figure 1.1-19. The brown color of the permeate is due to, or at least largely due to, oxidation of the Polywax. Thus, the iron content of the permeate was measured in the range of 18-30 ppm.

1.1.4.5. Slurry Particle Size Analyses

We attempted to extract periodic samples of the slurry with warm ortho-xylene in a 0.8 μm fiber thimble filters in a soxhlet extraction apparatus. Slurry samples taken

during this test were extracted in o-xylene and subsequently submitted for particle size analyses. Problems were encountered in recovering catalyst samples in the extraction thimbles, especially for the longer duration test runs. For the longer-durations samples, over 30-50% of the catalyst particles passed through the extraction thimble, indicating substantial attrition of the particles.

Qualitatively, the change in particle size may be observed over time by the particle settling of large slurry samples. After each test campaign, the slurry was emptied from the test system into metal buckets to cool and solidify over a 3-4 hour period. Solidified slurry (inverted bucket samples) from two tests of 12 and 26 days in duration are shown in the Figures 1.1-20 and 1.1-21, respectively. In the 12-day run, substantial catalyst settling had occurred, leaving a distinct dark band of catalyst at the bottom and a light brown layer of wax on top. Oppositely, the 26-day run sample showed no signs of gravity settling with a consistent dark reddish-brown appearance from top to bottom. From this observation, the slurry properties change significantly over the time-scale of the filtration tests.

Since the catalyst was unactivated in these cases and recirculated in an inert nitrogen atmosphere, it is likely that most of the particle attrition is from mechanical abrasion. The starting median particle size of the iron catalyst was 43 μm, yet a substantial portion of the slurry samples taken after 1 day of recirculating through the filtration system passed through a 0.8 μm filter thimble during the soxhlet extraction. Another possible attrition mechanism is the thermal shock of the catalyst particles during mixing with the 200^{o}C Polywax 500.

1.1.4.6. Solvent Wax Experiments

The objective of the initial filtration trials was to test the effectiveness of various cross-flow filtration procedures with simulant FTS slurries. The wax products from a FTS reactor can vary widely depending on the type of process implemented. In this study, the focus is on a high-alpha iron-based slurry-phase reaction process. We previously described using two mixtures of FTS wax simulants: Polywax 3000 (M.P. 132^{o}C) and C30 oil (liquid at room temperature); and a Polywax 500 (M.P. 85^{o}C). Each of these wax simulants, with iron catalysts, displayed a tendency to foul the 0.1 μm metal cross-flow membranes. The membranes were cleared by simply heating the filter elements to 500^{o}C in the presence of air. The mode of fouling was unknown; however, we suspected the wax may play a significant role because the membrane fouling rates was higher in tests using the higher molecular weight waxes.

A series of filter permeation tests, without catalyst or other solids, to test the long-term fouling characteristics of waxes with variable molecular weights were conducted. Polywax (purchased from Baker-Petrolite) is available in a variety of molecular weight ranges from 500 to 3000 g/mole. The Polywax materials used in the current permeation study were polyethylene polymers with a narrow carbon number distribution with nominal average molecular weights of 500, 655, 755, and 850 g/mole.

Approximately 6.6 kgs (15 lbs) of each Polywax, beginning with 500 g/mole wax, was melted and circulated through a 0.1 μm cross-flow membrane at a 20 psid trans-membrane-pressure (TMP). The resulting permeate flux was monitored. Once the test period for a given wax was completed, the system was drained and the next higher molecular weight wax was inserted and the test was repeated. The preliminary flux

results from the first three Polywax tests are shown in the Table 1.1-1. As expected, the permeation flux rate decreases with the increasing molecular weight (and thus increasing viscosity) of the wax.

1.1.5. CONCLUSIONS

Higher molecular weight components and catalyst fines from FTS contribute to membrane fouling. Initial test results using a commercial high-molecular weight product (Polywax 3000) through a 0.1 μm membrane proved that the wax alone could foul the filtration medium. It seems that the filter medium pores can be overwhelmed by the large molecular weight compounds of the heavy wax.

Filtration tests with a mixture of 5 wt% iron catalyst in a solvent of C_{30} oil and Polywax 3000 were conducted at 200°C. The initial permeate flux was 0.65 lpm/m^2 and steadily declined below 0.3 lpm/m^2 over a 6-day test. The lack of long-term flux stability was also attributed to the fouling from the higher molecular weight components from the Polywax 3000. Qualitative particle settling tests indicate that catalyst attrition is changing the slurry properties over the time-scale of the filtration tests.

A slurry mixture of 5wt% catalyst in a Polywax 500 and back-pulsing displayed more stability and higher permeate flux rates (0.58 lpm/m^2 or 20.6 GPD/ ft^2). When the permeate back-pulsing was stopped, the permeate flux dropped 25% from 0.58 to 0.43 lpm/m^2. The permeate samples consistently had a bright white appearance and contained less than 1 ppm as Fe. Results from the permeation rig have shown a significant degree of fouling due to the Polywax simulant slurries. However, calcining the cross-flow filtration elements in air returns the tubes to their original state.

The initial membrane fouling experienced with the unactivated catalyst is likely due to changes in the particle size distribution over time. Although the high molecular weight waxes can apparently foul the filter media, the test results for waxes with maverage olecular weight less than 855 g/mole have shown this effect to be minor compared to that of particle size changes.

The permeation flux with activated iron catalyst became stable after only 24-hours. However, the permeate quality suffered in terms of the iron content in the permeate.

Further research is needed to: (1) quantify velocity/shear effects; (2) optimize back-pulsing and other flux maintenance procedures; (3) quantify slurry particle size attrition; and (4) develop a more realistic slurry simulant with various molecular weight Polywax compounds and ultrafine iron catalyst particles.

REFERENCES

[1] Kirk-Othmer Encyclopedia of Chemical Technology (1993), vol. 10, pp. 841-847.

[2] Shoemaker, W., The Spectrum of Filter Media, *A.I.Ch.E. Symposium Series*, 171, Vol. 73 (1977) 26-32.

[3] Clyde Orr (ed), Filtration Principles and Practices, Marcel Dekker, Inc. (1977).

[4] L. Svarovsky (ed.), *Solid-Liquid Separation*, 2nd ed., Monographs in Chemistry and Chemical Engineering, 1981, Butterworths, pp. 242-264.

[5] R. J. O'Brien, L. Xu, D. R. Milburn, Y.-X. Li, K. J. Klabunde, and B. H. Davis, Topics in Catal. **2,** 1, (1995).

[6] B. Jager, R. Espinoza, Topics in Catal. **2**3, 17 (1995).

[7] R. Zhao, J. G. Goodwin, Jr., K. Jothimurugesan, S. K. Gangwal and J. J. Spivey, Ing. Eng. Chem. Res., 40 (2001) 1065.

[8] R. Srinivasan, L. Xu, R. L. Spicer, F. L. Tungate, and B. H. Davis, Fuel Sci. Techn. Int. **1**4, 10 (1996).

[9] Steynberg et al., “Handling of a Catalyst”, U.S. Patent 6,673,846 (2004).

[10] J. Anderson, “Internal Filter for Fischer-Tropsch Catalyst/Wax Separation”, U.S. Patent 6,652,760 (2003).

[11] C. Benham, P. Yacobson, and M. Bohn, “Catalyst/Wax Separation Device for Slurry Fischer-Tropsch Reactor”, U.S. Patent 6,068,760 (2000).

[12] P.Z. Zhou, “Status Review of Fischer-Tropch Slurry Reactor Catalyst/Wax Separation Techniques”, Prepared for the U.S. Department of Energy Pittsburgh Energy Technology Center, Burns and Roe Services Corporation (1991).

[13] N.J. Alderman and N.I. Heywood, “Improving Slurry Viscosity and Flow Curve Measurements”, Chemical Engineering Progress, Vol. 100, No. 4 (2004).

Table 1.1-1 Initial filtration flux results using Polywax.

Type of Polywax	Initial flux (GPD/ft^2)	Ending flux (GPD/ft^2)	% Flux decrease per day
500	36.9	26.0	-15%
655	18.2	10.2	-11%
725	9.8	8.6	-12%

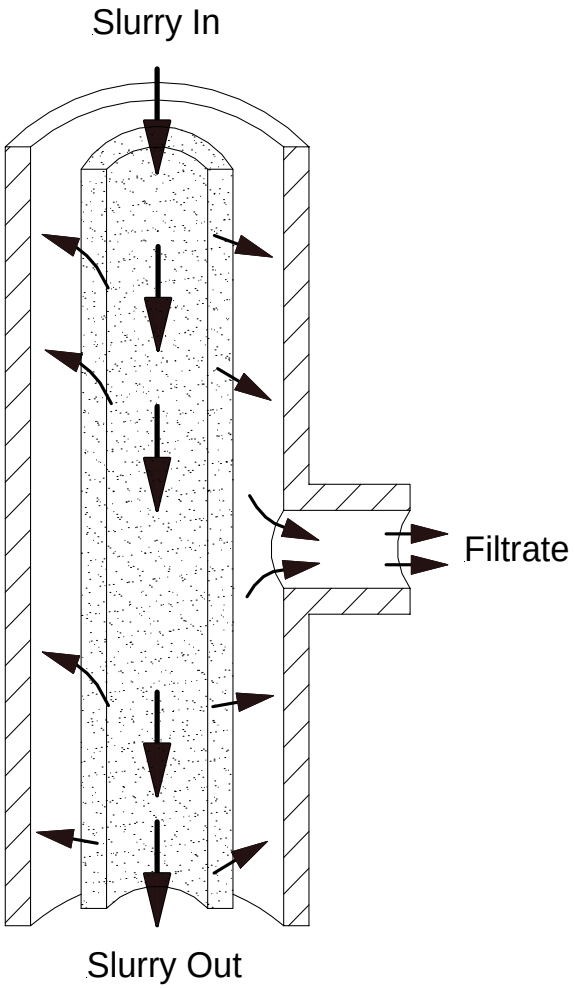

Figure 1.1-1. Cross-sectional view of a cross-flow filter element.

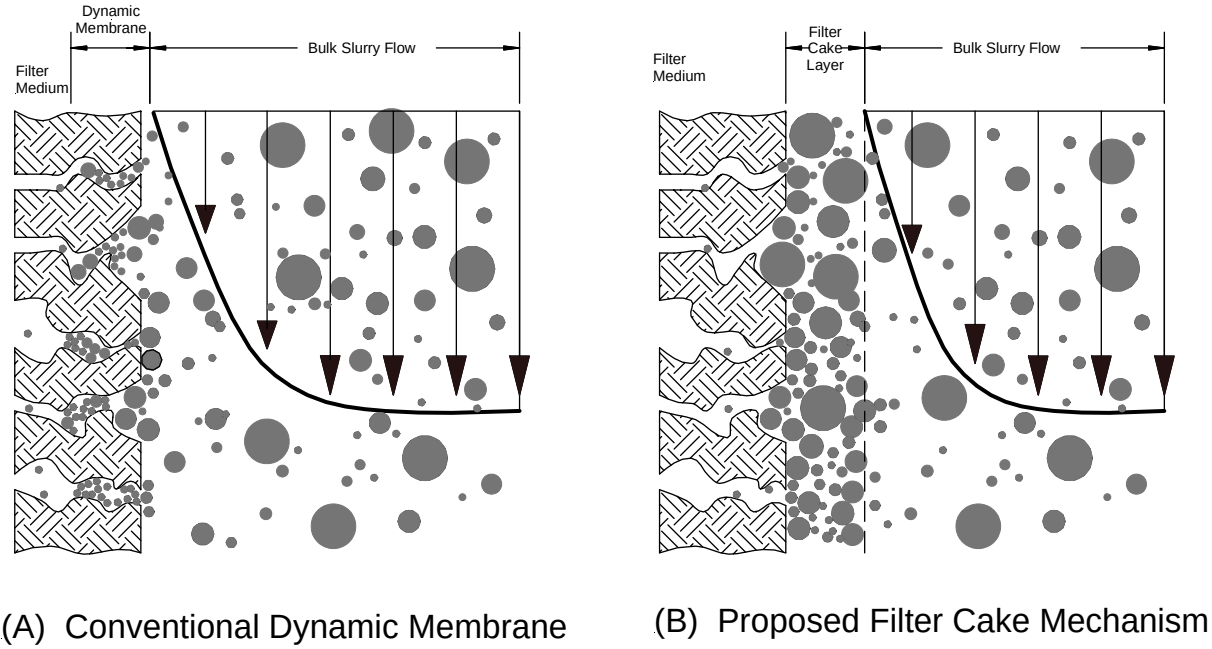

(A) Conventional Dynamic Membrane

(B) Proposed Filter Cake Mechanism

Figure 1.2-2. Models for filter-cake in cross-flow filtration.

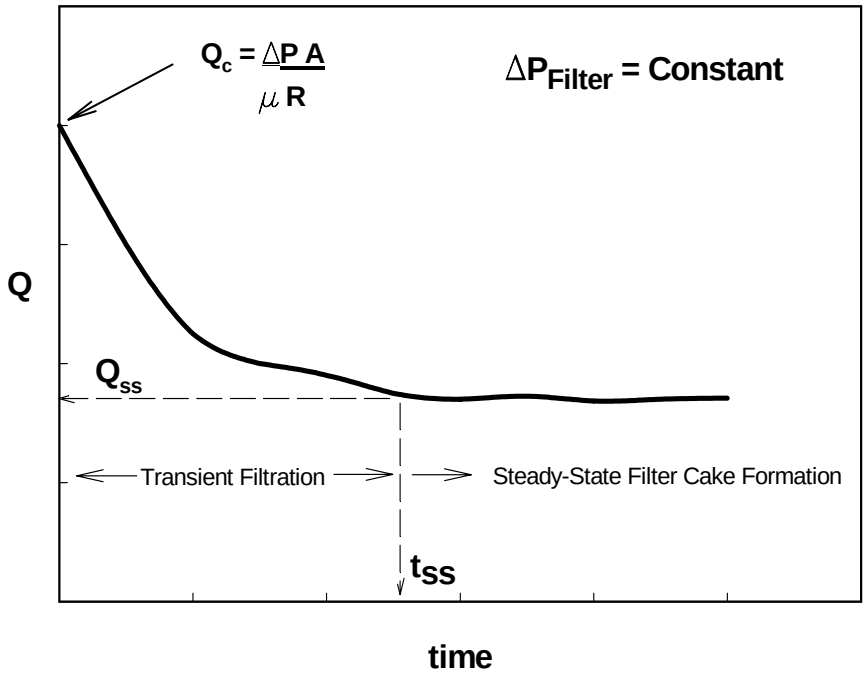

Figure 1.3-3. Variation of permeate flow against time in a typical cross-flow filtration test.

.

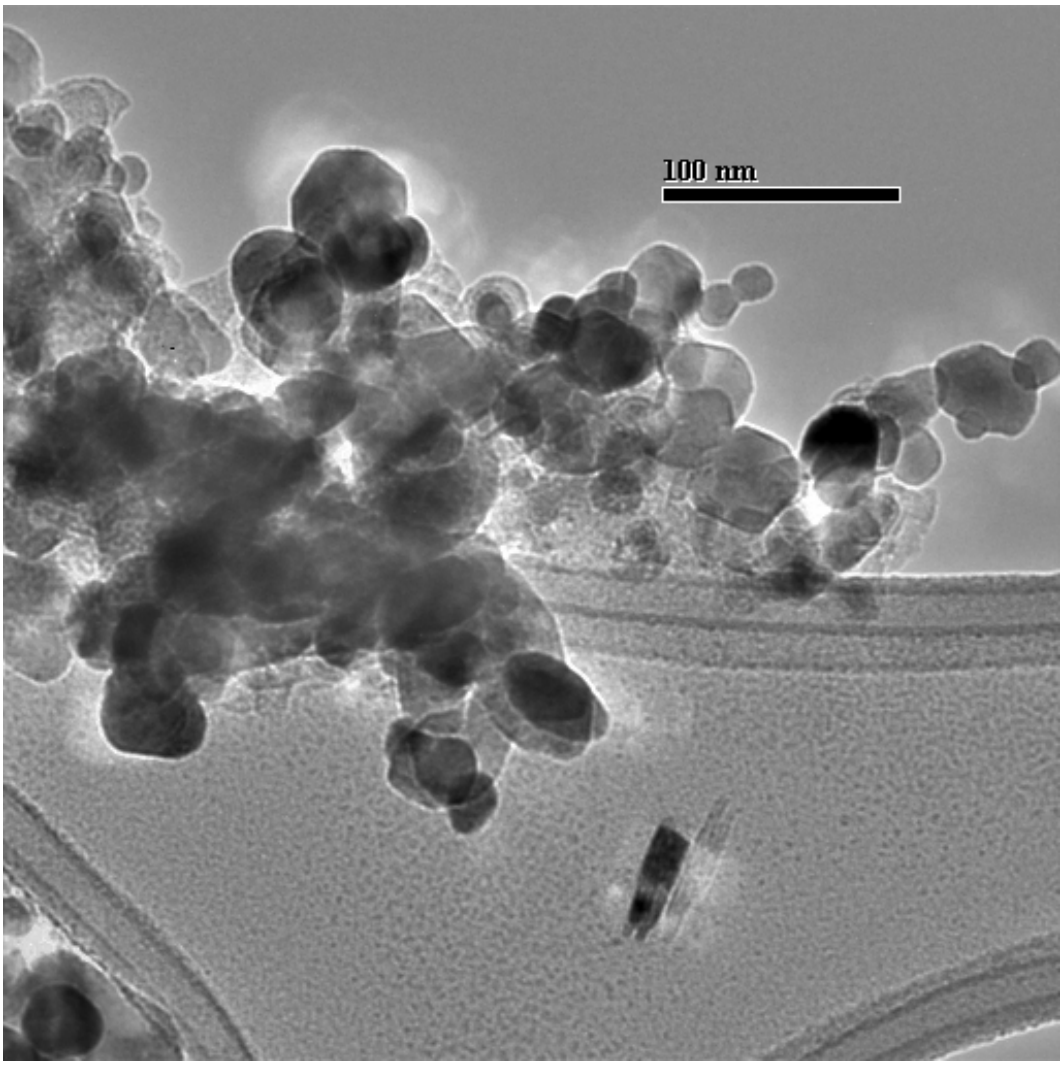

Figure 1.4-4. HRTEM images of iron catalyst agglomerates (after partial removal of wax) present in the slurry.

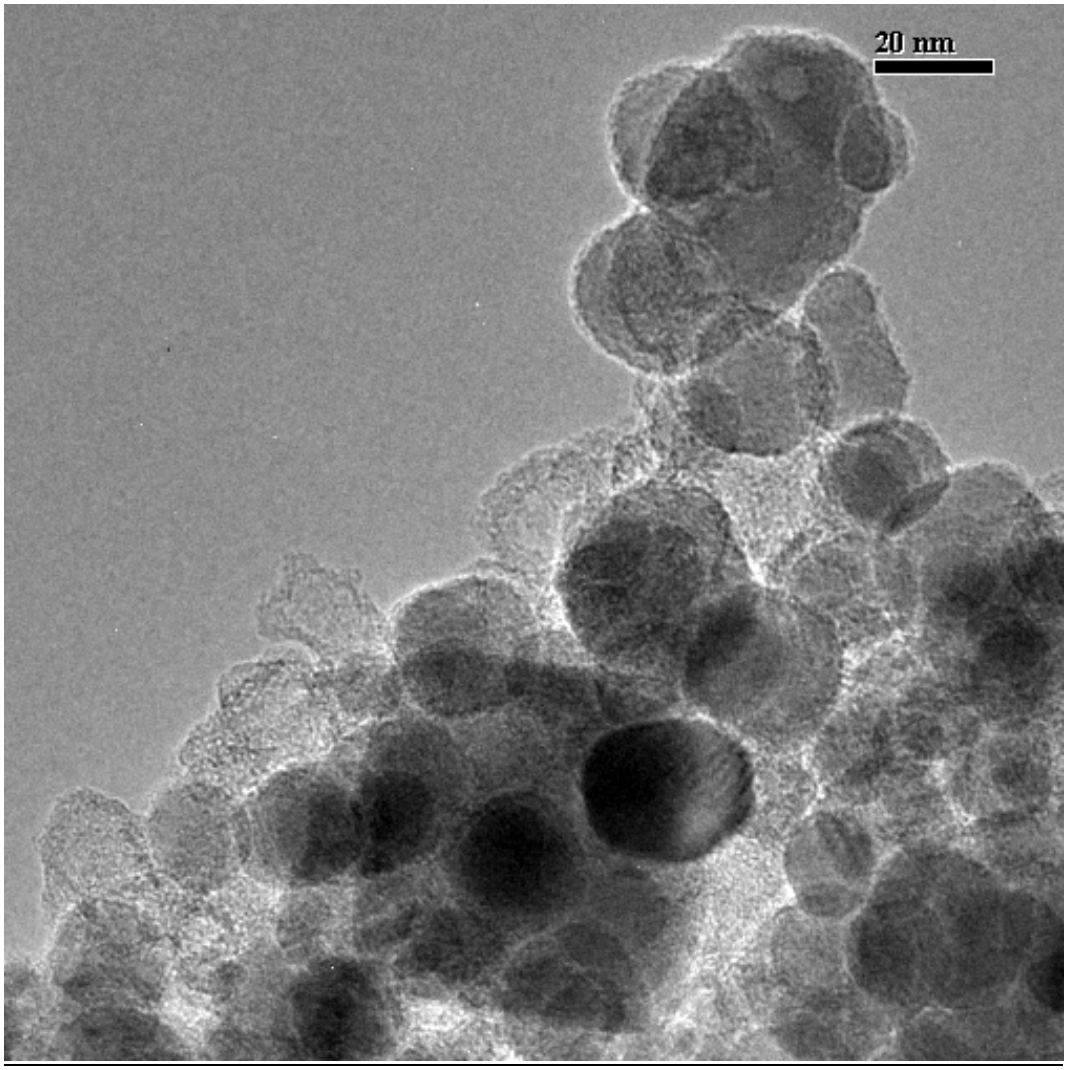

Figure 1.1-5. HRTEM image of iron catalysts used in slurry filtration.

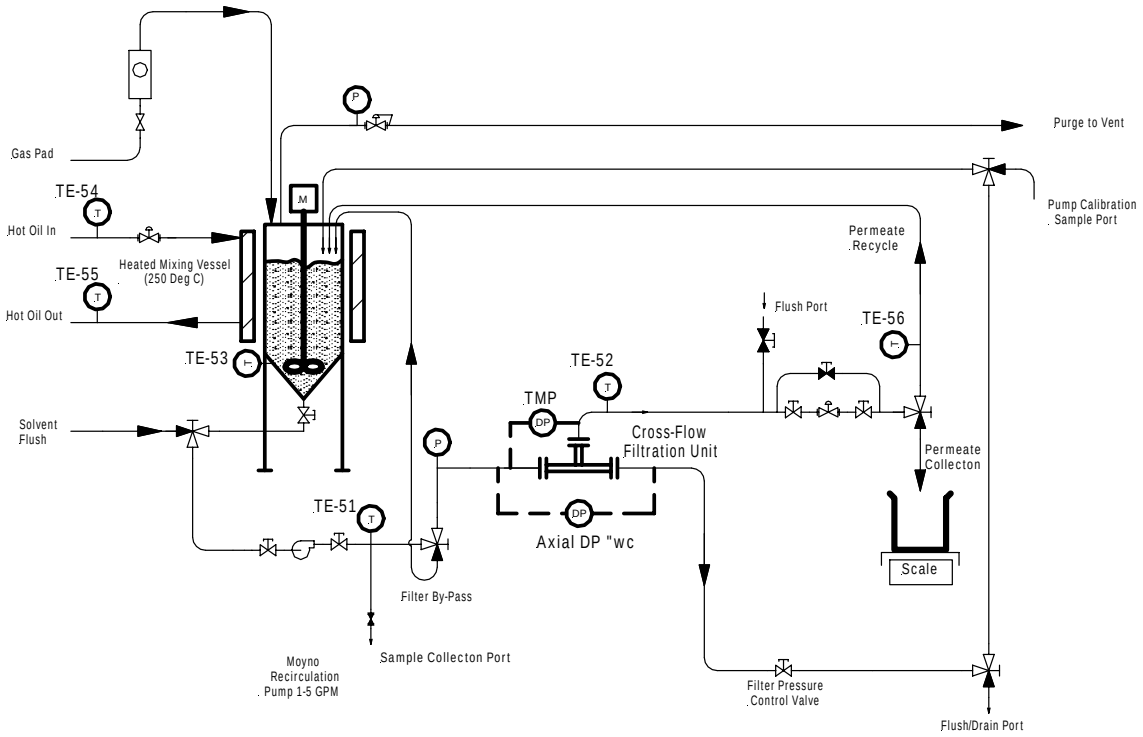

Figure 1.1-6. Schematic of the filtration test platform.

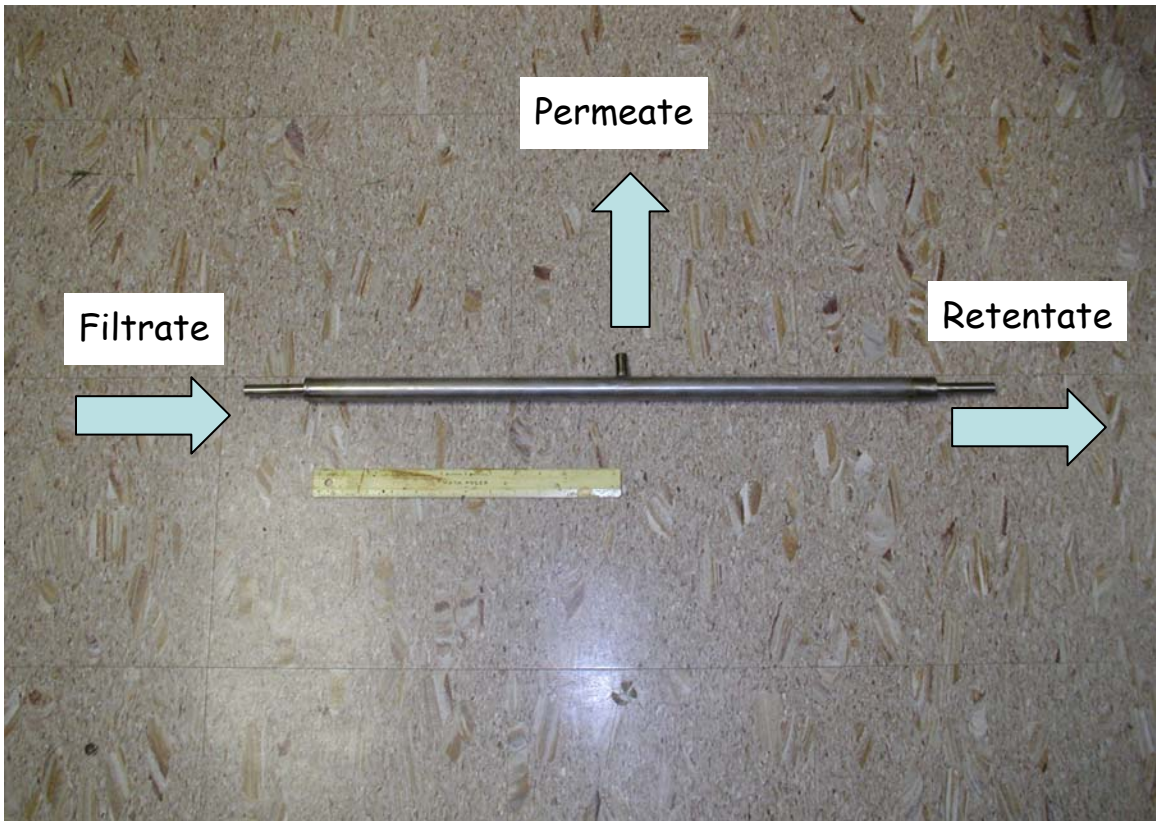

Figure 1.1-7. Photograph of a cross-flow filtration test module.

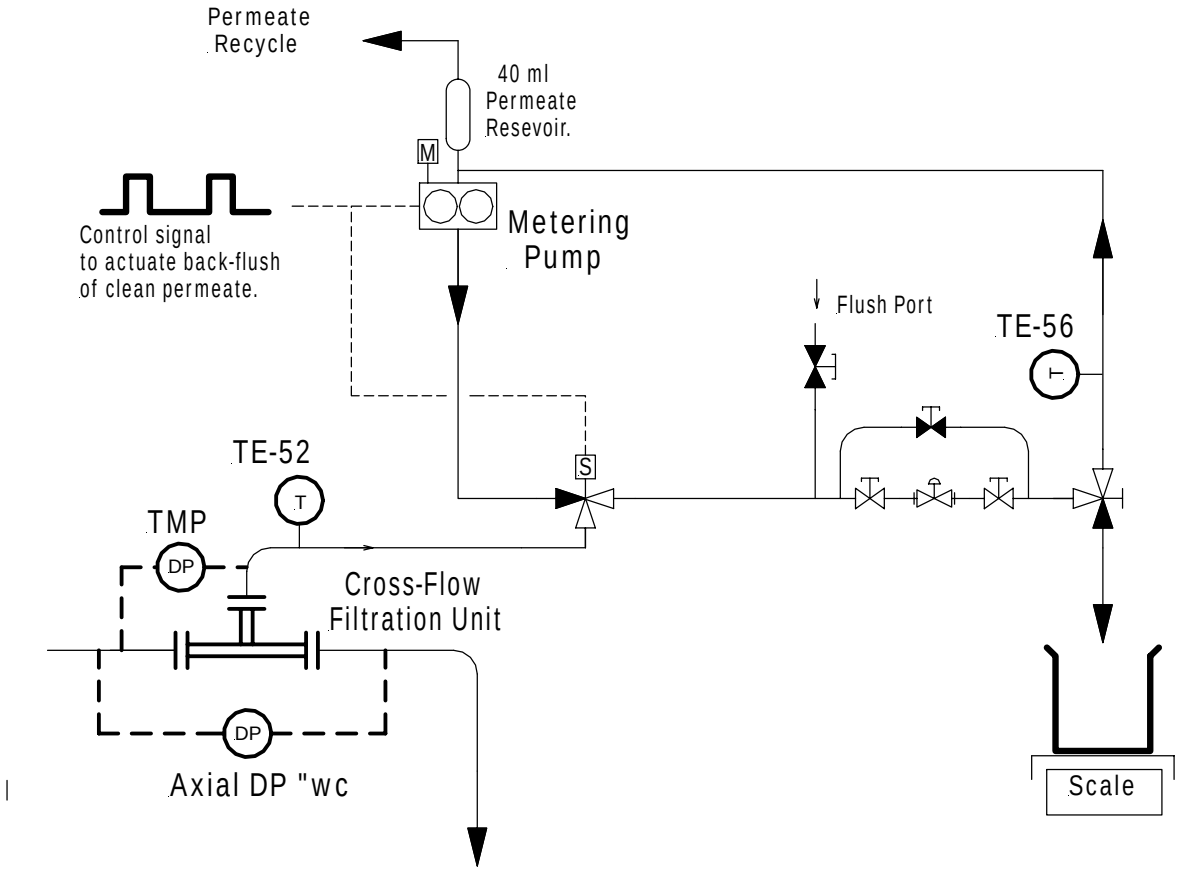

Figure 1.1-8. Schematic of the permeate back-pulse system.

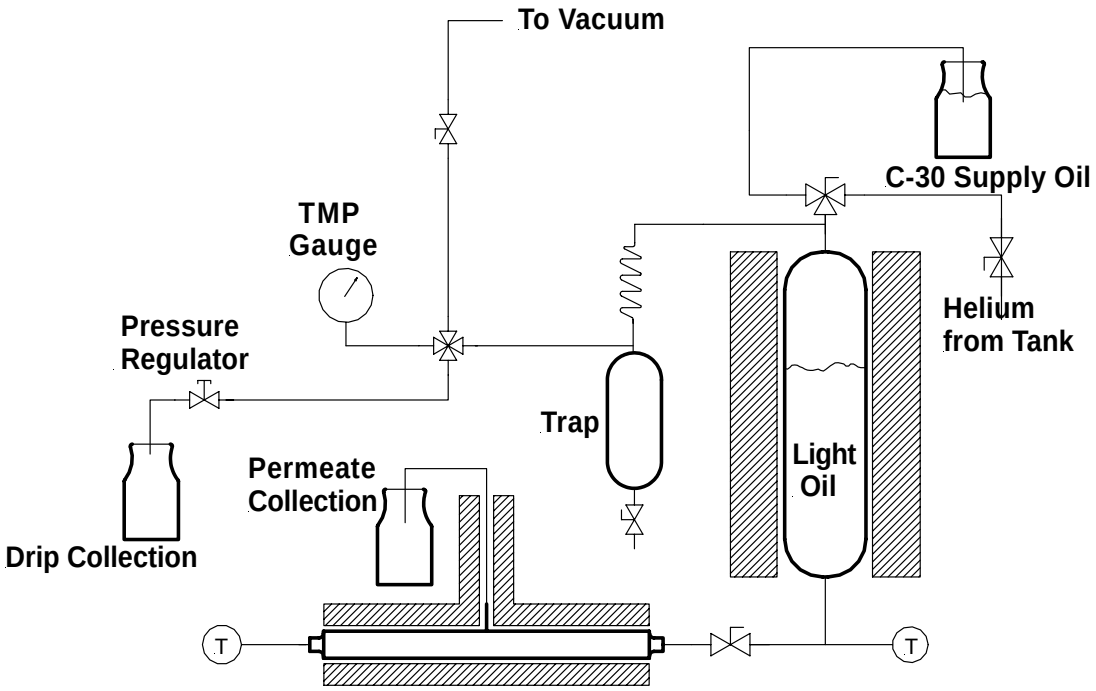

Figure 1.1-9. Schematic of the static permeation test apparatus.

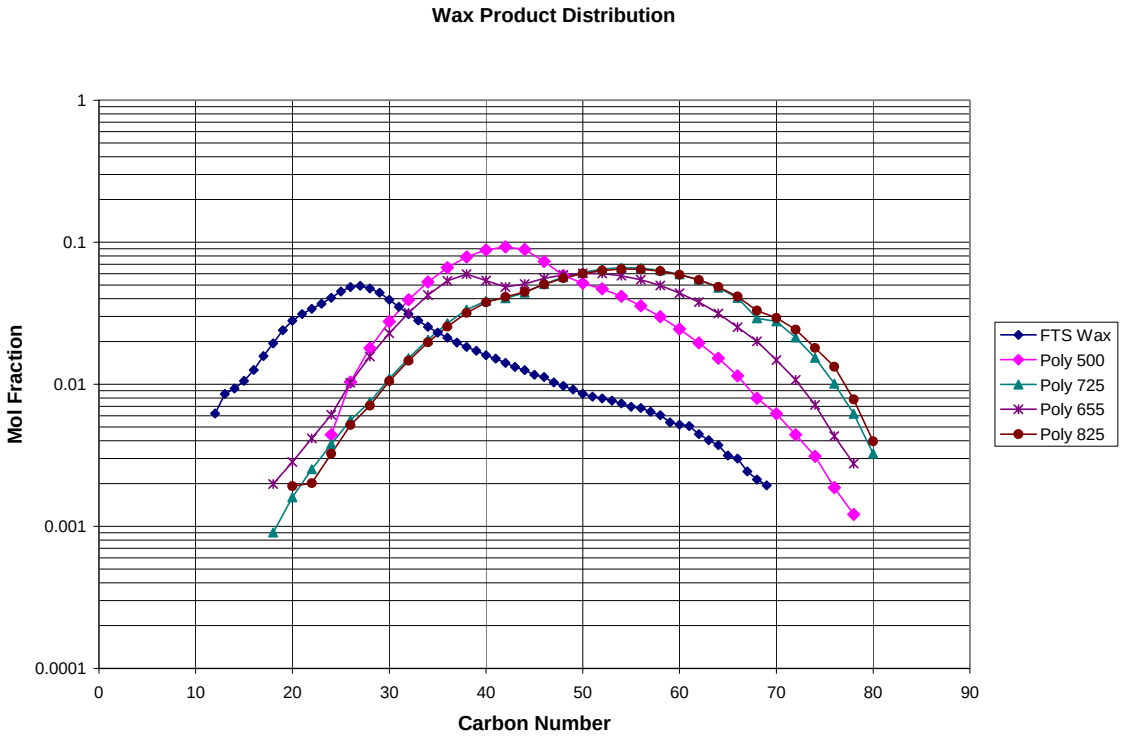

Figure 1.1-10. Carbon number distribution comparison of the polywax simulants with a high α Fischer-Tropsch wax.

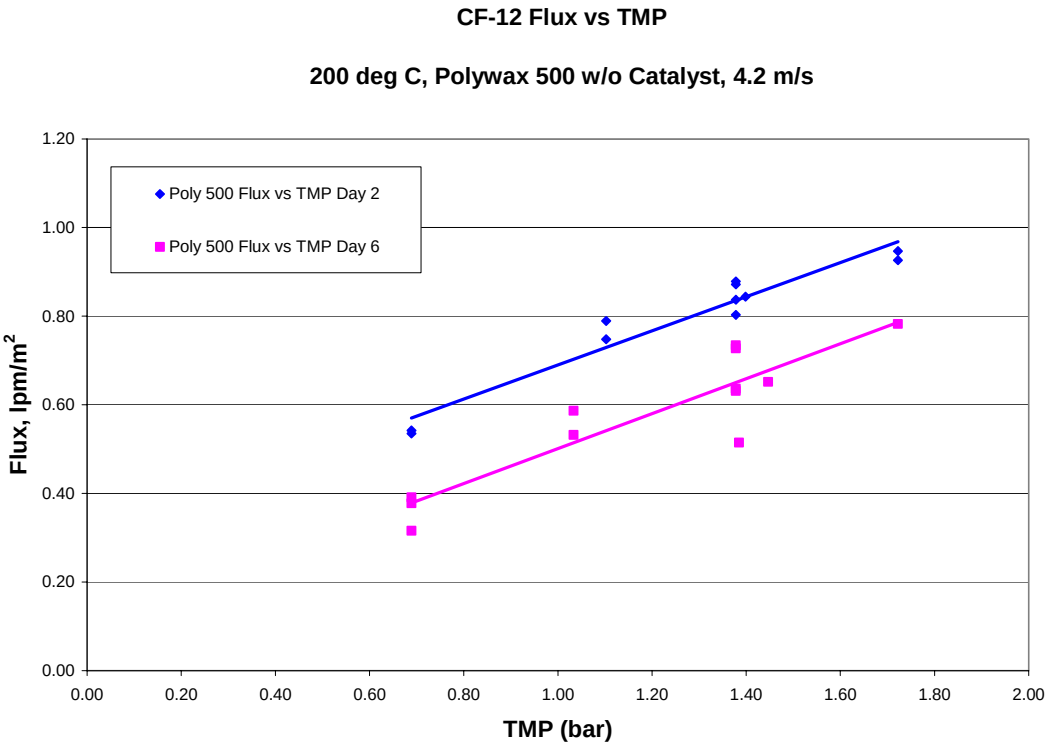

Figure 1.1-11. Plot of variation of polywax flux against. TMP without catalyst.

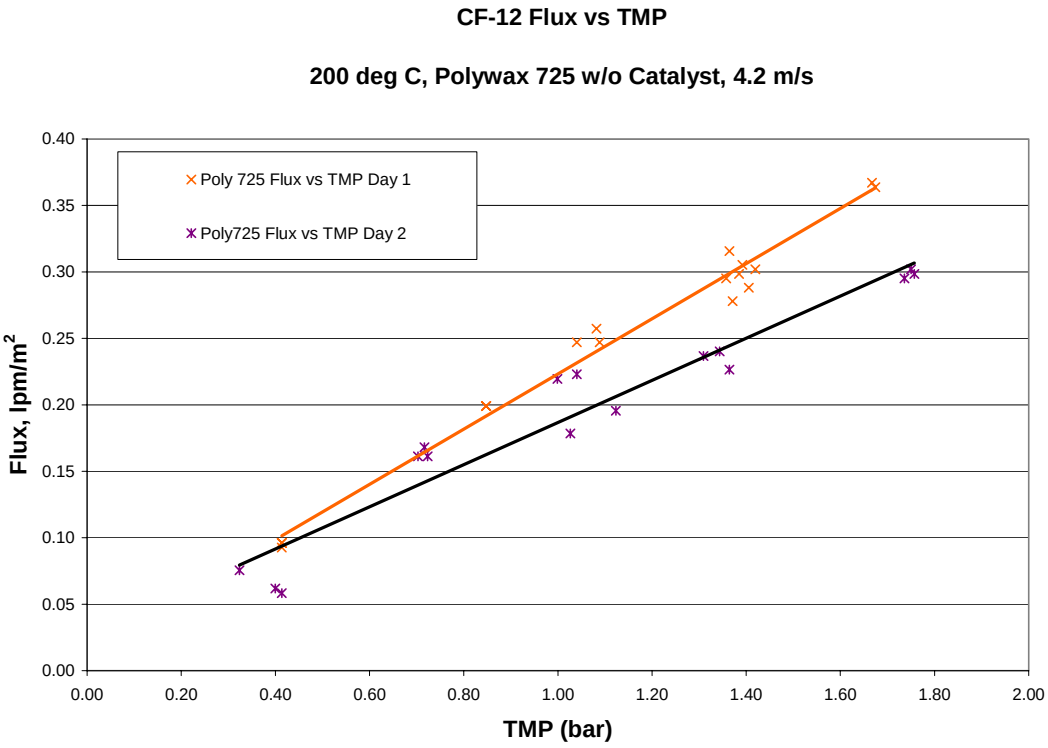

Figure 1.1-12. Plot of variation of Polywax 725 flux against. TMP without catalyst.

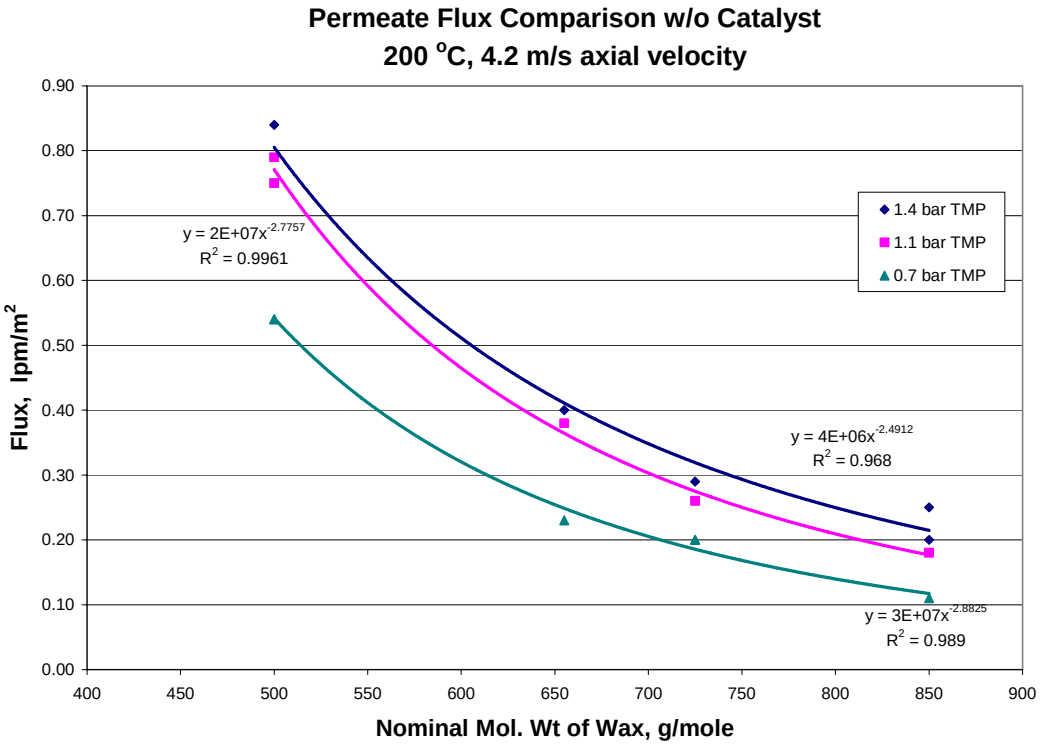

Figure 1.1-13. Effect of molecular weight on permeation flux.

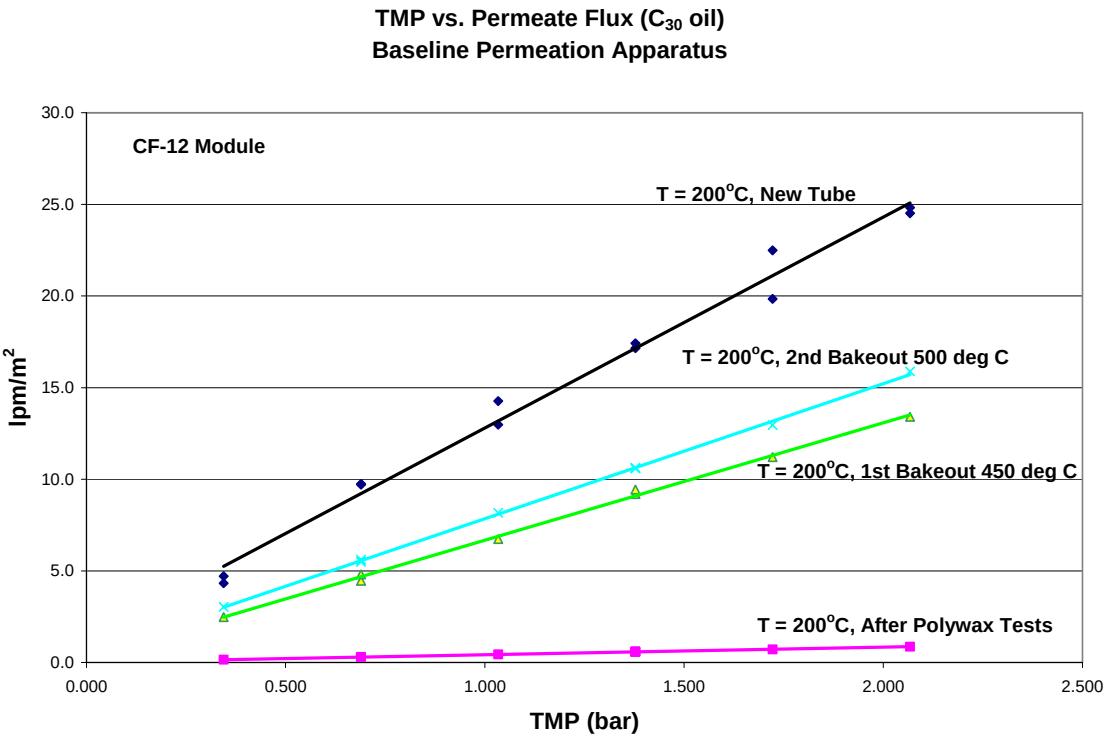

Figure 1.1-14. Variation of static permeation flux of a filter module with 1.0 μm opening against TMP using Durasyn 164.

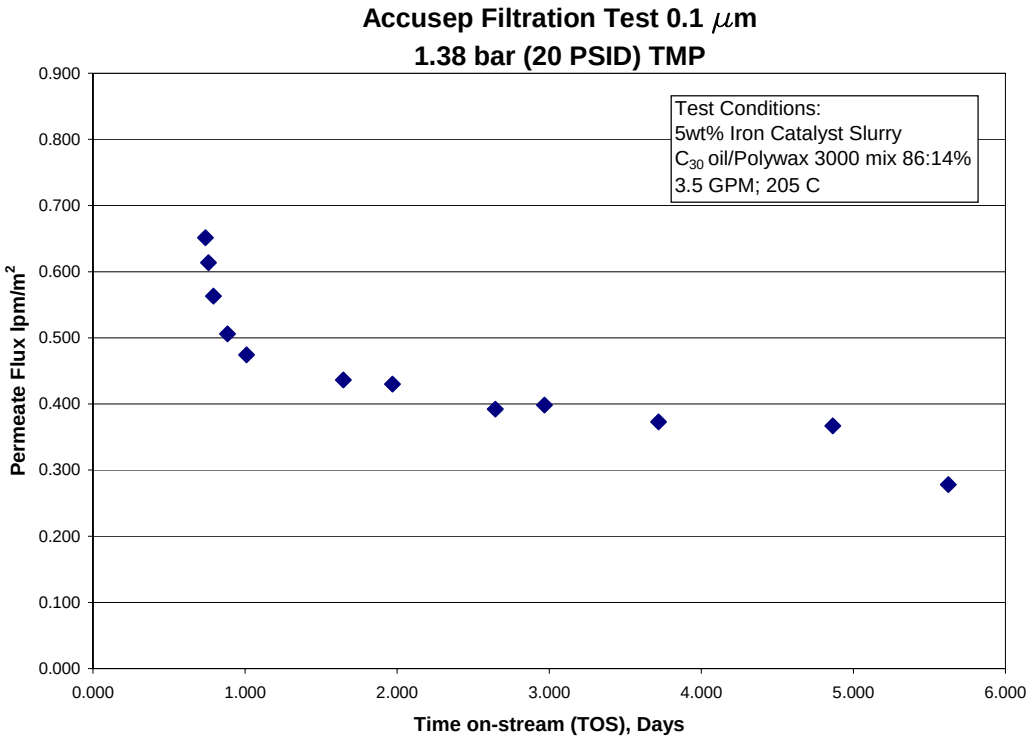

Figure 1.1-15. Initial filtration test using a mixture of Polywax 3000 and C_{30} oil.

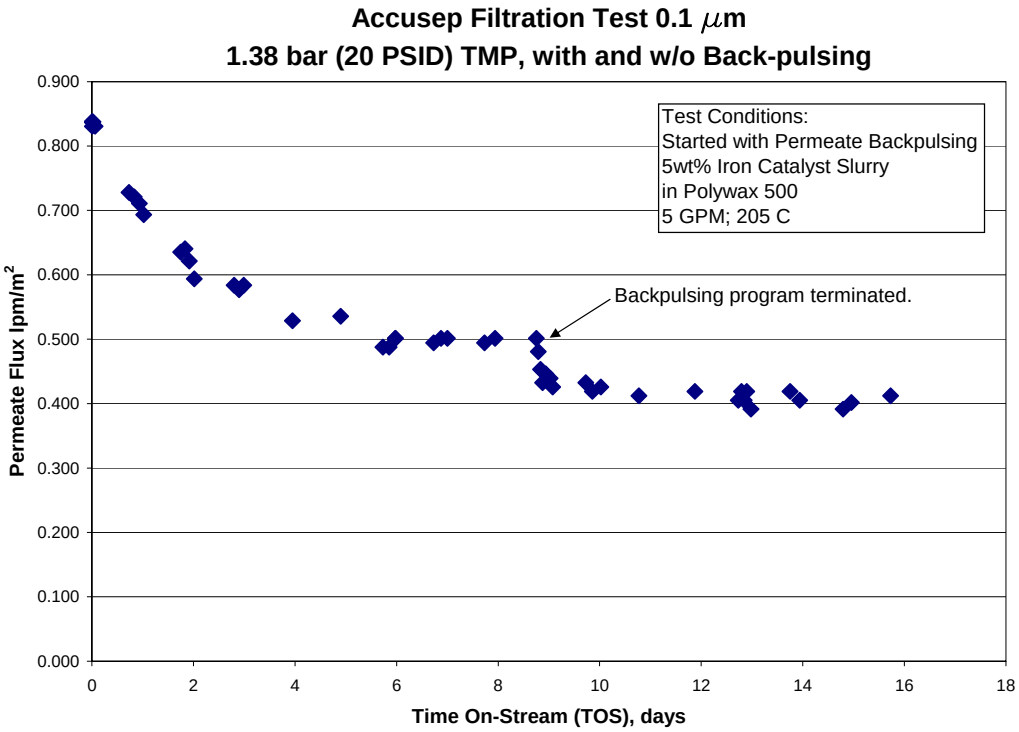

Figure 1.1-16. Filtration test with Polywax 500 simulant, with and without backpulsing.

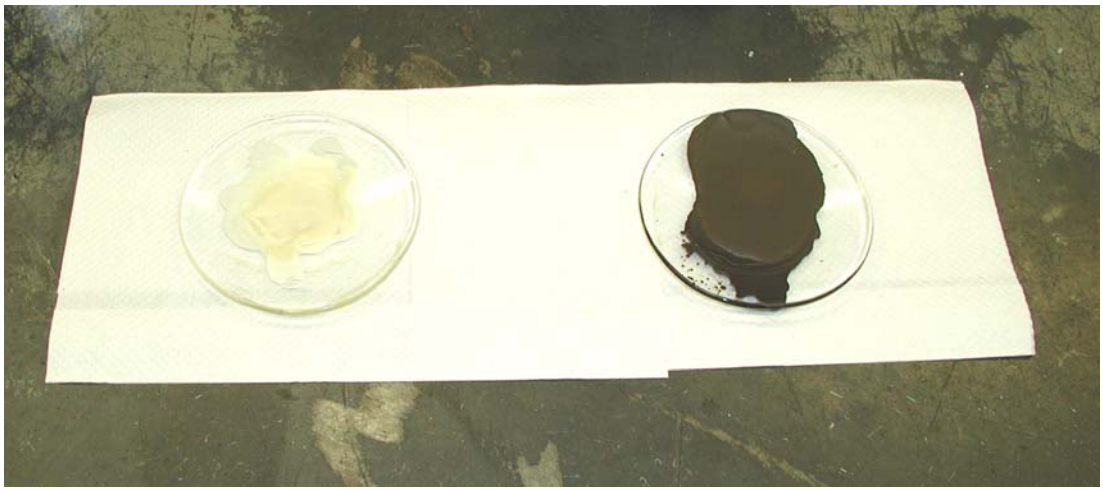

Figure 1.1-17. Photograph comparison of the permeate (at the left) and unfiltered slurry (at the right) using Polywax 500 simulant.

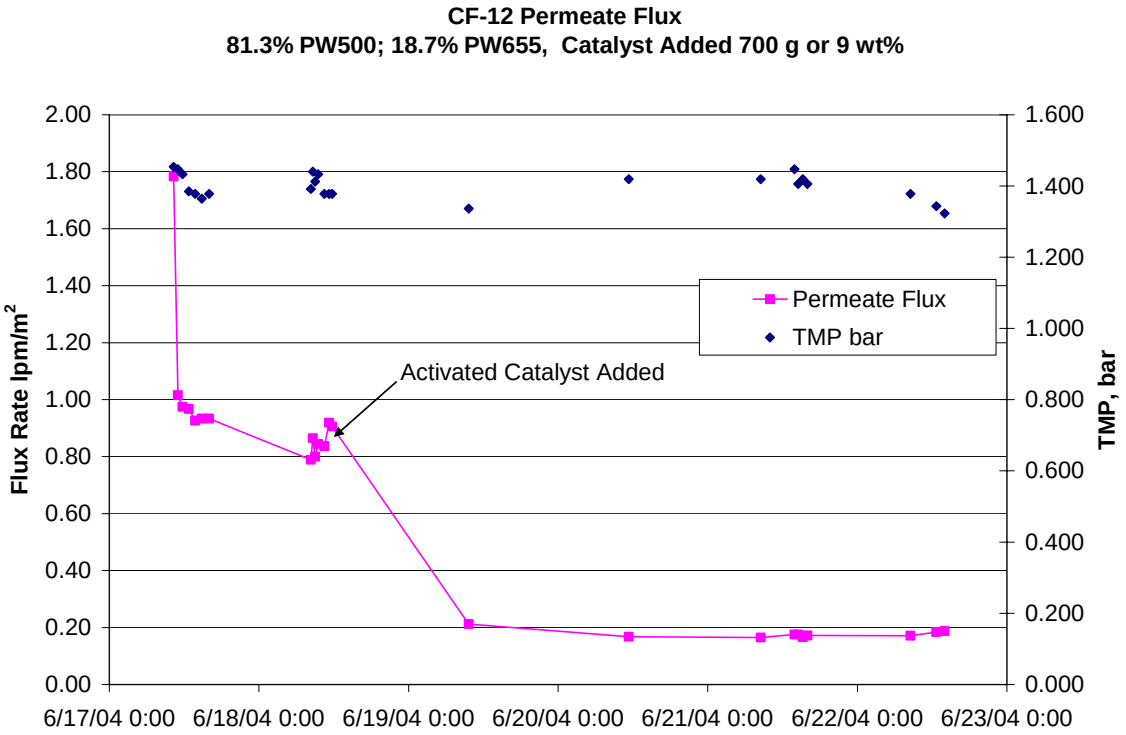

Figure 1.1-18. Variation of permeation flux, TMP against time-on-stream using activated catalyst.

Figure 1.1-19. Photograph of activated slurry (at the left) and permeate (at the right) from activated catalyst test.

Figure 1.1-20. Photograph of "frozen" catalyst/wax mixture after 12 days of circulation.

Slurry online 26 days
(from Polywax 500/Iron Slurry tests)

Figure 1.1-21. Photograph of "frozen" catalyst/wax slurry after 26 days of circulation.

Task 1.2. Filtration Studies with Doped Olefins and Alcohols

1.2.1. ABSTRACT

The effect of oxygenates produced during Fischer-Tropsch synthesis on the filtration flux during cross-flow filtration of Fischer-Tropsch wax at a constant trans-membrane pressure has been studied. Addition of 1-dodecanol (at a concentration of 6 wt%) was found to decrease the permeation rate of the crossflow filter used with an activated iron slurry. However, additional increases in the 1-dodecanol concentration (at 11% and 17% level) did not affect the permeation rates. No significant variation in the concentration of iron in the permeate was found when higher concentration of alcohol was added. Addition of an olefin (1-hexadecene) was found to have a very insignificant to no effect on the permeate flux and iron concentration in the permeate.

1.2.2. INTRODUCTION

1.2.2.1. Filtration of catalyst slurry containing added olefins and oxygenates

Traditionally, iron catalysts have been used for F-T synthesis when the syngas is coal-derived, because they have the ability to simultaneously carry out the FTS and WGS reactions. Complex mixtures of compounds are known to be formed during iron-based Fischer- Tropsch synthesis [1]. In addition to straight-chained paraffins, the formation of olefins and oxygenates can be substantial:

Paraffin formation: $(2n + 1)\ H_2 + n\ CO = C_nH_{2n+2} + n\ H_2O$

Alcohols: $2n\ H_2 + n\ CO = C_nH_{2n+2}O + (n-1)\ H_2O$

Olefins: $2n\ H_2 + n\ CO = C_nH_{2n} + n\ H_2O$

Olefin selectivity of iron catalysts is typically greater than 50% of the hydrocarbon products at low carbon numbers [1]. Of the olefins produced, more than

60% of are α-olefins. For iron, the olefin selectivity decreases asymptotically with increasing carbon number. For cobalt catalysts both the fraction of total olefins and alpha-olefins are smaller in comparison to that of Fe catalysts. From a chemical feedstock perspective, alpha-olefins are desirable since they can be processed into branched alkanes for high-octane gasoline and other value-added chemicals.

The degree to which these olefin and alcohol products affect the filtration has not been documented in the literature. Certainly, the presence of olefins and alcohols in catalyst slurry could influence the wax rheology to some degree. Consequently, one objective of this research program is to quantify effects of these side products on the separation of catalyst from wax.

1.2.3 EXPERIMENTAL

1.2.3.1. Filtration Test Platform

The pilot plant platform was modified into a crossflow filtration test unit (Figures 1.1-6 and 1.1-8). This unit, depicted schematically in Figure 1.1-8, will allow several types of crossflow filter media to be researched under simulated FTS conditions. For a further description of the unit refer to *Task 1.1 Experimental* (pages 16-17 of this document).

1.2.3.2. Filter Back-flush System

The test system is described in *Task 1.1.3.2.* and a schematic of the arrangement is also presented in Figure 1.1-5.

1.2.3.3. Static Permeation Apparatus

The test system is described in *Task 1.1.3.3.* and a schematic of the arrangement is also presented in Figure 1.1-8.

1.2.3.4. Olefin and Alcohol Sample Analysis

Approximately 0.25 g of wax and 7 ml of o-xylene (HPLC grade) are placed in a 16 x 125 mm culture tube and then put in a Thermoclyne dry heating bath. The sample is heated until the wax is dissolved and then transferred to a sample vial for analysis by gas chromatography. The sample is analyzed on an HP 5890 Series II Plus GC equipped with an FID detector. The column used is a 25 meter SGE aluminum clad HT5 of 0.53 inner diameter and 0.15 μm film thickness. Identification of the compounds of interest was accomplished by running standards and by spiking the sample with the standard compounds of interest and comparing the appropriate retention times.

1.2.4 RESULTS AND DICUSSION

1.2.4.1. Alcohol Filtration Tests with Polywax 500/655 Activated Catalyst Slurry

As previously reported [2], a blend of Polywax 500 and 655 (81.3wt% and 18.7%, respectively) with a CO-reduced iron catalyst was used for the evaluation of filtration with and without an alcohol compound. All of the filtration tests were conducted with a trans-membrane pressure (TMP) of 1.4 bar, 200 ^{o}C and an iron slurry concentration of 5 wt%. The axial velocity of the slurry within the filter was maintained at 13 m/s. Dodecanol (specifically 1-dodecanol, $CH_3(CH_2)_{11}OH$) was chosen as the alcohol additive since its low vapor pressure would insure a sufficient residence time in the slurry phase.

Given that alcohols are known to be reactive in the presence of an iron catalyst [3,4], an excessive quantity of 1-dodecanol was added once the filtration flux reached equilibrium. The initial dosages of dodecanol were 6, 11, and 17 wt%. In order to

maintain a constant iron catalyst concentration of 5 wt%, a mass of filtered permeate was extracted from the slurry that was comparable to the mass of the 1-dodecanol to be added.

The permeation flux versus time-on-stream for the alcohol addition run is shown in Figure 1.2-1. Before adding the 6 wt% 1-dodecanol, the permeate flux was allowed to reach an equilibrium during the filter membrane/slurry induction period. During this period the flux dropped from 0.65 to 0.40 lpm/m^2. Once the first aliquot of 1-decanol was added, the flux increased to 0.46 lpm/m^2 and subsequently dropped to less than 0.2 lpm/m^2 over a 2-day period. As shown in Figure 1.2-2, the permeate color changed from a bright white color to a brownish color after the docdecanol was added. This change in the permeate can attributed to the increase of iron (from 50 to 250 ppm) and possibly the existence of reaction products of the dodecanol to other oxygenates such as ketones, aldehydes, and/or acids. However, it is not known if these reaction products caused the initial decrease of the permeation flux.

Subsequent additions of the dodecanol (11 and 17 %) had only a minor effect on the permeation flux. In Figure 1.2-3, the equilibrium permeation flux is plotted versus the initial concentration of the dodecanol. Once the initial 6 wt% dose of dodecanol was added, the steady-state flux was maintained at 0.2 lpm/m^2. Likewise, the permeate quality, in terms of iron concentration, did not vary substantially with increasing alcohol concentration as shown in Figure 1.2-4.

In Table 1.2-1, the analytical results of the alcohol concentration of the permeate are listed for the duration of the filtration study. The column labeled “wt% Dodecanol (added)” is the target concentration of the alcohol based on mass percent. The adjacent column labeled “wt% Dodecanol (measured)” represents the measured concentration of

the alcohol in the permeate after a steady-state filtration flux was obtained. The analytical results were obtained using a GC. In addition to the dodecanol peak, two other unknowns were present in all but the initial samples before the alcohol was added (labeled "%Unknown-1" and "%Unknown-2", respectively). Further analytically work is needed to identify these unknown compounds and to characterize what effect they may have on the filtration flux.

1.2.4.2 Olefin-doping Wax Permeation Study

The base slurry specifications and operating conditions for the olefin doping study were identical to that of the previously mentioned alcohol doping tests. The method for doping the olefins in the catalyst was similar in that a constant 5 wt% concentration of iron was maintained thorough out the test run. 1-Hexadecene ($C_{16}H_{32}$) was selected as the doping agent since the vapor pressure of lower molecular weight olefins would cause material balance difficulties. The target concentration levels of the olefin were 0, 14, 26, and 29 wt%. This range of concentrations is typical for various iron-based FT processes [1].

As shown in Figure 1.2-5, the baseline flux, without 1-hexadecene added, stabilized to 0.30 lpm/m^2 at 200^{o}C with a 1.4 bar trans-membrane pressure. As with previous filtration runs using an activated iron catalyst slurry, the duration of the induction period for the catalyst particles and membrane was approximately 48 hours TOS. Initially, the permeate appearance was a bright white. With the first dosage of the olefin (14wt% as 1-hexadecene), the permeate flux remained essentially unchanged and stable after 48 hours TOS at 0.31 lpm/m^2. A slight permeate color change was observed with increasing TOS as shown in Figure 1.2-6. The iron content increased from 25 to

272 ppm with the addition of the olefin as shown in Figure 1.2-7. However, this can be attributed to the formation of finer catalyst particulate caused by attrition as was observed in the alcohol doping study. Likewise, no appreciable change in the permeate flux was observed at the 26 wt% or the 29 wt% olefin level (see Figure 1.2-8).

1.2.5. CONCLUSIONS

The addition of an alcohol (1-dodecanol) was found to decrease the permeation rate of a crossflow filter using an activated iron slurry. However, additional increases in the 1-dodecanol did not affect the permeation rates. Additionally, the color of the cleaned wax was significantly darker with the addition of the alcohol as compared to that of a paraffin-only catalyst wax. Much of this color difference may be due to side reaction products of the 1-dodecanol. The addition of an olefin (1-hexadecene) had little to no effect on the permeate flux and quality.

1.2.6. REFERENCES

[1] G. P. Van Der Laan and A. A. C. M. Beenackers, "Kinetics and Selectivity of the Fischer-Tropsch Synthesis: A Literature Review", Catalysis Reviews-Science and Engineering, Vol. 41 Nos. 3&4,pp. 255-318, 1999.

[2] J.K. Neathery, B.H. Davis, and G. Jacobs, "Separation of Fischer-Tropsch Wax Products from Ultrafine Iron Catalyst Particles", Technical Progress Report DE FC26-03NT41965, Report R41965R08, 2004.

[3] Y. Wang and B.H. Davis, Fischer-Tropsch Synthesis: Conversion of alcohols over iron oxide and iron carbide catalysts", Applied Catalysis A: General 180 (1999) 277-285.

[4] B. H. Davis, "Fischer-Tropsch synthesis: relationship between iron catalyst composition and process variables", Catalysis Today 84 (2003) 83-98.

Table 1.2-1. Concentration of 1-deodecanol and unknown reaction products.

Time on Stream (h)	Dodecanol added (wt%)	Dodecanol measured (wt%)	% Unknown-1 (wt%)	% Unknown-2 (wt%)
72	0	0	0	0
144	6	0	0.59	0
167	11	0.54	0.8	1.81
200	17	0.74	1.23	7.33

Table 1.2-2. Comparison of measured versus calculated 1-hexadecene permeate concentration.

Time on Stream (h)	**Hexadecene added (wt%)**	**Hexadecene Measured (wt%)**
0	0	0.34
50	14	14.1
76	26	25.7
170	29	29.4
190	29	40.3

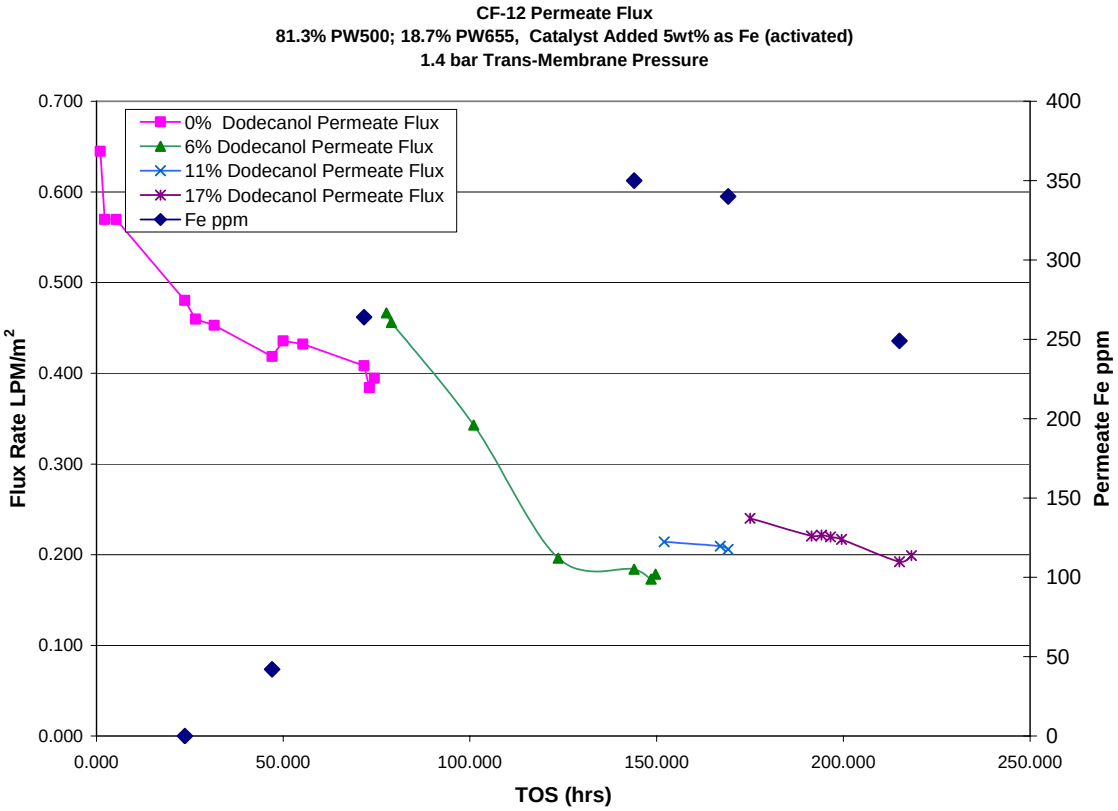

Figure 1.2-1. Variation of permeate flux against time-on-stream when 1-dodecanol was added.

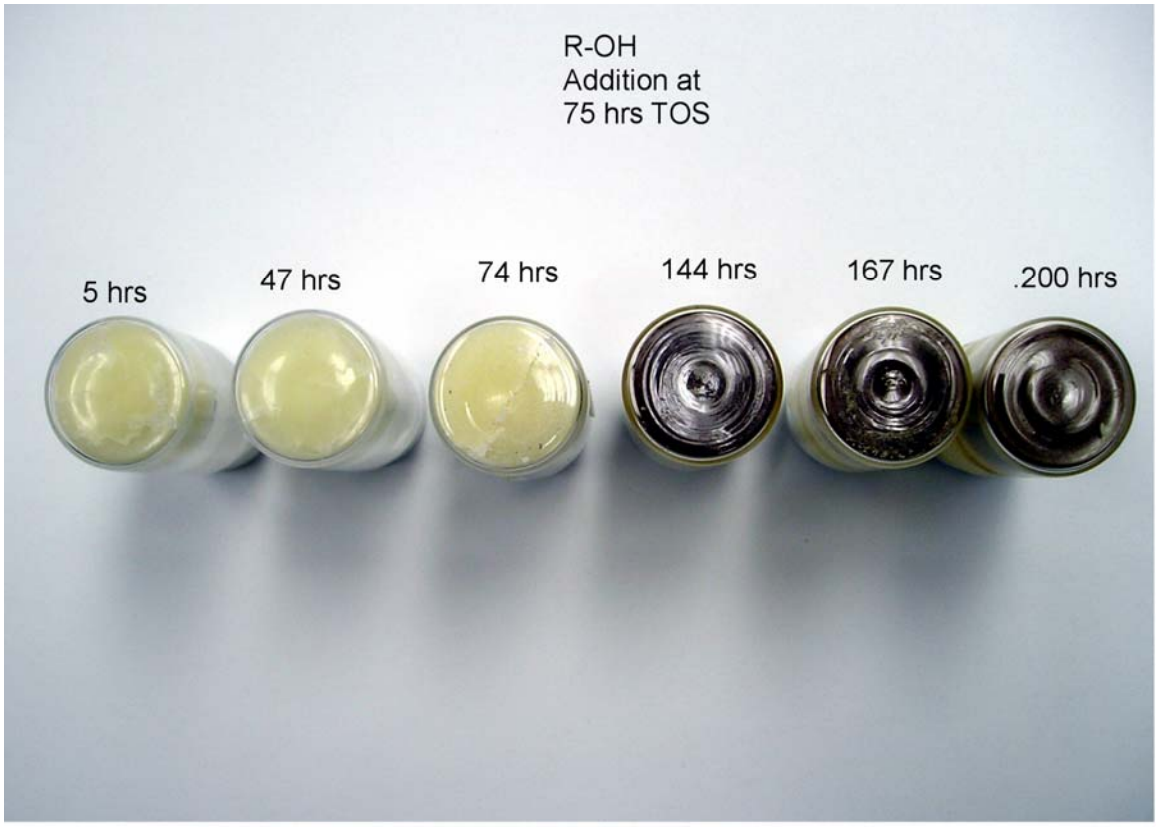

Figure 1.2-2. Photograph of permeate samples collected at different time-on-stream when alcohol was added.

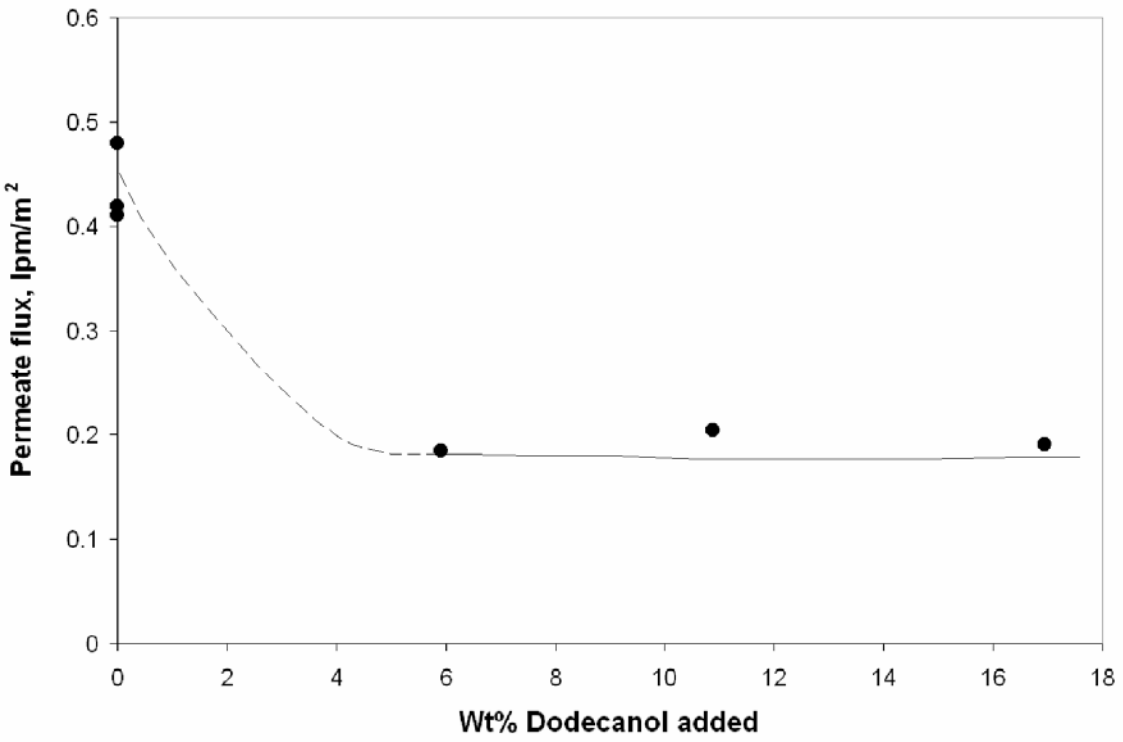

Figure 1.2-3. Variation of permeate flux against concentration of co-fed 1-dodecanol.

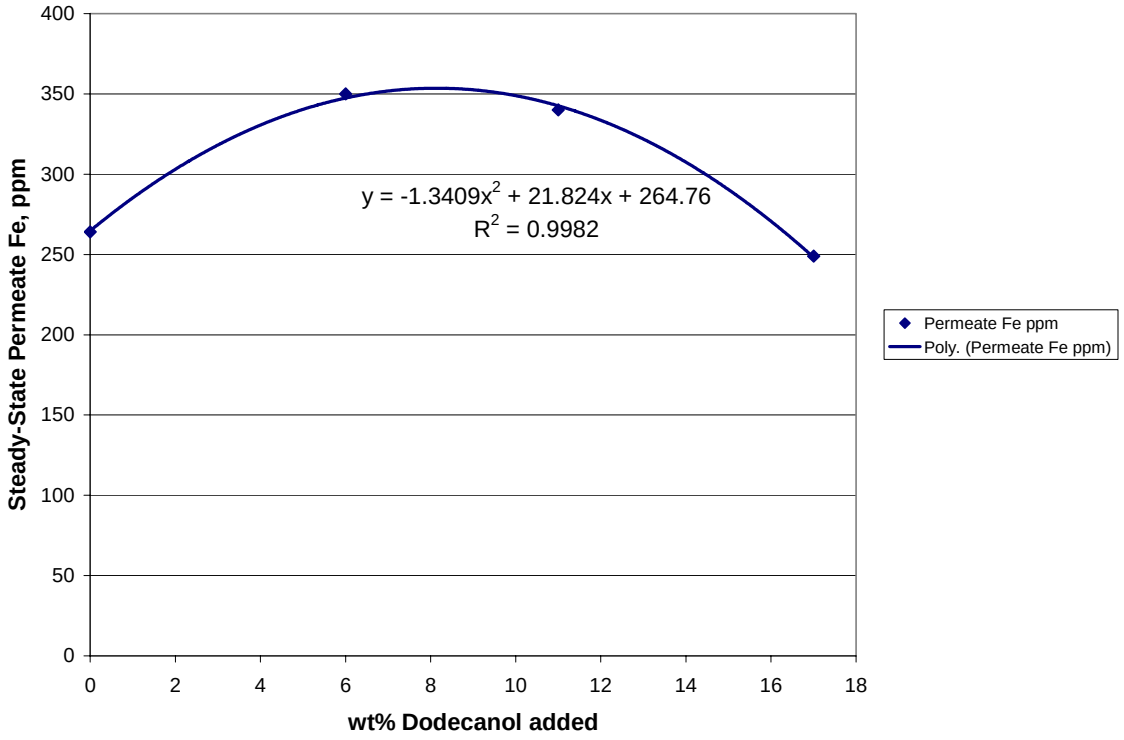

Figure 1.2-4. Variation of iron iron concentration in the permeate (at steady-state) against concentration of co-fed 1-dodecanol.

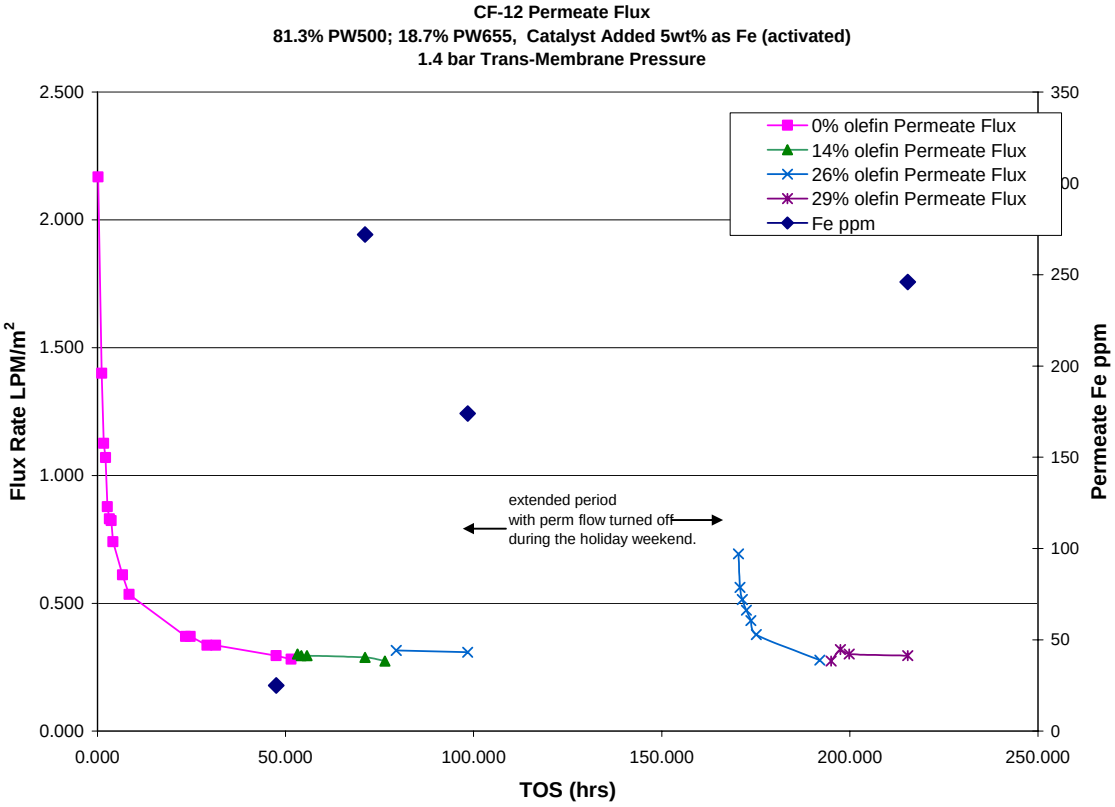

Figure 1.2-5. Effect of co-fed olefin (1-hexadecene) concentration on the permeate flux at different time-on-stream.

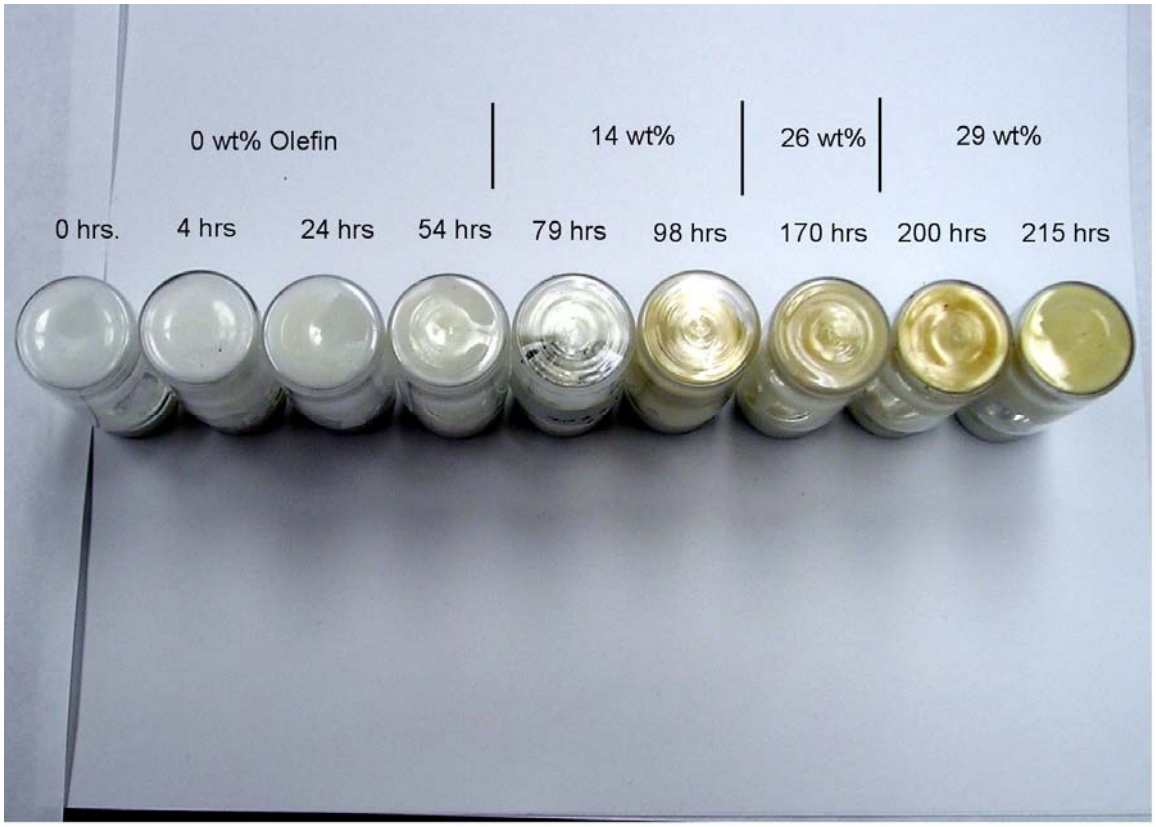

Figure 1.2-6. Photograph of permeate samples collected at different time-on-stream when olefin (1-hexadecene) was co-fed.

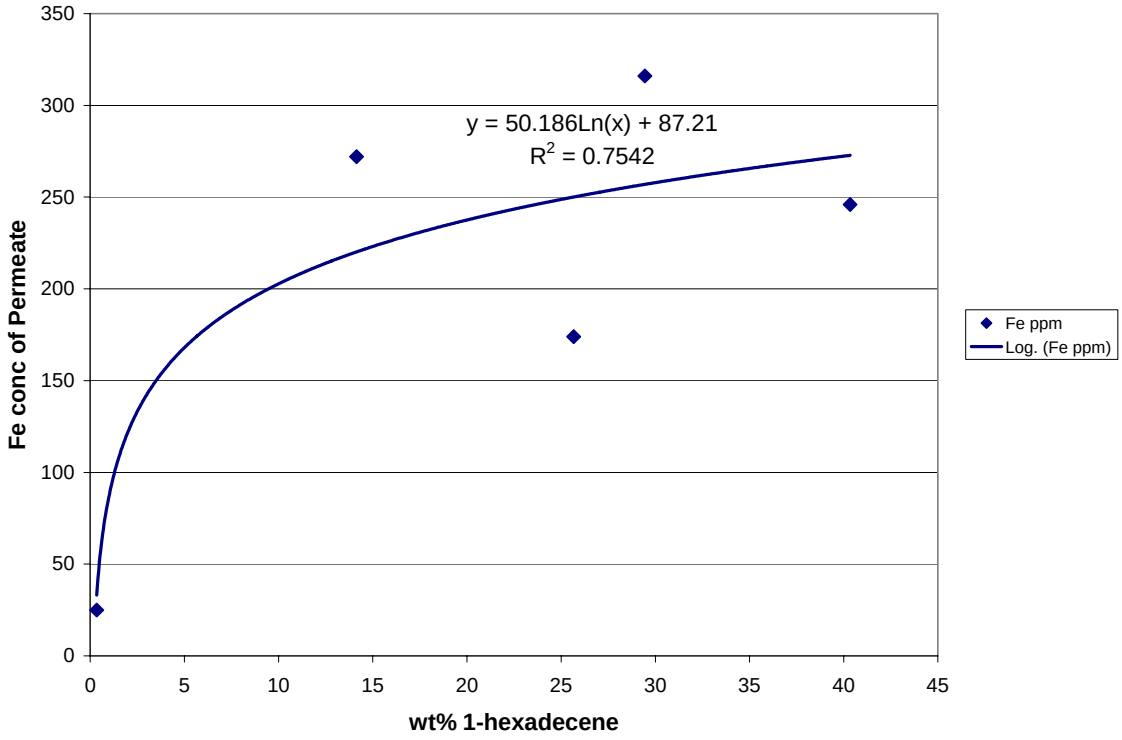

Figure 1.2-7. Effect of olefin (1-hexadecene) concentration on the iron concentration in the permeate.

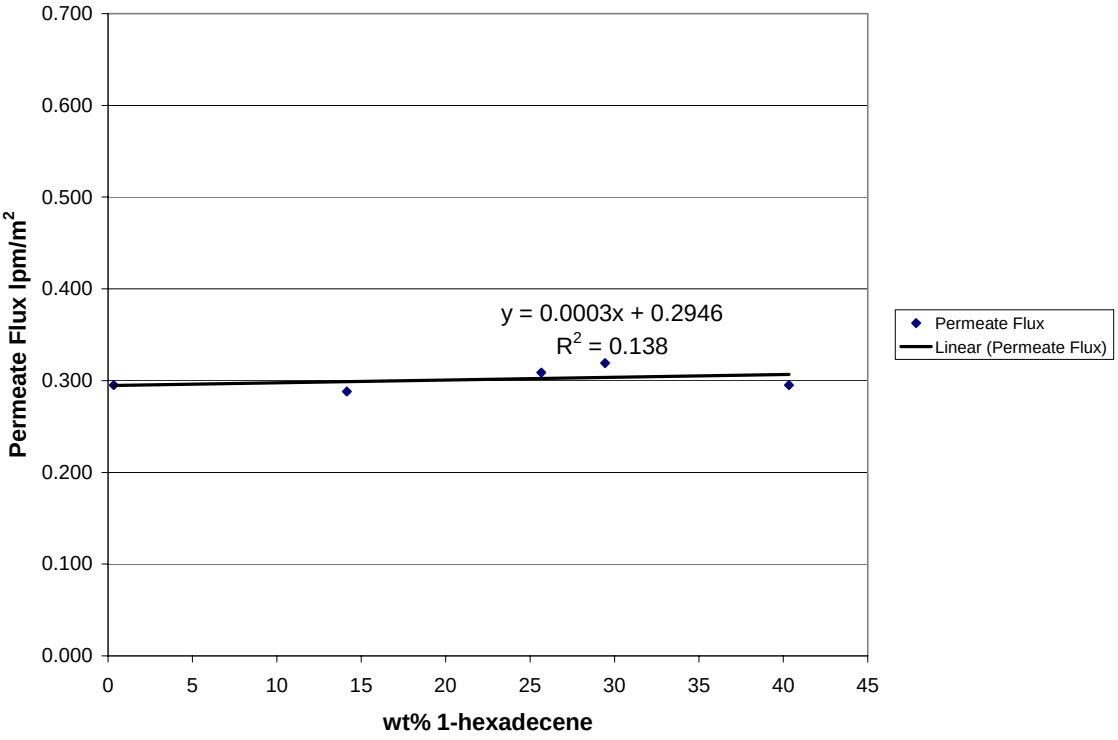

Figure 1.2-8. Effect of co-fed olefin (1-hexadecene) concentration on the permeate flux.

Task 1.3. Development of Filter Media Cleaning Procedure

1.3.1. ABSTRACT

The permeate flux in crossflow filtration can be maintained by occasional back-flushing of clear permeate which allows removal of a fraction of particles deposited at the boundary layer of the filtering medium. A passive technique has been developed by disrupting the permeation flow while allowing the retentate to circulate axially through the crossflow tube. This passive flux maintenance procedure was tested while TMP was suspended for an extended period. It was found that although the permeate flux can be increased by over 100%, it declines to the original steady-state flux over 24 hours. It was found that by interrupting the permeate flow for 30 seconds per half hour time period was highly effective in recovering the permeate flux although the long-term steady-state flux cannot be achieved with the method. Further studies showed that steady-state permeate flux can be maintained by increasing the permeate off cycle to 1 hour per day in addition to 30 seconds off per half hour cycle.

1.3.2. INTRODUCTION

Crossflow filtration systems utilize high liquid axial velocities to generate shear at the liquid-membrane interface. Shear is necessary to maintain acceptable permeate fluxes, especially with concentrated catalyst slurries. The degree of catalyst deposition on the filter membrane is a function of the shear stress at the surface and particle convection with the permeate flow [1]. Membrane surface fouling also depends on many application-specific variables such as: particle size in the retentate, viscosity of the permeate, axial velocity, and the trans-membrane pressure. All of these variables can

influence the degree of deposition of particles within the filter membrane and thus decrease the effective pore size of the membrane.

Several operating techniques have been used in industrial ultrafiltration applications to improve permeation flux performance [1-4]. These include: backflushing or backpulsing with clear permeate; backflushing an inert gas through the membrane; and the use of mechanical devices to increase turbulence near the membrane. Each of these techniques essentially disrupts the boundary layer of concentrated particles at the membrane surface.

A more passive technique suggested by Pall Corporation product engineers is to disrupt the permeation flow while allowing the retentate to circulate axially through the crossflow tube. This would in theory allow inertial lift of the particles on the membrane surface in the absence of the permeate convective force component. Unlike backpulsing, this passive approach would not expend cleaned permeate product or require high-pressure inert gas handling. The approach of switching a filter tube off momentarily would be simple and thus likely more economical to implement.

1.3.3. EXPERIMENTAL

1.3.3.1 Filtration Test Platform

An existing pilot plant platform was modified into a crossflow filtration test unit (Figures 1.1-3 and 1.1-5). This unit, as depicted schematically in Figure 1.1-3, allows several types of crossflow filter media to be researched under simulated FTS conditions. A complete description of the unit can be found at *Task 1.1 Experimental* section.

1.3.3.2 Filter Back-flush System

As shown in Figure 1.1-5, the back flush system consists of a piston pump that is triggered by a computer controlled timer. The back-flush fluid consists of cleaned permeate stored in a 40 ml tube bomb located near the suction side of the piston pump. However, backflushing with clean permeate is only used as a last resort. Preferably, the maintenance procedure is to turn off the permeate flow on a short but regular period. This system will be used throughout the study to develop an optimum cleaning program that can sustain a permeate flux rate over a many days.

1.3.3.3 Static Permeation Apparatus

In order to quantify the degree of filter media fouling, we constructed a static permeation rig to test the permeability of the membranes before and after catalyst filtration tests. A schematic of the apparatus is shown in Figure 1.1-6. A 4-liter vessel filled with clean/filtered C_{30} oil is heated to a temperature between 180 to 220^{o}C. The C_{30} oil is commercial polyalphaolefin known as Durasyn 164, produced by Amoco. A differential pressure or an effective TMP can be varied across the filter membrane via helium gas through a pressure regulator. The resulting permeation rate of the C_{30} oil is measured. The curve of the membrane flux vs. TMP will provide a snapshot of the tube's fouling condition.

1.3.4. RESULTS AND DICUSSION

An opportune chance to test the passive flux maintenance procedure came during a long holiday weekend. As presented in Figure 1.3-1, after 100 hours TOS the permeate valve was closed and thus the trans-membrane pressure fell to zero. The pilot plant remained in a stand-by mode and unmanned for approximately 75 hours. During this period, the catalyst slurry was circulated through the crossflow filter, without

permeate flow radially through the filter membrane (i.e., test conditions were constant with the exception of the absence of a trans-membrane pressure). Once the 1.4 bar trans-membrane pressure was reinstated, the flux momentarily increased by 116% (from 0.3 to 0.65 lpm/m^2); however, over the next 24 hours the flux returned to the baseline flux before interruption of the permeate flow.

Even though the flux returned to the steady-state value before the permeate valve was closed, there was a 24-hour period of increased flux. Further tests are needed to determine the optimum period of filter down-time. A possible flux maintenance scheme could employ two filters; one filter in the "permeate mode" while a duplicate filter is being regenerated with slurry without trans-membrane pressure. These units could be cycled at some optimum time period such that a higher permeate flux could be maintained than that of a single filter.

1.3.5. CONCLUSIONS

A passive flux maintenance procedure was tested in which the trans-membrane pressure is suspended for an extended period. The flux can be increased by over 100%, but decays back to the original steady-state flux over 24 hours. Simply interrupting the permeate flow for 30 seconds per half hour was effective in recovering the initial membrane fouling; however, the long-term steady-state flux was not achieved with the method. Flux stability was attained only after increasing the permeate off cycle to 1 hour per day in addition to 30 seconds off per half hour cycle.

1.3.6. REFERENCES

[1] M. Mietton-Peuchot, C. Condat, and T. Courtois, “Use of gas-liquid porometry measurements for selection of microfiltration membranes”, Journal of Membrane Science 133 (1997) 73-82.

[2] J. Poslethwaite, S. Lamping, G. Leach, M. Hurwitz, and G Lye, “Flux and transmission characteristics of a vibrating microfiltration system operated at high biomass loading”, Journal of Membrane Science 228 (2004) 89-101.

[3] R. Bhave, Inorganic membranes: Synthesis, Characteristics and Applications. Van Nostrand Reinhold, New York, (1991), pp. 95-107, 129-154.

[4] J. Cakl, I. Bauer, P. Doleček, and P. Mikulášek, “Effects of backflushing conditions on permeate flux in membrane crossflow microfiltration of oil emulsion”, Desalination 127 (2000) 189-198.

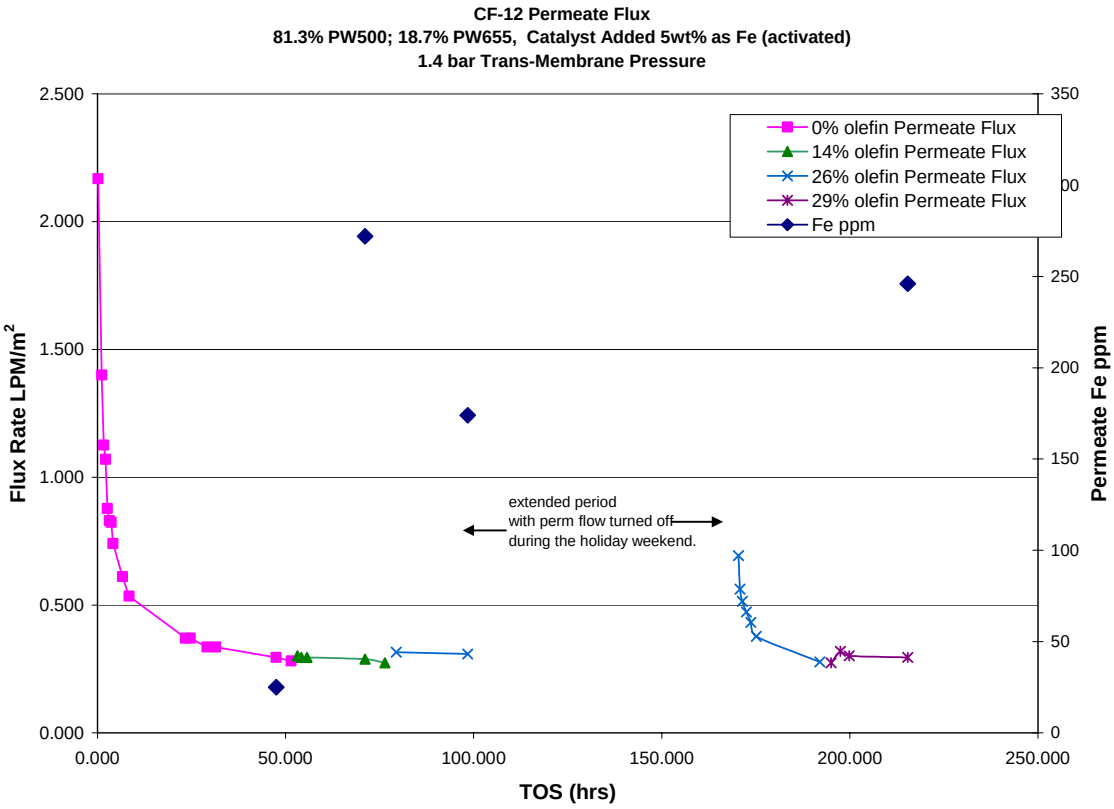

Figure 1.3-1. Variation of permeate flux against time-on-stream when co-fed olefin (1-hexadecene) was used.

TASK 2. Physicochemical Characterization of Ultrafine Iron Catalyst

Task 2.1. Precipitated Iron Fischer-Tropsch Catalyst: Effect of CO activation on the Morphology of Iron Hydroxide Oxide Nanoneedles

ABSTRACT

The effect of carbidization on the morphology of iron oxyhydroxide particles has been studied. Homogeneous oxidation of iron (II) sulfate results in predominantly $\gamma - FeOOH$ particles which have a rod-shaped crystalline structure. Carbidization of the prepared iron oxyhydroxide particles at 270 °C and atmospheric pressure without mechanical stirring was found to produce iron carbides with spherical layered structure residing in close proximity. HRTEM, EDS and electron microdiffraction analysis revealed that carbidization alters the initial nano-needle type morphology and generates ultrafine carbide particles with irregular spherical shape. When carbidization was performed under severe mechanical stirring, formation of spherical carbide particles completely separated from each other was obsrved. Initial activity of iron oxyhydroxide for Fischer-Tropsch synthesis was found to be high (a CO conversion of about 84%) which declined steadily with synthesis time (26% CO conversion after 340 h of synthesis).

1. Introduction

Iron oxyhydroxides ($\alpha - FeOOH$, $\gamma - FeOOH$ or $\delta - FeOOH$) are used extensively as catalysts, co-catalysts, pigments, flocculents, etc. [1-6]. The oxidation of $Fe(OH)_2$ in aqueous solution can produce Fe_3O_4 , $\alpha - FeOOH$ or $\gamma - FeOOH$ depending on the reaction temperature, oxidation rate, initial concentration of the reactants and pH of the medium. Fast oxidation produces $\gamma - FeOOH$ while slow oxidation results in the

formation of Fe_3O_4. The formation of $\gamma - FeOOH$ is restricted to the instances where the rapid aerial oxidation of ferrous ion is effected in a neutral or slightly basic suspension of $Fe(OH)_2$. However, $\gamma - FeOOH$ is not formed by the addition of a base to effect precipitation of iron from a solution prepared from a ferric salt [7].

$\gamma - FeOOH$ has been used extensively as an active catalyst for Fischer-Tropsch synthesis [7, 8], for recovering useful hydrocarbons from palm shell oil [1], oxidation of benzoic acid by hydrogen peroxide [2], and for direct liquefaction of coal [4]. The oxidation of $Fe(OH)_2$ and the mechanism of formation of $\gamma - FeOOH$ was studied extensively [9, 10]. Electron microscopy analysis of the samples withdrawn at different times of oxidation/precipitation reaction revealed a pattern of changes in the particle morphology during the formation of $\gamma - FeOOH$. The initial shapeless material transformed to needle-type structure of $\gamma - FeOOH$ particles via the formation of different dense spherical and hexagonal structure.

Phase-transformations during activation and/or Fischer-Tropsch synthesis (FTS) plays an important role in determining the structural integrity or attrition resistance of the catalyst particles. Sequential phase-modification during the activation process (with CO or synthesis gas) from hematite to magnetite and finally to iron carbides have been reported [11-13]. Application of in situ Mössbauer spectroscopy recorded during FTS using iron based catalyst showed that the level of CO conversion increases with the formation of iron carbides, i.e., $\varepsilon' - Fe_{2.2}C$ and $\chi - Fe_{2.5}C$ [8]. It has been shown that the formation of surface carbides is required before the catalyst can exhibit any activity [14]. The chemical conversion of iron oxides to iron carbides induce a volumetric change because of significant difference in the skeletal densities of carbide and oxide structures

(e.g., 7.7 g cm^{-3} for Fe_3C as compared to 5.2 g cm^{-3} for Fe_3O_4). The volumetric change can cause stress in the particle which can lead attrition and formation of small crystallites of iron carbide particles [13]. Physical attrition can also result from collision between catalyst particles and the reactor internals.

Although the transformations of amorphous $Fe(OH)_2$ to $\gamma - FeOOH$ and related structural details were studied extensively, those of the transformation of $\gamma - FeOOH$ phase to iron carbides upon CO activation are not yet reported in the literature. The objective of the present research is to investigate the effect of carbidization on the morphology of iron oxyhydroxide nano-needles both in the absence of, and under severe mechanical agitation. Ultrafine nano-needles of iron oxyhydroxide (predominantly $\gamma - FeOOH$ phase) were prepared by controlled oxidation of $Fe(OH)_2$. Activity of unpromoted iron oxyhydroxide catalyst for Fischer-Tropsch synthesis was evaluated in a CSTR and the details of changes in particle morphology was studied by XRD, HRTEM, electron micro-diffraction, and EDS analysis.

2. Experimental

2.1 Materials and Methods

2.1.1. Materials

$FeSO_4 \cdot 7H_2O$ (ACS reagent, $\geq 99.0\%$, 215422), NaOH (ACS reagent, $\geq 97.0\%$, pellets, 221465), and $BaCl_2 \cdot 2H_2O$ (ACS reagent, $\geq 99.0\%$, 217565) were purchased from Aldrich, Inc. and were stored in a desiccator to prevent deterioration. 99.99% O_2 (UHP grade, AGA Speciality Gas) and deionized water were used for the preparation of $\gamma - FeOOH$. For the carbidization (with CO) of the synthesized iron oxyhydroxide

particles and evaluation of its catalytic activity for FTS, 99.99% CO and H_2 (UHP grade, AGA Speciality Gas) were used. C-30 oil (hydrogenated polyalphaoleffins, CAS# 68037-01-4) was used as solvent.

2.1.2. Descriptions of Experimental Set-up

***Preparation of iron oxyhydroxide*:** A four-neck round-bottom flask (1 L) was used. The flask was fitted with a gas dispenser (fritted glass disc), pH electrode, motor driven stirrer, and gas inlet/outlet tubes. Inlet gas flow rate was monitored by a pre-calibrated mass flow controller and the outlet gas flow rate was monitored by a wet-test flowmeter. The reaction flask was placed in a constant temperature water bath maintained at 25 °C.

***Carbidization of iron oxyhydroxide in absence of mechanical agitation*:** The carbidization of iron oxyhydroxide particles (predominantly $\gamma - FeOOH$ phase) was performed in a glass cylinder (50.8 mm ID) fitted with fritted glass disc at the bottom. The gas inlet and outlet lines were fitted with valves. The inlet gas passed through the fritted glass disc and bubbled upward through the slurry (C_{30} oil and suspended iron oxyhydroxide particles) keeping the suspension stirred. In order to avoid the possibility of breakage of initial needle-type structure of iron oxyhydroxide particles, any mechanical stirring was avoided. The cylinder was wrapped with heating tape and a thermocouple placed outside to monitor the skin temperature of the cylinder which was controlled by a temperature controller (CN3251-R, Omega, Inc.).

***Carbidization of iron oxyhydroxide and evaluation of FTS activity under severe mechanical stirring*:** The carbidization of iron oxyhydroxide nano-needles and FTS experiments were conducted in a 1 L CSTR equipped with a magnetically driven stirrer with turbine impeller, a gas-inlet line, and a vapor outlet line with a SS fritted filter (2

micron) placed external to the reactor. A tube fitted with a SS fritted filter (0.5 micron opening) extends below the liquid level of the reactor for withdrawing reactor wax (rewax, solid at room temperature) to maintain a constant liquid level in the reactor. Another SS dip-tube (1/8" OD) extends to the bottom of the reactor and this was used to withdraw catalyst/wax slurry from the reactor after carbidization at different synthesis times. Separate mass flow controllers were used to control the flow of hydrogen and carbon monoxide at the desired rate. The gases were premixed in a mixing vessel before entering the reactor. Carbon monoxide was passed through a vessel containing lead oxide-alumina to remove any traces of iron carbonyl. The mixed gases entered the CSTR below the stirrer operated at 750 rpm. The reactor temperature was maintained constant ($\pm$ 1 °C) by a temperature controller.

2.1.3. Synthesis Procedure

***Synthesis of iron oxyhydroxide*:** 750 mL of deionized water was added to a 1 L round-bottom flask and nitrogen gas was bubbled through the water (stirred at 800 rpm) for 45 minutes to remove any dissolved carbon dioxide and oxygen, and then 41.7 g of $FeSO_4 \cdot 7H_2O$ was added. After 10 minutes, solid NaOH (10.3 g) was added to maintain a molar ratio of $[Fe(II)/[OH^{-1}]]$ of 0.5833 (= 7/12). The suspension was stirred for 15 minutes under nitrogen at room temperature until the suspension pH became constant. Oxygen was then passed into the solution at a constant rate of 18.5 cm^3 min^{-1}. Reaction time was measured from the start of oxygen flow. During the reaction, the pH value was recorded every minute. The extent of the oxidation reaction was easily recognized from a comparison of the outlet and inlet flow rate of oxygen, the pH and the color of the suspension. After 1 h the oxidation had essentially stopped. The product was then

collected by filtration and then washed with deionized water several times until significant concentration of SO_4^{2-} was not detected in the filtrate. A $BaCl_2$ solution was used to test for the presence of SO_4^{2-}. The filter cake was then washed with acetone to remove most of the water. The precipitate was dried in vacuum at room temperature for 24 h.

***Carbidization of iron oxyhydroxide*:** Carbidization of the prepared iron oxyhydroxide particles in absence of any mechanical stirring was performed at atmospheric pressure using C_{30} oil as the solvent. The solid loading of the slurry was 5 wt%. The CO flow rate (3.0 sl/h/g Fe) was controlled by a pre-calibrated mass flow controller. The temperature of the slurry was raised from 25 °C to 270 °C with a ramp rate of 1 °C min^{-1}. The flow rate of the exit gas was measured using a digital bubble flow meter and the composition was analyzed by a micro GC equipped with thermal conductivity detectors. At the end of the carbidization, the slurry sample was withdrawn and stored under C_{30} oil in a desiccator maintained at vacuum.

Carbidization the synthesized iron oxyhydroxide nano-needles under severe mechanical stirring was carried out in a CSTR operated at 750 rpm, 270 °C and atmospheric pressure for 24 h. The catalyst loading of the slurry (C_{30} oil was used as solvent) was 5 wt%. The reactor temperature was raised from room temperature to 270 °C at a rate of 1 °C/min. The space velocity of CO during carbidization was maintained at 3.0 sl/h/g Fe. At the end of 24 h activation period, a sample of carbided catalyst was withdrawn via the slurry withdrawal dip-tube of the CSTR and stored under C_{30} oil in a desiccator maintained at vacuum.

***FTS with iron oxyhydroxides*:** The as-synthesized iron oxide hydroxide particles were added to the CSTR to produce a slurry with 20 wt% catalyst loading. The catalyst was activated using CO at a space velocity of 3.0 sl/h/g Fe at 270 °C and 175 psig for 24 h. The reactor temperature was raised from room temperature to 270 °C at a rate of 1 °C/min. Following the activation, FTS was started by adding synthesis gas mixture to the reactor at a space velocity of 3.0 sl/h/g Fe and a H_2/CO ratio of 0.7. The conversions of CO and H_2 were measured from gas-chromatography analysis (micro-GC equipped with thermal conductivity detectors) of the product gas mixture and by measuring the flow rate of the reactor exit gas-stream with a digital flow meter. The reaction products were collected in three traps maintained at different temperatures – a hot trap (200 °C), a warm trap (100 °C) and a cold trap (0 °C). The products were separated into different fractions (rewax, wax, oil and aqueous) for quantification. However, the oil and the wax (liquid at room temperature) fractions were mixed prior to GC analysis.

2.2 Characterization

2.2.1. X-ray Diffraction

Powder X-ray diffraction pattern of the synthesized iron oxyhydroxide particles was measured using Cu Kα (1.5418 Å) radiation (operated at 40 kV and 20 mA) in a Philips x-ray diffractometer. For recording the powder X-ray diffraction pattern, the solid sample was ground and placed in the sample holder. Phases were identified by comparing diffraction patterns of the sample with those in the standard powder XRD pattern file compiled by the Joint Committee on Powder Diffraction Standards (JCPDS) published by the International Center for Diffraction Data (ICDD). Quantitative Rietveld analysis of

the powder XRD pattern of the sample was performed using X'Pert HighScore Plus® software from PANalytical, Inc.

2.2.2. HRTEM, Electron Microdiffraction and EDS Analysis

The slurry samples were diluted with hot (about 70°C) *o*-xylene to remove the C_{30} oil. Although it was not possible to completely remove the C_{30} oil by this method, the leftover oil did not interfere with TEM analysis and acted as a protective cover for the air-sensitive carbide particles. An optimum ratio of *o*-xylene to particles was used to make a slightly turbid suspension for TEM analysis. A drop of the suspension was placed onto a lacey carbon film on 200 mesh copper grid and loaded into the microscope.

The particle morphology was analyzed by a field emission analytical transmission electron microscope (JEOL JEM-2010F) operated at an accelerating voltage of 200 kV and equipped with a STEM unit with high-angle annular dark field (HAADF) detector, and a Gatan Imaging Filter (GIF)/PEELS system. Electron microdiffraction and EDS analysis was carried out in nanoprobe mode. The electron beam had a point-to-point resolution of 0.2 nm. Gatan Digital Micrograph® software was used for image processing.

3. Results and Discussions

A white precipitate was formed when $FeSO_4$ and NaOH were mixed in a ratio that produced a suspension with an initial pH of 8.3. In the present experiment, the molar ratio of $[Fe(II)/[OH^-]]$ was 0.5833 (7/12). Under this condition, essentially all of the added OH^- ions are consumed to form $Fe(OH)_2$, and (1/7)th of the Fe(II) remains in solution. Because the added base is consumed in the precipitation process, the suspension is only slightly basic (pH = 8.3). Thus the initial reaction can be described as follows:

$$7FeSO_4 + 12NaOH \rightarrow 6Fe(OH)_2 + 6Na_2SO_4 + Fe(II) + SO_4^{2-}$$

As oxygen is passed through the suspension, the white precipitate was oxidized and the color of the mixture turned first to green, then blue, and finally orange-yellow. The change in pH with reaction time during the oxidation process is presented in Figure 1. Several distinct stages can be observed. During the first stage, the pH of the suspension was reduced from 8.3 to about 7.9. At the end of this stage, the pH abruptly decreased to about 6.4 during 5-6 minutes with continuous oxygen flow. This sharp drop in pH is due to oxidation of Fe(II) by oxygen and the hydrolysis reactions of the oxidation species [7]. During the next stage of oxidation, the pH remained constant about 6.2. As with the first stage, there was finally an abrupt decrease in pH to about 4 following which the oxygen consumption became very low and the pH remained nearly constant.

During the initial course of oxidation, ferrous ions in the solution are oxidized to produce ferric ions which combine with ferrous ions to form an iron mixed-valence green complex. It has been reported that the green complex consists of Fe(II)-O-Fe(III) [15] which oxidized further to produce $\gamma - FeOOH$ during the second stage. It was calculated that at the end of first stage, $Fe(OH)_2$ completely converts to green rust and the molar fraction of Fe(III) in the green rust was estimated to about 30% [7]. Electron microscopy studies revealed that the initial amorphous material developed to form green rust with morphology of large thin hexagonal crystals which contains holes. With the initial, sudden pH decrease at about 33% conversion of the total amount of Fe^{2+} that is oxidized, small, dense, hexagonal Fe_3O_4 particles were formed in addition to the green rust hexagonal crystals. The disappearance of Fe_3O_4 and green rust particles with further oxidation was accompanied by the development of needle-type $\gamma - FeOOH$ particles [9].

The powder X-ray diffraction pattern of the final synthesized product is shown in Figure 2. Comparison of the diffraction pattern to those reported in JCPDS by ICDD, indicated the presence of synthetic lepidocrocite ($\gamma-\mathrm{FeOOH}$, orthorhombic, space group: Bbmm (63), PDF # 00-044-1415), synthetic goethite ($\alpha-\mathrm{FeOOH}$, orthorhombic, space group: Pbnm (62), PDF # 01-081-0464) and magnetite (Fe_3O_4, orthorhombic, space group: Pmc21(26), PDF # 01-076-0958). The sharp peak in the powder XRD pattern at $2\theta = 27.06^{o}$ corresponds to high-intensity peak from (210) face of $\gamma-\mathrm{FeOOH}$. Neither $\alpha-\mathrm{FeOOH}$ nor Fe_3O_4 have any characteristic high-intensity XRD peak in this region. The powder XRD spectrum also contains some peaks that are unique to $\gamma-\mathrm{FeOOH}$ and not present in the pattern of $\alpha-\mathrm{FeOOH}$ or Fe_3O_4; e.g., peak at $2\theta = 14.1^{o}$ and $2\theta = 46.9^{o}$ which correspond to peak from (200) and (020) face of $\gamma-\mathrm{FeOOH}$, respectively. The broad peak at about $2\theta = 36.25^{o}$ might originate due to joint contributions from the (301) face of $\gamma-\mathrm{FeOOH}$ and the (111) face of $\alpha-\mathrm{FeOOH}$. However, the peak at $2\theta = 33.25^{o}$ can be uniquely assigned to the (130) face of $\alpha-\mathrm{FeOOH}$. Another broad peak at $2\theta = 21.2^{o}$ can be assigned to a joint contribution from the high-intensity peaks from (110) face of $\alpha-\mathrm{FeOOH}$ and (220) face of magnetite. The XRD peak at $2\theta = 19.8^{o}$ can be assigned to high-intensity peak from (212) face of magnetite. Quantitative Rietveld analysis revealed that the synthesized phase has a composition of 51% $\gamma-\mathrm{FeOOH}$, 23% $\alpha-\mathrm{FeOOH}$ and 26% magnetite. Thus the predominant phase in the prepared sample is iron oxyhydroxide.

A reaction sequence, as described by Davis [7] representing the oxidation pathway from $\mathrm{Fe(OH)_2}$ to $\gamma-\mathrm{FeOOH}$, is presented in Figure 3. Precipitation and oxidation of

aqueous Fe^{2+} ions may result in the production of a number of iron oxyhydroxides depending upon the method of preparation, and the iron precursor. It is known that the $[Fe]/[OH^-]$ ratio, the oxidizing agent, and the reaction rate play key roles in determining the crystalline structure of oxyhydroxides and oxides [7]. On the other hand, temperature mainly controls the particle size rather than morphology. At higher oxidation temperatures (i.e., > 75 °C), the morphology as well as particles sizes are affected. The predominant crystalline phases and corresponding morphologies of the final oxidation product depend significantly on the reaction conditions such as temperature, pH, coexisting ions, etc.; for example, spherical [16], cubic [17-18], doubly-spherical [19], and disc like [20] $\alpha - Fe_2O_3$ were prepared by the hydrothermal treatment of iron salt solutions at elevated temperature. Kameshwari [21] reported the formation of $\delta - FeOOH$, $\alpha - Fe_2O_3$, and $\gamma - Fe_2O_3$ (needle shape) starting from $FeSO_4$, $\beta - FeOOH$ (spherical shape) from $FeCl_3$ and $\alpha - FeOOH$ (irregular shape) particles starting from $Fe(NO_3)_3$ precursors. The variation of the morphology of iron oxyhydroxides or oxides has been attributed to the effect of anions.

Naono and Nakai [22] have reported that the growth of $\gamma - FeOOH$ nuclei, formed in acidic medium, showed in the initial stage a number of ultrafine needle crystallites (50 Å wide) which grow from the central part of the nuclei to both sides along the z-axis of $\gamma - FeOOH$. As growth continues the gap between needle crystallites is gradually filled, then a flat surface appears and finally acicular fine particles having a well-developed (010) surface are formed. The appearance of the (010) surface has been claimed by a number of authors for both mineral and synthetic lepidocrocite, $\gamma - FeOOH$ [23-25]. With the growth of the particles, the diffraction intensity of the (020) or (120) peaks, i.e.,

(hkl) peaks for $l = 0$, increases more rapidly compared with the (031) or (002) peaks, i.e., (hkl) peaks for $l \neq 0$. This leads to the conclusion that the $\gamma - FeOOH$ particles grow preferentially along the z-axis of $\gamma - FeOOH$ and this result is consistent with the morphological observation based on HRTEM analysis as discussed later.

The HRTEM pictures of the synthesized iron oxyhydroxide particles are shown in Figures 4a-4d. The HRTEM images confirm that only nano-needle like structures are present and the final oxidation product does not contain other particle morphology such as hexagonal or spherical particles. The average length of the rod-shaped particles (nano-needles) is in the 150-200 nm range and the average particle diameter is about 5-10 nm. The crystalline needle-shaped particles have a three dimensional network with a characteristic d-spacing of 2.5 Å which corresponds to the high-intensity (301) face of $\gamma - FeOOH$. An electron microdiffraction pattern of synthesized particles is shown in Figure 5. The rings in the electron micro-diffraction pattern are indexed using Gatan Digital Micrograph® software and reported JCPDS data from ICDD. The rings a', b', c' and d' in Figure 5 correspond to reflections from the (210), (301), (020) and (002) faces of $\gamma - FeOOH$, respectively. On the other hand, rings a, b, c, d, e, and f, correspond to reflections from the (110), (120), (111), (140), (211) and (221) faces of $\alpha - FeOOH$, respectively. Thus the electron microdiffraction pattern together with the x-ray diffraction pattern confirms the presence of iron oxide hydroxides as the predominant phases.

Analysis of the outlet gas during CO activation provided the amount of CO_2 generated during the carbidization and this is represented in Figure 6 (mol of CO_2 per g of iron versus time). The first peak of this profile (around 3.75 h) corresponds to the transformation of $\gamma - FeOOH$ to Fe_3O_4. The second and broad peak (starting around 6

h) corresponds to the slow transformation of Fe_3O_4 to iron carbides which continues up to around 10 hours. After this period, the amount of CO_2 produced starts to decline.

The morphology and chemical nature of the particles after CO activation (in the absence of mechanical agitation) were examined by HRTEM, EDS and electron-microdiffraction techniques. The HRTEM images of the carbided particles are shown in Figures 7a-7d. The changes in the morphology of the particles are evident; the initial needle-type structures of the iron oxyhydroxide particles have disappeared upon carbidization. Formation of aggregates of ultrafine crystalline circular shaped structures can be noticed. These small crystallites (irregular shaped spheres) are multicrystalline in nature and form a layered structure. The non-smoothed and non-perfect spherical particles (Figure 7b and 7c) have a crumpled and boulder-like appearance. These structures originate from nanocrystalline grains within and on the nanoparticle surface. The carbide particles are made of aggregates of nanocrystals. An electron diffraction pattern of the carbided sample is shown in Figure 8. The a' ring corresponds to reflections from the (510) face of $\chi - Fe_5C_2$ while the rings a, b, c, d, e, f, and g correspond to reflections from (111), (220), (311), (400), (422), (511) and (440) faces of Fe_3O_4, respectively. The high resolution TEM image shown in Figure 7d indicates atomic planes of the crystalline grains in the particles. The characteristic d-spacing of these crystallites is 2.0 Å which can correspond to (510) face of $\chi - Fe_5C_2$.

The EDS analysis of the CO activated sample shown in Figure 9 also confirmed the generation of the carbide phase. The elemental compositions of the activated particles are shown in Table 1. The presence of a small amount of oxygen suggests that the transformation of oxide to carbide phase was not complete and this agrees with the results

obtained from electron microdiffraction analysis. It is difficult to reach full conversion in the oxide-carbide transformation. It has been reported that CO activation of ultrafine iron oxide at 270 °C and atmospheric pressure for 24 h results in 85% carbide [26]. Hence, it is unlikely to convert iron oxyhydroxide particles to iron carbides completely during a 10-12 h period. The leftover oxide is likely a central core that remains under the carbide phase.

Oxide-carbide phase-transformations during activation and/or Fischer-Tropsch synthesis induce a volumetric change due to a significant difference in densities and the resulting shear may lead to the formation of small crystallites of iron carbides which split off to form ultrafine particles [27]. The conversion of the oxide to carbide phase is dynamic and may be reversible depending upon the environment. Since the carbidization was performed without mechanical stirring, it can be concluded that the difference in densities of the two phases and the resulting stress induced in the particles were sufficient to break the needle-like structure to generate a structure which was composed of near-spherical particles residing in close proximity.

HRTEM images of the particles after carbidization performed in a CSTR with severe mechanical agitation are shown in Figures 10a-10b. Formation of spherical crystalline particles which are separated from each other can be seen. When the carbidization was performed without any mechanical agitation, particles generated from the needle-like structures were held together as aggregates. However the mechanical stirring was found to break the aggregates of particles and generate individual ultrafine particles.

EDS analysis of the carbided iron oxyhydroxides, as shown in Figure 9, indicated the presence of significant amounts of a sulfur species. The poisoning effect of sulfur on FTS

has been reported extensively [28-29]. The presence of a sulfur poison results in a decline in the adsorption of CO, thus preventing the formation of iron carbide, which is suggested to be the active sites for FTS [14]. $FeSO_4$ which was used as the iron precursor in the present synthesis acted as the source for this sulfur species. Attempts were taken to remove the residual SO_4^{2-} by successive washing with deionized water. However, it was found complete removal of SO_4^{2-} ions was difficult to achieve and the remaining SO_4^{2-} ions could act as a poison for FTS.

In order to avoid the presence of sulfur poisoning and to evaluate the FTS activity of iron oxyhydroxides, a fresh batch of catalyst was made using ferric nitrate as the iron precursor [7]. Conversion of CO during FTS using this catalyst in a CSTR is presented in Figure 11. The catalyst started with a CO and H_2 conversion of about 72% and rose to 84%, after 24 h of synthesis. Since the catalyst was unpromoted, the conversion declined steadily over the course of the synthesis. After 340 h of synthesis, the CO conversion had declined to 26%. The total hydrocarbon production rate paralled the conversion data, increasing to 166 g m^{-3} of synthesis gas after 48 h and decreasing steadily to 63 g m^{-3} of synthesis gas at the end of the run. The C_{3+} hydrocarbon production followed a similar trend, reaching a maximum of 145 g m^{-3} of synthesis gas at 48 h and decreasing to 53 g m^{-3} of synthesis gas at 336 h.

An HRTEM image of the catalyst sample collected after 24 h of FTS is shown in Figure 12. The shapes of the crystalline ultrafine particles are similar to those shown in Figures 10a and 10b. However some larger sized particles were also found which were believed to have grown in situ. An electron diffraction pattern of the catalyst sample collected after 96 h of FTS is represented in Figure 13. The a' ring corresponds to

reflections from the (510) face of $\chi - Fe_5C_2$ and the rings a, b, c, d, e, f, and g correspond to reflections from the (111), (220), (311), (400), (422), (511) and (440) faces of Fe_3O_4, respectively. Hence, the basic nature of this diffraction pattern is similar to that shown in Figure 8. However the intensity of the a' ring is greater in Figure 8 than in Figure 13, suggesting a decrease in carbide content of the catalyst. This is due to in situ re-oxidation of the carbide phase by FTS products, like water.

It was reported that while using iron oxide particles of 100-200 micron in size for FTS, the carbide phase forms as small nodules on the surface of the magnetite and the phase transformation proceeds slowly into the bulk [12]. The volumetric change during the oxide to carbide transformation results in the sprouting of carbide buds/nodules on the surface of the magnetite crystal. However, such phenomena were not observed in the present study using particles that are much smaller, at least in two of their dimensions. The carbide particles were identified as bulk phase with layers. The change of morphology (from nano-needles to spherical particles) is primarily due to changes in the chemical nature of particles.

4. Conclusions

Homogeneous oxidation of Fe(II) results in the precipitation of ultrafine iron oxyhydroxide particles (predominantly $\gamma - FeOOH$ phase) having a needle-like structure. Electron microscopy analysis revealed that carbidization caused the disapprearance of the initial needle-like morphology of the particles and generated small crystallites of irregular shaped spheres. Carbidization with CO at atmospheric pressure and 270 °C without mechanical stirring was found to produce multicrystalline layered iron carbides with irregular spherical structure residing in close proximity while

carbidization with severe mechanical stirring results in formation of spherical carbide particles that are separated from each other. Volumetric stress generated during the carbidization process is suggested to be responsible for the fragmentation of the nano-needle structures. Initial activity of iron oxyhydroxide catalyst for Fischer-Tropsch synthesis was high; however, the activity declined steadily.

References

1. T. Masuda, Y. Kondo, M. Miwa, T. Shimotori, S. R. Mukai, K. Hashimoto, M. Takano, S. Kawasaki, S. Yoshida, Chemical Engineering Science, 56 (2001), 897-904.
2. S. Chou, C. Huang, Y. H. Huang, Environmental Science and Technology, 35 (2001), 1247-1251.
3. S. Chou, C. Huang, C., Chemosphere, 38(1999), 2719-2731.
4. T. Kaneko, K. Tazawa, N. Okuyama, M. Tamura, and K. Shimasaki, Fuel, 79 (2000), 263-271.
5. R. M. Cornell, U. Schwertmann, The Iron Oxides: Structure, Properties, Reactions, Occurrence and Uses, VHC, Weinheim, Germany, 1996.
6. K. Asami, Y. Ohtsuka, Industrial & Engineering Chemistry Research, 32 (1993), 1631-1636.
7. B. H. Davis, Technology development for iron Fischer-Tropsch catalysts. Final Technical Report, US DOE, Contract # DE-AC22-91PC90056, 1993.
8. T. R. Motjope, H. T. Dlamini, G. R. Hearne, and N. J. Coville, Catalysis Today, 71 (2002), 335-341.
9. R. Srinivasan, R. Lin, R. L. Spicer, and B. H. Davis, Colloids and Surfaces, A: Physicochemical and Engineering Aspects, 113 (1996), 97-105.
10. R. Lin, R. L. Spicer, F. L. Tungate, and B. H. Davis, Colloids and Surfaces A: Physicochemical and Engineering Aspects, 113 (1996), 79-96.
11. C. S. Huang, B. Ganguly, G. P. Huffman, F. E. Huggins, and B. H. Davis, Fuel Science and Technology International, 11 (1993), 1289-1312.

12. M D. Shroff, D. S. Kalakkad, K. E. Coulte, S. D. Köhler, M. S. Harrington, N. B. Jackson, A. G. Sault, and A. K. Datye, Journal of Catalysis, 156 (1995), 185-207.
13. R. Zhao, J. G. Goodwin. K. Jothimurugesan, S. K. Gangwal and J. J. Spivey, Industrial & Engineering Chemistry Research, 40 (2001), 1320-1328.
14. S. Li, W. Ding, G. D. Meitzner, and E. Iglesia, J. Phys. Chem. B 106 (2002), 85-91.
15. T. F. Barton, T. Price, J. G. Dillars, Journal of Colloid and Interface Science, 141 (1991), 553-558.
16. E. Matijevic, P. Scheiner, J. Colloid Interface Sci. 63 (1978), 509-524.
17. S. Hamada, E. Matijevic, J. Colloid Interface Sci. 84 (1981), 274-277.
18. S. Hamada, E. Matijevic, J. Chem. Soc. Faraday Transactions 1: Phyical Chem. in Condensed Phases 78 (1982), 2147-2156.
19. S. Hamada, S. Niizeki, Y. Kudo, Bull. Chem. Soc. Japan 59 (1986), 3443-3450.
20. R. S. Sapieszko, E. Matijevic, J. Colloid Interface Sci. 74 (1980), 405-422.
21. S. Kameshwari, Proceeding of the symposium on Science of Catalysis and its Application to Industry, FPDIL, Sindri, India, February, 1979.
22. H. Naono and K. Nakai, J. Colloid Interface Sci. 128 (1989), 146-156.
23. T. Takada, M. Kiyama, S. Shimizu, Bull. Inst. Chem. Res. Kyoto Univ. 42 (1964), 505-510.
24. T. Takada, K. Nagasawa, M. Kiyama, S. Shimizu, Y. Bando, Bull. Inst. Chem. Res. Kyoto Univ. 47 (1969), 600-606.
25. R. Giovanoli, R. Brütsch, Thermochim. Acta, 13 (1975), 15-36.

26. Sarkar, U. M. Graham, J. K. Neathery, R. L. Spicer, and B. H. Davis, Proceeding of 6th Topical Conference on Natural Gas Utilization, Abstracts of Papers, AIChE Spring National Meeting, Paper # 181b, Orlando, FL, April 23-27, 2006.

27. R. Srinivasan, L. Xu, R. L. Spicer, F. L. Tungate and B. H. Davis, Fuel Science & Technology International, 14 (1996), 1337-1359.

28. M. E. Dry, in: J. R. Anderson, M. Boudart (Eds.), Catalysis – Science and Technology, Springer-Verlag, New York, 1981, pp. 201-202.

29. R. J. Madon, H. Shaw, Catal Rev. Sci. Eng. 15 (1977), 69-105.

Table 1. Quantitative EDS analysis of the γ – FeOOH particles after CO activation.

Element	**Weight%**	**Atomic%**	**% Uncertainty**
Carbon (Kα)	23	52	0.27
Oxygen (Kα)	10	16	0.1
Iron (Kα)	67	32	0.2

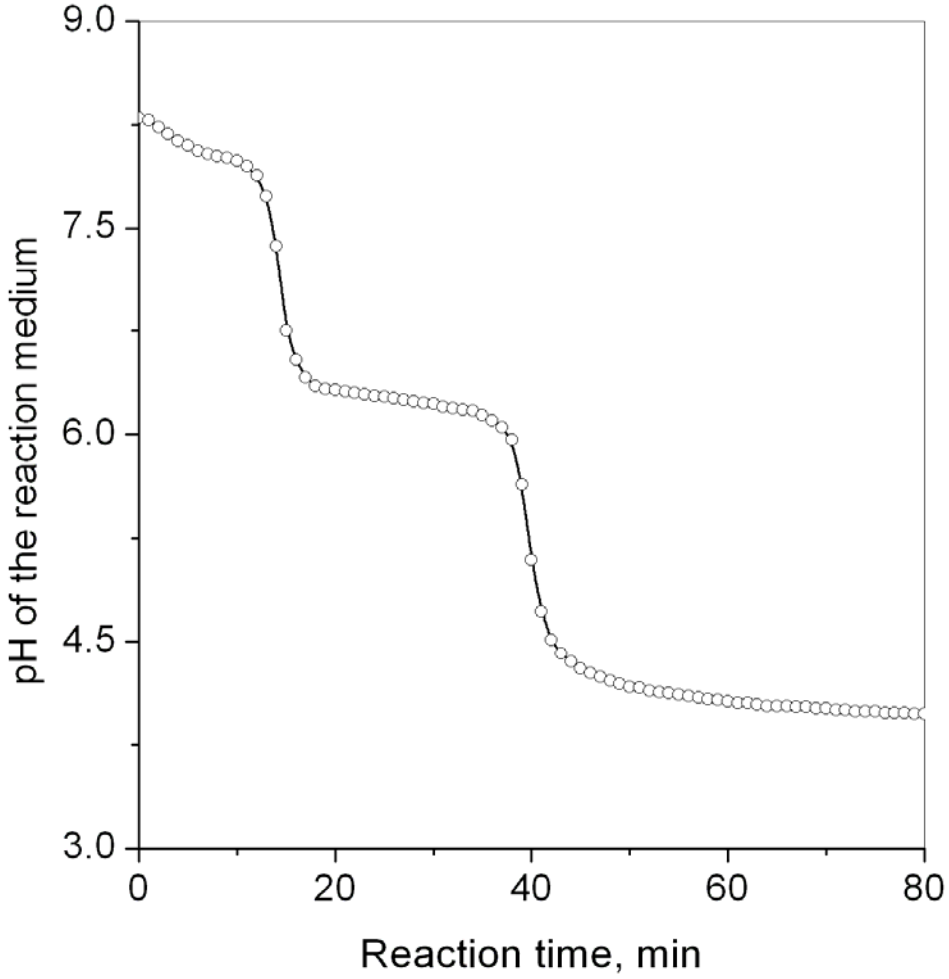

Figure 1. Variation in pH of the reaction medium with reaction time.

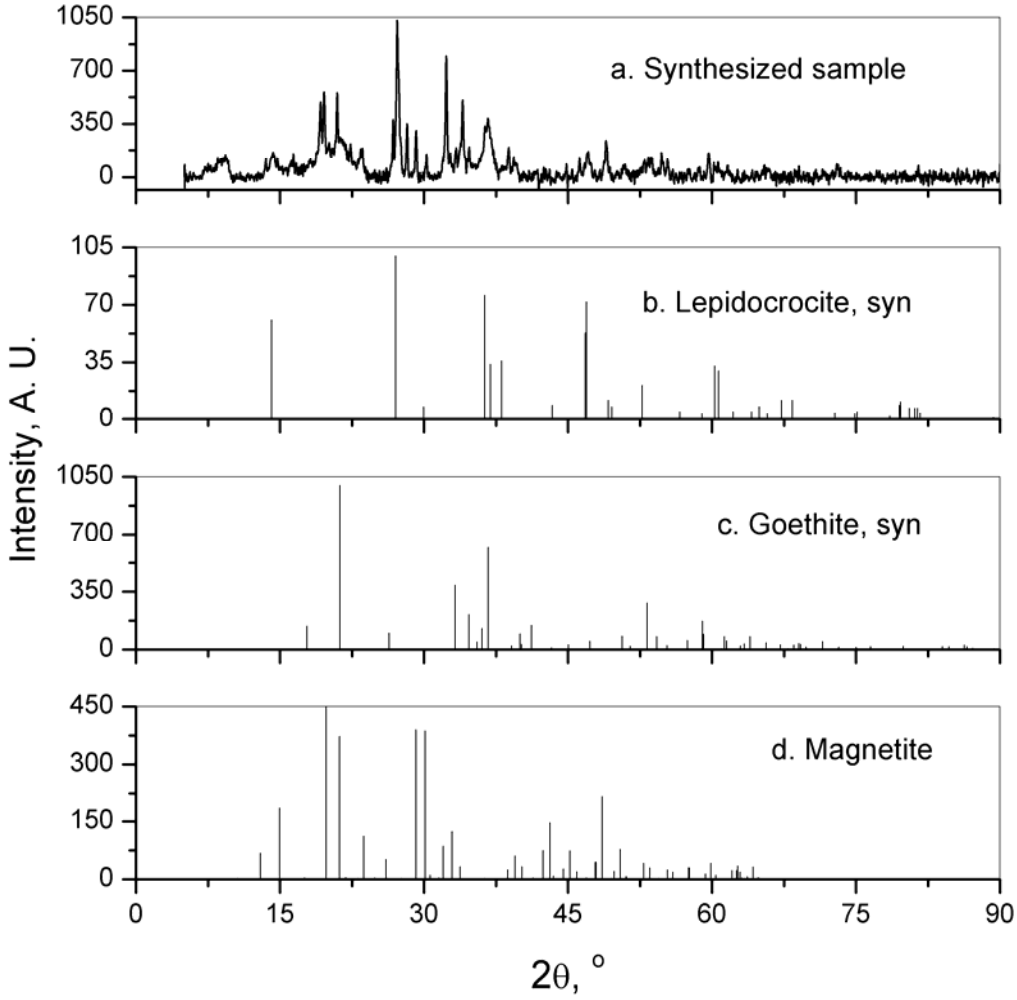

Figure 2. Powder x-ray diffraction pattern of the synthesized iron oxyhydroxide and reference JCPDS pattern of synthetic lepidocrocite ($\gamma-FeOOH$, PDF # 00-044-1415), synthetic goethite ($\alpha-FeOOH$, PDF # 01-081-0464) and magnetite (Fe_3O_4, PDF # 01-076-0958).

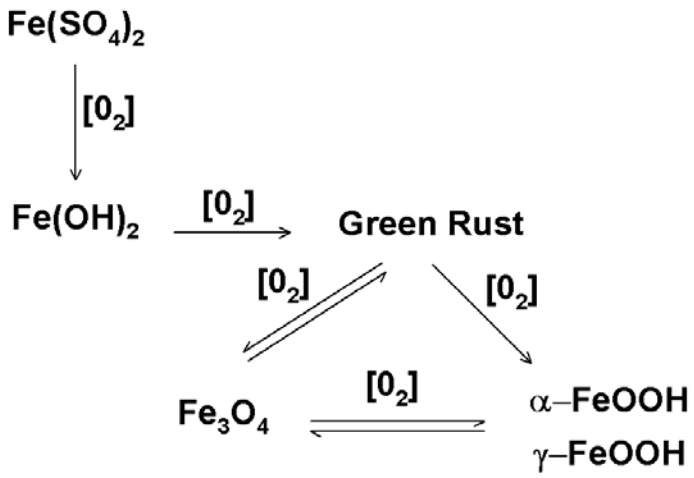

Figure 3. A pictorial reaction sequence representing the oxidation pathway from $Fe(OH)_2$ to different iron oxyhydroxides and oxides [7].

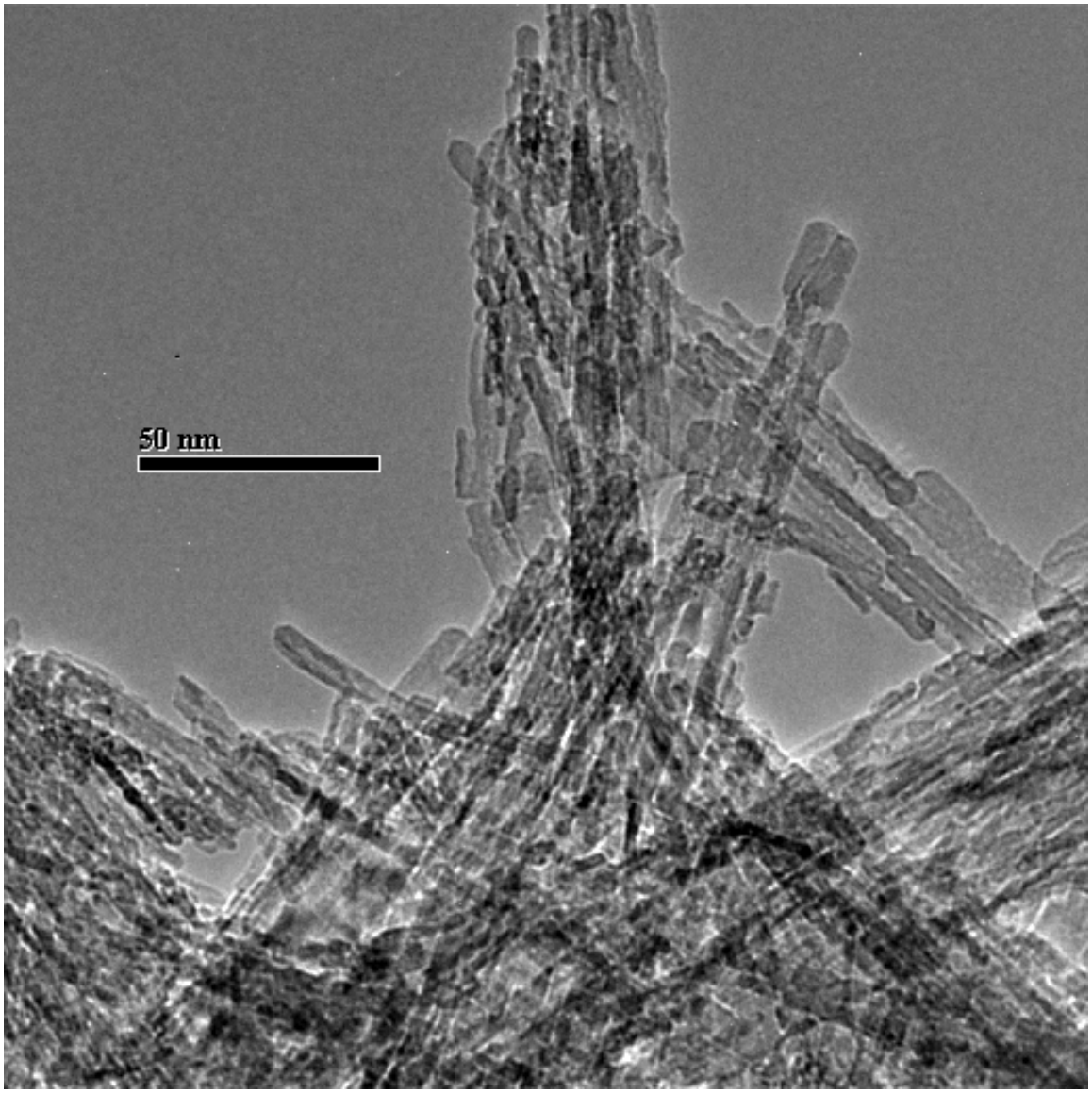

(4a)

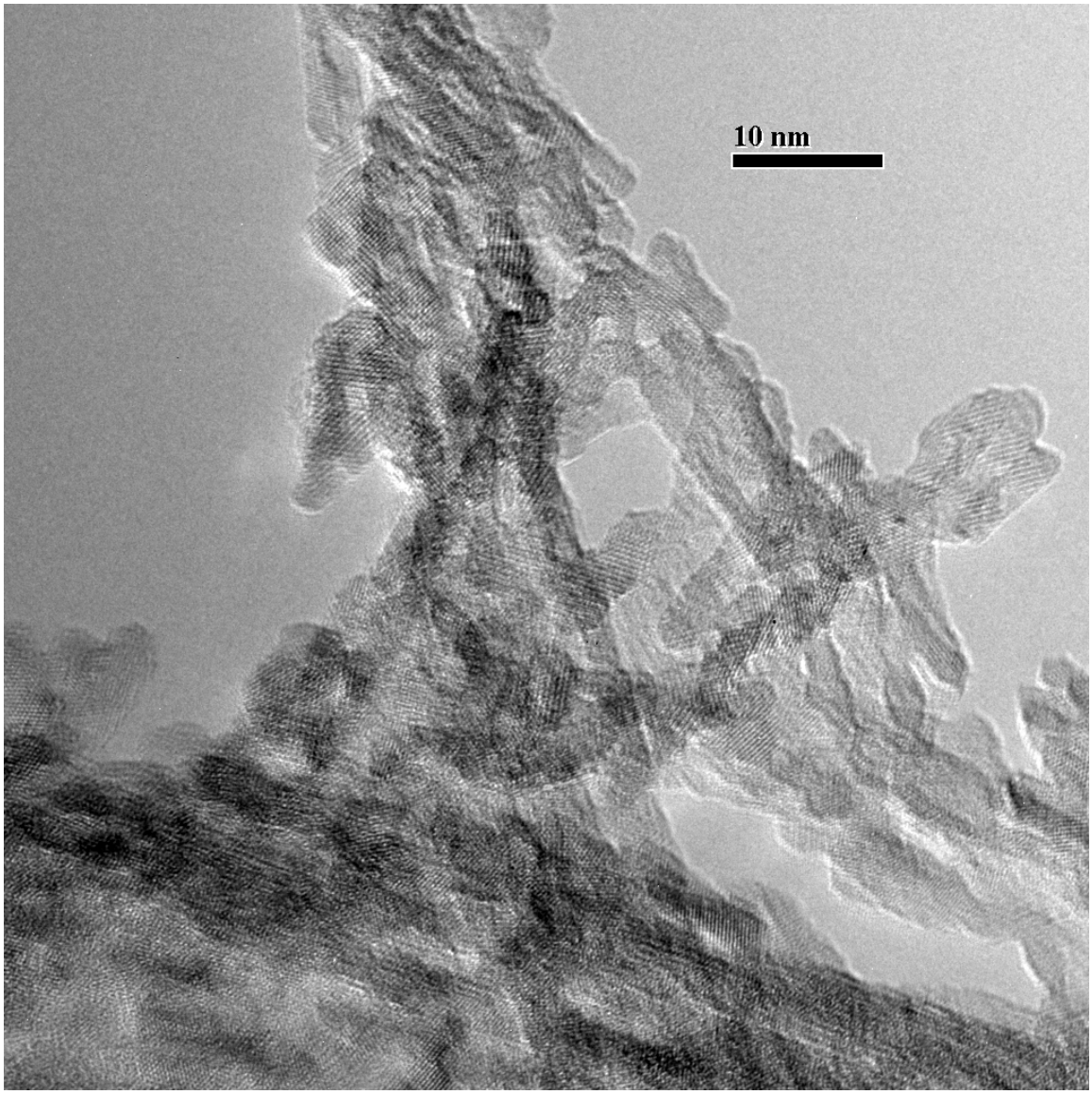

(4b)

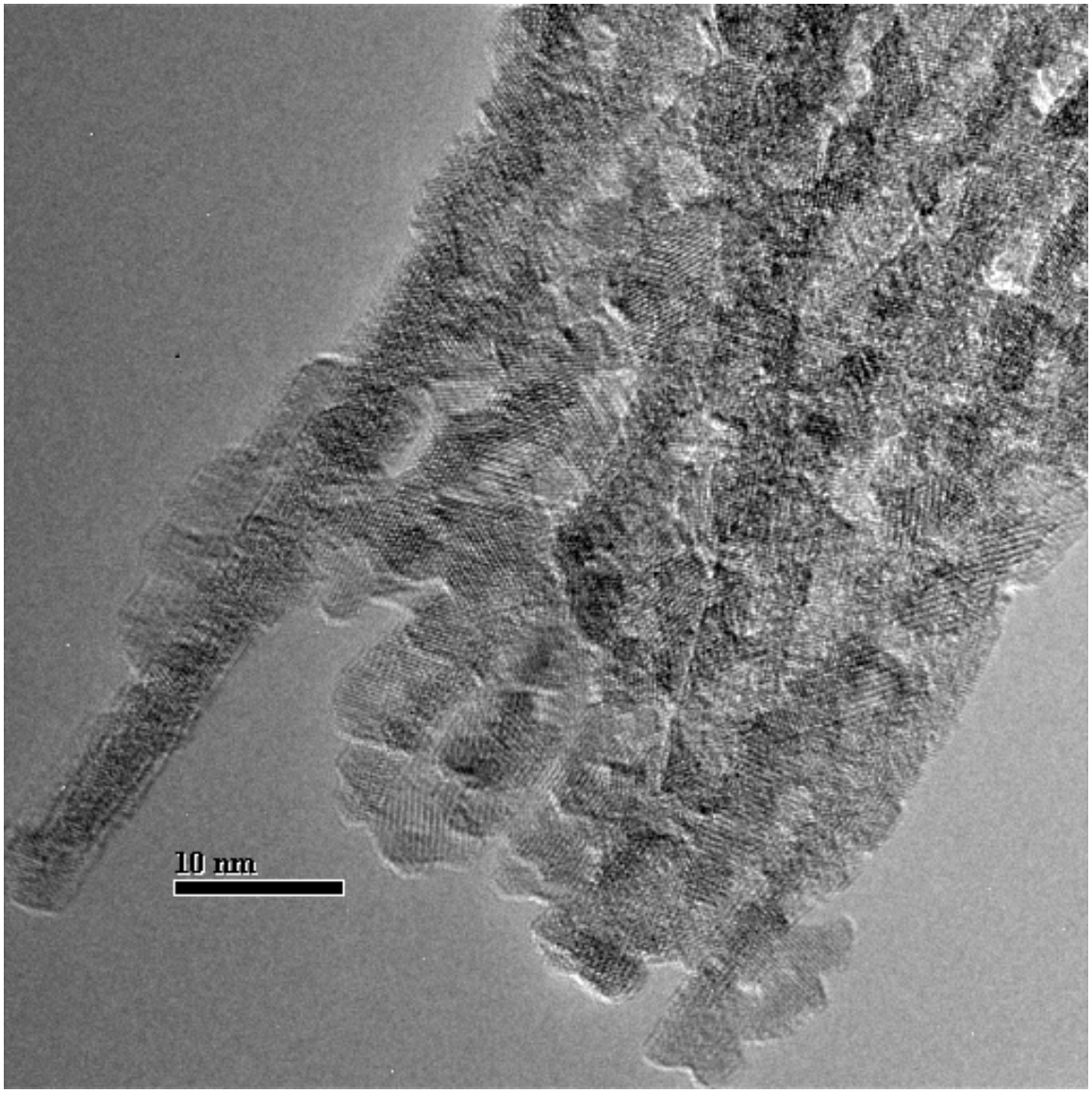

(4c)

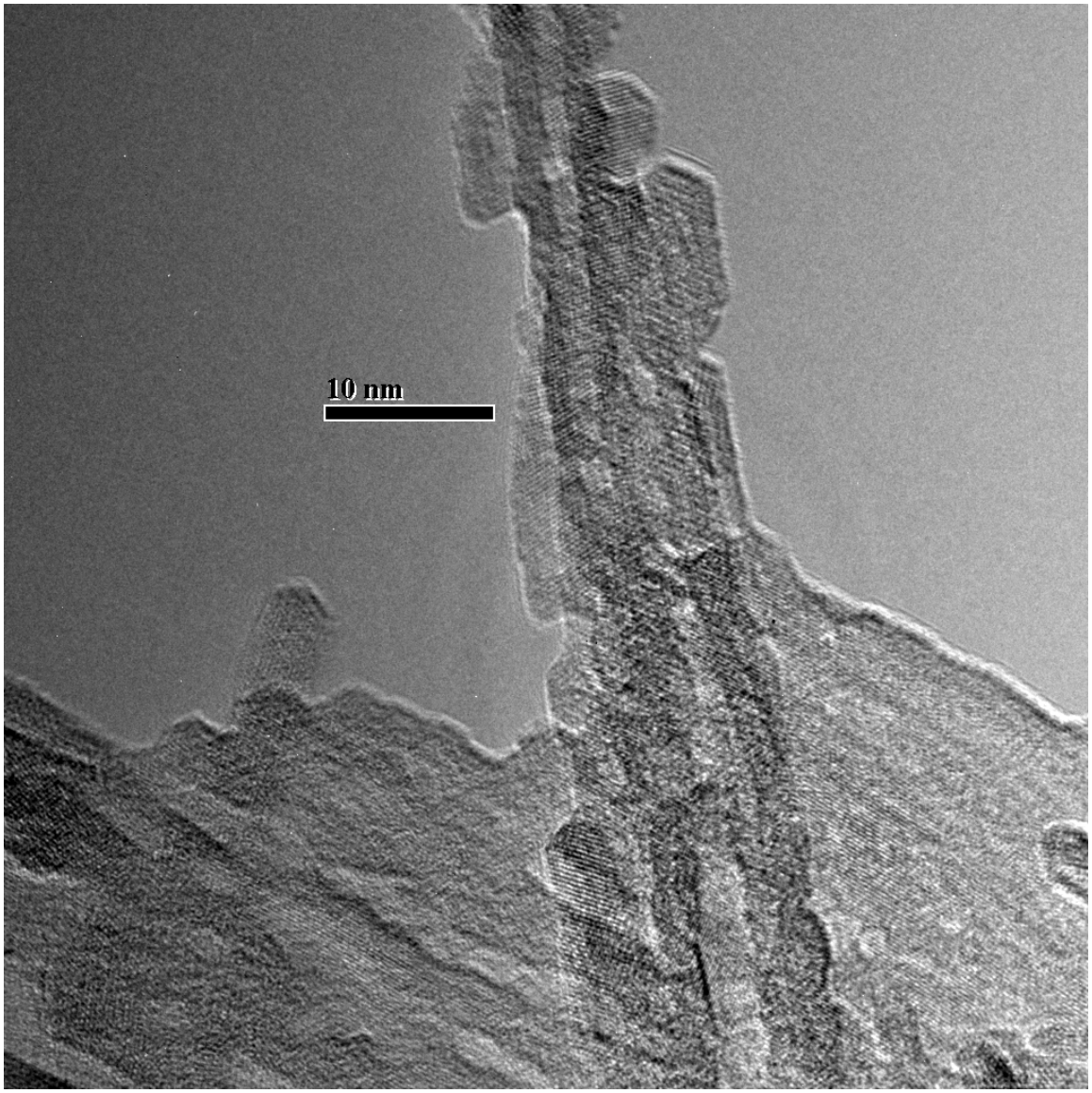

Figure 4. HRTEM image of the synthesized iron oxyhydroxide particles: (a) needle-shaped morphology; (b) crystalline structure with average diameter 5-10 nm; (c) aggregates crystalline nano-needle assembly; (d) crystalline nano-needle with a characteristic d-spacing of 2.5 Å.

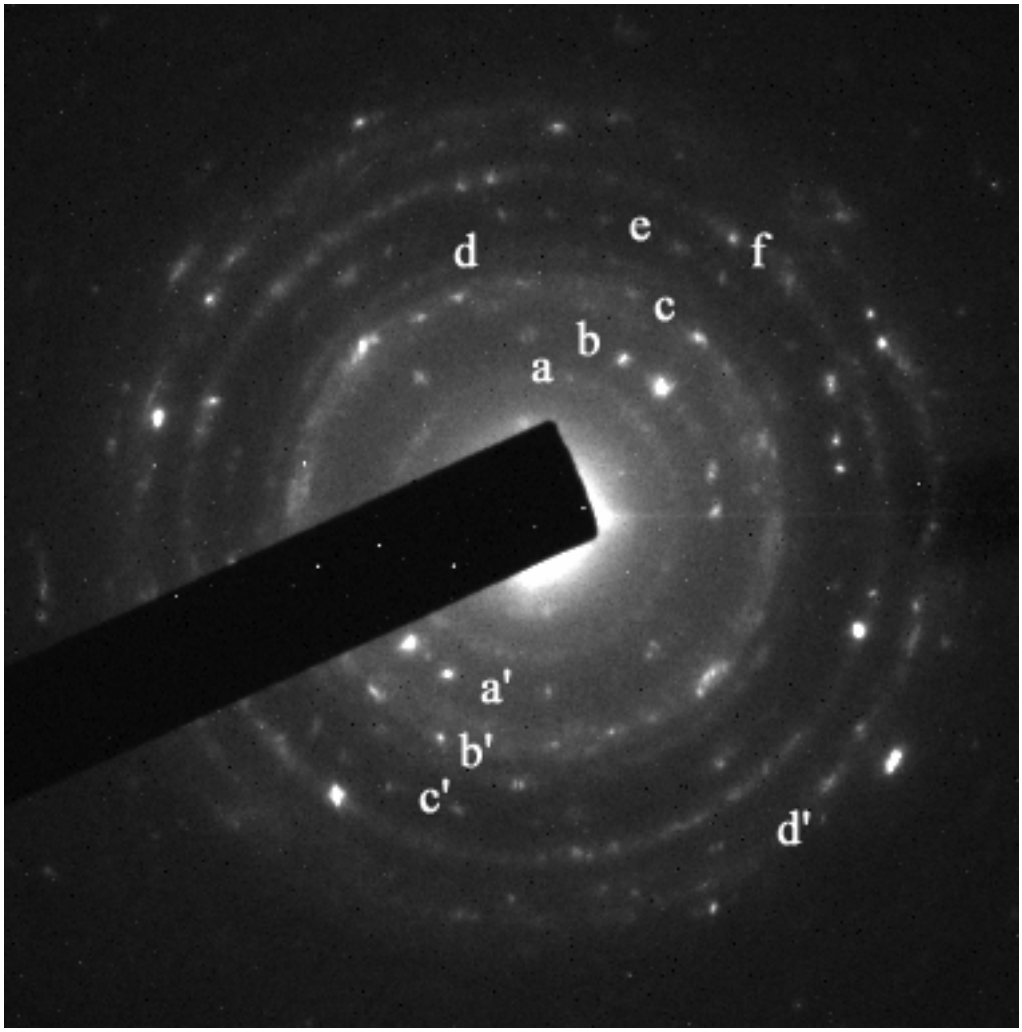

Figure 5. Electron microdiffraction pattern of the as-synthesized iron oxyhydroxide particles. Diffraction rings are index as: a', b', c' and d' from (210), (301), (020) and (002) faces of $\gamma - FeOOH$, respectively; a, b, c, d, e, and f, from (110), (120), (111), (140), (211) and (221) faces of $\alpha - FeOOH$.

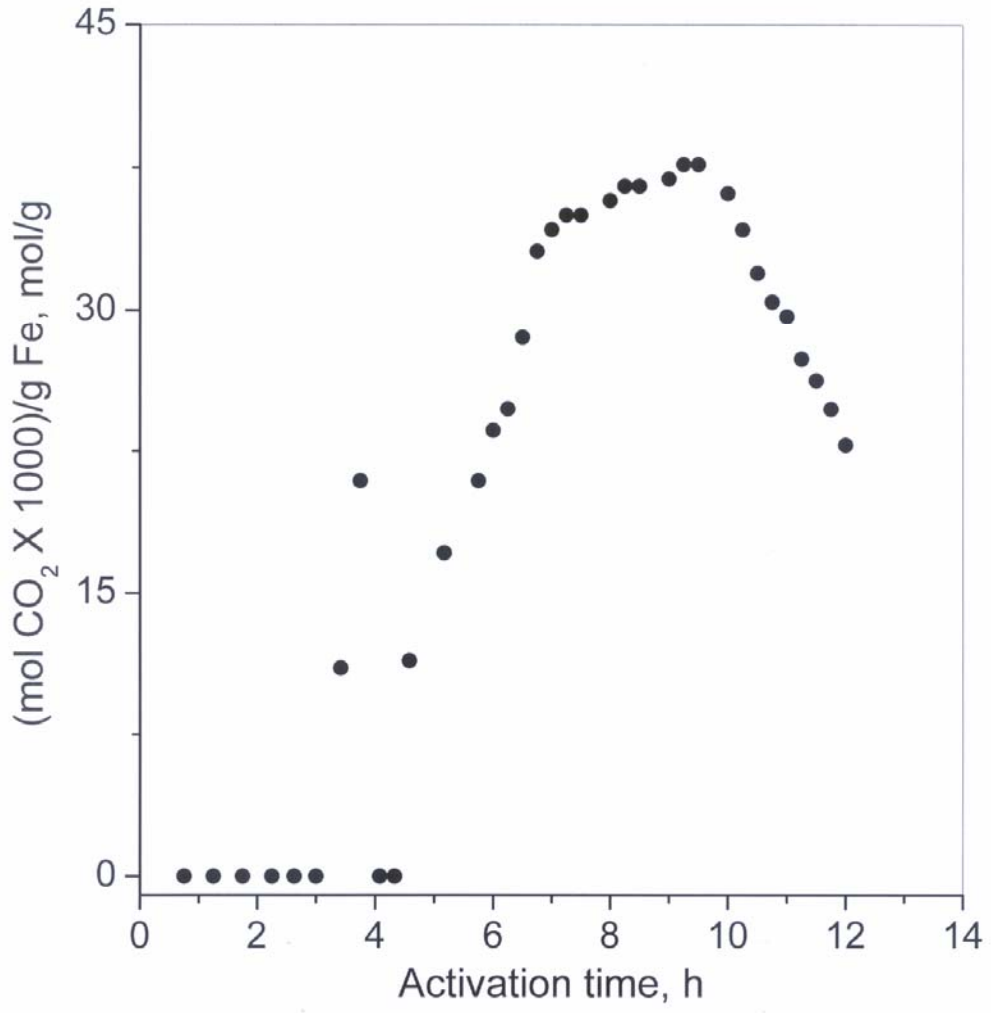

Figure 6. Variation in the amount of CO_2 generated (mol of CO_2 per g of iron) during the CO activation of the iron oxyhydroxide particles.

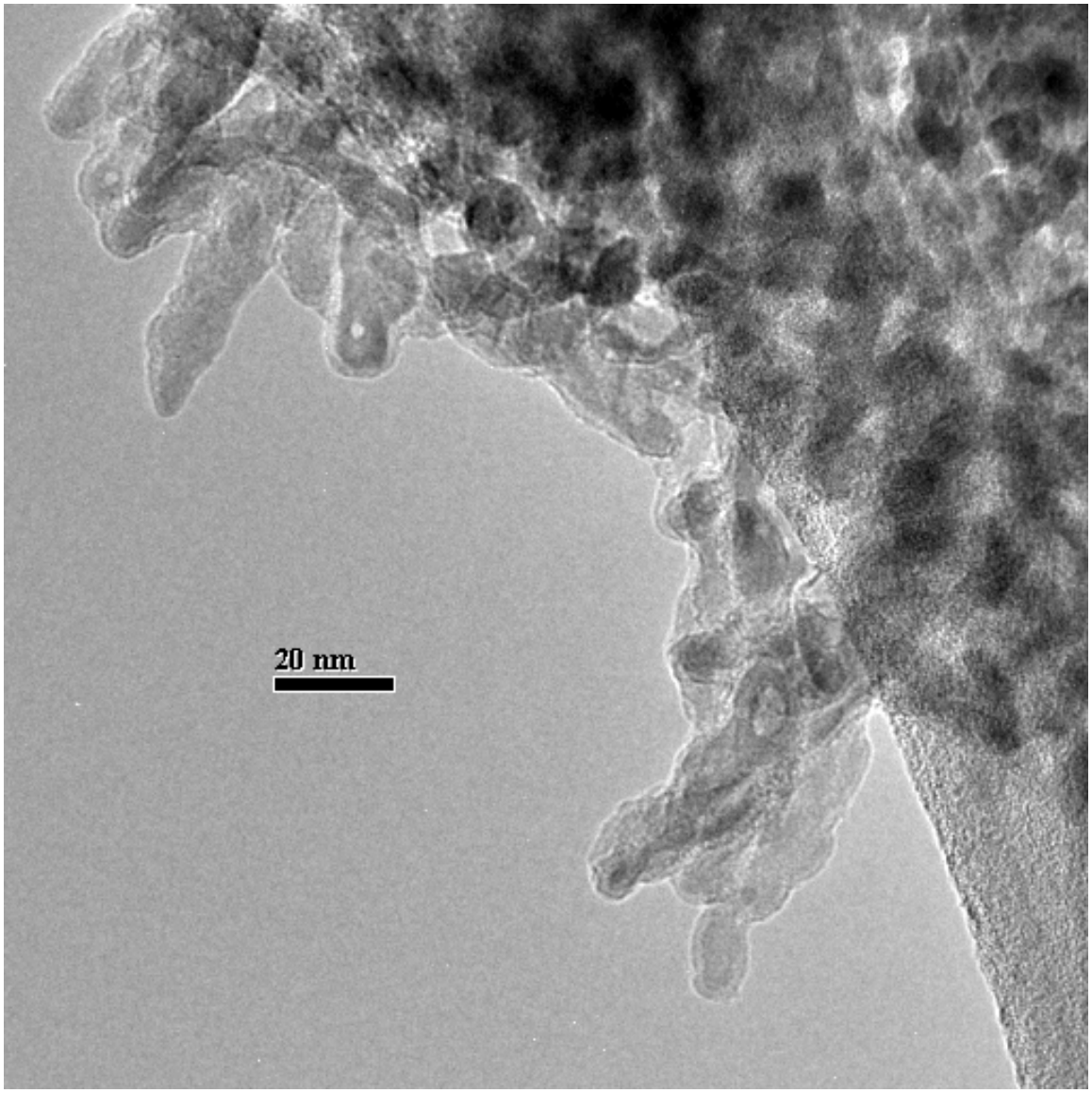

(7a)

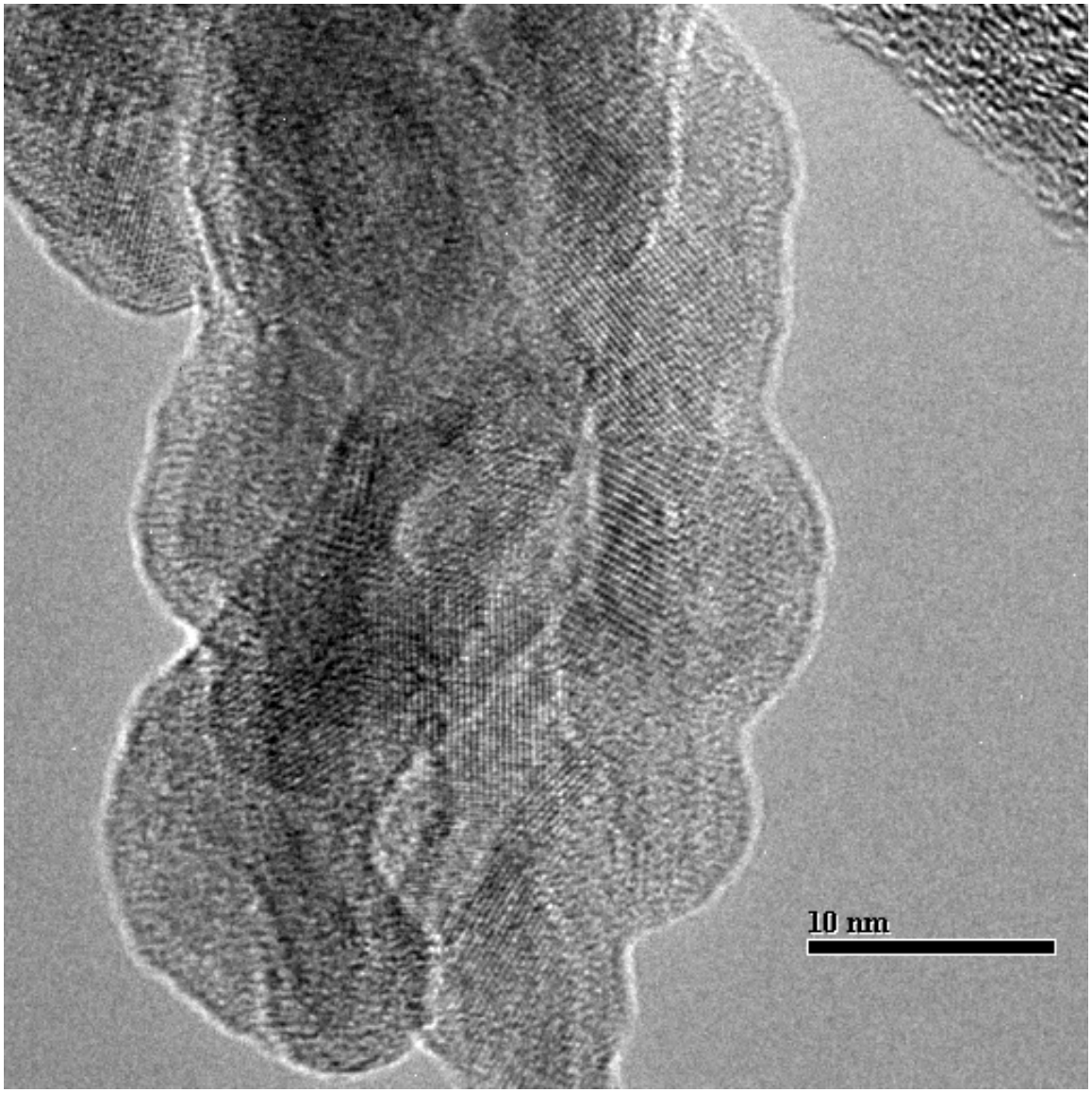

(7b)

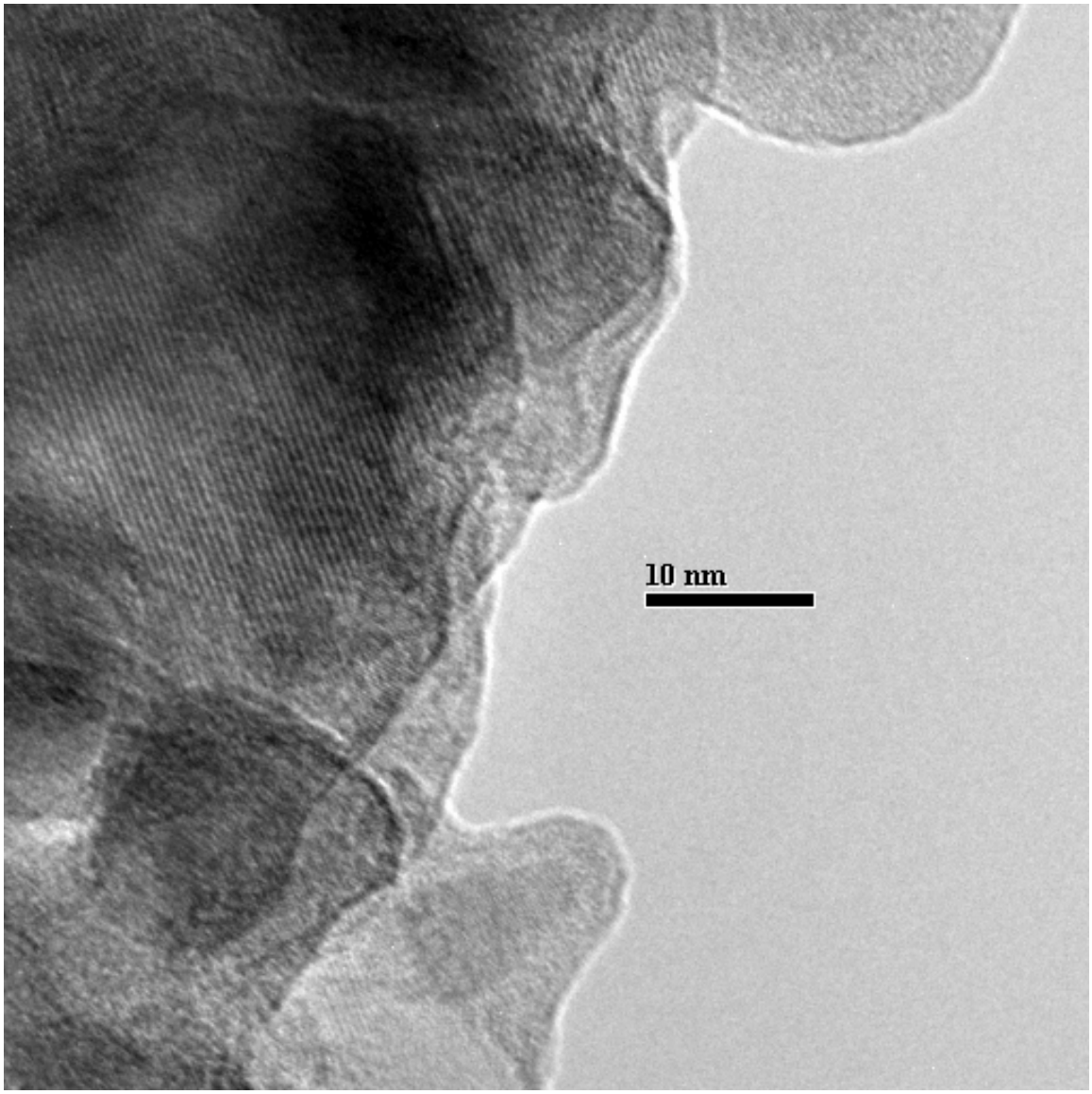

(7c)

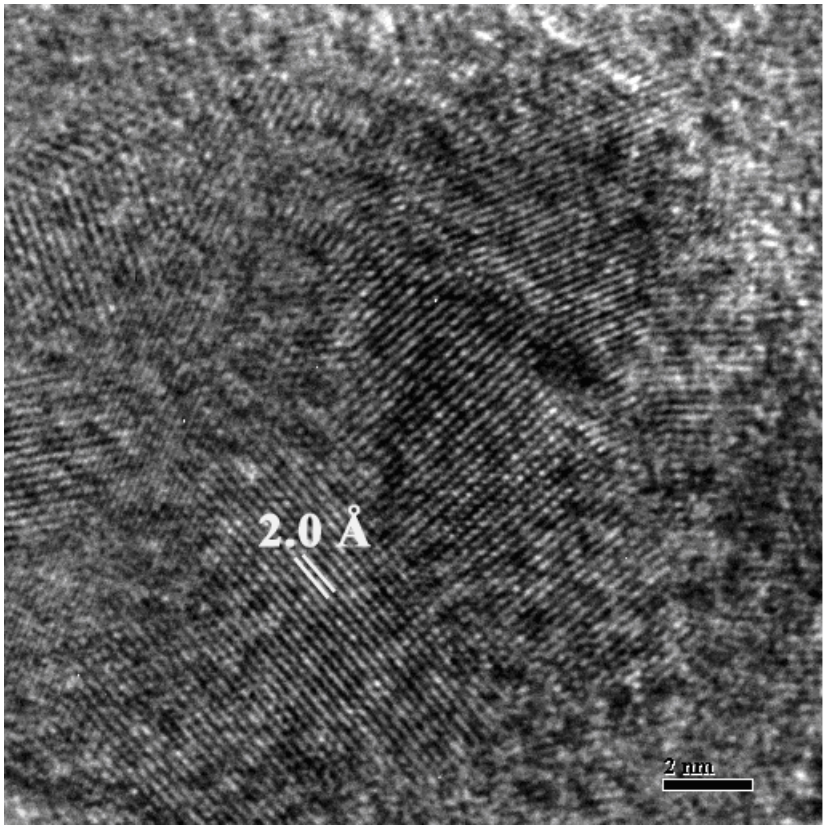

Figure 7. HRTEM images of the iron oxyhydroxide particles after carbidization in absence of any mechanical agitation: (a) loss of initial nano-needle like morphology - generation of non-perfect spherical particles; (b) generation of layered structure with crumpled and boulder like appearance; (c) aggregates of nano-crystalline planes; (d) crystalline iron carbides with a characteristic d-spacing of 2.0 Å.

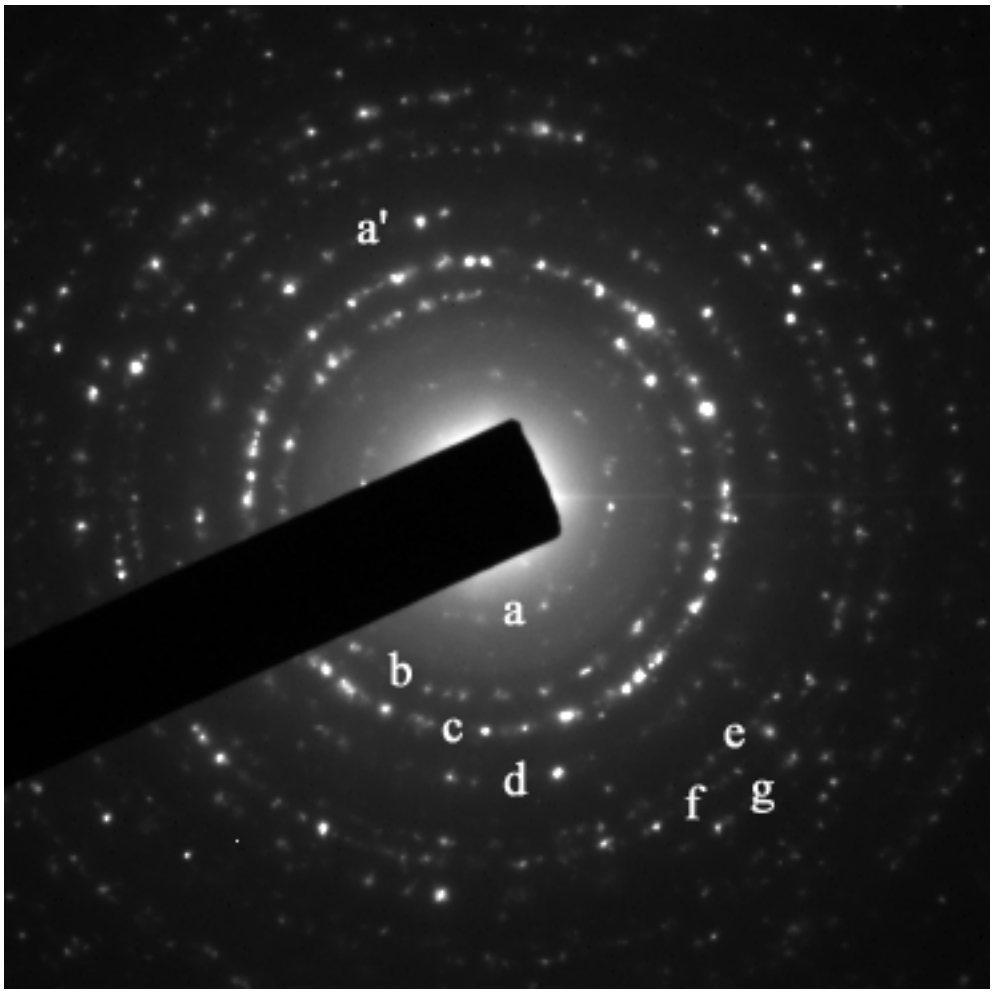

Figure 8. An electron microdiffraction pattern of iron oxyhydroxide particles after CO activation in absence of any mechanical agitation. Diffraction rings are indexed as: a' from (510) face of $\chi - Fe_5C_2$; a, b, c, d, e, f, and g from (111), (220), (311), (400), (422), (511) and (440) faces of Fe_3O_4, respectively.

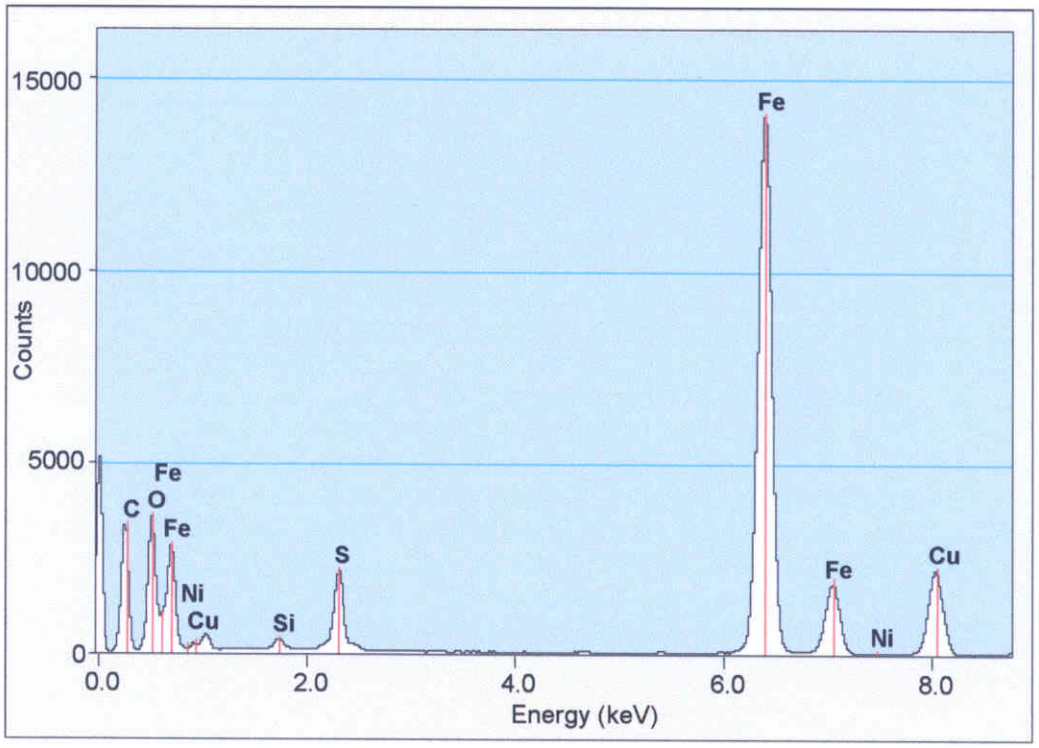

Figure 9. EDS analysis of the iron oxyhydroxide particles after CO activation at atmospheric pressure, 270 °C, without any mechanical agitation.

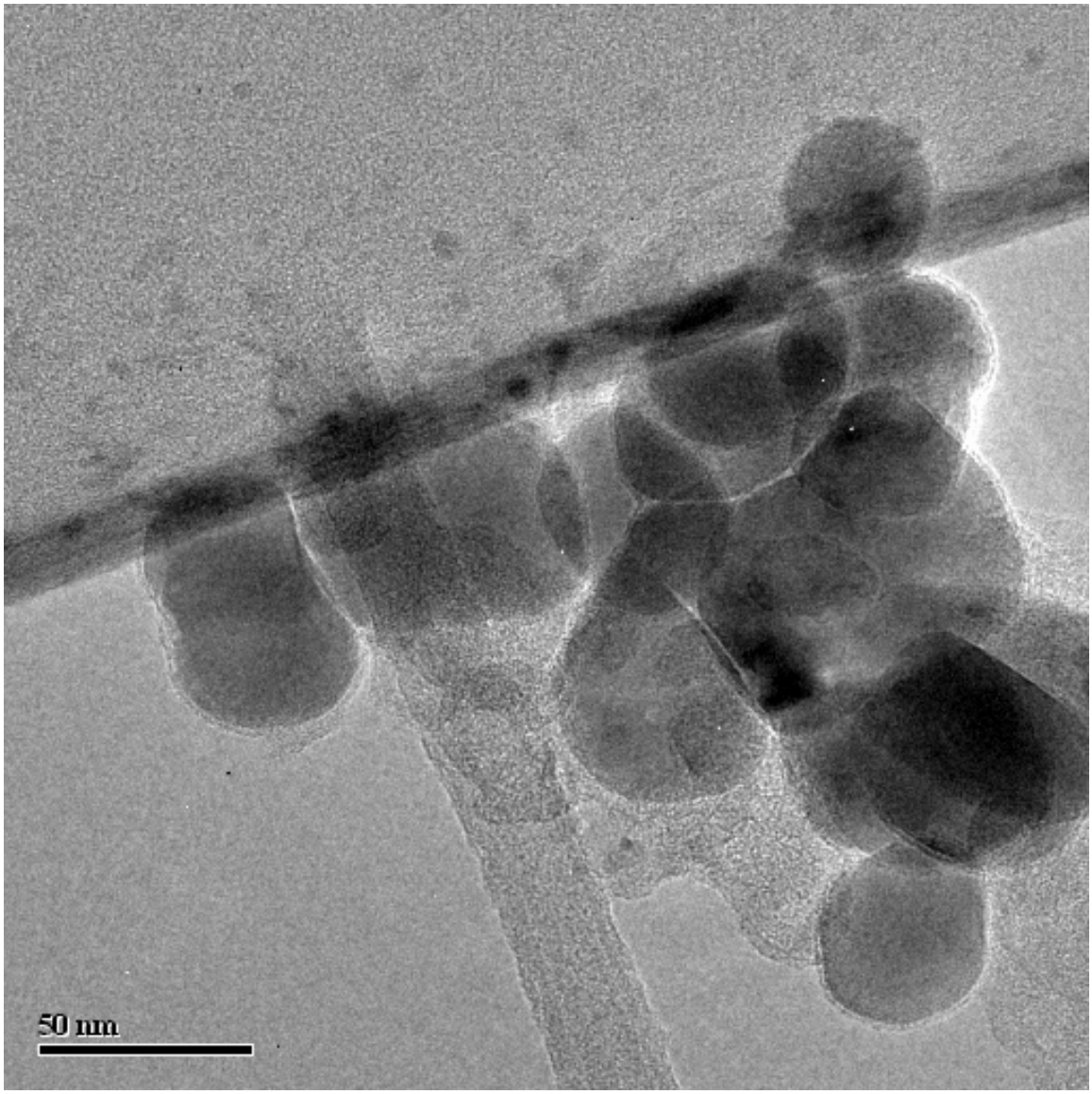

(10a)

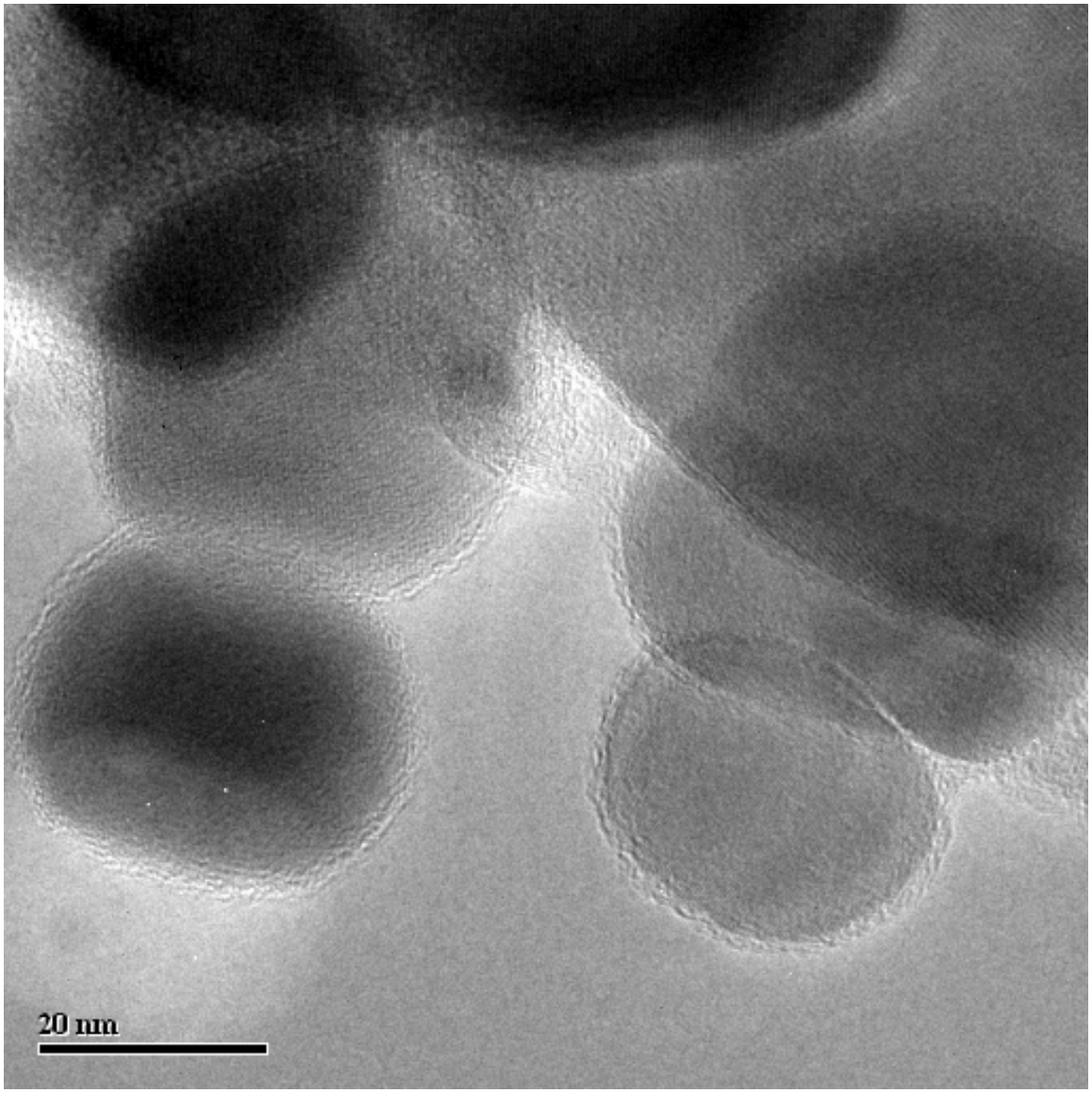

Figure 10. HRTEM images of the iron oxyhydroxide particles after carbidization at atmospheric pressure, 270 °C, under severe mechanical agitation: (a) generation of ultrafine particles with different shapes; (b) generation of completely separated near-spherical particles.

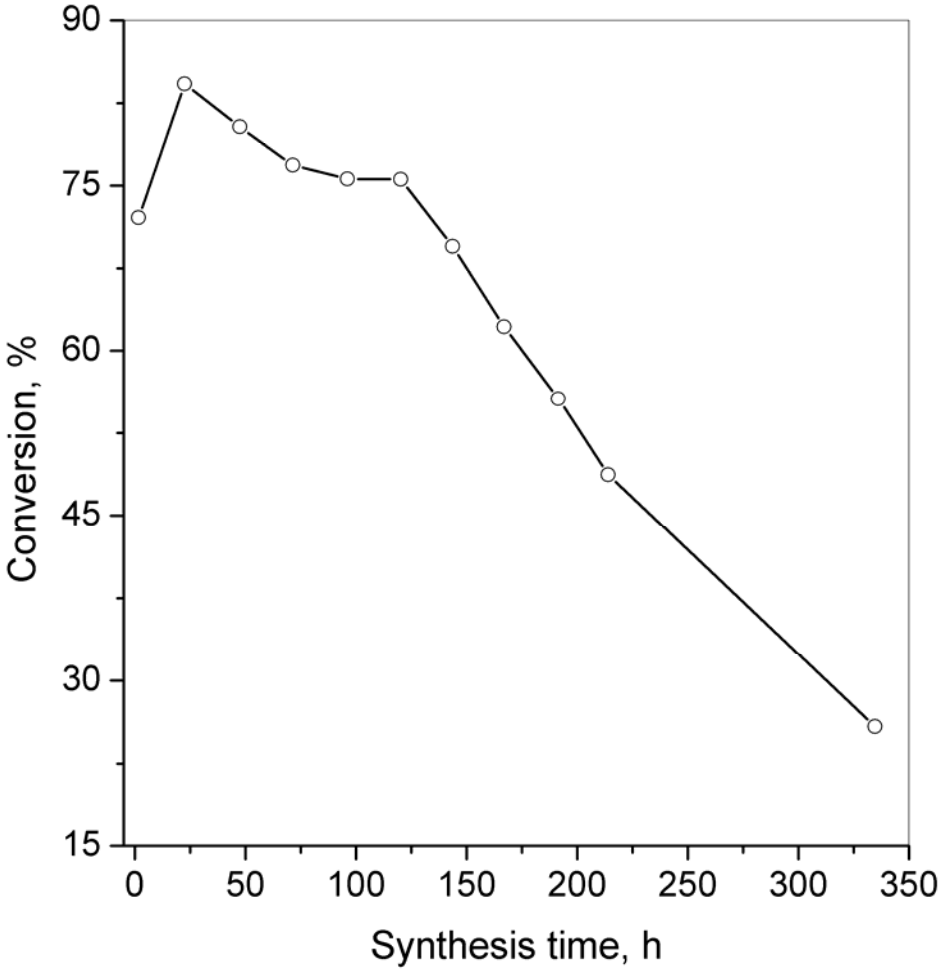

Figure 11. Conversion of CO and H_2 in FTS with iron oxyhydroxides activated with CO at 175 psig , 270 °C for 24 h with a CO SV of 3.0 sl/h/g Fe. FTS effected at 270 °C, 175 psig, $H_2/CO = 0.7$, and a syngas space velocity of 3.0 sl/h/g Fe.

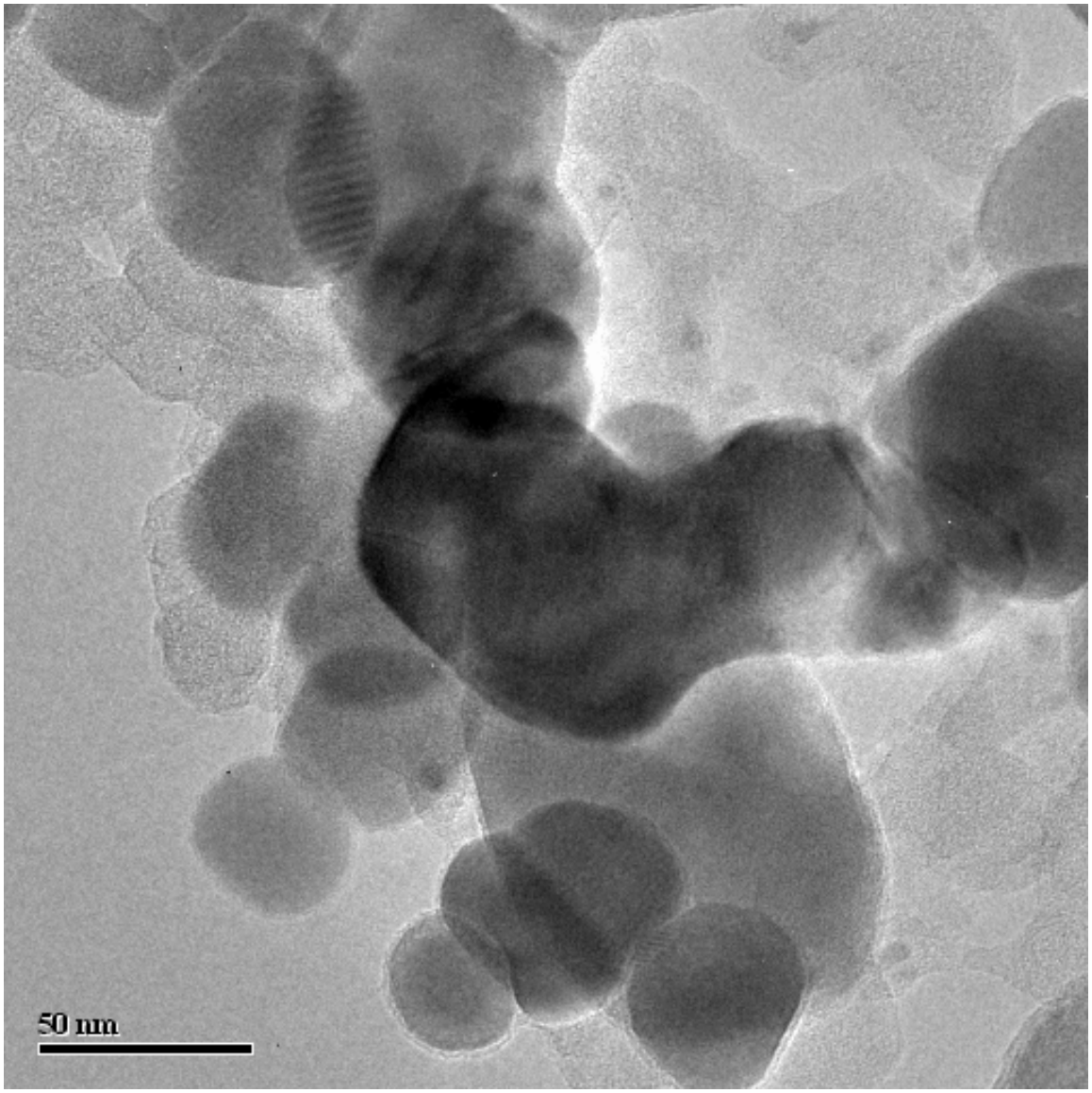

Figure 12. HRTEM images of catalyst particles collected after 24 h of FTS at 270 °C, 175 psig: ultrafine particles along with some larger sized particles are evident.

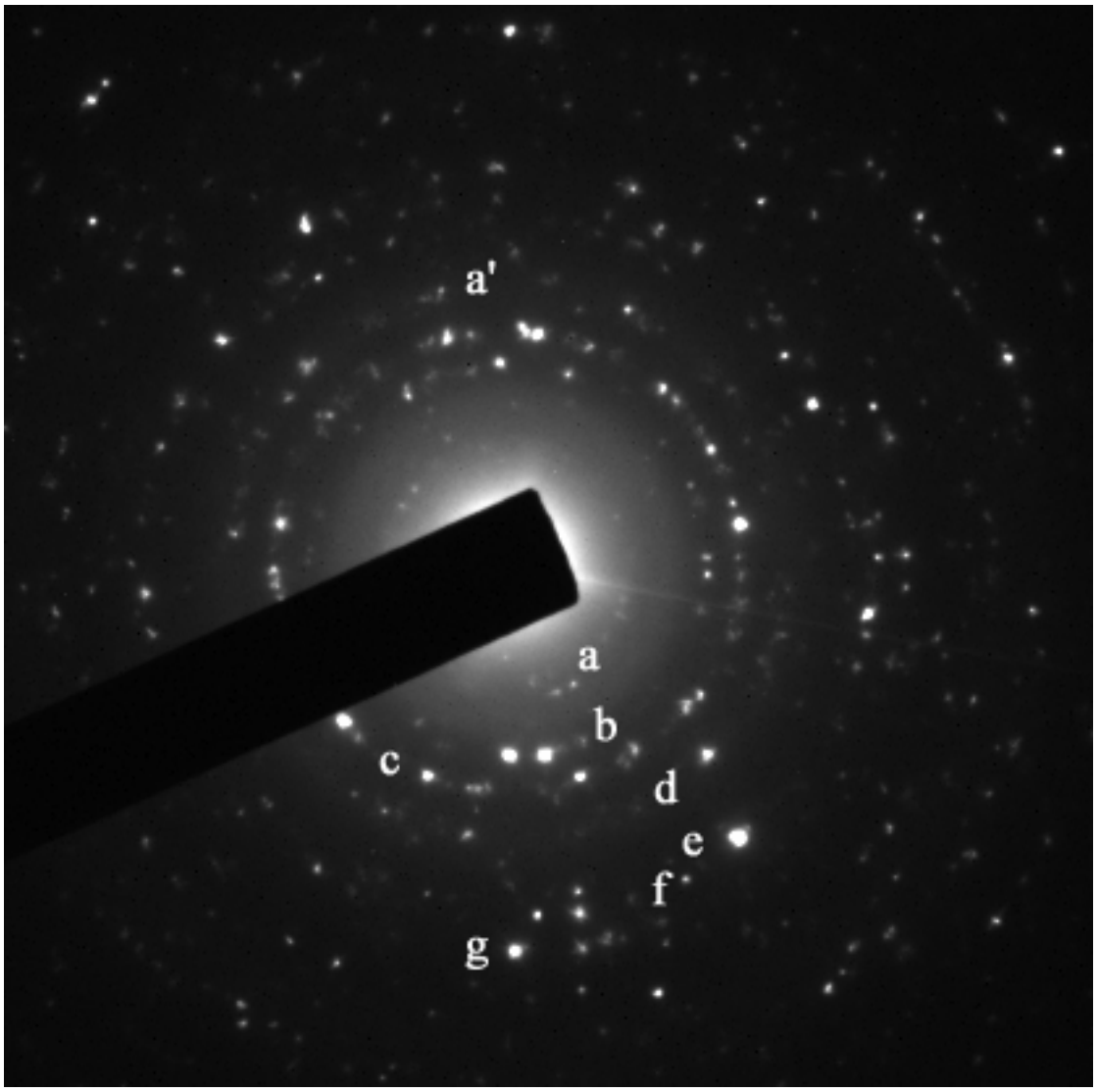

Figure 13. An electron microdiffraction pattern of catalyst sample collected after 96 h of FTS at 270 °C, 175 psig. Diffraction rings are indexed as: a' from (510) face of $\chi - Fe_5C_2$; a, b, c, d, e, f, and g from (111), (220), (311), (400), (422), (511) and (440) faces of Fe_3O_4, respectively.

Task 2.2. Nano-scale Growth of Particles in Slurry Phase Fischer-Tropsch Synthesis with Ultrafine Iron NANOCAT®: Morphology, Phase Transformation and Particle Size Distribution

2.2.1. ABSTRACT

An unpromoted ultrafine iron nanocatalyst was used for FTS in a CSTR at 270 °C, 175 psig, $H_2/CO = 0.7$, and a syngas space velocity of 3.0 sl/h/g Fe. Prior to FTS, the catalyst was activated in CO for 24 h which converted the initial hematite into a mixture of 85% $\chi - Fe_5C_2$ and rest magnetite as found by Mössbauer measurement. The activated catalyst results in an initial high conversion (ca. 85%) of CO and H_2; however the conversions decreased to ca. 10% over 400 h of synthesis time and after that remained nearly constant up to 600 h. Mössbauer and EELS measurement revealed that the catalyst deactivation was accompanied by structural evolution (by gradual in situ re-oxidation) of the catalyst from initial nearly pure $\chi - Fe_5C_2$ phase to pure magnetite after 400 h of synthesis time. Experimental data indicates that the nucleation for carbide/oxide transformation initiates at the center of the particle by water produced during FTS. Small amount of $\varepsilon' - Fe_{2.2}C$ phase was detected in some catalyst samples collected after 480 h of FTS which are believed to be generated by syngas during FTS. PSD measurements indicate nano-scale growths of individual catalyst particle. Statistical average diameters were found to increase by a factor of 4 over 600 h of FTS. Large particles with the largest dimension larger than 150 nm were also observed. Chemical compositions of the larger particles were always found to be pure single crystal magnetite as revealed by EELS analysis. Small number of ultrafine carbide particles was identified in the catalyst samples collected during later period of FTS. The results suggest that carbide/oxide

transformation and nano-scale growth of particles continues either in succession or at least simultaneously; but definitely not in the reverse order (in that case some larger carbide particles could be observed). EELS-STEM measurement reveals amorphous carbon rim of thickness 3-5 nm around some particles after activation and during FTS. Well ordered graphitic carbon layer on larger single crystal magnetite particles were found by EELS-STEM measurement. However the maximum thickness of the carbon (amorphous or graphitic) rim does not grow above 10 nm suggesting that the growths of particles are not due to carbon deposition.

2.2.2. INTRODUCTION

Conversion of syngas ($CO + H_2$) to liquid fuels and chemicals has enormous potential for utilization of the large world reserves of natural gas and coal [1]. Increasingly stringent environmental regulations for "clean-fuels" (low-sulfur, low-aromatics) and concerns about the depletion of fossil-fuel reserves make Fischer-Tropsch synthesis (FTS) as an environmental-friendly and economically-promising route for production of middle-distillate fuels, petroleum blending-stock, a wide variety of hydrocarbons and oxygenates from coal or natural-gas or biomass-derived syngas [2].

Iron-based catalysts are preferred for FTS utilizing synthesis gas derived from coal or biomass because of their excellent activity in water gas shift reaction which allow using a synthesis gas with a low H_2/CO ratio (typically 0.7) directly without an upstream shift-step. The use of iron-based catalysts is also attractive in view of their lower cost, lower methane selectivity, high olefin-selectivity, lower sensitivity towards poisons and flexible product slate. However, because of the non-selective nature of the FTS, a large amount of waxy material (heavy hydrocarbons) is produced when the catalyst and reactor operation

favors long chain growth. This wax can be refined and processed (via hydrocracking, oligomerization, alkylation, etc.) to produce premium quality fuels and chemical feed-stock. During the removal of wax, the catalyst particles, suspended in the liquid-phase of FTS reactor must be separated and recycled back to the reactor to maintain required conversion and to avoid catalyst loss. Catalyst/wax separation is also necessary from the standpoint of wax upgrading, since the catalyst fines may foul the equipments in subsequent wax processing and can degrade the final product quality. As a requirement of the downstream wax processing, the solid content of the slurry-phase FT wax should be limited to below 2-5 ppm [3].

The application of slurry bubble column reactor (SBCR) for liquid phase FTS is advantageous because of excellent control of highly exothermic reaction heat in large scale industrial operation. Nevertheless the use of iron catalysts in the most economical SBCR has been limited by their high rate of attrition to ultrafine particles leading to catalyst loss, high slurry viscosity and difficulty in wax/catalyst separation.

Phase-transformation of iron catalyst during activation/FTS plays an important role in determining the structural integrity or attrition resistance of the catalyst particles. Sequential phase-modification during the activation process (with CO or synthesis gas) from hematite to magnetite and finally to iron carbides have been reported [4-5]. Results of previous studies have shown that the formation of surface carbides is required before the catalyst can exhibit any activity [4-7]. The chemical conversion of iron oxides to iron carbide induce a volumetric change because of significant difference in the skeletal densities of carbide and oxide structures (e.g., 7.7 g cm^{-3} for Fe_3C as compared to 5.2 g cm^{-3} for Fe_3O_4). The volumetric change can cause stress in the particle which can lead

attrition and formation of small crystallites of iron carbides that split off rapidly to form ultrafine particles [6, 8-9]. Physical attrition can also result from collision between catalyst particles and the reactor internals. However, it has been shown that the conversion of iron oxides to iron carbide is dynamic and reversible depending upon the environment [4]. Under oxidizing conditions (e.g., at high water and CO_2 partial pressures), layers of surface Fe_3O_4 can form on an iron carbide kernel and ultimately pure Fe_3O_4 particles could be formed. It has also been reported that conversion of Fe_3C to Fe_3O_4 results in an increase in volume of 91%, and a similar increase for $\chi - Fe_5C_2$ [10]. Thus the reoxidation step also has the potential to provide severe stress in the individual particle and in the agglomerate to cause the formation of fine particles during FTS operation.

During activation and FTS, the gas composition in contact with the catalyst has the potential to exhibit either reducing or oxidizing properties. A variety of iron carbide/oxide phase may be evolved during the activation/synthesis process. Thus there exists a strong possibility that the catalyst particles may undergo either fragmentation or growth in size depending on the process condition. However, only Kuo et al. [11] have reported so far a tremendous increase in apparent particle size during the slurry-phase FTS which is contrary to what generally observed/reported in literature [6, 9, 12]. The particle size of most of the catalyst used for attrition studies available in the literature are in the micron range. It has been reported that spray dried and calcined iron-based catalyst ($Fe/Cu/K/SiO_2$) particles in the 30-50 micron range, disintegrated to 1-3 μm size ranges during 24 h stirring in CSTR under inert gas as well as under FTS conditions [13]. The observed extent of attrition with Fe catalysts is the result of both chemical attrition due to

phase transformation and carbon deposition. In view of the above result, it is important to examine the existence of any limiting size of the iron-based catalyst particles under typical FTS process condition. When carbidation/FTS is started with a bigger size particles, if the particle attrition and fragmentation results in the formation of particles in such a "limiting size range", then the same "limiting size range" should results in by growth of smaller particles when the initial particle size (i.e., before carburization/FTS) is in submicron range (e.g., nanoparticles). The use of submicron particles is particularly advantageous for efficient control and utilization of highly exothermic heat of reaction and enhanced mass transfer rate of gaseous reactants to the solid catalysts surface in a SBCR operation [14]. A detailed knowledge of the change of particle size of the submicron particles is therefore necessary for design and operation of SBCR and for any mechanical liquid/solid separation system.

The objective of the present study is to monitor the particle size distribution (PSD), morphological and chemical transformation of ultrafine iron nano-catalyst particles (with initial diameters of 3-5 nm) during the carbidation/FTS in a CSTR by HRTEM, HAADF-STEM, EELS and Mössbauer spectroscopy. The information on the change of PSD can be utilized for design and optimization of a continuous flow filtration unit for wax/catalyst separation.

2.2.3. EXPERIMENTAL

2.2.3.1. Materials

A commercial ultrafine iron oxide catalyst (NANOCAT® Superfine Iron Oxide, Mach I, Inc.) was used for all experiments. The reported average particle size of the catalyst = 3-5 nm, surface area = 250 m^2/g, and bulk density = 0.05 g/cm^3. Polywax 850

(polyethylene fraction with average molecular weight of 850) purchased from Baker Petrolite, Inc. was used as start-up solvent.

2.2.3.2. Methods

The FTS experiments were conducted in a 1 L CSTR equipped with a magnetically driven stirrer with turbine impeller, a gas-inlet line, and a vapor outlet line with a SS fritted filter (2 micron) placed external to the reactor. A tube fitted with a SS fritted filter (0.5 micron opening) extends below the liquid level of the reactor for withdrawing reactor wax (rewax, solid at room temperature) maintains a constant liquid level in the reactor. Another SS dip-tube (1/8" OD) extends to the bottom of the reactor was used to withdraw catalyst/wax slurry from the reactor at different synthesis times. Separate mass flow controllers were used to control the flow of hydrogen and carbon monoxide at the desired rate. The gases were premixed in a mixing vessel before entering to the reactor. Carbon monoxide was passed through a vessel containing lead oxide-alumina to remove any traces of iron carbonyl. The mixed gases entered the CSTR below the stirrer operated at 750 rpm. The reactor temperature was maintained constant ($\pm$ 1 °C) by a temperature controller. A schematic of the reactor set-up is presented in Figure 2.2-1a.

The as-received ultrafine iron oxide catalyst (54.7 g) was added to melted (150 °C) Polywax 850 (310 g) in the CSTR to produce a slurry that contained about 15 wt% iron oxide. The reactor temperature was then raised to 270 °C at a rate of 1 °C/min. The catalyst was activated using CO at a space velocity of 3.0 sl/h/g Fe at 270 °C and 175 psig for 24 h. At the end of activation period, a sample of activated catalyst (Sample S1) was withdrawn via the slurry withdrawal dip-tube of the CSTR. The FTS was then started by adding synthesis gas mixture to the reactor at a space velocity of 3.0 sl/h/g Fe and a

H_2/CO ratio of 0.7. The conversions of CO and H_2 were obtained by gas-chromatography analysis (micro-GC equipped with thermal conductivity detectors) of the product gas mixture. The reaction products were collected in three traps maintained at different temperatures – a hot trap (200 °C), a warm trap (100 °C) and a cold trap (0 °C). The products were separated into different fractions (rewax, wax, oil and aqueous) for quantification. However, the oil and the wax (liquid at room temperature) fractions were mixed prior to GC analysis.

Catalyst/rewax slurry was withdrawn at different reaction times via the dip-tube after sufficient purging. The withdrawal schedule is presented in Table 2.2-1. In a typical catalyst slurry sampling procedure, about 7-8 g of catalyst slurry was purged and then 2-3 g of catalyst slurry was collected as representative sample from the reactor each time. To minimize any possible change in the particle morphology, Soxhlet extraction procedure to remove the wax-products was avoided. The withdrawn samples were diluted with hot (about 70 °C) ortho-xylene to remove the high molecular weight FT-wax fractions. It was found that it is not possible to completely remove the FT-wax from the catalyst particles by this method. However, the leftover wax acts as a protective cover for the air-sensitive catalyst particles. Solution of relatively clean catalyst particles in ortho-xylene were prepared for use in high resolution transmission electron microscopy (HRTEM) measurements. An optimum ratio of ortho-xylene to catalyst slurry was used so that the catalyst particles form a slightly turbid suspension. A drop of the suspension was placed with a syringe onto a lacey carbon film on 200 mesh copper grid. After the ortho-xylene evaporated, the grid was loaded into the microscope for analysis.

The morphology and in-depth analysis of individual particles were analyzed by using an field emission analytical transmission electron microscope (JEOL JEM-2010F) operated at an accelerating voltage of 200 kV and equipped with a scanning transmission electron microscope (STEM) unit with high-angle annular dark field (HAADF) detector, and a Gatan imaging filter (GIF)/PEELS system. HRTEM images were recorded under optimal focus condition at a typical magnification of 100K-500K. The electron beam had a point-to-point resolution of 0.5 nm. EELS spectra were recorded in TEM imaging mode with an energy resolution from 1 eV (full width at half maximum of zero loss peak) and dispersion rate 0.2 eV/channel. Gatan Digital Micrograph® software was used for image and EELS data recording and processing.

Mössbauer spectra were collected in a transmission mode by a standard constant acceleration spectrometer (MS-1200, Ranger Scientific). A radiation source of 30 mCi ^{57}Co in Rh matrix was used and spectra were obtained using a gas detector. The catalyst samples collected from the CSTR were in the rewax/PW 850 matrix and were in solid phase at room temperature. This solid matrix was mounted in plexiglass compression holders that present a thin aspect to the γ – ray beam. All samples were investigated at room temperature as well as at cryogenic temperatures, typically over a velocity range of $\pm$ 10 mm/s. For the low temperature measurements, the samples were placed inside a vibration free closed cycle cryostat (Cryo-Industries of America). The structural analysis of the samples was done by least-squares fitting of the Mössbauer spectra to a summation of hyperfine sextets. The least-square fitting procedure was done using user defined functions within the PeakFit program. The parameters for each sextet in the fit consisted of the position, width and height of the first peak, the hyperfine magnetic field, and the

quadrupole electric field. These parameters were allowed to vary freely to obtain the best fit of the experimental data. Errors in the determined percent Fe values are about ± 3% for well-resolved spectra; in those that contain several iron oxide and carbide phase the uncertainty increases with the complexity of the spectrum (i.e., depending on the degree of overlapping and the weakness of the signal). However, these complex spectra are obtained during the course of change from a predominantly iron carbide or iron oxide phase and conform to a greater trend.

2.2.4. RESULTS

2.2.4.1. Catalytic activity and stability

The initial activity of the ultrafine iron catalyst was found to be high. When FTS was started with the carbided catalyst, the observed conversion level for CO and H_2 was about 85% and 80%, respectively. Since the ultrafine catalyst did not contain any structural promoter, the catalytic activity showed a slow and gradual decrease during a total time-on-stream (TOS) of about 600 h. The TOS in this case has been counted from the starting of FTS using synthesis gas. The variation of conversion levels of syngas, hydrogen and CO, as calculated from gas analysis, against synthesis time is shown in Figure 2.2-1b. A total of eight catalyst slurry samples were collected during the whole experiment - one sample after carburization and seven samples during FTS. It should be noted that apart from catalyst deactivation during FTS, the withdrawal of the catalyst particles during the experiment also contributed the decrease in conversion. The ultrafine Fe catalyst used in the present study did not contain any structural promoter, so the rate of deactivation is expected to be quite high. The combination of above two factors results in CO and H_2 conversion levels of 9.8% and 20.8%, respectively, after 597 h of FTS.

2.2.4.2. Phase composition by Mössbauer spectroscopy

Mössbauer spectroscopy was used to follow the dynamic phase transformation between iron oxide and iron carbide during carbidation and FTS. Representative Mössbauer spectra for sample S1, S2, S5 and S8 are shown in Figure 2.2-2a – 2.2-2d, respectively. All of the Mössbauer spectra in the present study represented a complex pattern comprising magnetite, carbide and paramagnetic components. The extent of the resulting magnetic hyperfine splitting, smaller than observed for $\alpha - Fe$, was in the range typical of the iron carbides [15]. The shape of the individual magnetic component indicated the presence of three distinct sextets. It is known that Mössbauer spectra of octahedral carbides (ε, χ, χ' and χ'' iron carbides with carbon atom in octahedral interstices) contain three distinct sextets; while Mössbauer patterns of trigonal prismatic (TP) carbides (ε' and θ iron carbides with carbon atom in TP interstices) appear as single sextet [16]. Reliable identification of different carbide phase is based on the number of constituent sextets, corresponding hyperfine magnetic fields, and their relative intensities. Compositional changes in terms of percent peak area of the different iron species as determined from curve fitting for all the samples along with corresponding sampling times are listed in Table 2.2-2 for two different temperatures.

During the carbidation with CO, the catalyst was first transformed from hematite (Fe_2O_3) to magnetite (Fe_3O_4) and then reduced to iron carbide. The conversion of hematite to magnetite is generally very rapid and difficult to monitor unless special attention is paid [17]. At the end of 24 h activation period (sample S-1, Table 2.2-2), the room temperature Mössbauer results revealed that about 85% of iron phase in the catalyst was present as Hägg carbide ($\chi - Fe_5C_2$), with the remaining iron phase was present in

superparamagnetic (spm) form. Low-temperature (20 K) Mössbauer measurement of the same sample (i.e, sample S1) indicated that the spm phase was Fe_3O_4, and not the iron carbide, which can also be present in a spm phase. Combining the above results it is found that at the end of the 24 hours activation with CO at 270 °C, the initial hematite converted to a mixture of 85% $\chi - Fe_5C_2$ and 15% Fe_3O_4 which is in complete agreement to the results reported earlier [18]. A synthesis gas conversion of 85% was observed with this catalyst. Oxidation of iron carbide initially present after activation continues with the synthesis times and the amount of carbide phase gradually decreases with a corresponding increase of fraction of Fe_3O_4 phase during FTS. Since the catalyst used in the present study was pure iron oxide without any promoter; the rate of re-oxidation of the carbides was found to be significantly large. 50% of iron in the sample S2 (collected after 28.9 h of FTS) was found to be present as carbides while rest was in oxide phase. At the end of 311 h of synthesis time, the fraction of iron present as Fe_3O_4 was found to be 96% (sample # S5) with remaining iron in spm phase and the synthesis gas conversion dropped dramatically to a level of about 16% only. Low temperature Mössbauer results indicated that after 382.8 h of FTS, the phase composition of the catalyst (sample # S6) was 99% Fe_3O_4 and 1% spm phase which can be surface carbide species. Activation of iron-based catalysts for FTS is generally practiced with CO or syngas [10]. The iron oxide produced via in situ re-oxidation of carbide phase remains in contact with the syngas during FTS and fraction of the oxides can potentially be transformed to carbides (i.e., in situ regeneration). Since the present catalyst did not contain any structural promoter, the rate of in situ regeneration can be very small. Mössbauer spectra of sample S7 (collected after 481.6 h of synthesis) revealed that a

small fraction of iron (about 5%) was present as hexagonal ε'−$Fe_{2.2}C$ phase. Activation of iron based catalyst with syngas is known to predominantly result in ε'−$Fe_{2.2}C$ [10, 19]. Hence, it is believed that the ε'−$Fe_{2.2}C$ phase observed in the present study was generated in situ by carbidation with syngas. No trace of $\chi - Fe_5C_2$ phase was identified in any of the catalyst samples among S5-S8 by Mössbauer analysis. Major fraction of iron (about 90-95%) was found to be present as Fe_3O_4 in catalyst samples S5-S8 (Table 2.2-2) and the magnitude of CO conversion remained almost constant around 10% during the 200 h of FTS period when these samples were collected. Thus the presence of some fraction of iron carbide is necessary for a catalyst to exhibit high conversion.

2.2.4.3. Phase transformation and morphology by HRTEM, STEM and EELS

The morphology, chemical nature and phase transformation of the nanocatalyst during CO activation and FTS is studied by HRTEM, STEM and EELS. The initial Mach I catalyst had a narrow size distribution (3-5 nm) with a regular near-spherical morphology as shown in Figure 2.2-3. The vendor indenfied the as-received sample as $\gamma - Fe_2O_3$ based on electron diffraction pattern. $\gamma - Fe_2O_3$ has a simple cubic structure; hence, reflections from all the planes are possible. An electron microdiffraction pattern of the as-received material is shown in Figure 2.2-3 (inset) which exhibits diffuse rings. The distance from the center to the rings or diffraction spots is indicative of the lattice spacing of the particular crystallographic plane. Diffraction rings can appear for polycrystalline materials but those would be sharp and distinct with the continuous array of reciprocal-lattice points which are concentric spheres in reciprocal space indicating random orientation. However, for amorphous materials where a lack of well-ordered crystal

structure is evident, or materials containing nano-sized particles, these rings will be diffused. The diffuseness and variations in intensity profiles result from inelastic scattering phenomena.

The TEM image of the catalyst sample collected after CO activation for 24 h (sample S1) is shown in Figure 2.2-4. The initial size of the nanocatalyst was in the range of 3-5 nm. Figure 2.2-4 reveals an increase in the particle size during carbidation. Formation of crystalline structure is evident from this figure. Some of the particles were found to have an outer rim of 3-5 nm thickness. An electron microdiffraction pattern of the sample is also shown in Figure 2.2-4 (inset). The diffraction pattern confirmed the presence of loose aggregates of iron carbides [20]. The magnetite particles yield well defined spots in the diffraction pattern while the presence of carbide phase causes only diffuse rings originated from the presence of small particles. A high-resolution TEM image of this sample shown in Figure 2.2-5 indicates well defined crystalline structure with an outer rim of amorphous material having thickness 3-5 nm. The chemical nature of this amorphous rim is critical for purpose of both catalyst characterization and activity. High-resolution STEM and EELS measurements were used to identify the chemical composition of this rim. The amorphous outer rim is clearly evident from the high-resolution STEM images shown in Figure 2.2-6a (inset) and Figure 2.2-6b (inset). The red dots in these figures indicate the position where the EELS spectra were recorded (i.e., the electron beam was focused). The EELS spectra taken at the center of the particle indicates the characteristics edge structure of Fe ($L_{2,3}$ edge structure at about 720-740 eV), oxygen (K edge structure at about 530-535 eV) and carbon (K edge structure at about 285-310 eV) as presented in Figure 2.2-6a. A magnified view of carbon K-edge

structure in EELS spectra is also shown in Figure 2.2-6a inset. Higher intensity of Fe and C edge spectrum over oxygen edge suggest that the particle is mainly composed of mainly carbides and little oxide. The EELS spectra recorded at the center of outer rim as shown in Figure 2.2-6b consists of only carbon K edge structure. Probing by EELS is a very sensitive technique and very low concentration can be detected. The carbon K-edge structure clearly shows a weak π^* shoulder peak and an intense σ^* peak, which are characteristic of amorphous carbon species. Since the EELS spectra of the rim do not contain any characteristic edge for Fe or oxygen, it can be concluded that the outer rim consists of amorphous carbon only. A HRTEM image of another particle of sample S1 is represented in Figure 2.2-7a which shows the particle are nano-aggregates with atomic planes indicating crystalline structure. These structures originate from nanocrystalline grains within and on the nanoparticle surface. The carbide particles are made of aggregates of nanocrystals. Carbide particles formed in layers overlapping with each other as found by HRTEM (Figure 2.2-7a). The characteristic d-spacing of these crystallites is 2.0 Å (which can correspond to high intensity (510) or (021) plane of $\chi - Fe_5C_2$). The non-smooth particles have a crumpled and boulder-like appearance and formed with different overlapping layers of iron carbides. However, HRTEM image of another portion of the same particle shown in Figure 2.2-7b reveals two different types of crystal d-spacing - 2.0 Å and 2.6 Å. The crystallite with characteristic d-spacing of 2.0 Å may represent iron carbide as above while the one with a d-spacing of 2.6 Å can be assigned to high intensity (311) plane of magnetite. Coexistence of magnetite and iron carbides in the same particle indicate that oxide to carbide transformation during carbidation was not complete and the activated catalyst contains some amount of oxide

which is in complete agreement with results obtained from Mössbauer analysis as shown earlier.

A high-resolution TEM image of a particle from sample S2 (collected after 28.9 h of FTS) is presented in Figure 2.2-8. The image shows that the particle has an outer rim of thickness about 5 nm. The spreading of the material forming the rim around the particle and the adjacent particle suggest that it is not the amorphous carbon rim as described above. This rim may originate from leftover wax produced during FTS and remained during o-xylene extraction step. In this case this rim will act as a protective layer and prevent any aerial oxidation during catalyst characterization. The distribution of the crystalline zone in this particle reveals two concentric nano-regions with two distinct crystal axis spacing - the inner crystalline core has a characteristic d-spacing of 2.6 Å (can corresponds be high intensity (311) plane of Fe_3O_4, and the outer crystalline region consist of a characteristic d-spacing of 2.0 which can be assigned to high intensity (510) or (021) plane of $\chi - Fe_5C_2$. The zone boundary of these two nano-regions (as indicated by a white circle in Figure 2.2-8) reveals a sharp change in the magnitude of characteristic d-spacing values indicated above. The iron oxide encapsulated by iron carbide concentric layers significantly indicates a definite pattern in the in situ reoxidation phenomena during FTS and will be discussed in details in the "Discussion" section.

TEM image of sample S4 (collected after 167.7 h of synthesis) as shown in Figure 2.2-9a indicates bigger particles with irregular hexagonal shape structures. Appearances of several small "nodule/bud" which are sprouted on the top of the bigger particles are also evident. HRTEM image of a bigger catalyst particle from this sample is presented in

Figure 2.2-9b which reveals well defined single crystal of iron oxide (with a characteristic d-spacing of 2.6 Å corresponding to high intensity (311) plane of Fe_3O_4). No amorphous carbon rim outside this particle is observed. The initial wrinkled and boulder-like loose aggregates of multicrystalline iron carbides and oxides (as shown in Figure 2.2-8) transformed into large single crystal of iron oxide.

A representative TEM image of sample S5 (collected after 311 h of FTS) is shown in Figure 2.2-10a. Some of the particle from this figure has the largest dimensions that are larger than 100 nm. The FTS was started with a catalyst having a size range of 3-5 nm. Thus, appearance of such big particles clearly reveals that these are formed in situ during FTS. A high-resolution image of a particle from sample S5 is also shown in Figure 2.2-10b. This image clearly reveals that encapsulation of single crystal iron oxide (with a characteristic d-spacing of 2.6 Å corresponding be high intensity (311) plane of Fe_3O_4) core by an external well-ordered graphitic carbon layer of thickness about 5 nm.

The TEM images of sample S6 (collected after 596.8 h of FTS) is shown in Figure 2.2-11a. Presence of large single crystal with largest dimension that is larger than 150 nm can be noticed. Appearances of outer carbon rim structure in some of the particles are also evident. High-resolution TEM image of a particle from sample S6 as presented in Figure 2.2-11b clearly shows that single crystal of iron oxide is covered by a layer of ordered graphitic carbon of thickness about 10 nm. The thickness of the carbon rim around the particle does not grow above about 10 nm. Hence, the appearance of the bigger particles does not originate from the deposition of carbon on the catalyst particles.

Appearance of small “buds” sprouted on large particles in TEM image of some samples has been observed. HRSTEM-EELS measurement was used to identify the

chemical nature of these big particles and small buds. Figure 2.2-12a represents the EELS spectra of a large particle carrying a "small bud" on the surface (sample after 311 h of FTS). A high resolution STEM image of this particle is also shown in Figure 2.2-12a (inset) where the red dot indicates the point of focus for recording EELS spectrum. Presence of characteristics EELS edge structure of Fe ($L_{2,3}$ edge structure at about 720-740 eV) and oxygen (K edge structure at about 530-535 eV) and absence of carbon edge structure suggests that the particle is composed of iron oxide. The characteristic shape of Fe $L_{2,3}$ edge in the EELS spectrum reveals the presence of magnetite [21]. However, similar HRSTEM-EELS analysis of the nodule sprouted on the big particle as shown in Figure 2.2-12b indicate the presence of only Fe and carbon edge structure in the EELS spectrum. The point of electron beam focus is shown in Figure 2.2-12b (inset) by a red dot. This data clearly reveal that the small buds are composed of iron carbides only. It was reported that while using particles of 100-300 μm in size, the carbide phase forms as small nodules on the surface of the magnetite and the phase transformation proceeds slowly into the bulk [4, 7]. However, such phenomena were not observed in the present study. It was not possible to determine the physical nature of attachment of these small buds with the big particles in the present study. Presence of very few small buds on the surface of big particles suggests that the small nodules are only physically supported on the big particle without any chemical or other type of binding.

2.2.4.4. Particle size distribution: nano-scale growth

The size of a spherical (equi-dimensional) homogeneous particle can uniquely be specified by its diameter while any regular compact particles (e.g., cube, tetrahedron), a

single dimension can be used to define size. A single irregular particle has an infinite number of linear dimensions and it is only when selected dimensions are averaged that a meaningful value results. To specify “true representative size” of any irregular shaped particle, some approximations are required. Particles that are non-equidimensional are often characterized by specifying the second largest dimension also. Particle sizing by microscopy involves in observation and measurement of individual particles with each measurement quantifying the particle size in only one direction. If the particles are in random orientation, and if sufficient particles are counted, then the results of these measurements reflects the size distribution of the projected areas of the particles (assuming stable orientation) perpendicular to the viewing direction (i.e., plane of paper). Since, the particle sizes in the present study are measured from the HRTEM images, a statistical diameter, the Feret diameter, defined as the distance between pairs of parallel tangents to the projected outline of the particles on the plane of paper [22], is used to specify the particle size. Since the particles were non-equidimensional, the arithmetic average of the largest Feret diameter in x- and y-axis was considered as the “representative particle diameter” of an individual particle. For each catalyst sample mentioned in Table 2.2-1, a large number of particles (about 1200-1500 particles per sample) were counted and there individual Feret diameter was determined. Having defined the relevant particle size, the relative frequency $\left(n_i / \sum n_i\right)$ of there occurrence in each representative size range was calculated and continuous, normalized relative frequency distributions (particle size distribution, PSD) are generated for each sample assuming following relations:

$$\sum_{i=1}^{n} f(x_i) = 1; \quad \text{and} \quad F(x) = \sum_{j \le x} f(j)$$

Once the PSD is determined, several average statistical parameters considered to quantify any change in average particle size of catalyst particles during FTS. Since the PSD in the present study is of interest to the active surface area of the catalyst particles, these parameter include (a) mode (the most commonly occurring particle size) of the distribution; (b) median (the 50% size on the cumulative PSD curve) of the distribution; (c) number mean diameter ($\bar{x}$ or $d_{1,0}$), the center of gravity of the number distribution; (d) surface area moment mean diameter ($d_{3,2}$) or Sauter mean diameter (SMD) – the average diameter based on unit surface area of a particle; and (e) volume moment mean diameter ($d_{4,3}$) – the average diameter based on the unit volume of a particle. For the number mean diameter ($\bar{x}$) of the distribution, the moment of the sums of the elementary areas of the relative frequency distribution of width ∂x, about the ordinate, equals the sum of the moments of the elements about the ordinate [22]:

$$\sum_{0}^{\bar{x}} (x - \bar{x}) \frac{d\phi}{dx} \partial x = \sum_{0}^{\bar{x}} (\bar{x} - x) \frac{d\phi}{dx} \partial x \Rightarrow \bar{x} \sum_{0}^{\bar{x}} d\phi = \sum_{0}^{\bar{x}} x d\phi \Rightarrow \bar{x} = \frac{\sum x d\phi}{\sum d\phi} = \frac{\sum x dN}{\sum dN}$$

where ϕ is the cumulative number frequency, x is the particle size in nm and for a number distribution $d\phi = dN$. The SMD and volume moment mean diameter were calculated according to the following equations [22]:

$$d_{3,2} = \frac{\sum d_i^3 N_i}{\sum d_i^2 N_i}; \qquad d_{4,3} = \frac{\sum d_i^4 N_i}{\sum d_i^3 N_i}$$

where d_i is the particle diameter, and N_i is the number of particles of size d_i.

The PSD in terms of relative number frequency of different catalyst samples are

shown in Figure 2.2-13a – 2.2-13f and the results of PSD analysis are presented in Table 2.2-3. The PSD of all the six samples in terms of cumulative number frequency is also presented in Figure 2.2-14. The results reveal significant increase in the representative diameters ($d_{1,0}$, $d_{3,2}$ and $d_{4,3}$) and other statistical parameters of the PSD for catalyst sample with synthesis time. The percent increases in the three statistical diameters are also presented in Table 2.2-3 which clearly indicates continuous nano-scale growth of particles during FTS. Cumulative number frequency distribution shown in Figure 2.2-14 reveals that for a certain cumulative fraction, the corresponding representative size of the catalyst particles increase with synthesis time. Appearance of larger particles in the HRTEM images also suggests nano-scale growth of particles during FTS. The frequency distribution plots shown in Figure 2.2-13a - 2.2-13c indicate unimodal distribution of particle size with the width of distribution increasing with the synthesis time. The PDS plots for these samples reveal predominantly growth of particles. However, the PSD plot presented in Figure 2.2-13d and 2.2-13e clearly indicate bimodal distribution of particle size. This bimodal distribution arises from growth of smaller particles and simultaneous nano-scale attrition or breakage of bigger particles already present in the system. This growth and breakage phenomena occur simultaneously and the frequency distribution reaches a quasi-equilibrium stage. At this point the distribution becomes unimodal and the width of the PSD reaches maximum as shown in Figure 2.2-13f.

2.2.5. DISCUSSION

Phase transformation during activation and evolution of active phase under FTS determine the performance of the catalyst. It is known that during the activation (using either CO, H_2 or syngas) process, iron oxide (hematite, $\alpha - Fe_2O_3$) transforms quickly to

magnetite (Fe_3O_4) which converts to different iron phases depending on activation environment. Activation using H_2 results in metallic iron (Fe^0) which evolves slowly into mixture of iron carbides and oxides on exposure to syngas during FTS [23]. When CO or syngas is used for activation, based on initial composition of the catalyst, different types of iron carbides have been identified [5, 10, 24].

Rao et al. [18] has reported that 24 h CO activation of a promoted iron catalyst (Fe/Cu/K/Kaolin) results in only $\chi - Fe_5C_2$. When the same catalyst was activated with syngas, both $\chi - Fe_5C_2$ and $\varepsilon' - Fe_{2.2}C$ was identified. No $\varepsilon' - Fe_{2.2}C$ was detected in samples collected during carbidation using CO [19]. However, activation of iron based catalyst with syngas predominantly results in $\varepsilon' - Fe_{2.2}C$ [10, 19]. In general, CO activation was found to lead to a higher fraction of carbide phase and to high catalytic activity than similar syngas or H_2 activation. The fraction of iron present as the carbide following the activation was found to be dependent on catalyst composition. Rao et al. [19] studied the activation of a promoted iron-based catalyst using syngas at 280 °C and 150 psig. Mössbauer characterization of the catalyst sample collected after 12.5 h of carbidation indicated a phase composition of 23% $\varepsilon' - Fe_{2.2}C$, 12% $\chi - Fe_5C_2$ and 17% spm phase. Zarochak and McDonald [25] studied the effect of pretreatment on the activity and the selectivity of slurry phase FTS with a potassium promoted precipitated iron catalyst and characterized the catalyst by Mössbauer spectroscopy. Prior to FTS the catalyst was activated for 24 h using CO and syngas. It was found that the catalyst activated in CO was completely converted in $\chi - Fe_5C_2$ while the catalyst activated in syngas was converted partly to $\varepsilon' - Fe_{2.2}C$ during 24 h activation, and was completely

converted to ε'−$Fe_{2.2}C$ only after 503 h of FTS. The FTS activity and stability of the catalyst subjected to CO pretreatment was found to be higher than that found for the catalyst activated in syngas.

Analysis of simultaneous reaction kinetic, Mössbauer and X-ray diffraction measurements have indicated a linear relation between the amount of bulk carbide content of the catalyst and FTS rate [15, 26]. Phase composition of unpromoted precipitated Fe catalysts were studied during various periods of FTS by Li et al [27] using Mössbauer spectroscopy, XANES and EXAFS techniques. Activation in CO was found to transform the initial oxide into $\chi - Fe_5C_2$ while Fe_3O_4 was the only detectable iron phase after 450 h of FTS. Bulk Mössbauer and X-ray absorption spectroscopy results revealed a consistent decrease in carbide concentration with FTS time while the CO conversion decreased by a factor of 10 during the structural evolution of almost purely iron carbide (after CO activation) to pure Fe_3O_4 (after 450 h of FTS). Based on the above results it was concluded that re-oxidation of carbides and catalyst deactivation are concurrent process caused by changes of chemical potential of absorbed species at the carbide surface, which render higher concentration of oxidizing species on surface than in the adjacent gas phase. These conditions, in turn, lead to the oxidation of carbides even in the reducing environments (i.e., presence of syngas). H_2O and CO_2 produced in FTS is generally considered as an oxidizing agent for the iron carbides [23].

The results obtained from Mössbauer analysis are consistent with the above mentioned results. $\chi - Fe_5C_2$ was the only carbide phase detected in the present study after carbidation of unpromoted iron catalyst using CO for 24 h. The carbides can be oxidized during FTS via two processes: (a) the reaction of in situ generated water vapor

with carbides to produce in one case magnetite and elemental carbon and in the other magnetite and methane; and (b) the reaction of hydrogen with carbidic or elemental carbon to form methane. Re-carbidation of produced magnetite at the surface in contact with syngas (i.e., under reducing environment) can regenerate some carbide phase during FTS. This situation will be somewhat similar to activation of catalyst using syngas except that a parallel oxidation reaction will compete with the re-carbidation. Small fraction of (about 5%) hexagonal $\varepsilon'-Fe_{2.2}C$ phase was identified in some sample collected after 480 h of FTS. This carbide phase is believed to be generated in situ via re-carbidation of magnetite by syngas. The magnitude of regeneration of the carbide phase depends on amount and type of promoters present in the catalyst. Since the catalyst used in the present study did not contain any promoter, the extent of re-carbidation was found to be small. The catalytic activity at this point was found to be lower by a factor of almost 10 as compared to fresh (CO activated) catalyst.

Mössbauer analysis is informative about the changes in bulk phase composition of iron catalysts which may not directly track the catalytic activity always. Presence of small amount of surface carbide which can not be detected properly by Mössbauer spectroscopy measurement can even results in low conversion level. Li et al. [28] claimed that even carbidation of only a near-surface region in bulk Fe_3O_4 is sufficient to achieve steady-state FTS turnover rates. The above conclusion was drawn based on methane formation rate up to 15 h of synthesis time which may not necessarily represent steady-state result. However, methane is not a representative Fischer–Tropsch product because it is not formed from the polymerization of the monomeric $-CH_2-$ units. Nevertheless, it should be emphasized that true steady-state activity (and selectivity) of iron catalyst is

not reached in minutes or hours but rather over periods of several hundred hours [29]. Results from present study indicate that it is necessary for some carbide to be present to have a catalyst with a high activity; however, it was evident that the activity of the catalyst cannot be predicted solely from the fraction of iron that is present as the carbide.

Integral FTS rates decreased by almost a factor of 10 leading to a decrease in CO conversion from 85% to 9.8% after 597 h on-stream (Figure 2.2-1). It is evident from the results that the change in chemical composition of catalyst (i. e., iron carbide to magnetite) has the major role for such a significant decrease in activity. Definitely the high conversions in the early stages of the reaction lead to much higher H_2O/H_2 and CO_2/CO ratios than those present at the low conversions prevalent at later reaction times. Hence the oxidizing potentials of the reactant–product mixtures in the gas phase and in the liquid phases in equilibrium with this gas phase are significantly higher during the early stages of the experiment. Although CO_2 can lead to the oxidation of iron carbides, Li et al [27] reported that during FTS using unpromoted, precipitated iron catalyst, the presence of added $CO_2\left(CO_2/CO=0.3\right)$ in the feed gas did not influence CO conversion rates (or apparently alter the structure of the catalytic phases). Hence, CO_2 can be regarded as essentially inert at reaction conditions used for the present study. Li et al. [27] has also discussed about possible transformation pathway of re-oxidation of iron carbides during FTS. They eliminated the possibility of nucleation of re-oxidation at surface (surface oxidation) and claimed that re-oxidation and deactivation is caused by changes of chemical potential of absorbed species at the carbide surface which render higher concentration of oxidizing species on surface than in contacting gas phase, thus, prevents re-carbidation at FTS environment.

The surface and bulk composition of a catalyst during steady-state FTS is determined by a balance among several simultaneous processe which include the amount of CO that is converted to products in the Fischer–Tropsch and the water-gas shift reactions, and the amount of CO that is dissociated on the catalyst surface in a form that maintains the carbide phase. Any imbalance between these rates would lead to the net introduction or removal of carbon or oxygen atoms into the inorganic structure, and to the dynamic interconversion of iron oxides and iron carbides. It has been reported [28] that magnetite crystallite become almost immediately active after exposure to syngas and incipient conversion of near surface oxide layers to iron carbides can result low magnitude of methane production rate.

We were able to successfully identify some catalyst particle at initial synthesis period which has a tiny iron oxide core and an outer iron carbide layer (Figure 2.2-8). However, after 250 h of synthesis time, only single crystal large magnetite particles were observed. Appearances of very small iron carbide particles were also noticed. Since ultrafinne catalyst particles were used in the present study, it is likely that the reaction occurred at the whole volume of the particles. The water produced in the outer rim of the particle can be escaped easily while the water produced at the center of the particle needs to be diffuse out slowly. Also the outer surface of the particle is in contact of syngas (i.e., under reducing environment), which can potentially replenish the carbide surface (re-carbidation). On the contrary the center of the particles is at oxidizing environment (high concentration of water and CO_2 and low concentration of CO and H_2). Considering the above facts it is believed that the nucleation of re-oxidation starts at the center of the catalyst particle. Since the catalyst is unpromoted, the rate of re-carbidation is much

slower than the rate of re-oxidation. The magnetite patches grows and become larger single crystal. Some surface carbide species can be generated when these bigger magnetite particles comes in contact with syngas which in turn can results in lower magnitude of conversion (ca. 10% as observed experimentally for a long period of synthesis time. This dynamic transformation of oxide to carbide and vice versa has result a "steady" low conversion although the bulk composition of catalyst remains primarily magnetite.

Appearance of amorphous and graphitic carbonaceous compounds on the surface of supported/unsupported and/or promoted/unpromoted iron catalysts have been reported by several researchers [7, 15, 29-32]. Dwyer and Hardenbergh [32] reported the formation of graphite-like carbonaceous compound on Fe foil used for FTS reaction by in situ XPS and observed that the deactivation of Fe foil accompanies with the increase of C 1s peak intensity for the graphite-like carbonaceous compound. However, Shroff et al. [7] reported the formation of amorphous carbon layers on iron carbide particles after the FTS reaction with precipitated iron based catalyst while Jin et al. [33] from the same research group observed the appearance of large amount of the graphitic carbon layer on catalyst pretreated by CO at higher temperature (773 K). Bartholomew and co-researchers [29, 31] have identified and quantified up to six different carbonaceous species onto the surface of iron-based catalysts after FTS reaction. The reactivity of these species was assigned from the temperature value of the methane formation peak in the temperature-programmed surface reaction with hydrogen (TPSR-H_2); that is, the more reactive the species, the lower the methane formation temperature. They suggested a series of transformation of C_α (atomic carbonaceous species, and lightly polymerized surface

carbon species formed by CO dissociation on catalyst surface) to $\varepsilon'-Fe_{2.2}C$ to $\chi-Fe_{2.5}C$. It was also proposed that the $\varepsilon'-Fe_{2.2}C$ to $\chi-Fe_{2.5}C$ transformation might occur through precipitation of graphitic carbon. Niemantsverdriet et al. [15] claimed that the deactivation of precipitated iron catalyst activated in H_2 is caused by the formation of inactive carbon (graphite like) that blocks up the active site of the iron carbides.

The appearance of both amorphous and well-ordered graphitic carbon layer on the surface of nano-catalysts in the presence has been observed. No graphitic carbon phase was identified after CO activation of the catalyst. When amorphous carbon rims were observed, the composition of the core was identified as iron carbide and the particle sizes were found to be relatively smaller. When graphitic carbon rims were identified, the particles were quite large and the core was identified as pure magnetite (Figure 2.2-10b and 2.2-11b). The surface of magnetite particles was always found to be free from amorphous carbons.

Both graphitic and amorphous carbons affect the high-energy loss portion of the EELS spectrum at the carbon K-edge. The difference between the two spectra is due to differences in carbon-carbon bonding. The morphology of amorphous and crystalline carbon is determined by the fraction of sp^3-bonded carbon. The differences between the EELS spectra of graphitic and amorphous carbon are due to differences in carbon-carbon bonding. The relative intensity of carbon $1s \rightarrow \pi^*$ and $1s \rightarrow \sigma^*$ core-level transitions provides a robust measure of the percentage sp^2-bonded carbon. A strong π^* peak suggests that the material is primarily sp^2-bonded. Due to more ordered crystal structure and regular bonding, the spectra of both ordered and disordered graphite show a sharp π^* peak followed by a higher energy wide, flat-topped σ^* peak [34]. At the front edge of the

σ^* peak is another sharp peak called the "A" peak. The EELS spectrum for amorphous carbon, however, only has a small π^* shoulder, a sloping σ^* peak, and no "A" peak.

The relative intensity of π^* (at 284 eV) to σ^* (at 292 eV) peak and a strong π^* peak in the carbon K-edge EELS spectrum (Figure 2.2-6a) recorded at the center of the catalyst particle indicates well-defined crystalline structure of iron carbide. When the electron beam was focused in the outer rim of the particle, the carbon K-edge fine structure (Figure 2.2-6b) reveals an intense σ^* peak (at 295 eV) and a weak π^* shoulder peak (at 285 eV) only. This clearly indicates the presence of amorphous carbon.

The appearance of well-ordered crystalline graphitic carbon phase on single crystal magnetite particles are evident from the HRTEM images shown in Figure 2.2-10b and 2.2-11b. These graphitic carbon layers can inhibit the re-carbidation of magnetite in the FTS environment and results in permanent catalyst deactivation. The surface carbon layers (amorphous and graphitic) can be formed by disproportionation of CO as: $2CO \leftrightarrow CO_2 + C$ (Boudouard reaction) or inter-conversion of iron carbides [29]. At higher conversion level (like at the initial period of the present study), the dissociated CO species can be rapidly converted into hydrocarbon products ($-CH_2-$ units). However at lower conversion level (typically 10-20%), the result will be favorable for the graphitization of the surface carbonaceous compounds. In other words, the FTS reaction at quite lower conversion levels could facilitate the formation of the graphitic carbon as observed in the low conversion period of the present study.

Combining the results from Mössbauer, EELS, HRTEM and PSD measurements it was found that all the bigger particles grown during FTS are single crystal magnetite. On the contrary, the ultrafine particles were found to be iron carbides. No single larger

particle of iron carbide was observed. These strongly suggest that either the nano-scale growth of particles continue with a simultaneous transformation of iron carbide to oxide or the two phenomena runs in successive steps. If the reverse phenomena would have been true, then at least a few of larger particles formed in situ should have composed of iron carbide. The polycrystalline structure of iron oxides used in the current study is also favorable for diffusion along grain boundaries [35]. The iron carbide is believed to transform into iron oxide first and then its growth continues.

2.2.6. CONCLUSION

CO activation of unpromoted ultrafine iron nanocatalyst for 24 h converts the hematite into a mixture of 85% $\chi - Fe_5C_2$ and magnetite. FTS using this catalyst results in an initial high conversion (ca. 85%) of CO and H_2. However the conversions decreased by a factor of almost 10 over 400 h of synthesis time and after that remained constant (ca. 10%) up to 600 h of FTS. Mössbauer and EELS measurement revealed that the catalyst deactivation was accompanied by structural evolution of the catalyst from initial nearly pure iron carbides (after CO activation), to their gradual in situ re-oxidation, and ultimate transformation to pure magnetite after 400 h of synthesis time. It is concluded that for an iron based catalyst to exhibit high activity in FTS, the carbide contents of the catalyst should be reasonably high. Experimental data suggests that the nucleation for carbide/oxide transformation initiates at the center of the particle. It is believed that the re-oxidation is caused by water produced during FTS. Small amount of $\varepsilon' - Fe_{2.2}C$ was detected in some samples collected after 480 h of FTS. These carbide species are believed to be generated simultaneously by syngas during FTS. PSD measurements indicate growths of individual catalyst particle. Statistical average diameters were found

to increase by a factor of 4 over 600 h of synthesis time. The breadth, mode and median of PSD were found to increase continuously with time-on-stream. Some particles with the largest dimension larger than 150 nm were also observed. Chemical compositions of the larger particles were always found to be pure single crystal magnetite by EELS measurement. Small number of ultrafine carbide particles was identified in the catalyst samples collected during later period of FTS. It appears that carbide/oxide transformation and nano-scale growth of particles continued either in series or simultaneously; but definitely not in the reverse order (in that case some larger carbide particles would have been observed). EELS-STEM measurement reveals amorphous carbon rim of thickness 3-5 nm around some particles after activation and during FTS. Well ordered graphitic carbon layer on larger single crystal magnetite particles were found by EELS-STEM measurement. The maximum thickness of the carbon (amorphous or graphitic) rim does not grow above 5 nm. Thus the growths of particles are not due to carbon deposition.

Acknowledgement

We gratefully acknowledge financial support for this work from US Department of Energy (under contact DE-FC26-03NT41965) and Commonwealth of Kentucky.

REFERENCES

1. I. Wender, Fuel Processing Technology 48 (1996), 189.
2. A. P. Steynberg in: A. P. Steynberg, M. E. Dry (Eds.), Fischer-Tropsch Technology, Studies in Surface Science and Catalysis, 152, Elsevier, USA, 2004, p. 8.
3. A. Sarkar, U. Graham, J. K. Neathery, R. L. Spicer, and B. H. Davis, Fischer-Tropsch Synthesis with Ultrafine Iron-Based Catalyst: Nano-Scale Growth of Particles and Associated Effects on Wax/Catalyst Separation, Proc. AIChE Spring National Meeting,

Orlando, FL, USA, April 23-27, 2006, paper 181b.

4. S. Li, W. Ding, G. D. Meitzner, and E. Iglesia, J. Phys. Chem. B 106 (2002), 85.
5. C.-S. Huang, B. Ganguly, G. P. Huffman, F. E. Huggins, and B. H. Davis, Fuel Science and Technology International 11(9) (1993), 1289.
6. R. Zhao, J. G. Goodwin, K. Jothimurugesan, S. K. Gangwal, and J. J. Spivey, Industrial and Engineering Chemistry Research, 40 (2001), 1320.
7. M. D. Shroff, D. S. Kalakkad, K. E. Coulter, S. D. Köhler, M. S. Harrington, N. B. Jackson, A. G. Sault, and A. K. Datye, Journal of Catalysis 156 (1995), 185.
8. H. N. Pham, A. K. Datye, Catalysis Today, 58 (2000), 233.
9. R. Srinivasan, L. Xu, R. L. Spicer, F. L. Tungate, and B. H. Davis, Fuel Science and Technology International, 14(10) (1996), 1337.
10. B. H. Davis, Technology Development for Iron Fischer-Tropsch Catalysis, US DOE Final Technical Report, Contract # DE-AC22-94PC94055-13 (1999).
11. J. C. W. Kuo, F. P. D. Sanzo, W. E. Garwood, K. M. Gupte, C. K. Lang, T. M. Leib, M. Malladi, T. Molina, D. M. Nace, J. Smith, N. Tarallo, and J. F. Kirk, Slurry Fischer-Tropsch/Mobil Two-Stage Process of Converting Syngas to High Octane Gasoline, US DOE Final Technical Report, Contract # AC22-80PC30022 (1983).
12. D. B. Bukur, W. P. Ma, V. C. Vazquez, L. Nowicki, A. A. Adeyiga, Industrial and Engineering Chemistry Research, 43 (2004), 1359.
13. R. J. O'Brien, L. Xu, S. Bao, A. Raje, and B. H. Davis, Applied Catalysis A 196 (2000), 173.
14. H. Kölbel and M. Ralek, Catalysis Reviews – Science and Engineering, 21 (1980), 225.
15. J. W. Niemantsverdriet, A. M. van der Krann, W. L. van Dijk, and H. S. van der Baan,

Journal of Physical Chemistry, 84 (1980), 3363.

16. J. B. Butt, Catalysis Letters, 7 (1990), 61.
17. A. Sarkar, A. K. Dozier, U. Graham, and B. H. Davis, submitted to Applied Catalysis A: General.
18. K. R. P. M. Rao, F. E. Huggins, G. P. Huffman, R. J. Gormley, R. J. O'Brien, and B. H. Davis, Energy & Fuels, 10 (1996), 546.
19. K. R. P. M. Rao, F. E. Huggins, G. P. Huffman, R. J. O'Brien, R. J. Gormley, and B. H. Davis, Preprints of Papers, ACS Division of Fuel Chemistry, 40(1) (1995), 153.
20. O. S. Morozova, Y. V. Maksimov, D. P. Shashkin, P. A. Shirjaev, V. V. Matveyev, V. A. Zhorin, and O. V. Krylov, Applied Catalysis 78(1991), 227.
21. C. Colliex, T. Manoubi, and C. Ortiz, Physical Review B 44(20) (1991), 402.
22. T. Allen, Particle Size Measurement, Volume 1, Chapman and Hall, London, 1997, p. 44-111.
23. M. E. Dry, in: J. R. Anderson, M. Boudart (Eds.), Catalysis – Science and Technology, Springer-Verlag, New York, 1981, p. 59.
24. P. H. Emmett (Ed.), Crystallite Phase and Their Relationship to Fischer-Tropsch Catalysis, Reinhold, New York, 1956, p. 407.
25. M. F. Zarochak, M. A. McDonald, Slurry-phase Fischer-Tropsch synthesis, CONF-86/288-1, Proceedings of Indirect Liquefaction Contractor's Conference, December 2-4, 1986 at Monroeville, PA, USA.
26. G. B. Raupp, and W. N. Delgass, Journal of Catalysis 58 (1979), 361.

27. S. Li, R. J. O'Brien, G. D. Meitzner, H. Hamdeh, B. H., Davis, and E. Iglesia, Applied Catalysis A 219 (2001), 215.

28. S. Li, G. D. Meitzner, and E. Iglesia, Journal of Physical Chemistry B 105 (2001), 5743.

29. J. Xu, and C. H. Bartholomew, Journal of Physical Chemistry B 109 (2005), 2392.

30. A. Loaiza-Gil, B. Fontal, F. Rueda, J. Mendialdua, and R. Casanova, Applied Catalysis A: Gen 177 (1999), 193.

31. S. A. Eliason, and C. H. Bartholomew, Studies in Surface Science and Catalysis 111 (1997), 517.

32. D. J. Dwyer and J. H. Hardenbergh, Journal of Catalysis 87 (1984), 66.

33. Y. Jin, and A. K. Datye, Journal of Catalysis 196 (2000), 8.

34. A. Fernández, P. Prieto, C. Quirós, J. M. Sanz, J. M. Martin and B. Vacher B, Appied Physics Letters 69 (1996), 764.

35. W. J. Kim, O. A. Ruano, J. Wolfenstine, G. Frommeyer, and O. D. Sherby, Journal of Material Research, 12 (1997), 2317.

Table 2.2-1. Schedule of sample collection during FTS at 270 °C, 175 psig, $H_2/CO = 0.7$, and a syngas space velocity of 3.0 sl/h/g Fe. The first sample (S1) was collected after carbidation with CO for 24 h at 270 °C, 175 psig, and a space velocity of 3.0 sl/h/g Fe.

Sample #	FT Synthesis Time, h
S1	0 (after 24 h CO carbidation)
S2	28.9
S3	73.2
S4	167.7
S5	311
S6	382.8
S7	481.6
S8	596.8

Table 2.2-2. Summary of phase identification of iron from Mössbauer spectroscopy analysis.

Sample #	**FT Synthesis Time, h**	**Fraction (%) of Fe at 300 K**	**Fraction (%)of Fe at 20 K**
S1	0 (after 24 h CO carbidation)	85 in $\chi - Fe_5C_2$ 15 in spm	84 in $\chi - Fe_5C_2$ 16 in Fe_3O_4
S2	28.9	33 in Fe_3O_4 48 in $\chi - Fe_5C_2$ 19 in spm	50 in Fe_3O_4 50 in $\chi - Fe_5C_2$
S3	73.2	65 in Fe_3O_4 18 in $\chi - Fe_5C_2$ 17 in spm	76 in Fe_3O_4 22 in $\chi - Fe_5C_2$ 2 in spm
S4	167.7	89 in Fe_3O_4 11 in spm	91 in Fe_3O_4 6 in $\chi - Fe_5C_2$ 3 in spm
S5	311	93 in Fe_3O_4 7 in spm	96 in Fe_3O_4 4 in spm
S6	382.8	100 in Fe_3O_4	99 in Fe_3O_4 1 in paramag
S7	481.6	93 in Fe_3O_4 7 ε-Fe_2C	93 in Fe_3O_4 5 in ε'–$Fe_{2.2}C$ 2 in paramag
S8	596.8	100 in Fe_3O_4	90 in Fe_3O_4 4 in ε'–$Fe_{2.2}C$ 6 in paramag

Table 2.2-3. Summary of particle size distribution measurement result. The % increase of statistical diameters are calculated as: $\Delta d_{x,y} = \left[\left(d_{x,y}(t+\Delta t) - d_{x,y}(t)\right)/ d_{x,y}(t)\right] X\, 100$ where x = 1, 3, 4, and y = 0, 2, 3, respectively.

FT Synthesis Time (h)	**Mode (nm)**	**Median (nm)**	$d_{1,0}$ **, nm (** $\Delta d_{1,0}$ **, %)**	$d_{3,2}$ **, nm (** $\Delta d_{3,2}$ **, %)**	$d_{4,3}$ **, nm (** $\Delta d_{4,3}$ **, %)**
0	19.02	18.05	19.15 (-)	23.48 (-)	25.86 (-)
112.6	25.5	25.75	27.24 (42.3)	34.04 (44.9)	41.04 (58.7)
258.3	26.05	28.17	30.48 (11.9)	41.73 (22.6)	49.02 (19.5)
406.3	41.51	35.54	36.14 (18.6)	51.88 (24.3)	58.79 (19.9)
505.6	36.51	40.41	44.29 (22.6)	65.35 (25.9)	75.68 (28.8)
620.8	46.5	51.97	57.15 (29.1)	82.52 (26.3)	99.89 (31.9)

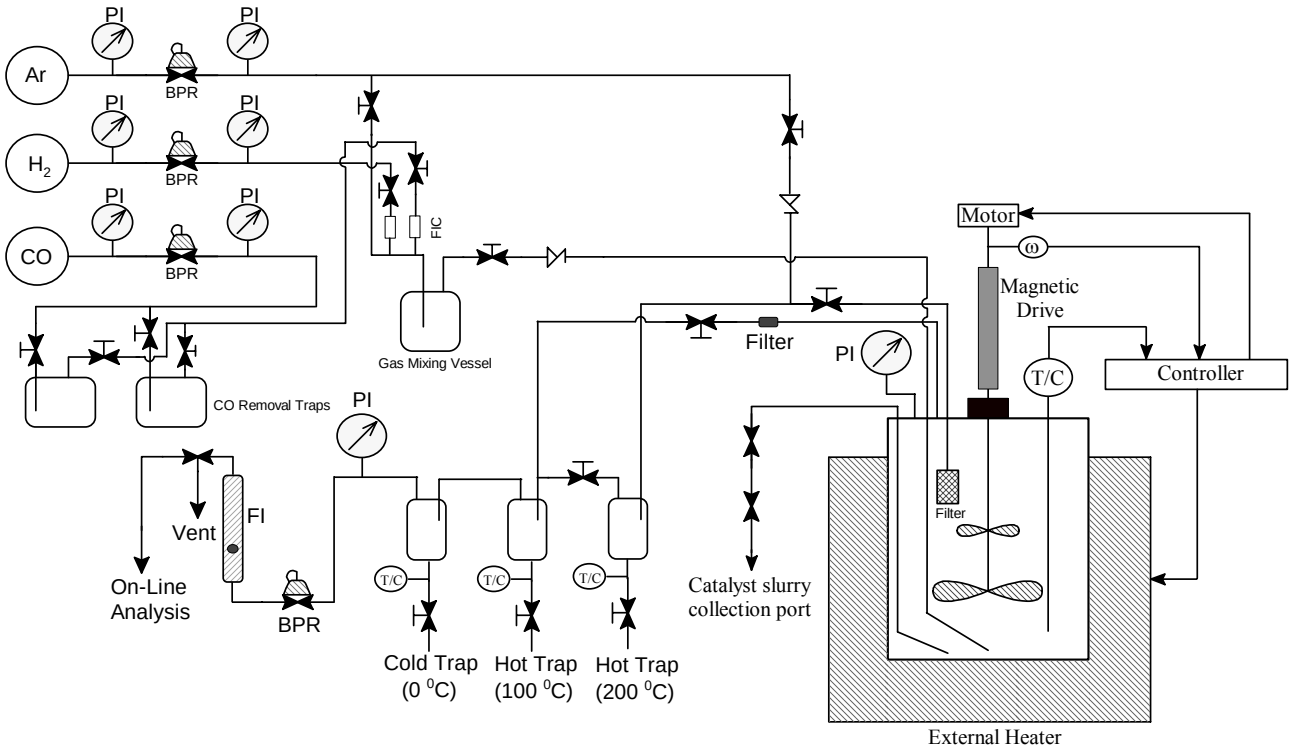

Figure 2.2-1a. A simplified schematic of the CSTR set-up used for Fischer-Tropsch synthesis in the present study.

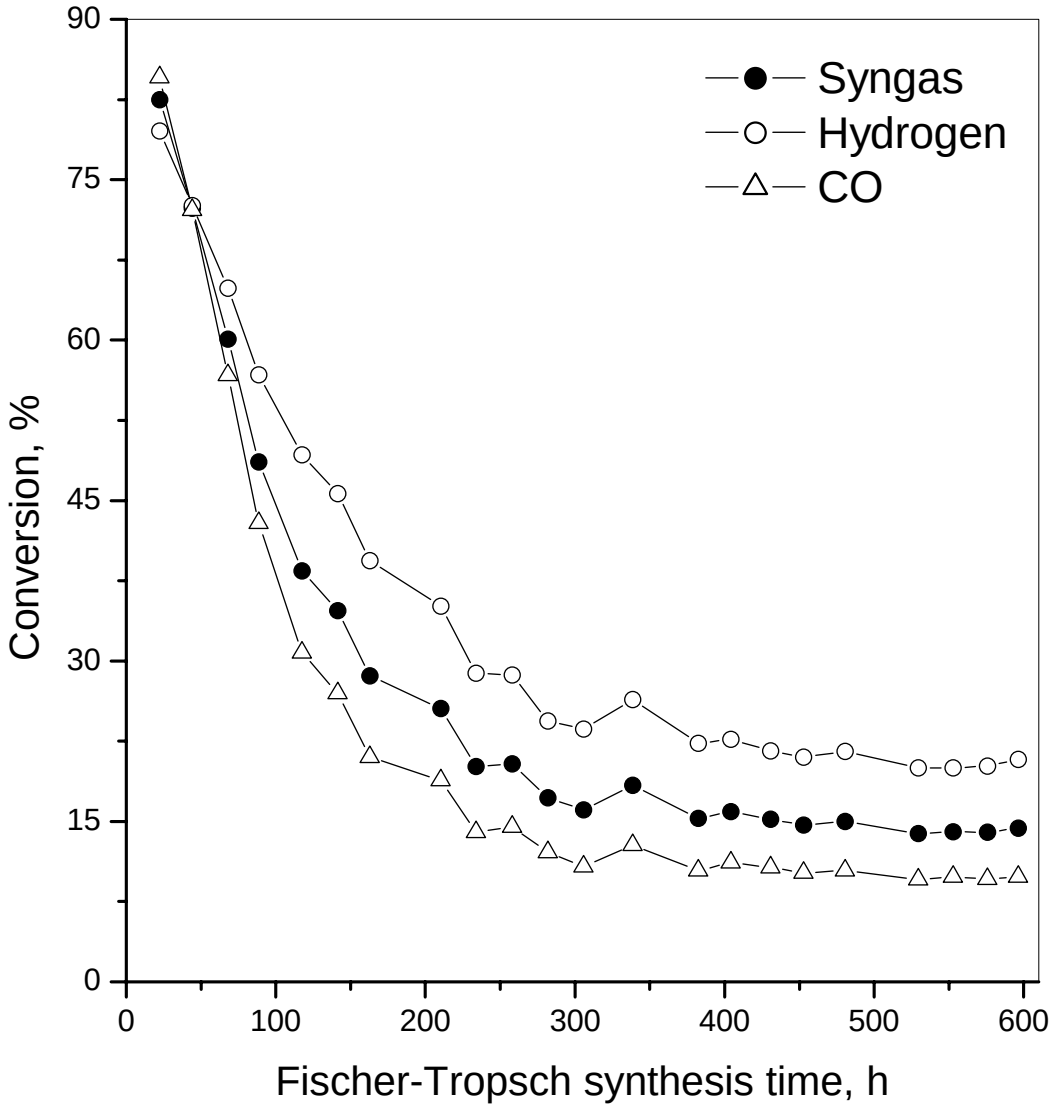

Figure 2.2-1b. Conversion of syngas, hydrogen and CO against time-on-stream. FTS effected at 270 °C, 175 psig, $H_2/CO = 0.7$, and a syngas space velocity of 3.0 sl/h/g Fe.

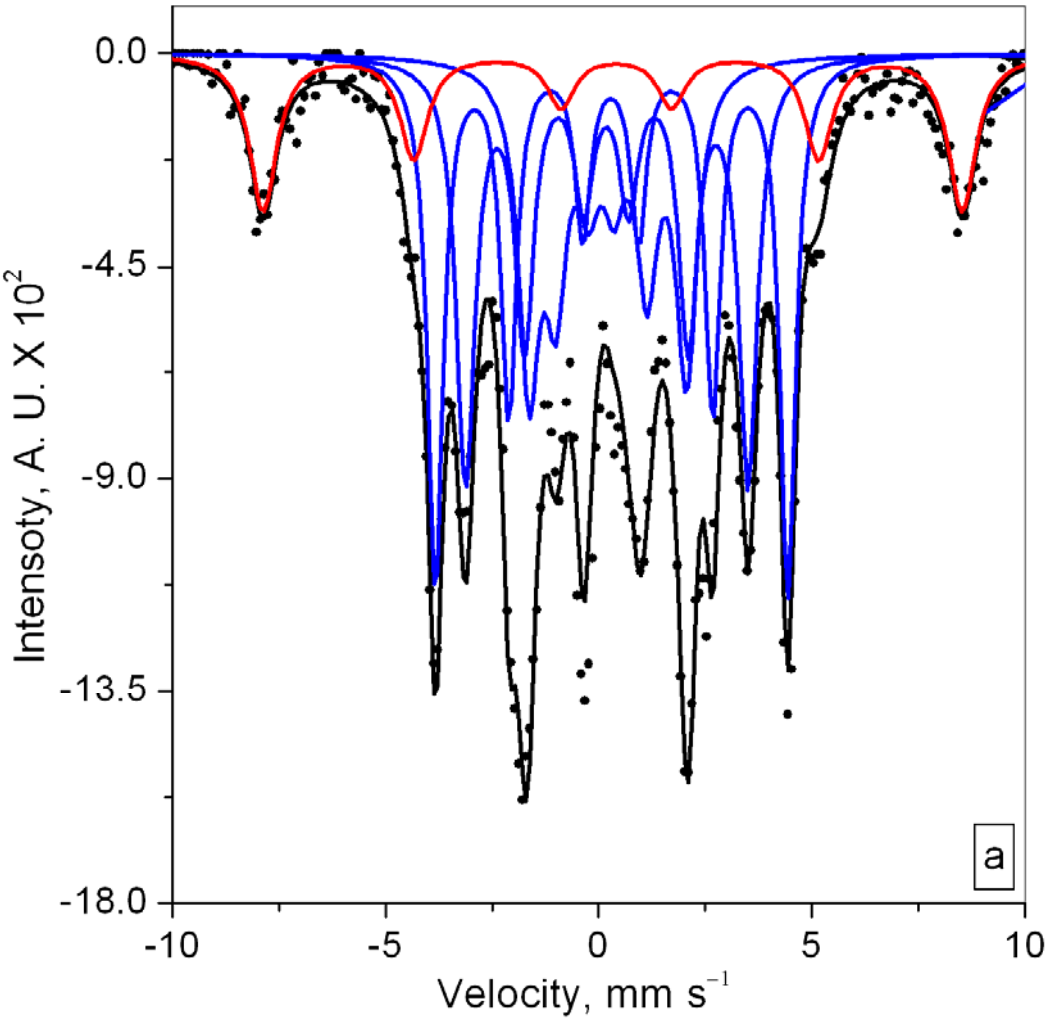
0.0
-4.5
-9.0
-13.5
-18.0
-10
-5
0
5
10
Intensoty, A. U. X 10^2
Velocity, mm s^{-1}
a

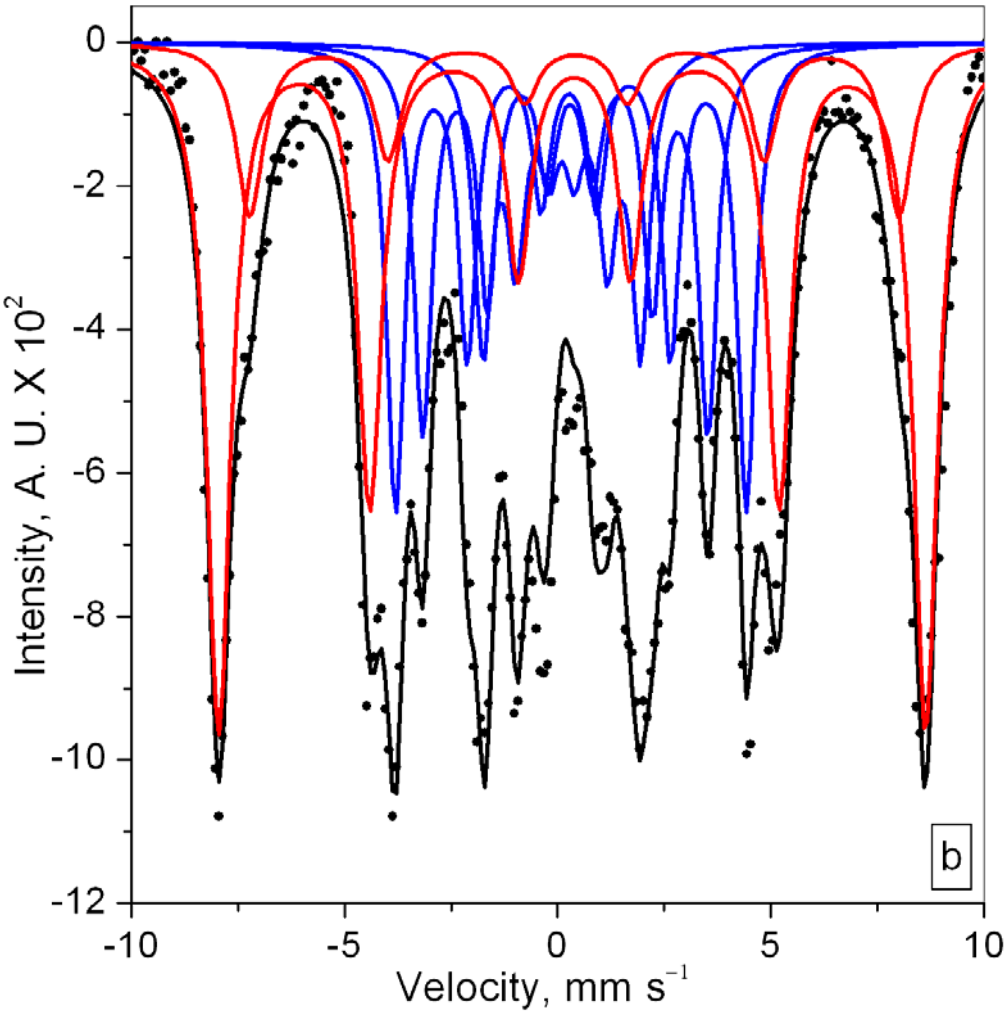
0
-2
-4
-6
-8
-10
-12
-10
-5
0
5
10
Intensity, A. U. X 10^2
Velocity, mm s^{-1}
b

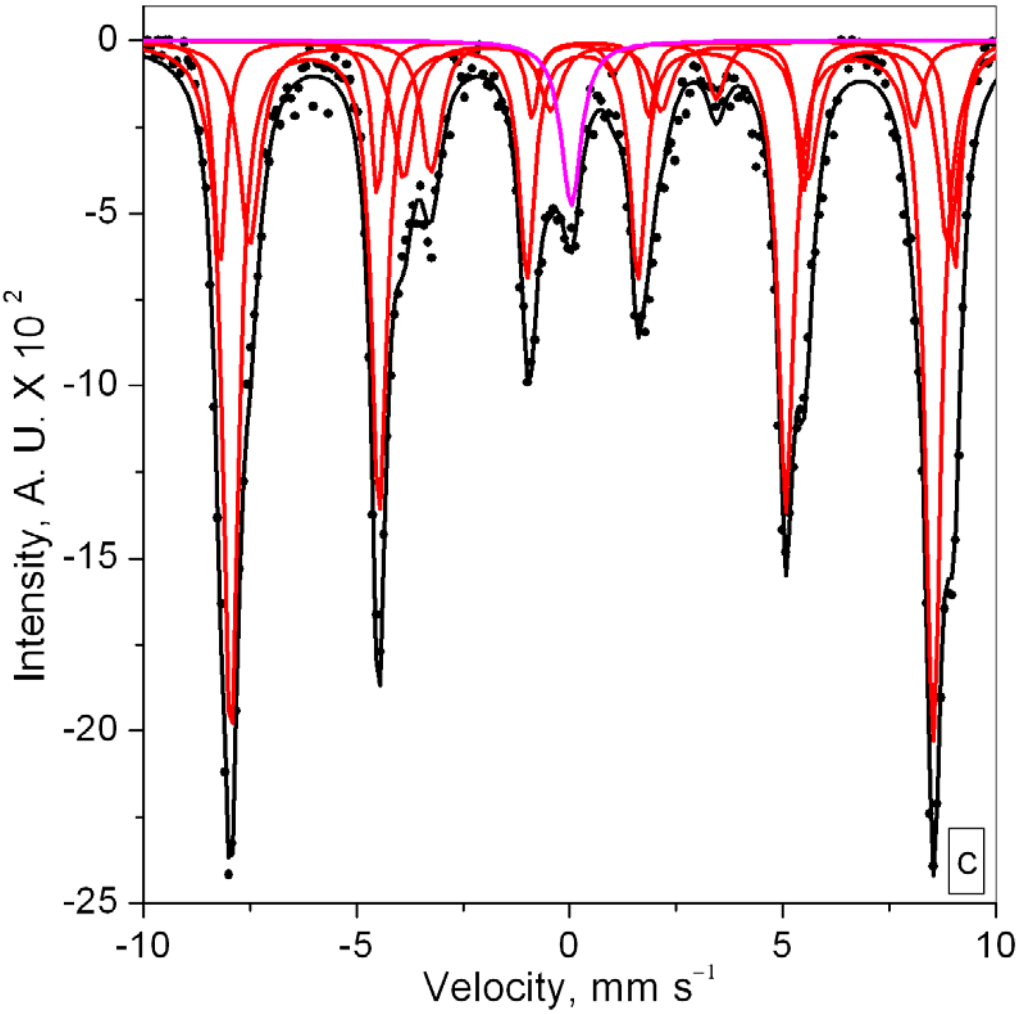
0
-5
-10
-15
-20
-25
Intensity, A. U. X 10 2
-10
-5
0
5
10
Velocity, mm s−1
C

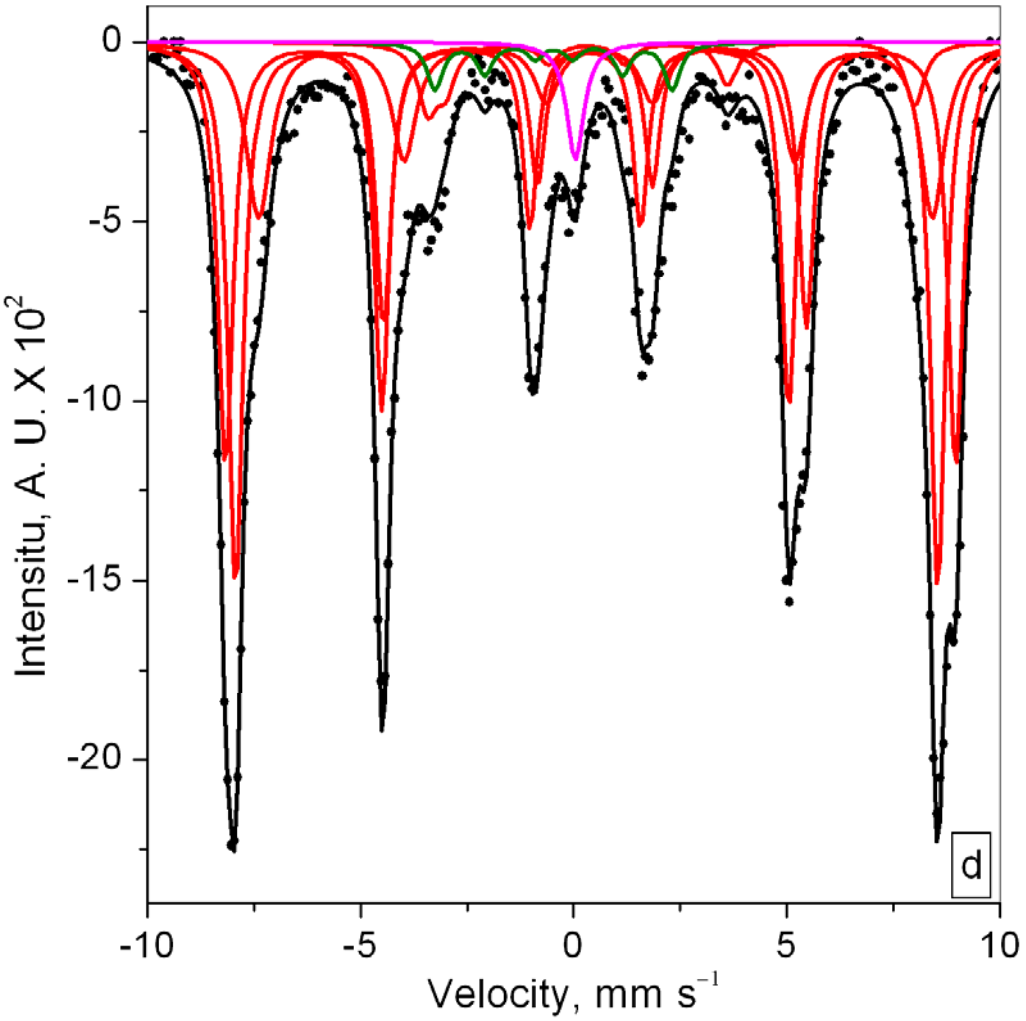

Figure 2.2-2. Representative Mössbauer spectra of samples collected after activation and during FTS at 270 °C, 175 psig, $H_2/CO = 0.7$, and a syngas space velocity of 3.0 sl/h/g Fe: (a). sample S1 collected after carbidation with CO for 24 h at 270 °C, 175 psig, and a space velocity of 3.0 sl/h/g Fe; (b). sample S2 collected after 28.9 h of synthesis; (c). sample S5 collected after 311 h of FTS; and (d) sample S7 collected after 481.6 h of synthesis. The fitted curves are shown in solid lines: black, total spectra; red, oxide; blue, $\chi - Fe_5C_2$; green, $\varepsilon' - Fe_{2.2}C$; and magenta, spm phase.

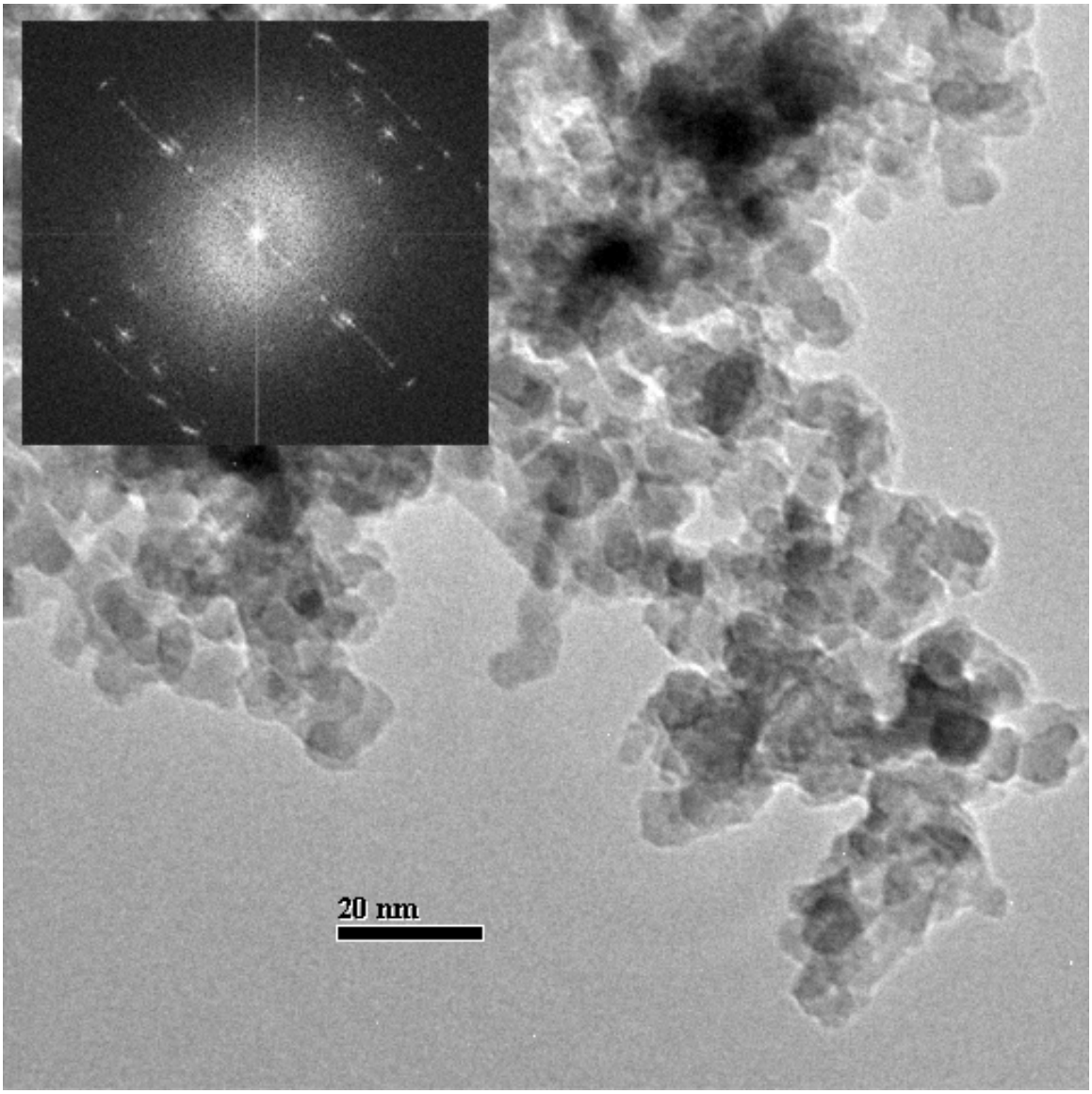

Figure 2.2-3. TEM image of as received ultrafine iron NANOCAT® material. An electron microdiffraction pattern is also shown in inset.

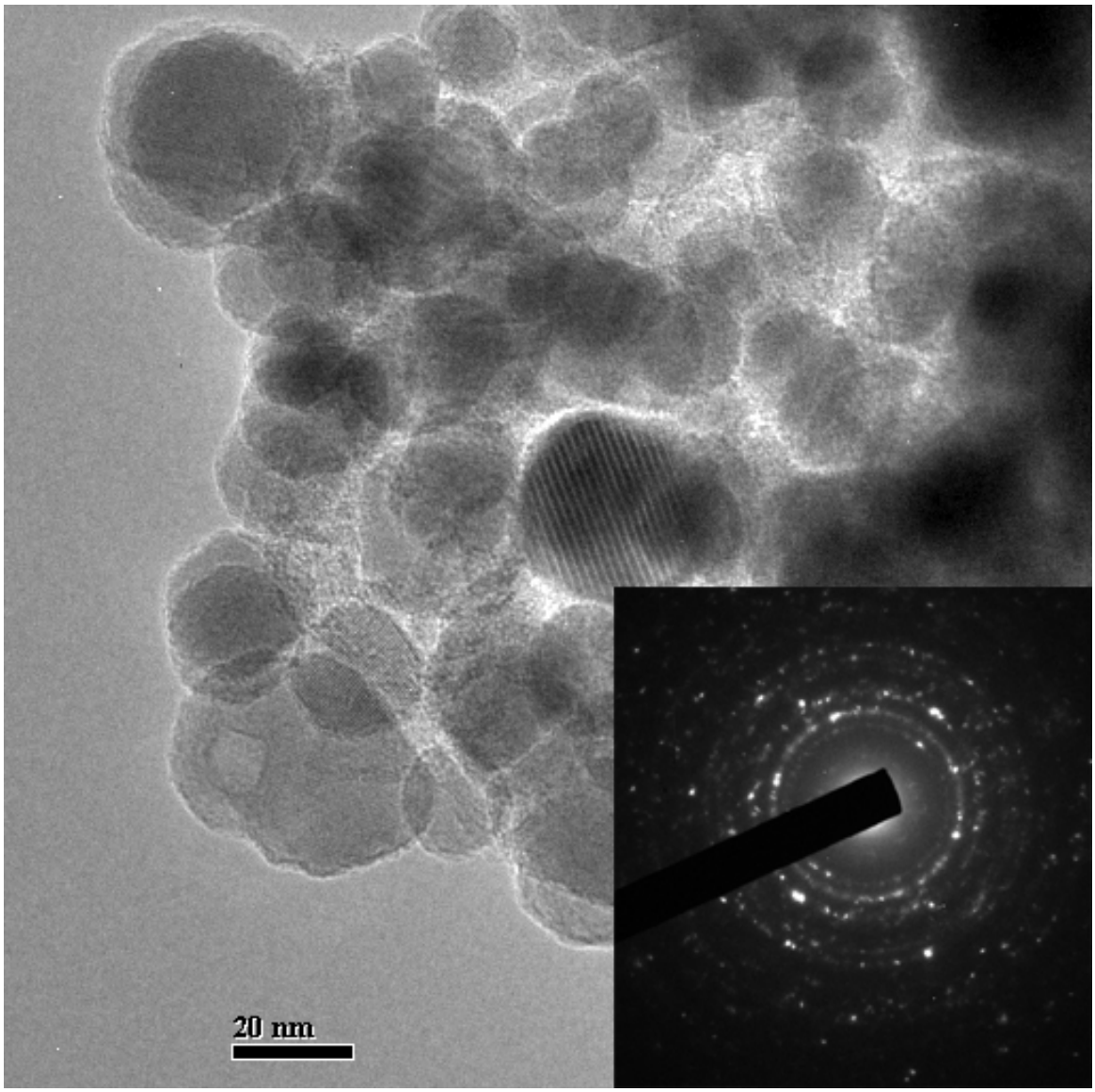

Figure 2.2-4. TEM image of the nanocatalyst after CO activation for 24 h at 270 °C, 175 psig, and a space velocity of 3.0 sl/h/g Fe. An electron microdiffraction pattern is also shown in inset.

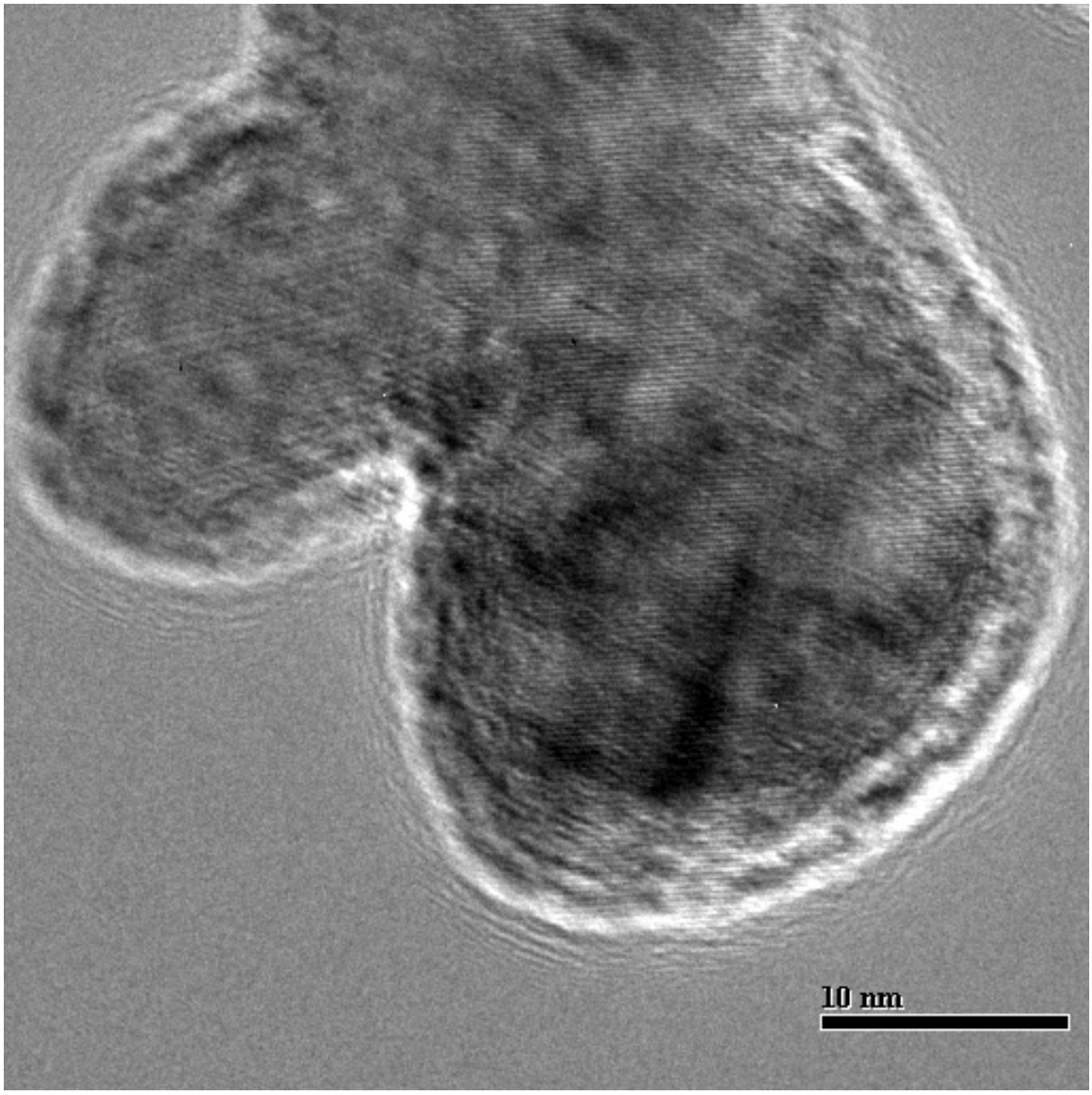

Figure 2.2-5. High-resolution TEM image of the nanocatalyst after CO activation for 24 h at 270 °C, 175 psig, and a space velocity of 3.0 sl/h/g Fe. Well defined crystalline structure and an outer rim of amorphous material is evident.

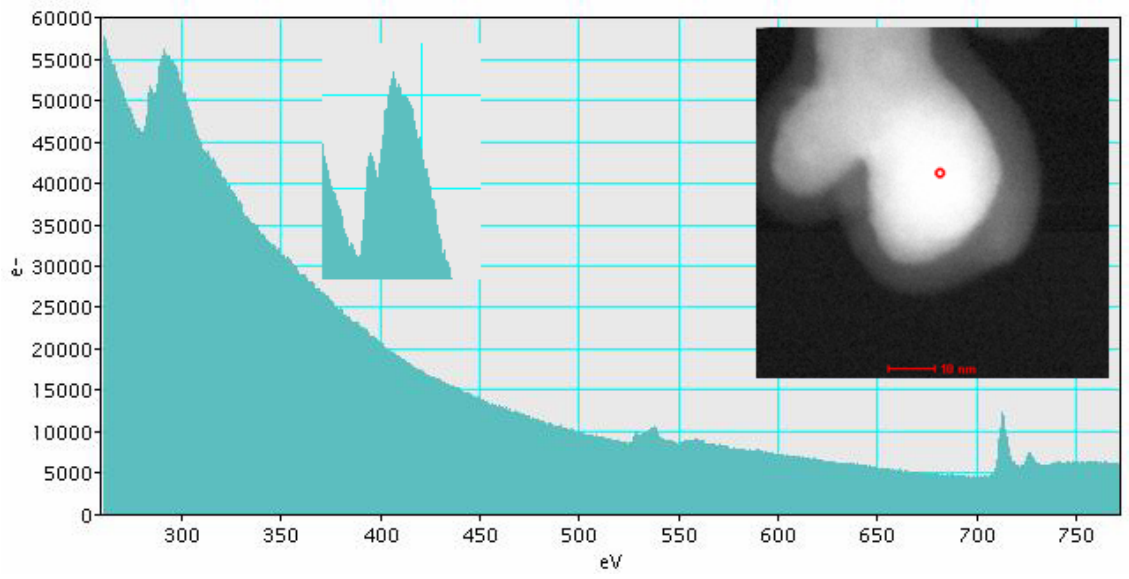

(a)

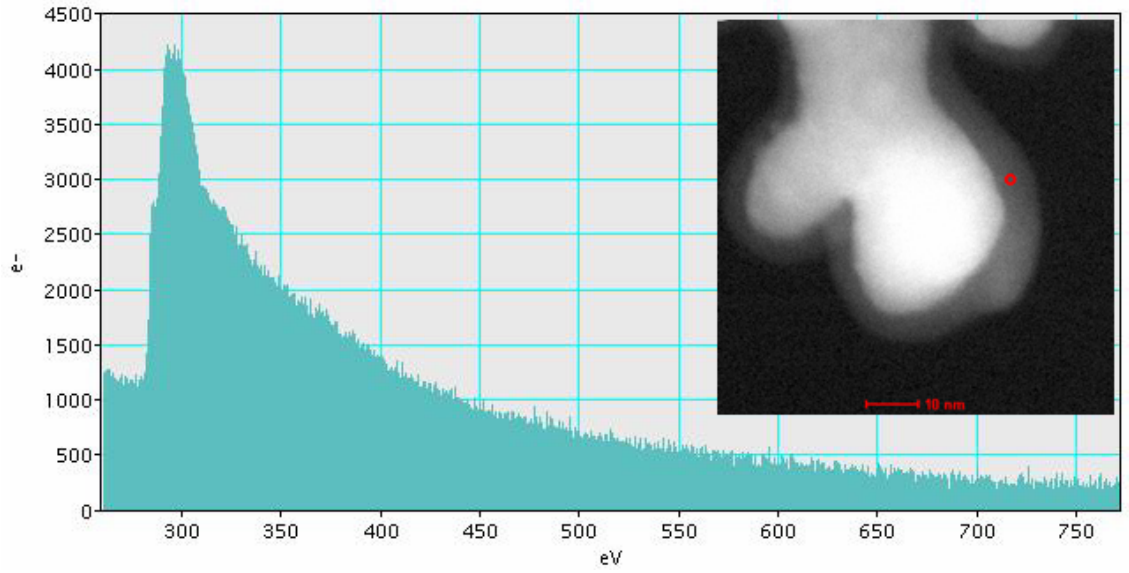

(b)

Figure 2.2-6. EELS spectrum of the catalyst sample collected after CO activation for 24 h at 270 °C, 175 psig, and a space velocity of 3.0 sl/h/g Fe. High-resolution STEM images are shown in insets. The red dots in HRSTEM images indicate the position where the EELS spectra were recorded. A magnified view of carbon K-edge structure in the EELS spectra is also shown in Fig. 6a (inset).

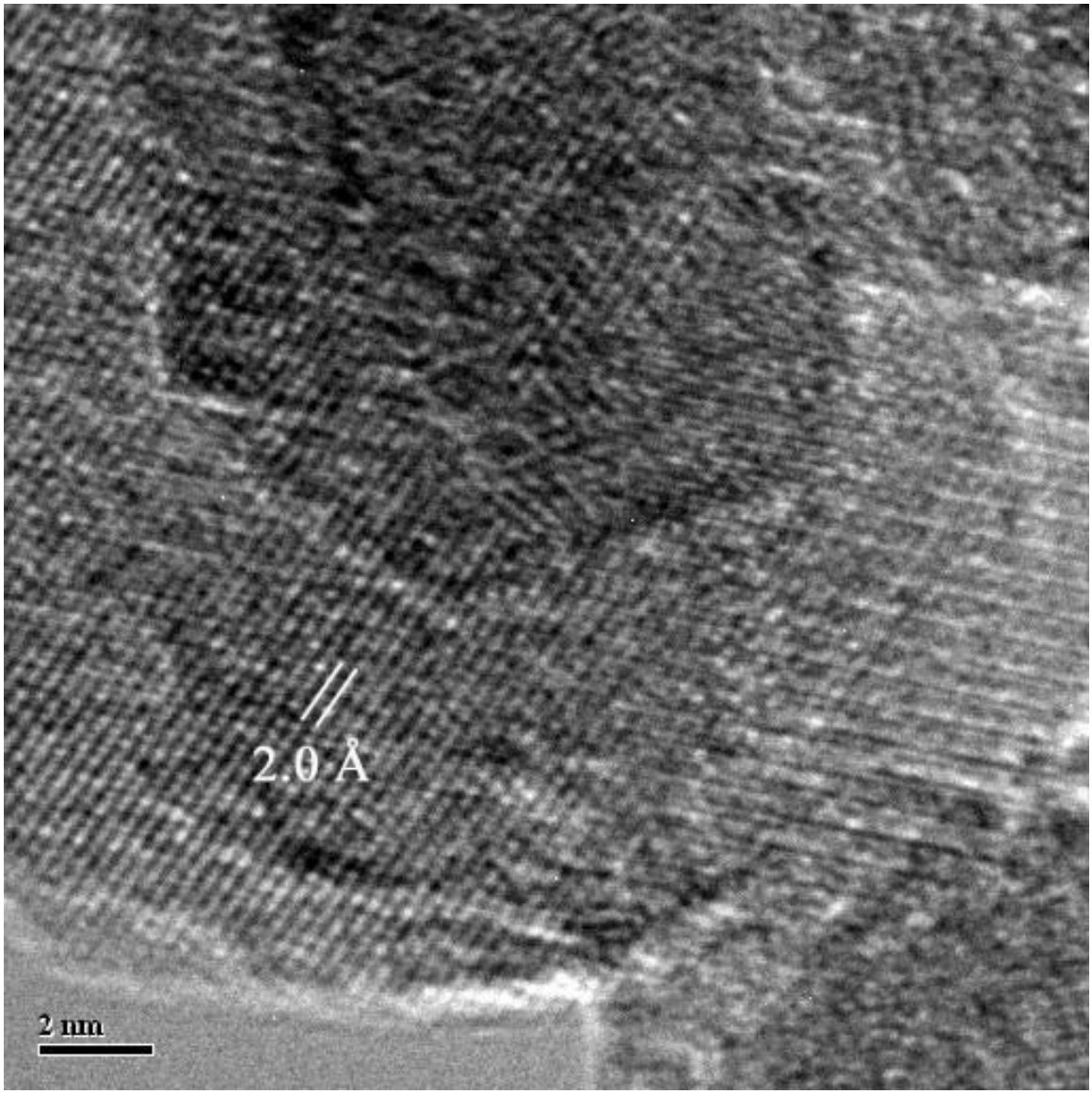

(a)

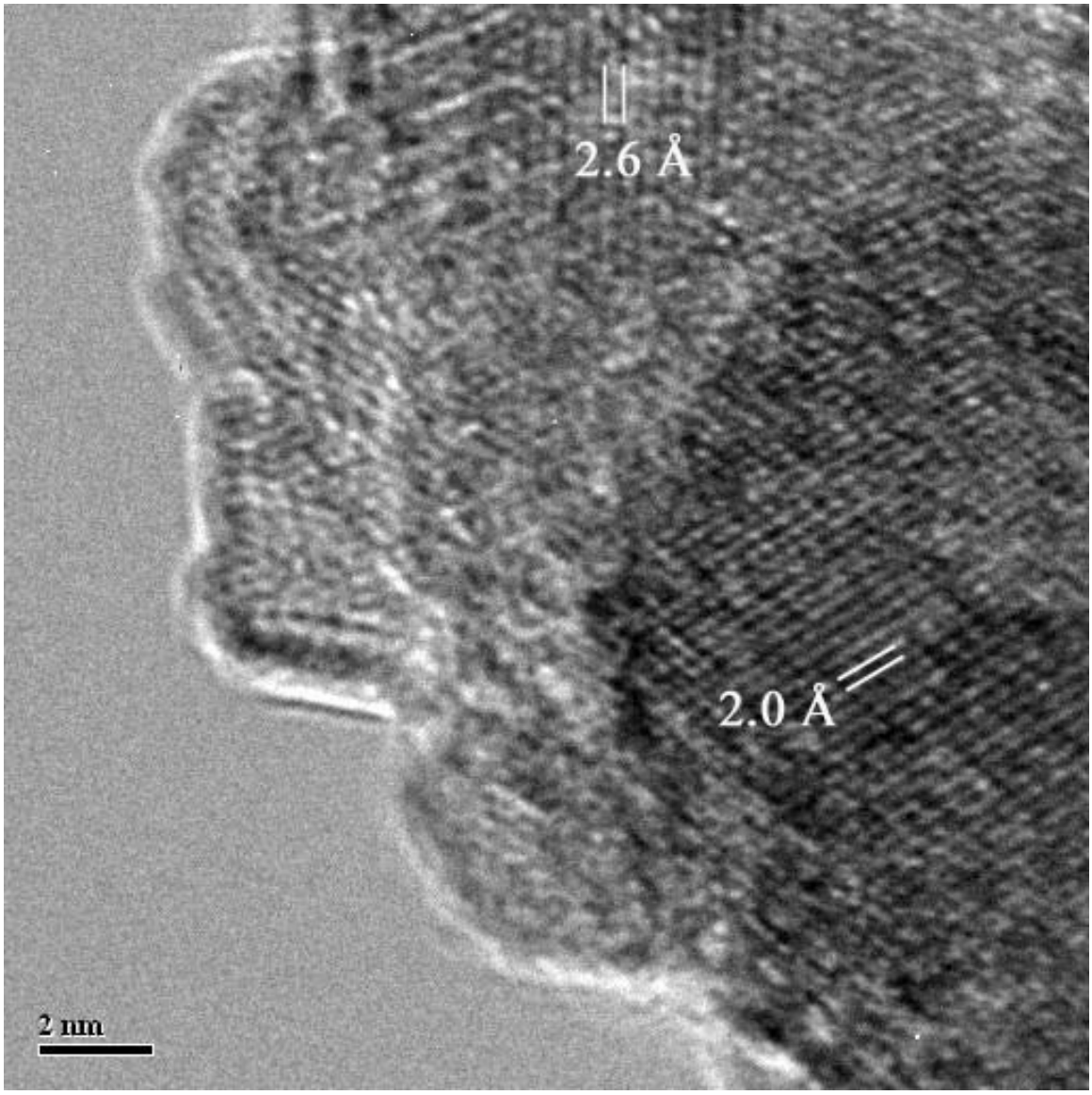

(b)

Figure 2.2-7. HRTEM image of a particle of sample S1 (collected after carbidation with CO for 24 h at 270 °C, 175 psig, and a space velocity of 3.0 sl/h/g Fe): (a) nano-aggregates of iron carbides - the characteristic d-spacing of 2.0 Å can correspond to high intensity (510) or (021) plane of $\chi - Fe_5C_2$; (b) nano-aggregates of iron carbides and oxide: the d-spacing of 2.6 Å can be assigned to high intensity (311) plane of Fe_3O_4 .

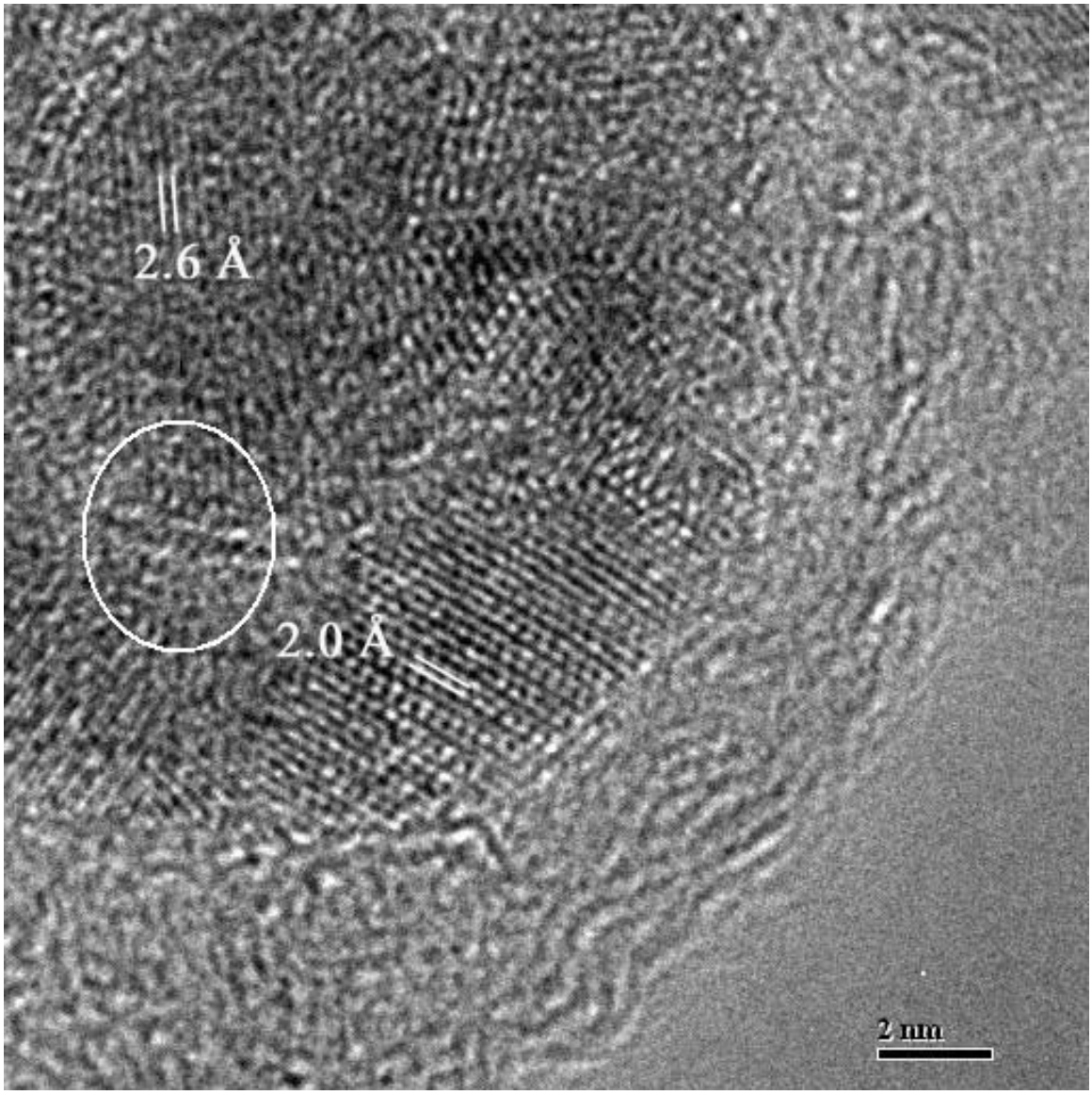

Figure 2.2-8. HRTEM image of a particle of sample S2 (collected after 28.9 h of FTS at 270 °C, 175 psig, and a syngas space velocity of 3.0 sl/h/g Fe): concentric crystalline nano-regions of iron oxide and carbide. The inner oxide core is encapsulated by an outer carbide core.

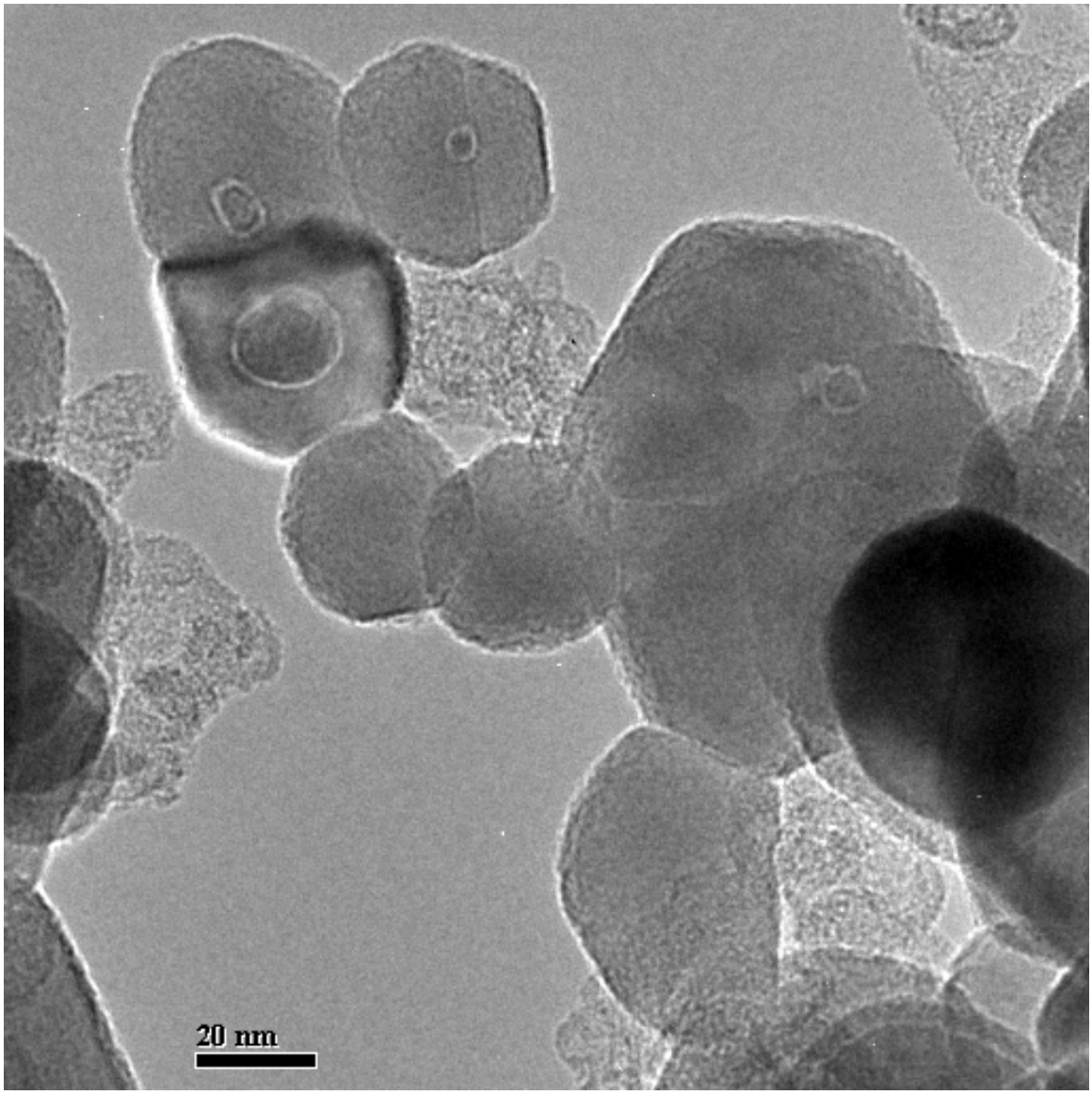

(a)

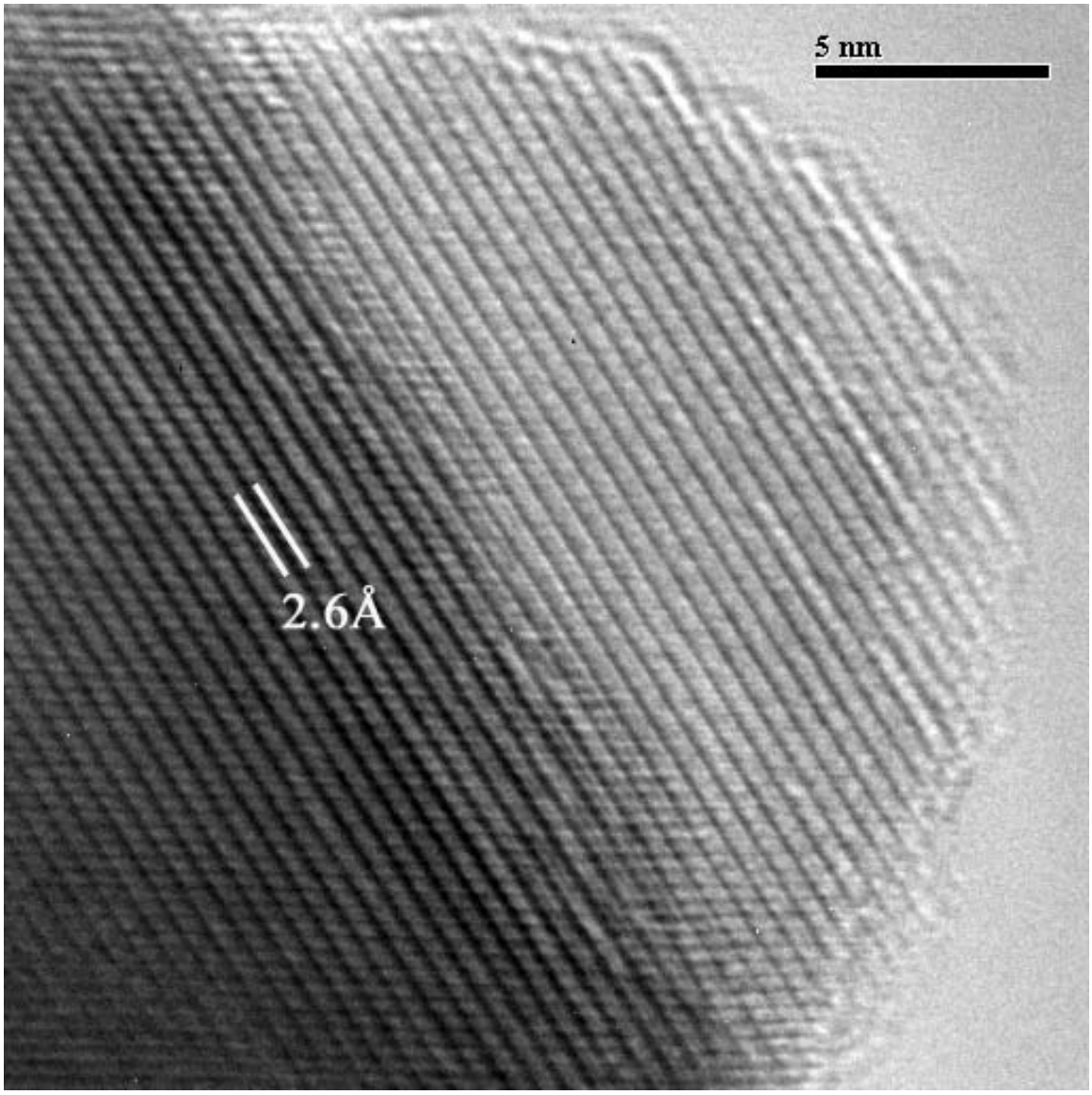

(b)

Figure 2.2-9. TEM image of a particle of sample S4 (collected after 167.7 h of FTS at 270 °C, 175 psig, and a syngas space velocity of 3.0 sl/h/g Fe): (a) appearance of several small "bud" sprouted on the top of the bigger particles with irregular hexagonal shape structure; (b) well defined single crystal of iron oxide (with a characteristic d-spacing of 2.6 Å corresponding be high intensity (311) plane of Fe_3O_4).

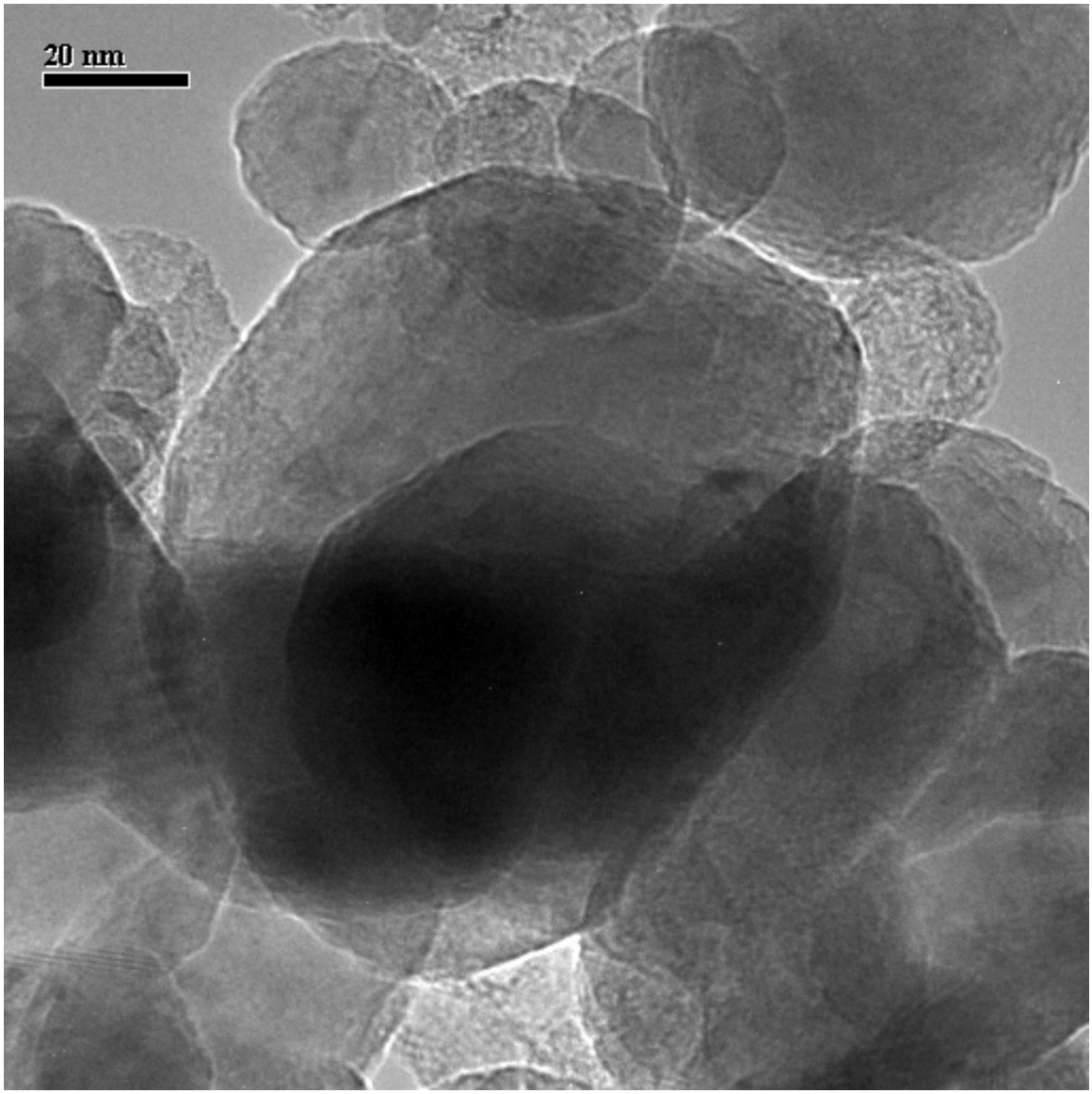

(a)

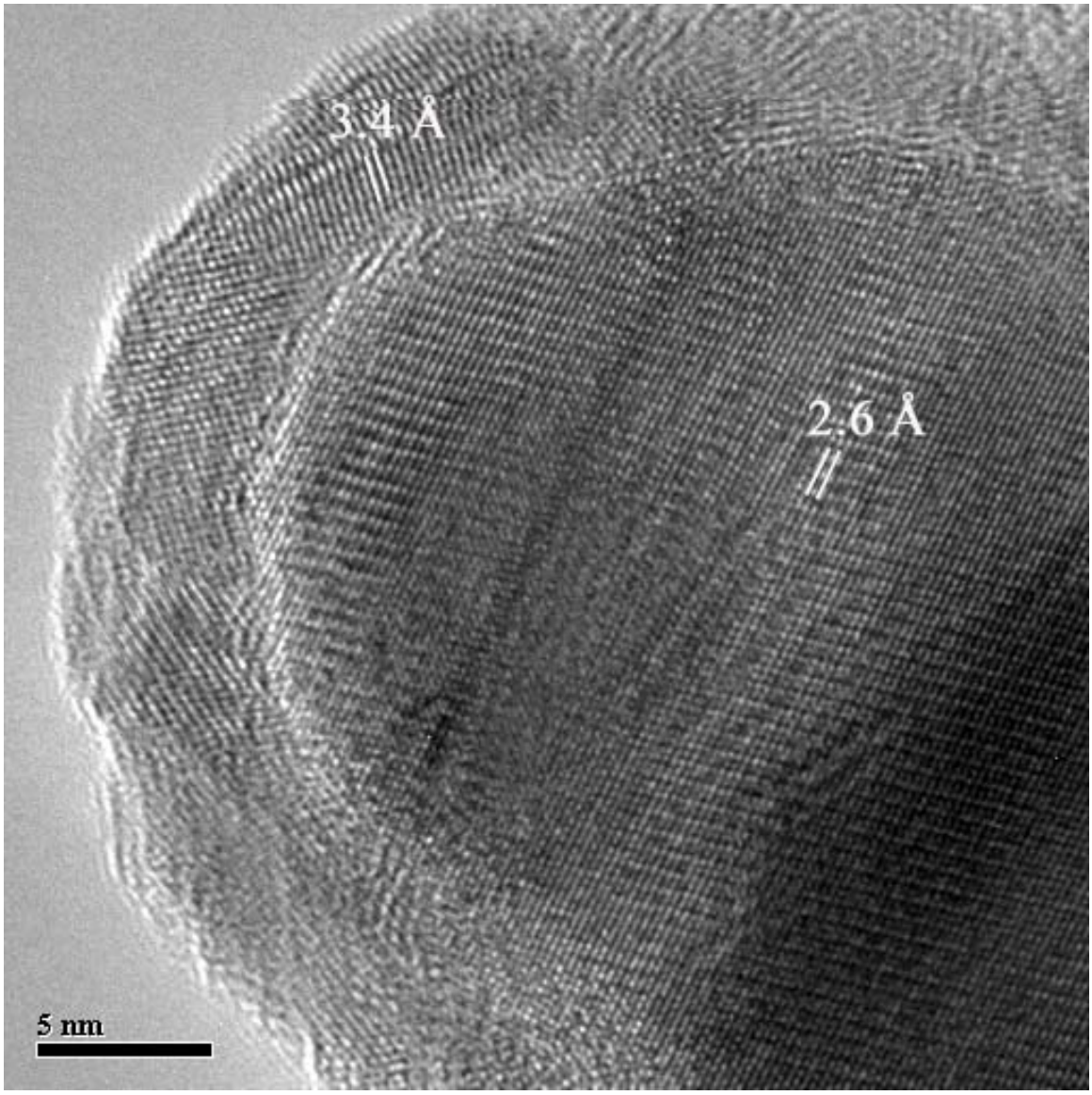

(b)

Figure 2.2-10. HRTEM image of a particle of sample S5 (collected after 311 h of FTS at 270 °C, 175 psig, and a syngas space velocity of 3.0 sl/h/g Fe): (a) big particles with largest dimension higher than 100 nm; (b) single crystal of iron oxide (with a characteristic d-spacing of 2.6 Å corresponding to high intensity (311) plane of Fe_3O_4) is encapsulated with well ordered graphitic carbon rim of thickness about 5 nm.

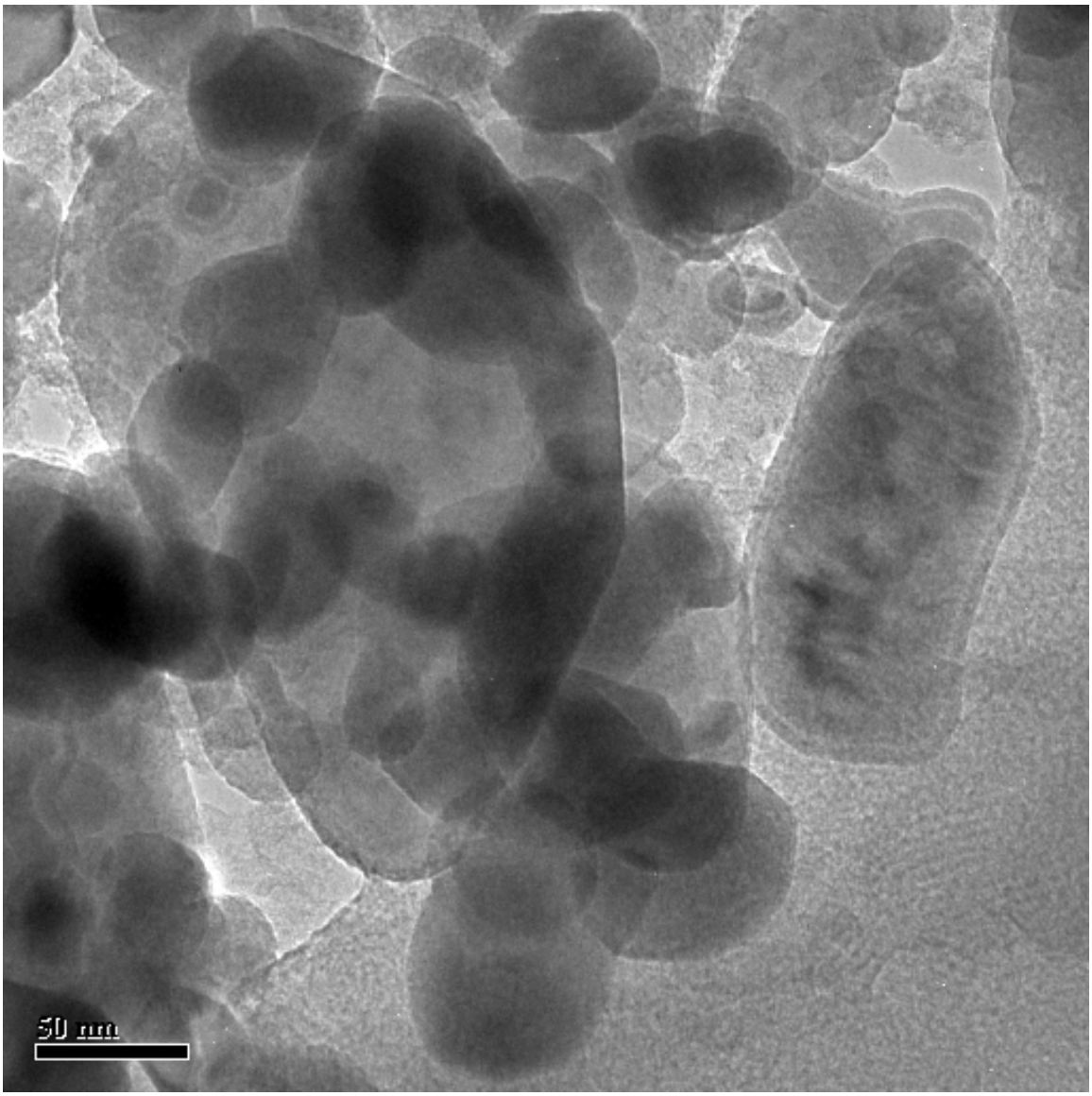

(a)

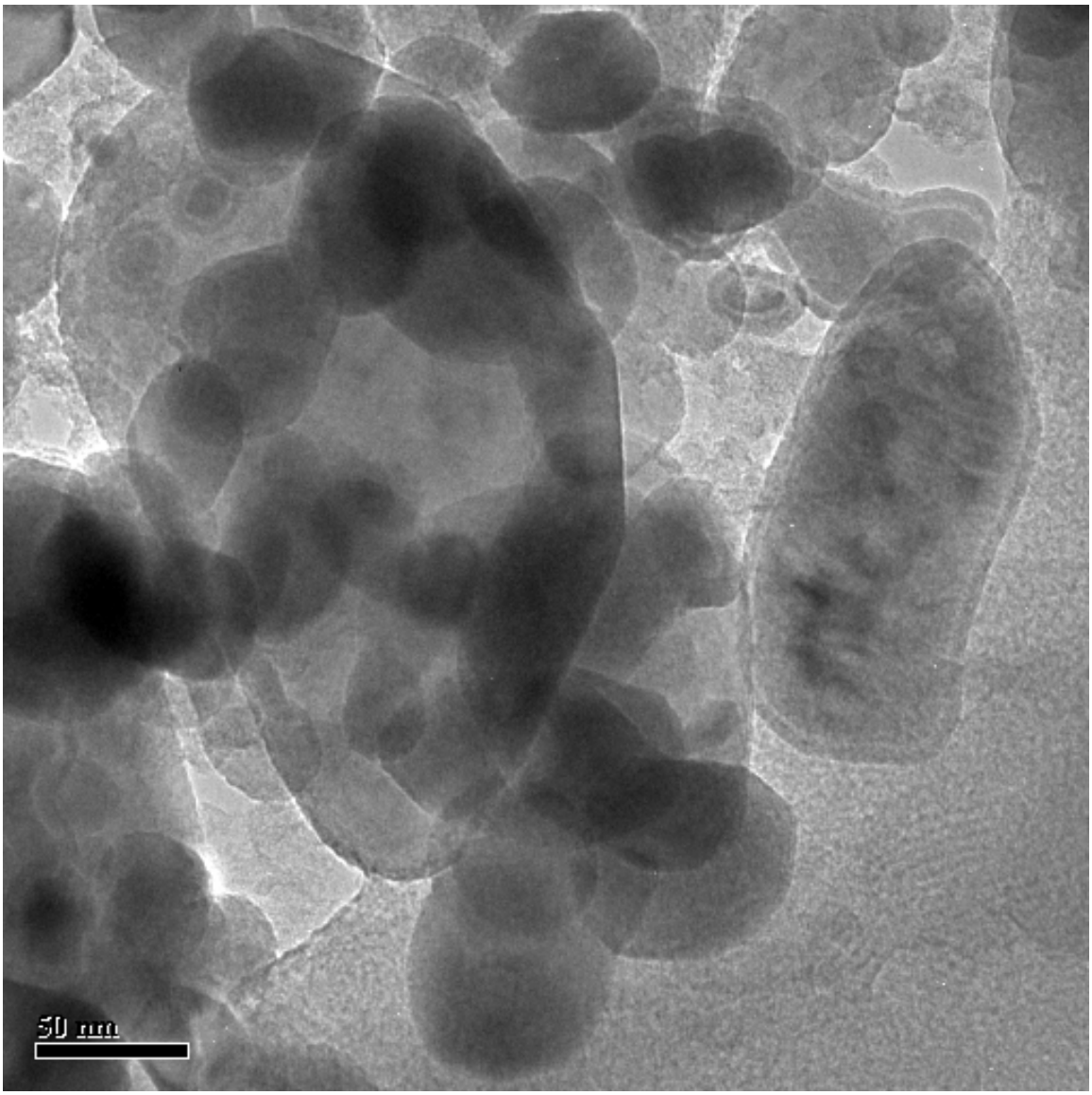

(b)

Figure 11. HRTEM image of a particle of sample S6 (collected after 596 h of FTS at 270 °C, 175 psig, and a syngas space velocity of 3.0 sl/h/g Fe): (a) large single crystal with largest dimension larger than 150 nm and some of the particle have outer rim structure; (b) single crystal of iron oxide covered with an outer layer of amorphous carbon of thickness about 10 nm.

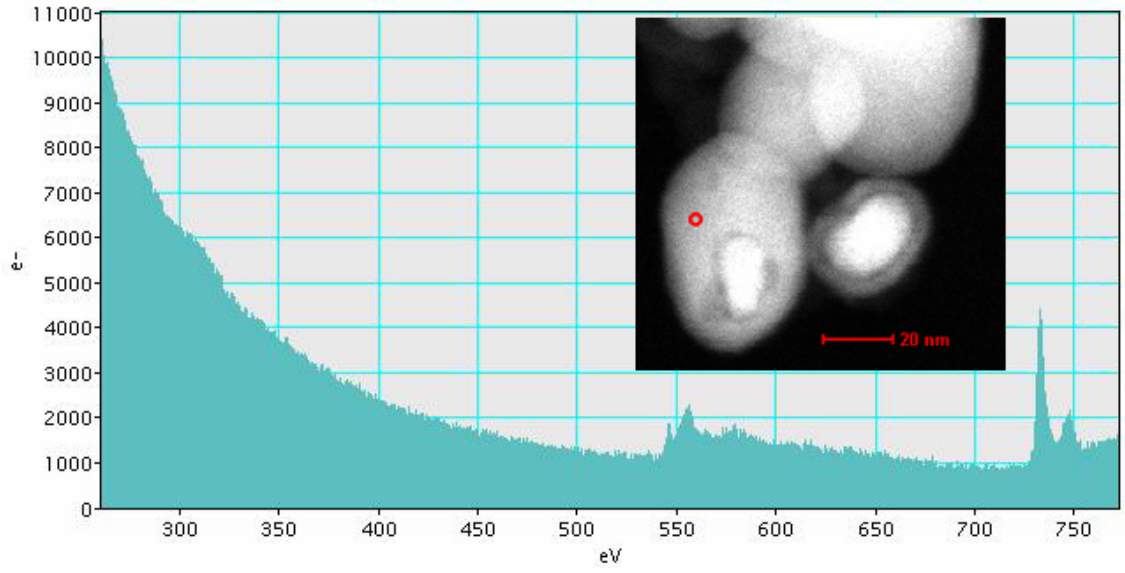

(a)

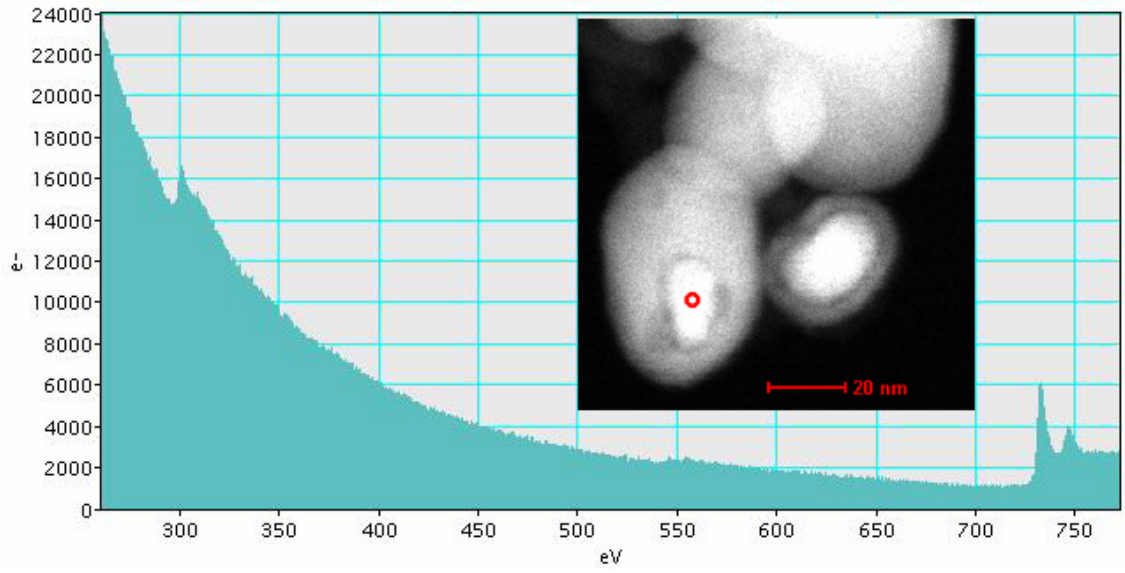

(b)

Figure 2.2-12. STEM-EELS measurements of the catalyst sample collected after FTS for 311h at 270 °C, 175 psig, and a syngas space velocity of 3.0 sl/h/g Fe. High-resolution STEM images are shown in insets. The red dots in HRSTEM images indicate the position where the EELS spectra were recorded.

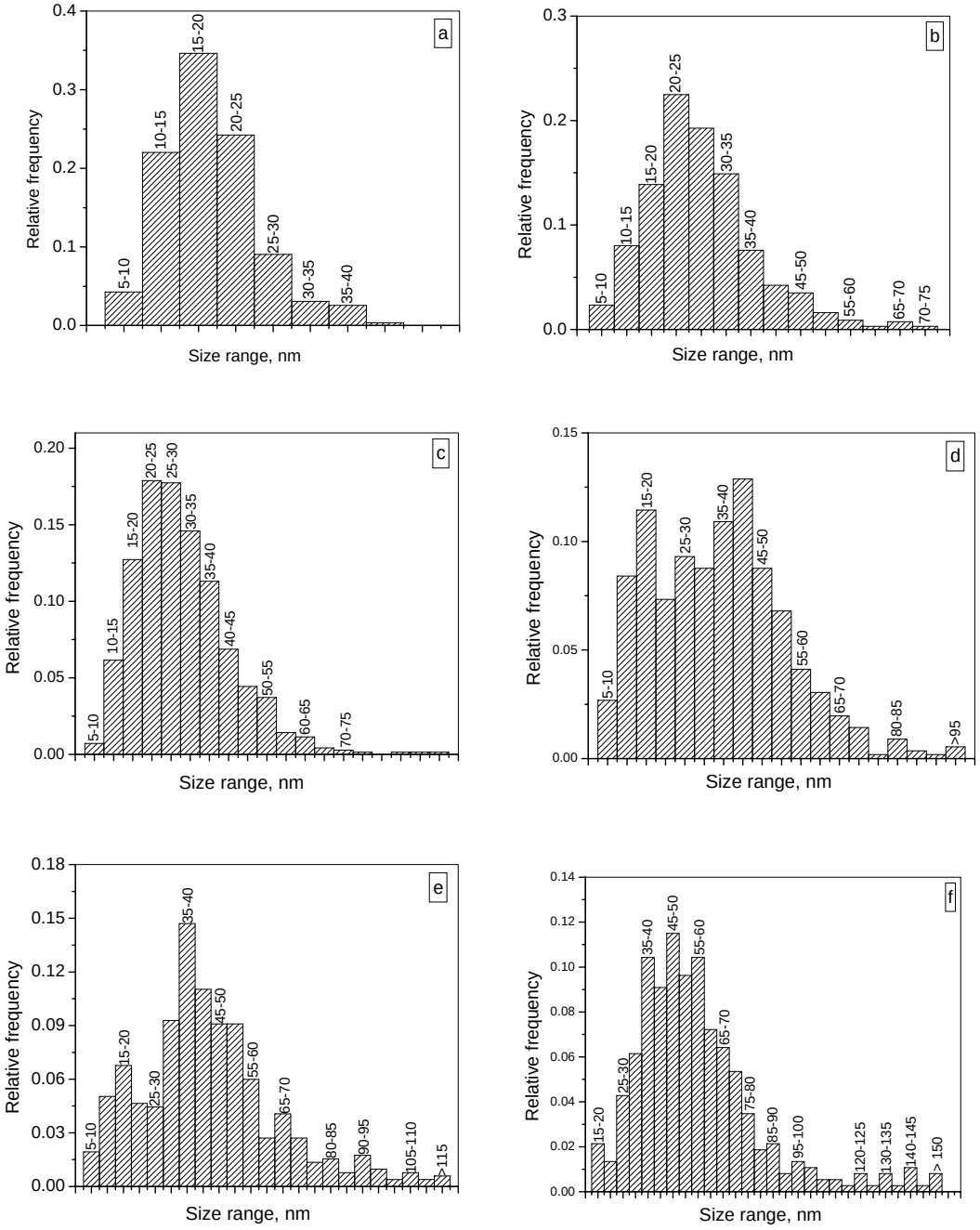

Figure 2.2-13. Relative particle size distribution of catalyst samples collected at different time-on-stream during FTS at 270 °C, 175 psig, and a syngas space velocity of 3.0 sl/h/g Fe: (a) after CO activation for 24 h; (b) 112.6 h; (c) 258.3 h; (d) 406.3 h; (e) 505.6 h; (f) 620.8 h.

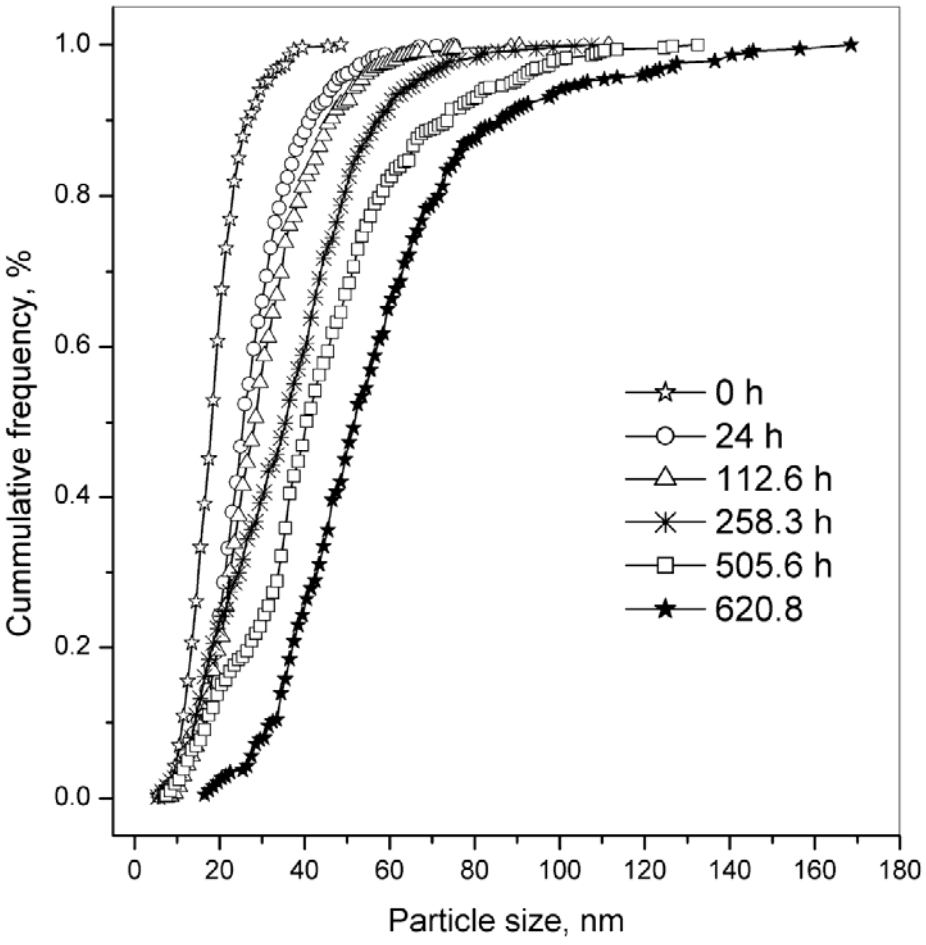

Figure 2.2-14. Cumulative number frequency distribution of the catalyst sample collected at different time-on-stream during FTS at 270 °C, 175 psig, and a syngas space velocity of 3.0 sl/h/g Fe.

Task 3. Phase II Slurry Bubble Column Pilot Plant Studies

3.3.1. ABSTRACT

A modified design of an existing slurry bubble column reactor pilot plant has been developed by integrating a filtration scheme which is composed of a low flow circuit (1-2 lpm) passing through the SBCR, and a higher flow rate circuit through the cross-flow filter. Filtration demonstration experiments using a mixture of FT wax and an ultra-fine iron were studied. In most of the times, the target purity level of less than 15 ppm iron in the permeate was attained. A constant flux maintenance module was developed which consists of interrupting the permeate flow for 30 seconds per half hour. This module was found to be effective in recovering the initial membrane fouling; however, the long-term steady-state flux was not achieved with the method. Flux stability was attained only after increasing the permeate off cycle to 1 hour per day in addition to 30 seconds off per half hour cycle.

3.3.2. INTRODUCTION

In the second phase of the current program, a pilot-scale SBCR system was to be integrated with a filtration scheme with procedures and equipment developed in Phase I. In Phase-I, filtration properties of various iron-based catalyst slurries was determined and the chemical and physical changes occurring during activation and FTS synthesis were evaluated. Our research has focused on understanding of the phase changes during activation/reduction and their associated effects on filtration properties. Additionally, cleaning/flux maintenance procedures were optimized for the various filter media types test in the research program.

In the beginning of this research program, our objective was to develop a single-stage filtration scheme that would produce a wax with clarity with a iron concentration less the 5 ppm. Based on our operating experience and analytical information gathered with the pilot-scale filtration module in Phase I, this objective was overly optimistic in hindsight. A two-stage system is required because of the combined stresses of catalyst loading and the formation of nano-scale carbide particles formed during activation and synthesis. Additionally, the fouling rate of the filter media is directly proportional to catalyst slurry concentration; thus, a primary separation stage would have the potential to lower the stress on the filtration membrane.

In Phase II, the objective was to address the technical barriers associated with integrating an improved filtration strategy into commercial FTS unit and to begin work to modify the CAER's 4 liter bubble column reactor to include the FT wax filtration scheme developed during the previous Phase of this research program. In the modified reactor system, a Moyno-type progressive cavity pump will be included to convert the reactor from a natural to forced circulation liquid circuit. The wax/catalyst slurry will have two separate flow paths: (1) a low flow circuit (1-2 lpm) passing through the bubble column, and (2) a higher rate slurry path through the cross-flow filter.

3.3.2.1. Existing Filtration Technologies for FTS Catalyst

Heavy wax products must be continuously separated from catalyst slurry before being removed from the reactor system. This insures that steady-state operation and nominal reactor liquid levels are maintained. Achieving an efficient wax product separation from the catalyst is one of the most challenging technical problems associated with slurry-phase Fischer-Tropsch synthesis.

Wax products obtained from internal filters (primary separation) still contain more than 0.1-1 wt% of iron [1]. Further processing or "polishing" is required to achieve an acceptable wax quality. The processing equipment located downstream determines the specifications for wax purity. For hydrocracking, the concentration of iron in the wax feed should be less than 2 ppm. Lowering iron content of the wax will reduce fouling of downstream hydrocracking catalyst, thus reducing product-upgrading costs. Achieving a high level of wax purity also minimizes the FTS catalyst make-up requirements. Accordingly, employing an efficient wax/separation process will improve the economic viability of FTS for both coal and natural gas-based systems.

A number of processes have been proposed in the literature to separate heavy wax liquids from catalyst slurries [1]. Most of these techniques can be classified as "primary" and "secondary" filtration. The former is to remove up to 90-99.5% of the catalyst fines while the latter is a polishing method that provides wax clarity sufficient for upgrading (less than 2 ppm as Fe). These methods can be further categorized as either internal (filter elements located inside the reactor vessel) or external.

Internal filtration methods, usually primary in nature, have the disadvantage of being easily accessible during normal operation of the reactor. Therefore, in anticipation of plugging problems, at least duplicate filtration systems must be installed to achieve high reliability in commercial settings. External filtration systems have the advantage of being more accessible for maintenance purposes; however, they usually require external pumps that could accelerate catalyst attrition. External piping circuits also tend to add to the complexity of the filter system design.

3.3.2.2. Internal Filtration Methods

Sasol [2] patented an internal filtration system for Fischer-Tropsch slurry bubble column reactor (SBCR) systems. Their filtration process consists of a plurality of wire mesh filter units connected in parallel within the bubble column reactor vessel. Critical parameters such as filtration and back-flushing rates per unit area of filter are specified in the patent. This system has the advantage of minimizing the hold-up of catalyst slurry outside the reactor vessel. However, internal systems are difficult or sometimes impractical to service without taking the reactor vessel off-line.

Lorentzen [3] developed and patented a process in which liquid products are separated from a slurry phase containing catalyst particles using a series of vertical reaction tubes in parallel. A separate filter member ring is provided near the top of each tube. The filtrate from each ring overflowed into a weir and centrally collected for further processing. Several configurations of the filtration zone are described in detail.

3.3.2.3. External Filtration Methods

A simple method commonly used for Fischer-Tropsch catalyst/wax separation is sedimentation by gravity and/or centrifugal force. The practicality of sedimentation is limited due to the low terminal velocity of submicron particles that are abundant in the catalyst fines. Large settling chambers with residence times exceeding 3 hours are needed to achieve a reactor wax of less than 0.1 wt%. Many of the new separation techniques described in the literature employ simple hydroclones or dynamic settlers as “primary” separation device before undergoing secondary “polishing” of the wax product.

ConocoPhillips [4] patented a simple settling device reported to produce a “sub-particle rich” stream and a catalyst-lean stream that removed from the SBCR system. The settling device relies on laminar “Stokes Law” gravitational settling where large particles, partially impeded by a baffle, exit near the bottom of the device. The catalyst-lean stream exits near the top of the settling chamber after flowing under the baffle. Here, catalyst-lean is defined as “A stream of slurry from which the majority of the catalyst particles have been removed”.

Rentech [5,6] patented a dynamic settler that in one embodiment utilizes the momentum of catalyst particles exiting an enclosed nozzle to force solids to exit near the bottom of settling chamber enclosure. Clarity of the wax exiting the top of the settler depends on the superficial velocity of the wax in the annular region above the nozzle. Thus, a larger settler diameter results in a clearer wax. Typically, the wax concentration of the clarified wax is less than 0.5 wt% with an entering slurry concentration of 10-20wt%. The dynamic settler was further refined by the addition of several parallel channels (or a “honeycomb” type structure) that minimizes turbulence in the clarified wax region. Thus the mixing of the clarified wax with the slurry exiting the nozzle jet is limited. They report in their patent that with particle sizes greater than 6 μm, a clarified wax purity of less than 0.5wt% can be achieved.

Mobil patented a process for removing catalyst fines from wax slurry using a magnetic separator [7]. Catalyst fines are held by a magnetized filter element while the wax passes unabated. Two external pumps are used in the system; one pump extracts a portion of the reactor slurry while another pump returns the captured catalyst particles to

the BCR. The operational cost of their system is relatively low; however, the capital costs of the magnet assemblies are reported to be expensive.

Shell Oil [8], outlined a cross-flow filtration process in a U.S. Patent. Their system extracts gas and catalyst slurry from a BCR column via an external pump. The slurry is degassed by a hydroclone and is directed to a cross-flow inertial filter. A slurry velocity of 1 to 6 m/s must be maintained for efficient filter operation. The system has the disadvantage of requiring an external pump that could accelerate catalyst attrition.

3.4. EXPERIMENTAL

3.4.1. Original SBCR Configuration

In the initial configuration, the CAER bubble column had a 5.08 cm diameter and a 2 m height with an effective reactor volume of 3.7 liters (Figure 3.1). The synthesis gas passed continuously through the reactor and was distributed by a sparger near the bottom of the reactor vessel. The product gas and slurry exited the top of the reactor and passed through an overhead receiver vessel where the slurry was disengaged from the gas-phase. Vapor products and unreacted syngas exited the overhead vessel, entered a warm trap (333 K) followed by a cold trap (273 K). A dry flow meter down stream of the cold trap measured the exit gas flow rate.

A dip tube, inserted into the reactor vessel, recycled the Fischer-Tropsch catalyst slurry via a natural convection loop. The unreacted syngas, Fischer-Tropsch products, and slurry exited into a side port near the top of the reactor vessel and enter a riser tube. The driving force for the recirculation flow is essentially the difference in density between the fluid column in the riser (slurry and gas) and that of the dip-tube (slurry only). The dip tube provided a downward flow path for the slurry without interfering

with the upward flow of the turbulent syngas slurry mixture. Thus, to some degree, back mixing of the slurry phase and wall effects in the narrow reactor tube were minimized.

An automatic level controller was located in the overhead slurry/gas separation tank. This insured a constant inventory of catalyst particles being maintained in the reactor vessel as long as the superficial gas velocity within the column was constant.

A sintered metal cross-flow filter tube was located in the liquid downcomer between the overhead separation vessel and the reactor. The filter was a flow-through device having a sintered metal tube in a shell. Filtered wax was extracted radially through the tube while slurry flowed downward in the axial direction. The shear force of the axial slurry flow prevented excessive caking of the catalyst around the filter media. Filtered wax was metered into a storage tank through a letdown valve operated by the overhead liquid level controller. Pressure drop across the filter media (or trans-membrane pressure) was varied manually by varying the wax storage tank pressure. The filter assembly was configured such that the filter media could be replaced on-line, without aborting or interrupting the reactor run.

The level or volume of the slurry within the receiver was continuously monitored by measuring the differential pressure across the height of the vessel. Argon was purged through each of the pressure legs to keep the lines free of slurry. Slurry volume within the receiver was controlled to be no more than 1.3 liters by removing wax from the reactor system via the level control valve. The unfiltered slurry flowed back to the reactor via a natural convection loop through a dip-tube exiting near the bottom of the reactor.

3.4.2. Modified 2-Stage Filtration System for the SBCR Pilot Plant

The SBCR filtration scheme for Phase II is shown schematically in Figure 3.2. As with the previously mentioned SBCR configuration, the modified unit consists of a gas/liquid separator located above the reactor vessel (see Figure 3.3). The internal liquid downcomer was removed. Instead, the downcomer was moved outside the reactor vessel and was connected to the suction side of a moyno-type (Liberty progressive cavity) pump. The pump discharge is connected to a primary separation device (an inertial separator similar to a hydroclone, see Figure 3.4). Since the slurry pump is a positive displacement device (i.e., no slurry slippage inside the pump), the total flow should remain the same regardless of pressure changes incurred by the temporary switching of the reactor circuit. A catalyst rich stream is recycled to the reactor vessel while the lean catalyst/slurry stream is diverted to a secondary filtration loop.

The fraction of clarified slurry entering the secondary loop is controlled via a throttle valve. The secondary flow rate is measured by a coriolis flow meter (see Figure 3.5). Quantifying the flow is important because the slurry velocity is crucial in cross-flow filtration. Polishing of the clarified slurry is by a cross-flow filter element (eg, Aucusep), similar to the type supplied by Pall Filtration in Phase I (see Figure 3.6). The stainless steel membranes of the filter have a nominal pore size of 0.1 μm. The surface of the filter media substrate is coated with a proprietary sub-micron layer of zirconia. Ideally, the axial velocity through the crossflow unit should be greater than 4-6 m/s to minimize the boundary layer of particles near the membrane surface. The wax permeate flow from the filter is limited by a control valve actuated by a reactor level controller. Hence, a constant inventory of slurry is maintained within the SBCR system as long as

the superficial gas velocity remains constant. Changes in the gas hold-up due to a variable gas velocity will need to be calculated so that the space velocity can be accurately quantified.

The flux of the clean permeate through the cross-flow unit wax is controlled by the pressure in the let-down vessel or hot trap. Therefore, the trans-membrane pressure (TMP) can be fixed for a given filtration event. The TMP can be changed manually by varying the set point of the pressure regulator connected to the let-down vessel. The flux rate is measured by weighing the mass of permeate accumulated in the collection vessel hot trap.

A filtration event is initiated by the overhead vessel level controller. The wax permeate flow from the filter will be switched on by a control valve between the permeate discharge of the cross-flow unit and the collection vessel. Hence, a relatively constant inventory of slurry will be maintained within the SBCR system as long as the superficial gas velocity remains constant. Changes in the gas hold-up due to a variable gas velocity will need to be calculated so that the space velocity can be accurately quantified.

The level or volume of the slurry within the overhead receiver is continuously monitored by measuring the differential pressure across the height of the vessel. Argon is purged through each of the pressure legs to keep the lines free of slurry. Slurry volume within the receiver is controlled to be no more than 1.3 liters by removing wax from the reactor system via the level control valve. A more detailed piping diagram is shown in Figure 3.7.

The flux maintenance system developed in Phase I was added to the permeate side of the filtration system. As shown in Figure 3.8, the back flush system consists of a piston pump that is triggered by a computer controlled timer. The back-flush fluid consists of cleaned permeate stored in a 40 ml tube bomb located near the suction side of the piston pump. This system is used throughout the study to develop an optimum cleaning program that can sustain a permeate flux rate over a many days.

3.4.3. Filtration Test Platform

An existing pilot plant platform was modified into a crossflow filtration test unit. This unit, depicted schematically in Figure 1.1-6, allows several types of crossflow filter media to be investigated under simulated FTS conditions. Three prototype filtration modules were received from Pall, Inc. The modules have an inlet (permeate or filtrate) and outlet (retentate) ports with ½" tubing ends, and a permeate port, located near the midpoint of the unit. The filters' stainless steel membranes have a nominal pore size of 0.1 μm. The surface of the filter media substrate is coated with a proprietary sub-micron layer of zirconia.

The filtration piping and instrumentation is heated via several circuits of copper heat-trace tubing. A Therminol 66 heat transfer fluid is circulated through the heat-trace tubing using an electrically-heated hot oil system. The temperature controller was calibrated to operate over a temperature range of 180 to 250 ^{o}C.

Data gathering and process control functions are accomplished by a National Instruments real-time computer system. A 98 liter (26 gallon) slurry mixing tank is heated by hot-oil circulation jacket. Slurry mixtures of catalyst and wax are loaded batch-wise into the system. A Liberty Process Equipment (progressive cavity) pump is

used to circulate the mixture through the crossflow filter element. A manually-actuated valve, located downstream of the filter element, maintains a slurry flow rate set-point of 2 to 40 lpm.

Unfiltered slurry (or retentate) passing through the filter tube is recycled to the mixing tank. The differential pressure across the filter medium or trans-membrane pressure (TMP) is automatically controlled by a let-down valve. The permeate can be recycled to the slurry tank for continuous filtration simulation (in order to maintain a constant solids concentration in the system) or can be collected and removed from the system to test semi-batch filtration schemes. The permeation rate is periodically measured by diverting the stream into a collection flask over a convenient time interval. Samples can be collected before the filter for characterization. In tests where the catalyst is activated, a gas pad of CO or syngas can be applied to the system; otherwise the system vapor space is purged with inert gas such as argon or nitrogen. Slurry temperature, simulating the FTS activation conditions, can be controlled up to 240 °C. Modular filtration media can be tested under various filtration rates, differential pressures and operating modes. The system is designed so that the filter unit can be bypassed in order to change filters while the slurry continues recirculation.

3.4.4. Constant Filter Flux Maintenance System

The flux maintenance system is capable of back flushing the membrane with a piston pump that is triggered by a computer controlled timer. The back-flush fluid consists of cleaned permeate stored in a 40 ml tube bomb located near the suction side of the piston pump. However, backflushing with clean permeate is only used as a last resort. Preferably, the maintenance procedure is to turn off the permeate flow on a short

but regular period. This system was used throughout the study to develop an optimum cleaning program that can sustain a permeate flux rate over a many days.

3.5. RESULTS AND DISCUSSION

During the start-up of the modified SBCR/Filtration system, several problems were encountered with the pump used to circulate the wax/catalyst slurry though the cross-flow filter element and reactor. The pump was purchased specifically for this purpose and was manufactured by Liberty. It is a Moyno-type progressive cavity design capable of delivering 20 lpm of FT slurry at 230 ^{o}C. The unit has a stainless steel rotor with a Viton® (fluoroelastomer) stator designed for pumping slurries at Fischer-Tropsch synthesis and activation conditions.

Initially, the as-received pump could not pass a 13.8 bar (200 psig) static pressure test at ambient temperature. Consequently, the pump was returned to the manufacturer for extensive seal modifications. Upon receiving the modified pump, the unit was placed into service for a "hot" shakedown test with Durasyn oil at pressure (175 psig). The modified seal continued to leak at a small but acceptable rate on the order of 1 g/min. However, leak problems were encountered in the threaded seal of the stator and the pump housing. The stator was resealed with a thick Teflon tape and a high-temperature pipe sealant which initially slowed the total system leaks to less than 50 g/hr.

At this point, the system was tested with catalyst for activation and synthesis, in the hopes that the seal leak rates would be impeded by the presence of small catalyst particles. The FTFE 20-B (L-3950) [Fe, 50.2%; Cu, 4.2%; K, 1.5% and Si, 2.4%] was utilized. This is part of the batch used for LaPOrte run II. The catalyst was activated at 270°C with CO at a SV of 9 sl/h/g catalyst for 48 h. A total of 1100 g of catalyst was

taken and 7.9 l of C30 oil was used as the start-up solvent. At the end of the activation period, an attempt was made for Fischer-Tropsch synthesis at 230 °C, 175 psig, syngas SV = 9 sl/h/g catalyst, $H_2/CO = 0.7$. However, the catalyst was found to be completely inactive for Fischer-Tropsch synthesis. Sulfur and fluorine is known to poison iron based Fischer-Tropsch catalysts. Since stator of the pump is made of Viton®, which is a fluoroelastomer, it was suspected that activation of the catalyst with elevated temperature (> 270 ^oC) results in release of fluorine which acted as severe catalyst poison. Sulfur content of the catalyst slurry was found to be 0.3 wt%. We were not certain about the source of the sulfur poisoning as the elastomers inside pumps are commercial products and detailed compositions are not available. It is possible that during the activation of the catalyst at elevated temperature (> 270 ^oC) the elastomer inside the pump released sulfur compounds thereby totally deactivating the iron-based catalyst. Additionally, difficulties in maintaining an acceptable leak rate from the pump seal and stator housing continued after an exhaustive effort of implementing counter measures. Consequently, the system leak rate always exceeded the expected production rate of wax; therefore, no online filtration could be accomplished.

In order to test the filtration scheme during a long-term test, the filtration system was operated independent of the SBCR pilot system in the continuous filtration plant at low pressure (1.7 bar at the pump discharge). In lieu of FT wax produced directly from the bubble column, we prepared a test slurry batch containing FT wax obtained from previous pilot SBCR and CSTR reactor tests and activated ulrafine Mach I iron catalyst (0.26 wt% as raw catalyst). The molecular weight distribution of the composite wax is shown in Figure 3.9. The goal of this test was to monitor and record filter flux

measurements over long time on-stream periods (500+ hours). Various flux maintenance or filter cleaning procedures were employed over the long term test, attempting to stabilize the flux over time.

3.5.1. Long Term Filtration Run with FT Wax (Ultrafine Iron Catalyst and FT Composite Wax)

Various flux maintenance or filter cleaning procedures were employed over the long term test, attempting to stabilize the flux during use. These studies examined flux values for the 26" filter with a media area of 0.0198 m^2 (0.213 ft^2), a slurry density of approximately 0.69 g/cm^3 at 200°C, an ultrafine iron (NANOCAT®) catalyst concentration of 0.26 wt%, 17 kg (37.5 lbs) of FTS wax, and a TMP of 1.4 bar (20 psid). The filtration process was run in a recycle mode, whereas clean permeate was added back to the slurry mixture, thus allowing the catalyst concentration to remain approximately constant over the course of the run (given minor adjustments for ~5 ml permeate and slurry samples taken throughout the test).

Initial flux readings decreased dramatically as a mass transfer boundary layer formed on the filter media. This boundary layer appears to remain somewhat constant after about 6 hours online, whereas the slope of the flux versus time graph (Figure 3.10) becomes fairly linear. This linear decrease in flux continues over the next 43 hours. This could be attributed to fouling of the membrane by the small iron/iron carbide particles.

At this point, a passive flux maintenance procedure was employed (at 49.33 hours TOS), introducing a 30 second flux shut-off period every 30 minutes. This allowed the catalyst slurry to recirculate through the filter with no radial permeate flow through the filter membrane. This axial flow is designed to relax the filter membrane, possibly

releasing any embedded particles and aiding in increasing the flux. The flux did not initially increase after the TMP was reinstated to 1.4 bar. It did however, slowly increase after a few of the back pulse cycles were able to have an effect on the filter membrane. After 12 of the 30 second back pulse cycles (~6 hours), the flux increased 161% overall (from 0.5 to 1.3 lpm/m^2 or 17.6 to 46.0 GPD/ft^2). Thereafter the flux slowly decreased over the next 280 hours, down to 0.76 lpm/m^2 or 27.0 GPD/ft^2 (a 41.3% loss in flux over that span).

An active flux maintenance procedure was initiated at this point, beginning with a 2 second back flush of clean permeate through the filter membrane. Again, this flux maintenance cycle was continued every 30 minutes for just over 24 hours. The flux initially recovered to 0.90 lpm/m^2 (32.0 GPD/ft^2), but fell again within 24 hours to baseline value of 0.76 lpm/m^2 (26.7 GPD/ft^2) without including clean permeate backflush. The flux maintenance was again returned to passive flux maintenance (no backpulse with clean permeate), only increasing the flux off time to 60 seconds every 30 minutes. Thereafter, the flux steadily decreased over the next 120 hours from 0.77 to 0.58 lpm/m^2 (27.3 to 20.4 GPD/ft^2). At 480 hours online a 1 hour flux off cycle was attempted, increasing the flux back to 0.62 lpm/m^2 (29.1 GPD/ft^2), a 42.6% increase. The flux off cycle was then returned to the 60 second off cycle for the next 48 hours, once again showing a flux decrease to 0.62 lpm/m^2 (21.9 GPD/ft^2). Another 1 hour flux off cycle returned the flux to 0.72 lpm/m^2 (25.3 GPD/ft^2 only, a 15.5% increase). The next 23 hours using a 1 minute flux off cycle every 30 minutes showed a much more slight decrease in flux (down to 0.65 lpm/m^2 or 23.1 GPD/ft^2). A final 1 hour flux off cycle showed minimal flux increase (0.04 lpm/m^2 or 5.6%).

In Figure 3.11, the iron content of both the slurry and permeate samples is displayed versus the time-on-stream. The permeate purity was consistently below 35 ppm (as Fe) for the entire run with over 85% below 16 ppm level. The variation over iron content could be due to sampling during or after flux maintenance events which can disturb the boundary layer of submicron particles on the membrane surface.

At about 560 hours online the flux was shut off for the overnight period to clean the filter for a flux versus TMP test. The flux versus TMP test (see Figure 3.12) indicated a rather linear relationship between the two variables, with the highest flux (0.85 lpm/m^2 or 29.9 GPD/ft^2) obtained at the upper end of the TMP range 1.72 bar (25 psig).

3.6. CONCLUSIONS

A successful filtration demonstration run using a mixture of FT wax and an ultra-fine starting catalyst was completed. For the most part, the target purity level of less than 15 ppm iron was attained in the final wax products. A simple flux maintenance procedure of interrupting the permeate flow for 30 seconds per half hour was effective in recovering the initial membrane fouling; however, the long-term steady-state flux was not achieved with the method. Flux stability was attained only after increasing the permeate off cycle to 1 hour per day in addition to 30 seconds off per half hour cycle.

REFERENCES

[1] Zhou, P.Z. “Status of Fischer-Tropsch Slurry Reactor/Catalyst Wax Separation Techniques”, Prepared for the U.S. Department of Energy, Burn and Roe Services, 1991.

[2] Jager, et al., “Process for Producing Liquid and Optionally Gaseous Products from Gaseous Reactants”, United States Patent 5,599,849, February 4, 1997.

[3] Lorentzen, et al., “Solid/Liquid Slurry Treatment Apparatus and Catalytic Multi-phase Reactor ”, United States Patent 5,520,890, May 28, 1996.

[4] Espinoza, R.L., et al., “Solid-Liquid Separation System”, United States Patent 6,833,078; December 21, 2004.

[5] Benham, et al., “Catalyst/Wax Separation Device for Slurry Fischer-Tropsch Reactor”, United States Patent 6,068,760, May 30, 2000.

[6] Bohn, M.S., and J.E. Siebarth, “Dynamic Settler”, United States Patent 6,730,221, Mat 4, 2004

[7] Brennan, et al. , “Separation of Catalyst from Slurry Bubble Column Wax and Catalyst Recycle ”, United States Patent 4,605,678, August 12, 1986.

[8] Engel, et al., “Method for Separating Liquid from a Slurry ”, United States Patent 5,900,159, May 4, 1999.

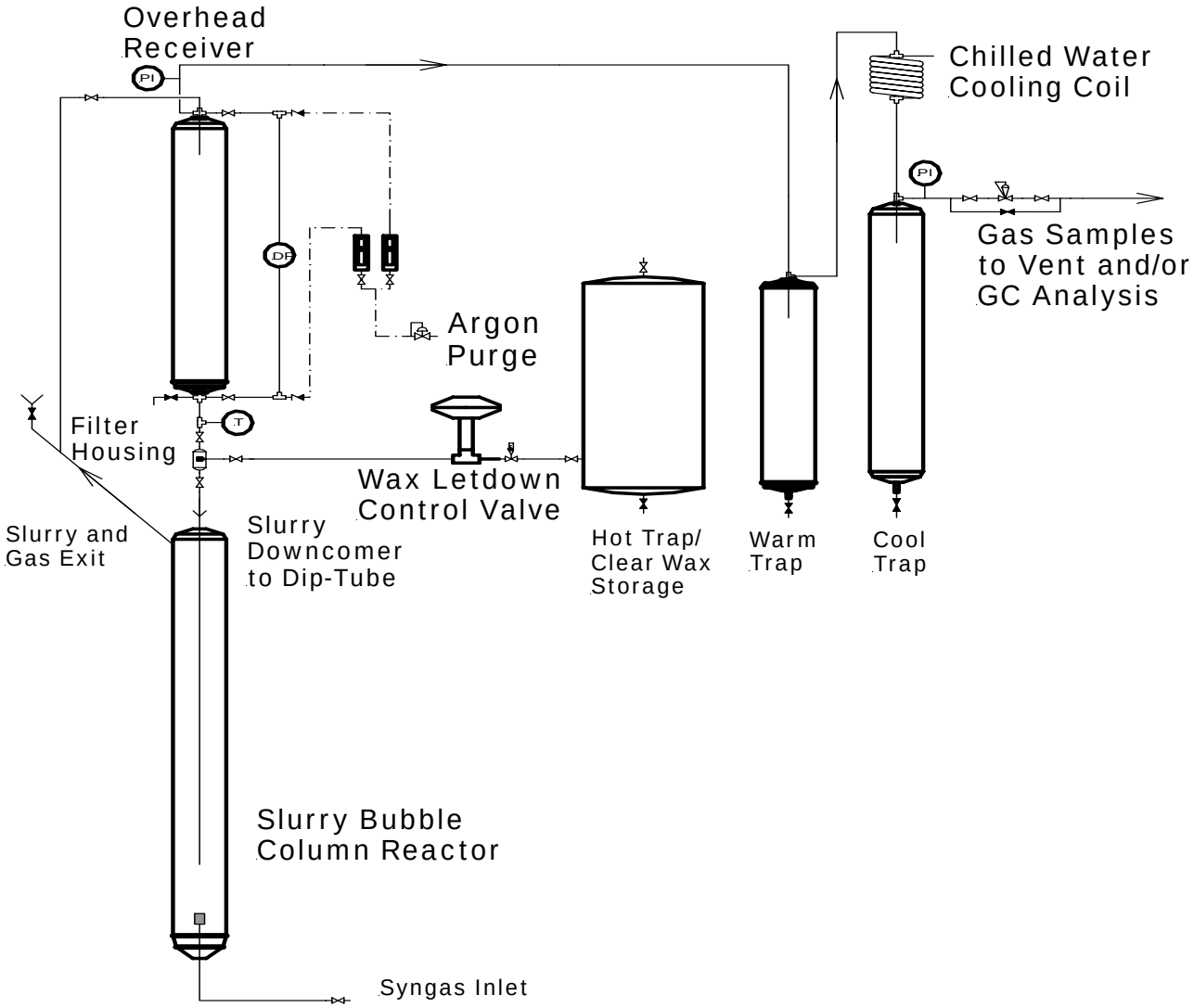

Figure 3.1. Schematic of the original configuration of CAER slurry bubble column reactor pilot plant.

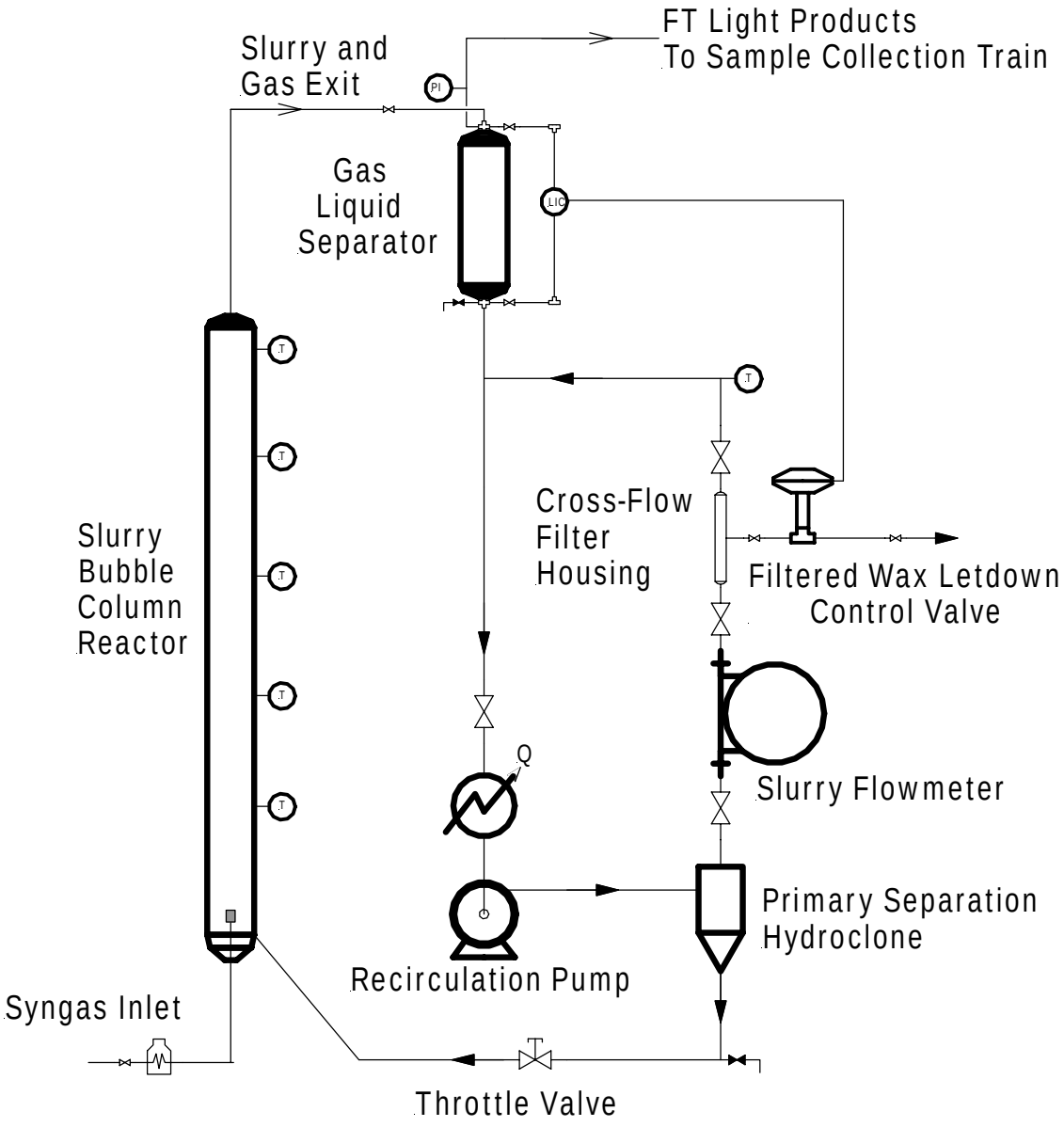

Figure 3.2. Modified SBCR with improved filtration scheme.

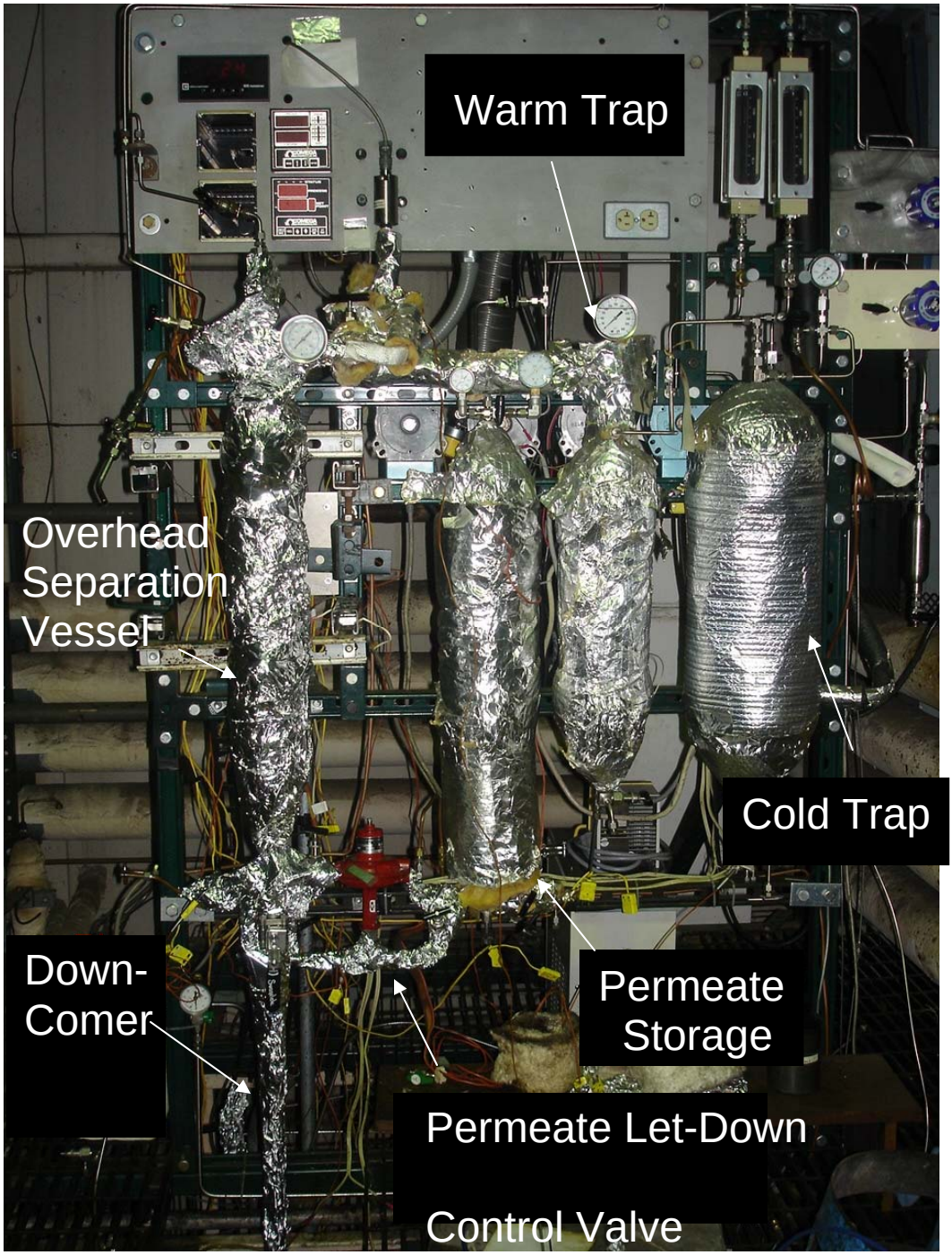

Figure 3.3 Overhead receiver and sample traps.

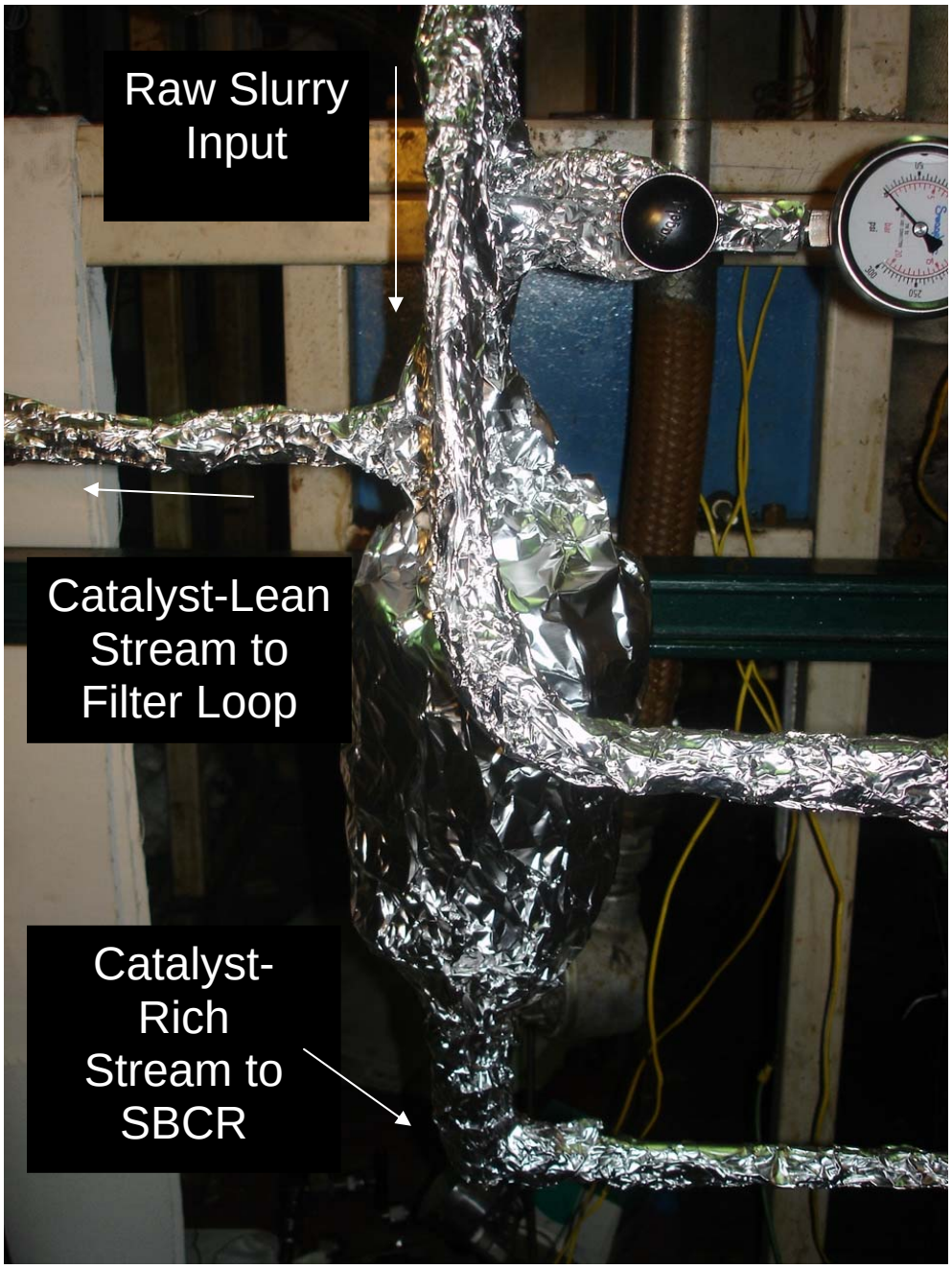

Figure 3.4. Hydroclone-type primary separation device.

Figure 3.5. Newly installed slurry coriolis flowmeter.

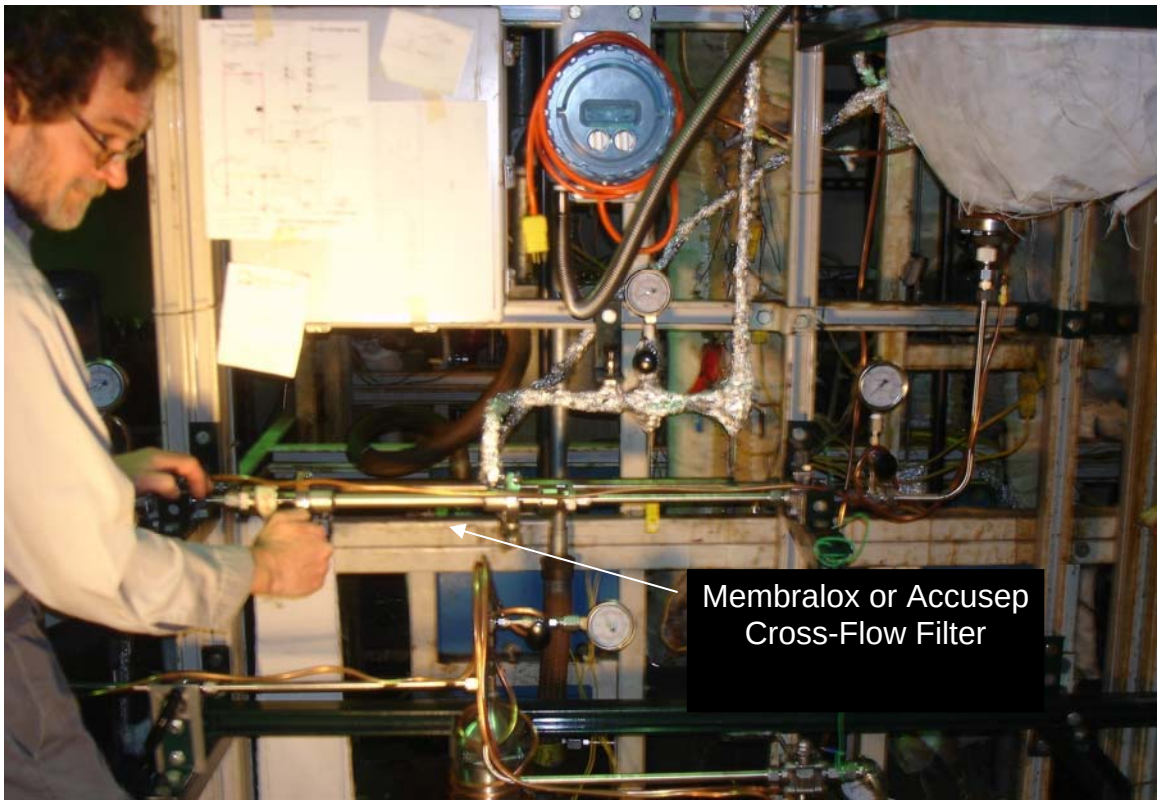

Figure 3.6 Installation of the filter tube assembly.

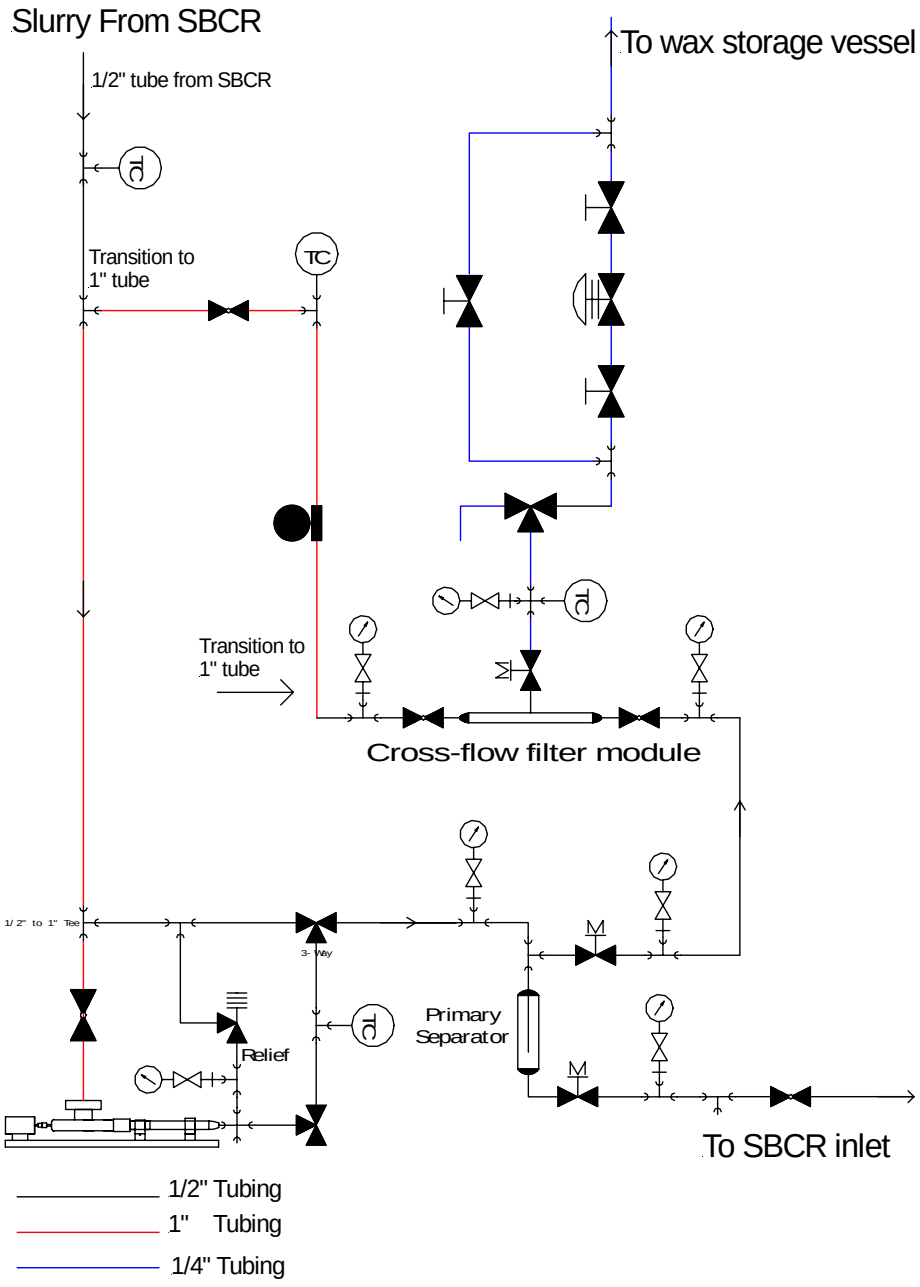

Figure 3.7 Piping diagram detail of the filtration loop.

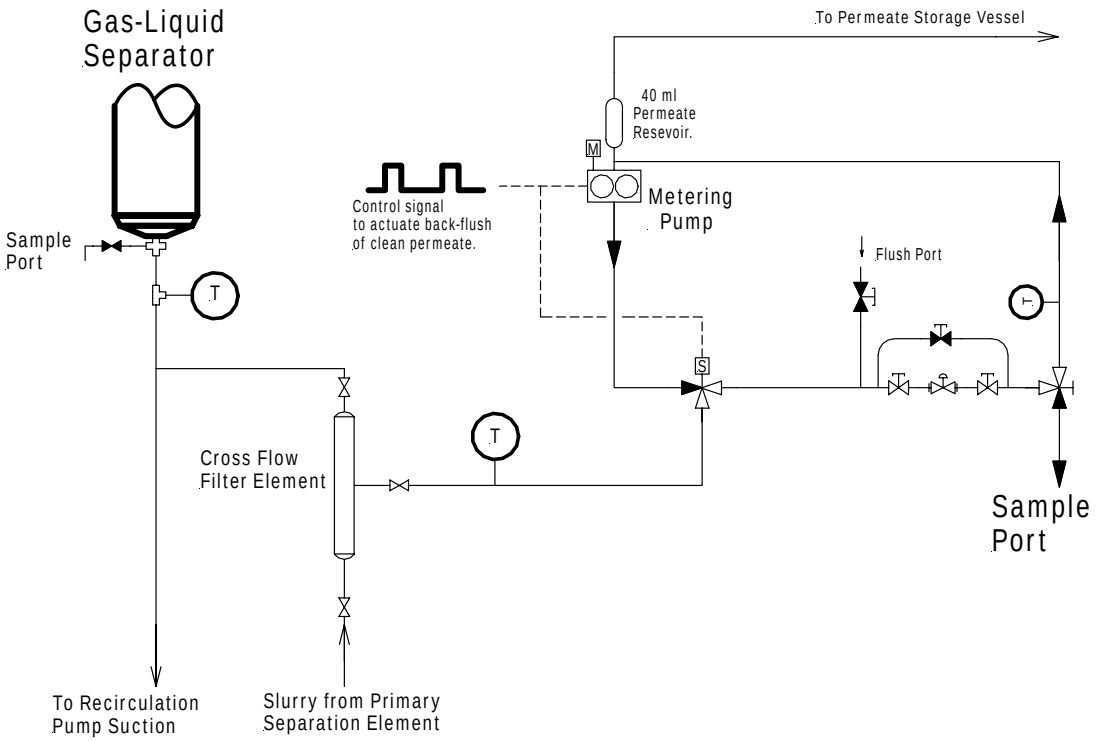

Figure 3.8. Proposed constant flux maintenance system in the modified design of SBCR unit.

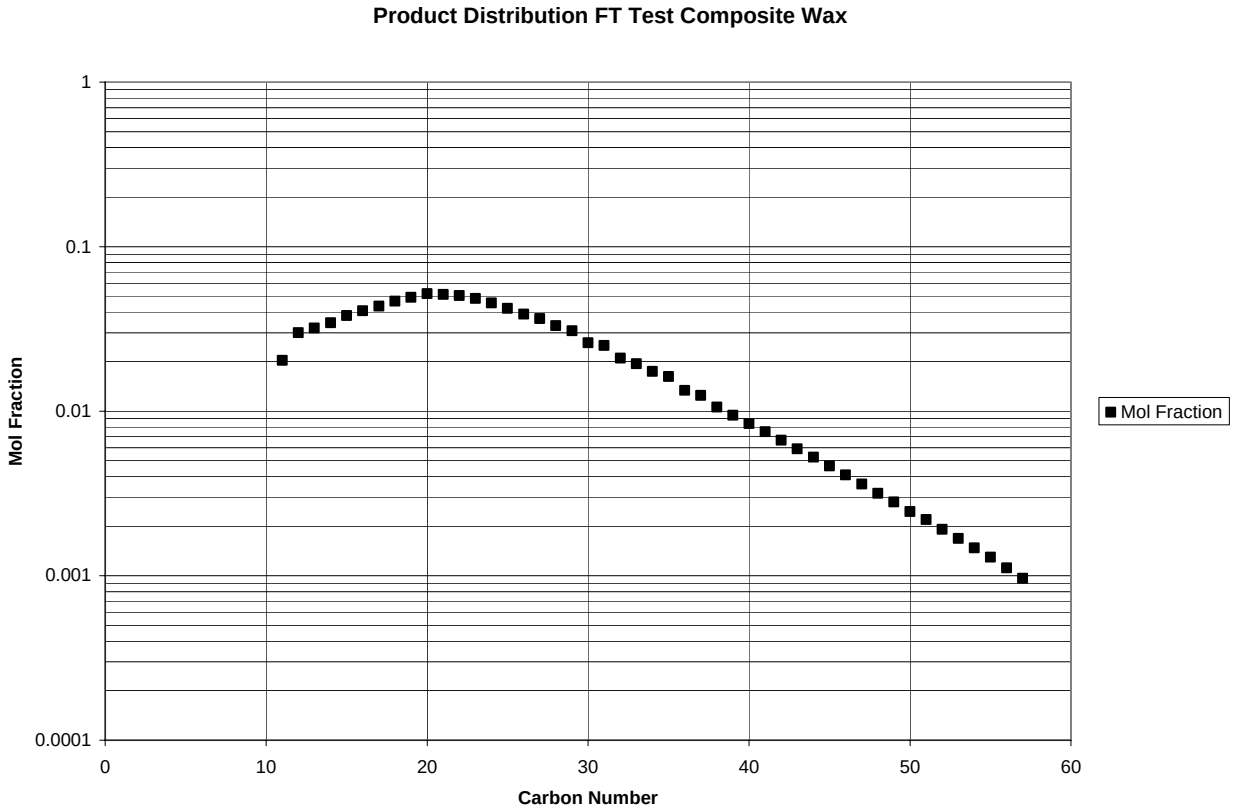

Figure 3.9 Product Distribution of the Composite FT Wax Used in the Long-term Filtration Run

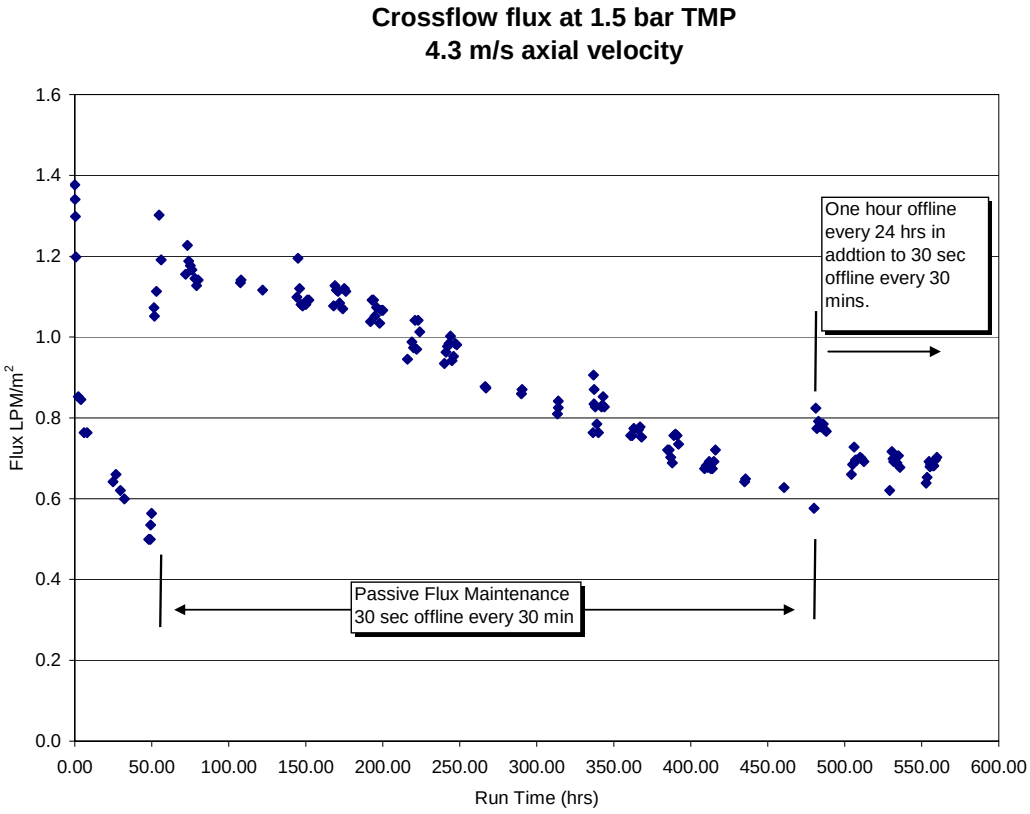

Figure 3.10. Variation of permeate flux against time.

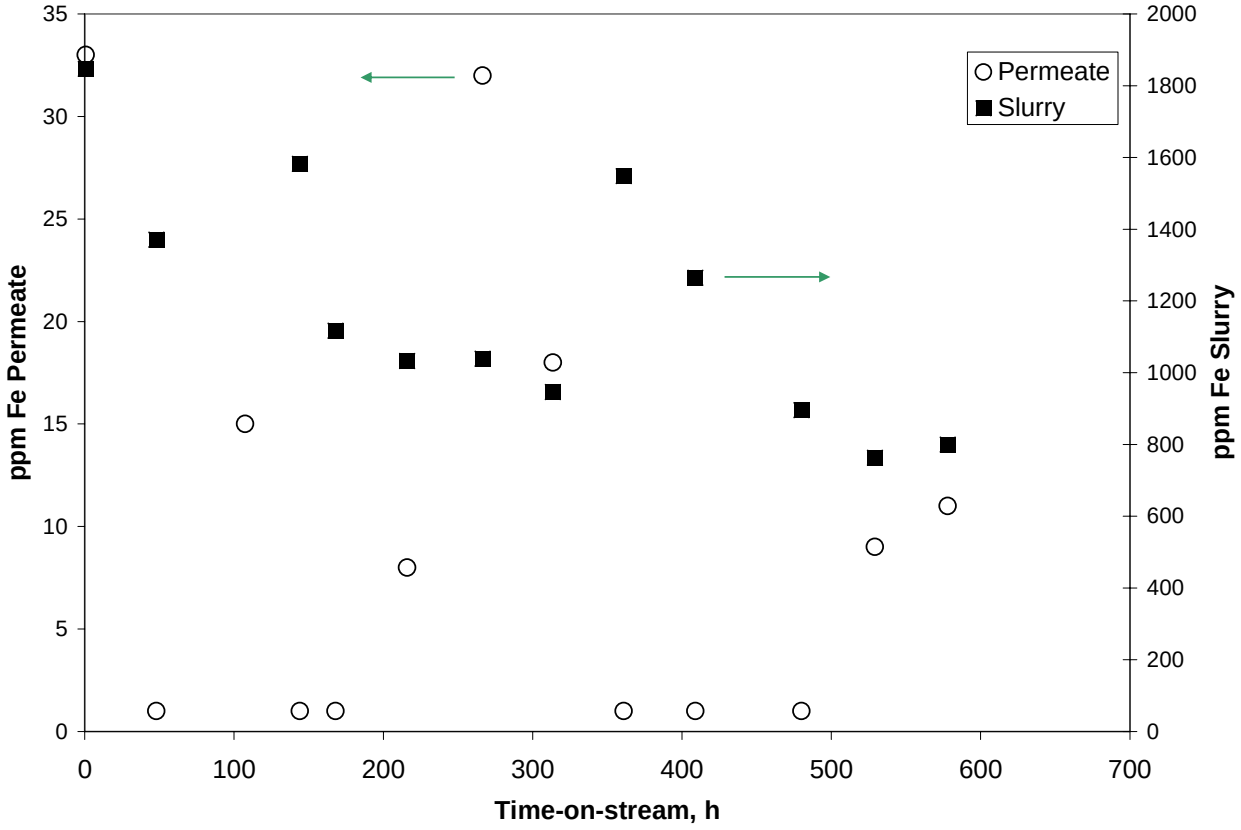

Figure 3.11. Demonstration run in the filtration pilot plant: variation of iron concentration of slurry (retentate) and permeate samples at different times.

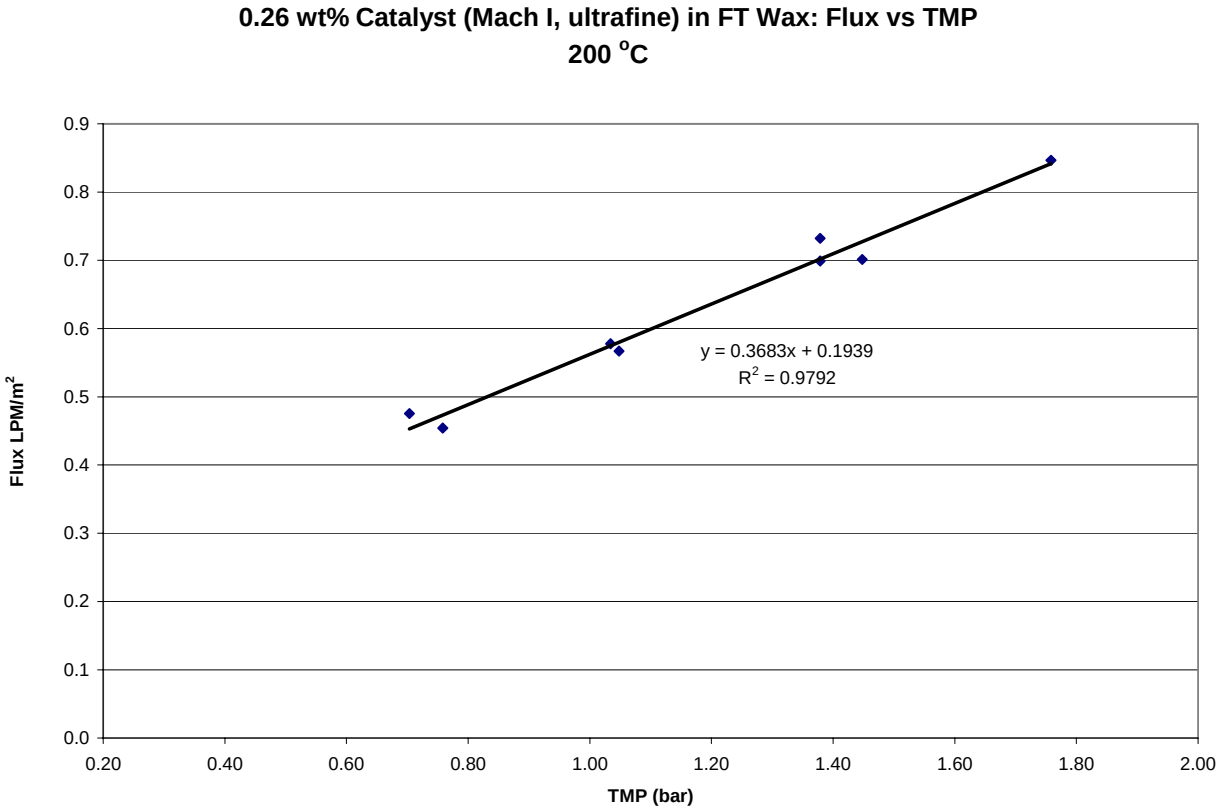

Figure 3.12 Plot of permeate flux against trans-membrane pressure. Data taken after 500 h (near end) of continuous experiment.